

THÈSE DE DOCTORAT

Soutenue à Aix-Marseille Université
le 17 novembre 2020 par

Teobaldo Luda di Cortemiglia

Modélisation intégrée du confinement des plasmas de tokamak
combinant la physique du coeur et du piédestal au bord

Discipline

Physique et Sciences de la Matière

Spécialité

Energie, Rayonnement et Plasma

École doctorale

Physique et sciences de la matière (352)

Laboratoire/Partenaires de recherche

PIIM - Physique des Interactions Ioniques et Moléculaires, Marseille, France
Max-Planck-Institut für Plasmaphysik, Garching, Germany

Composition du jury

Olivier SAUTER EPFL	Rapporteur
Howard R. WILSON York Plasma Institute	Rapporteur
Clarisse BOURDELLE IRFM, CEA	Examinatrice
Alexei POLEVOI ITER	Examineur
Yann CAMENEN CNRS	Invité
Peter BEYER Aix-Marseille Université	Directeur de thèse
Clemente ANGIONI IPP Garching	Co-directeur de thèse



DOCTORAL THESIS

Sustained at Aix-Marseille University
on November, 17th 2020 by

Teobaldo Luda di Cortemiglia

Integrated modeling of tokamak plasma confinement combining
core and edge pedestal physics

Discipline

Physique et Sciences de la Matière

Specialty

Energie, Rayonnement et Plasma

Doctoral school

Physique et sciences de la matière (352)

Laboratory/Research partners

PIIM - Physique des Interactions Ioniques et Moléculaires, Marseille, France
Max-Planck-Institut für Plasmaphysik, Garching, Germany

Board of examiners

.....
Olivier SAUTER
EPFL

Referee

.....
Howard R. WILSON
York Plasma Institute

Referee

.....
Clarisse BOURDELLE
IRFM, CEA

Examiner

.....
Alexei POLEVOI
ITER

Examiner

.....
Yann CAMENEN
CNRS

Invited

.....
Peter BEYER
Aix-Marseille Université

Thesis director

.....
Clemente ANGIONI
IPP Garching

Thesis co-director

I, undersigned, Teobaldo Luda di Cortemiglia, hereby declare that the work presented in this manuscript is my own work, carried out under the scientific direction of Peter Beyer and Clemente Angioni, in accordance with the principles of honesty, integrity and responsibility inherent to the research mission. The research work and the writing of this manuscript have been carried out in compliance with both the french national charter for Research Integrity and the Aix-Marseille University charter on the fight against plagiarism.

This work has not been submitted previously either in this country or in another country in the same or in a similar version to any other examination body.

Garching, 10.09.2020



Cette œuvre est mise à disposition selon les termes de la [Licence Creative Commons Attribution - Pas d'Utilisation Commerciale - Pas de Modification 4.0 International](https://creativecommons.org/licenses/by-nc-nd/4.0/).

Résumé

La conception et l'opération des futurs réacteurs tokamak à fusion thermonucléaire nécessitent une prédiction précise du confinement et des profils de température et densité. Les lois d'échelle obtenues par des régressions sur des bases de données expérimentales multi-machines permettent de prédire le temps de confinement de l'énergie en fonction des principaux paramètres d'opération du tokamak. Leur application est cependant limitée au domaine de paramètres sur lequel l'analyse statistique a été effectuée. L'extrapolation aux conditions d'un réacteur, largement en dehors de ce domaine, génère de grandes incertitudes sur la prédiction. Dans cette thèse, une nouvelle approche de modélisation intégrée a été développée, qui combine des modèles théoriques et des éléments empiriques pour prédire le confinement et les profils de température et densité des plasmas en mode de confinement amélioré (mode H), uniquement à partir des paramètres d'opération du tokamak. L'évolution des profils est simulée à l'aide du code de transport ASTRA en utilisant, au coeur du plasma, les modèles de transport turbulent et collisionnel TGLF et NCLASS, au bord, un nouveau modèle de transport dans le piédestal et, à l'extérieur de la séparatrice, un modèle simple développé pour spécifier les conditions limites. Aucune mesure de profil n'est requise et les seuls paramètres d'entrée du modèle sont le champ magnétique, le courant plasma, la puissance de chauffage, le taux d'injection de particules et d'impuretés et la géométrie du plasma. Le modèle de transport développé pour le piédestal, basé sur des observations expérimentales multi-machines, contraint l'évolution du piédestal entre deux effondrements des profils dus aux ELMs (edge localized modes). Ce modèle fournit les températures et densités ioniques et électroniques au sommet du piédestal pour une largeur de piédestal donnée. La stabilité au mode "peeling-ballooning" est ensuite évaluée à l'aide du code de stabilité MHD MISHKA pour un ensemble de simulations ASTRA, chacune avec une largeur, et donc une pression, de piédestal différente. Le profil ne déstabilisant pas le mode "peeling-ballooning" et ayant la pression la plus élevée correspond aux conditions pré-ELM. Il constitue le résultat final de l'analyse et est utilisé pour calculer le temps de confinement de l'énergie du plasma. Ce processus de prédiction automatisé a été largement testé en simulant 50 phases stationnaires de plasmas du tokamak ASDEX Upgrade sélectionnés pour couvrir une vaste gamme de paramètres opérationnels, tels que la puissance de chauffage, le courant, le champ magnétique, la triangularité et le taux d'injection de particules. Les énergies thermiques prédites sont en bien meilleur accord avec les observations expérimentales que celles obtenues par les lois d'échelle. Le modèle reproduit non seulement les principales dépendances décrites par les lois d'échelle, telles que le courant plasma ou la puissance de chauffage,

mais inclut également les dépendances liées au taux d'injection des particules, à la triangularité et au champ magnétique. Il peut également fournir des informations physiques sur l'origine de ces dépendances dans les différents domaines radiaux ainsi que sur les limites et la spécificité au tokamak choisi des différents modèles. La cohérence interne du modèle, notamment concernant les conditions aux limites, est un élément essentiel pour reproduire la dégradation du confinement observée lors de l'augmentation du taux d'injection de particules. Le modèle de transport du piédestal donne une estimation précise de sa structure et offre pour la première fois la capacité de prédire séparément les profils de températures et densités ioniques et électroniques dans cette région. Le modèle reproduit également les plasmas dans le régime des petits ELMs et les scénarios de référence d'ITER, démontrant que cette approche a le potentiel d'améliorer la prédiction des performances de fusion des futurs réacteurs tokamaks.

Abstract

The design of future thermonuclear tokamak fusion reactors and the definition of the operational scenarios require an accurate prediction of plasma confinement and the temperature and density profiles. Scaling laws from regressions on multi-device experimental data-sets allow the prediction of the energy confinement time. However, while this approach can describe the dependence of confinement on the main engineering parameters, it contains large uncertainties in the extrapolation to reactor conditions, which are largely outside of the multi-dimensional domain of data over which the statistical analysis is performed. In this thesis a new integrated modeling workflow has been developed, which combines theory-based models and empirical elements to predict the confinement and temperature, density and rotation profiles of plasmas in the high confinement (H-) mode, using only global engineering parameters as inputs. A new edge pedestal transport model is included into the ASTRA transport code, which, together with the TGLF and NCLASS turbulent and collisional transport models, simulates the evolution of the profiles. A simple scrape-off layer (SOL) model has been also implemented, providing the boundary conditions at the separatrix. No profile measurements are required as input, and the only inputs of the model are the magnetic field, the plasma current, the heating power, the fueling rate, the impurity seeding rate and the plasma geometry. The adopted pedestal transport model, which is based on multi-device experimental observations, sets a transport constraint for the pedestal evolution between edge localized modes (ELMs). This provides the electron and ion temperatures and densities at the top of the pedestal for a given pedestal width. Many ASTRA simulations are run in parallel, each with a different pedestal width, providing a scan of the pedestal pressure. The MISHKA MHD stability code is run on each ASTRA simulation result, to find the highest pedestal pressure which is stable to peeling-ballooning modes, corresponding to pre-ELM conditions. The kinetic profiles associated to this pedestal width are the final result of the workflow and are used to calculate the plasma stored energy and the energy confinement time. This automated modeling framework has been extensively tested by simulating 50 stationary phases of ASDEX Upgrade discharges. The database selected for this validation includes wide variations in the operational parameters, such as heating power, current, magnetic field, triangularity, and fueling. The model reproduces the main dependencies which are captured by multi-device scaling laws, such as those on the plasma current and on the heating power. Moreover, the stored energies predicted by the model are in significantly better agreement with the experimental observations than those obtained by scaling laws. As an advantage over the scaling laws, the model also

describes the change in confinement caused by fueling, triangularity, and magnetic field. It can also provide physical insights on the origin of these dependencies in the different radial domains, core, pedestal and SOL, as well as the respective limitations and device specific elements of the various modeling components. In particular, the SOL model describes the effect of the fueling rate on the separatrix density. A self-consistent treatment of the boundary conditions is a key element of this approach, and is necessary to capture the widely observed confinement degradation caused by an increase in the fueling rate. The pedestal transport model gives an accurate estimate of the pedestal structure, providing for the first time the capability of separately predicting the pedestal profiles of electron and ion temperatures and densities. The model also reproduces plasmas in the small ELM regime and ITER baseline scenarios, demonstrating that this approach has the potential to improve the prediction of the fusion performance in future tokamak reactors.

Summary

Global warming and the receding amounts of fossil fuels require the transition to carbon free energy sources. This makes energy production one of the most substantial challenges for humanity at present. Renewable sources, such as wind, water, solar, and geothermal energy sources, seem good candidates for solving this problem, since they provide a virtually unlimited source of clean energy. However, due to the high costs, low power density, and inefficient distribution of energy to areas with restricted production opportunities these sources are not suitable alone for producing energy on the enormous scale necessary to replace fossil fuels. Moreover, discontinuous energy production caused by the weather, the day cycle, and the seasons put under severe stress backup power sources and storage capacities. An additional feasible option is represented by nuclear fission, as it produces energy without emission of substances contributing to global warming. However, it produces long-lived radioactive waste, and fission reactors are prone to accidents. Recent technological developments have significantly reduced the risk of nuclear disasters, but at the expense of a much higher cost of the installation of power plants. The exploitation of energy from nuclear fission is currently hampered by the high investment costs and by the negative public and political opinion, influenced by serious accidents in Chernobyl, Three Mile Island, and Fukushima.

Harnessing the atomic energy is extremely attractive, due to its vast energy yield per reaction. This energy can also be accessed by combining very light nuclei, a reaction which is called nuclear fusion. Compared to nuclear fission, it is a more technically challenging solution. Solving this challenge would guarantee a safe and clean source of energy fueled by an almost unlimited amount of natural resources. The material necessary for the fuel production, deuterium and lithium, are equally distributed over the world and their supplies are sufficient for millions of years of energy production, given today's consumption.

To ensure that a fusion reaction can occur, the reacting positively charged nuclei must get sufficiently close to allow the nuclear force to overcome the Coulomb repulsion. This requires that the reactants have a sufficiently high kinetic energy. In order to produce a sufficiently large amount of fusion reactions, to allow an efficient production of electricity, a temperature of over $T > 2 \times 10^8$ °C must be reached, which is more than ten times the temperature of the core of the sun. In this condition the fuel, originally in the form of gas, becomes fully ionized and enters in the so called *plasma* state.

Since the plasma is ionized, the presence of a magnetic field constrains the particles to move in a spiral around the magnetic field lines. One of the possible strategies to

confine the plasma is therefore to use an appropriate magnetic field. This approach is the usually called *magnetic confinement*. The *tokamak* is a toroidal shaped device which uses this strategy. A set of coils arranged periodically around the torus creates a toroidal magnetic field. By continuously increasing or decreasing the current in the central solenoid a toroidal current is inductively driven in the plasma itself. A poloidal magnetic field is then generated by this plasma current. The toroidal and poloidal components of the magnetic field constitute a magnetic configuration with closed field lines which confine the plasma particles, with orbits which are completely closed in the direction perpendicular to the confining magnetic field.

The *high confinement mode (H-mode)* is a regime in which the energy confinement of the plasma is strongly increased with respect to the standard *low confinement mode (L-mode)*. To access this regime, the plasma needs to be heated with a sufficient amount of power, in general in a diverted configuration, enabling in particular low net impurity influx from the walls. The increased confinement stems from the edge of the confined plasma. A layer of plasma in this region (of the extent of a few centimeters) exhibits strongly reduced perpendicular transport by means of an edge transport barrier (ETB), and consequent development of steep gradients of both temperature and density. This steep gradient region is called *pedestal*, as it looks like a structure elevating the core temperature and density profiles.

The strong pressure gradients arising from the turbulent transport suppression constitute the drive for magneto-hydrodynamic (MHD) instabilities in the pedestal region, called *Edge Localized Modes (ELMs)*. The ELMs are periodic events that cause strong plasma transport, causing a relaxation of the edge pressure profile and limiting the growth of the pedestal. Given the large amount of power that is released by the ELMs, they represent a serious concern for the wall and divertor materials of future fusion reactors. A high pedestal pressure on the one hand increases the plasma confinement and therefore the fusion performance of a future reactor, on the other hand it leads to larger heat loads on the materials due to the ELMs. The H-mode is the operational regime foreseen for ITER, a new generation tokamak which aims at demonstrating the technological feasibility of magnetic confinement fusion, and potentially also for future fusion reactors given its good confinement properties, but a special attention will be required to satisfy the limits imposed by power exhaust. Due to its importance for the next tokamaks generations, the ELMy H-mode regime is the one considered in this PhD thesis.

One of the main challenge of controlled thermonuclear fusion consists in keeping the plasma at a high temperature to produce fusion reactions, while spending the minimum possible amount of external heating power, so that more energy is produced than consumed. The problem is that the confinement of the energy of the plasma is rather weak in present tokamaks, leading to a large amount of power lost due to transport. This leads to the requirement of a large heating power to sustain a certain plasma energy, which makes the problem of obtaining a highly efficient fusion reactor extremely challenging. The recognized cause of the observed large transport is plasma turbulence.

The energy confinement time is the characteristic time describing the rate at which the plasma loses its energy if it is no longer heated by any source. In order to produce electricity via controlled thermonuclear fusion, reactors must be built with sufficiently high performance, that is a high energy confinement time and high plasma temperature and density. This constitutes a difficult scientific and technological challenge, which requires an economically sustainable solution. The design of a future fusion reactor has to be optimized in order to contain the investment cost, and therefore it has to rely on an accurate and robust prediction of at least the plasma energy confinement time, but possibly also of the radial profiles of densities and temperatures.

The main parameters in the design of ITER are largely based on scaling laws from regressions on multi-device experimental data-sets, which allow the prediction of the energy confinement time. However, while this approach can potentially capture the dependencies of confinement on the principal engineering parameters, it contains large uncertainties in the extrapolation to reactor conditions, which are largely outside of the multi-dimensional domain of data over which the statistical analysis is performed.

A different and complementary way of estimating the energy confinement time, is by predicting the plasma kinetic profiles (i.e. the plasma quantities, such as temperature, density) by means of one dimensional (1D) approaches which combine different modules describing plasma transport and sources at various levels of integration, and various levels of realism. Such integrated models can capture physics phenomena, which can have a strong impact on confinement, beyond the possibilities of scaling laws, and have therefore the potential to more accurately describe the plasma performance. However, this approach usually requires to include empirical elements (e.g. for the definition of the boundary conditions) or to make assumptions which can be specific to an existing device, and thereby which can limit their reliability and predictive capabilities when applied to other present and future devices.

Within this framework, during this PhD thesis a new integrated modeling workflow has been developed that for the first time describes the entire confined plasma domain in H-mode conditions, including the pedestal, up to the last closed flux surface. This allows an accurate prediction of plasma confinement and of the radial kinetic profiles only using global parameters as inputs, the same that are also used for planning a tokamak plasma discharge, without the need of any experimental information from profile measurements. This was achieved by including into the ASTRA transport code a new pedestal transport model in combination with a state-of-the-art core turbulent transport model, which allow for a simultaneous evolution of the core and pedestal kinetic profiles, and a simple but sufficiently realistic analytical model for the open field line scrape-off layer (SOL) region, which self-consistently calculates the boundary conditions.

The workflow combines theory-based components (like the quasilinear TGLF [1] model for core turbulent transport, the NCLASS [2] model for neoclassical transport,

the MHD code MISHKA [3] for the pedestal stability and the two-point model for the SOL [4, 5]) with empirical elements, in particular for the description of the transport in the pedestal region and for the connection between divertor and SOL parameters.

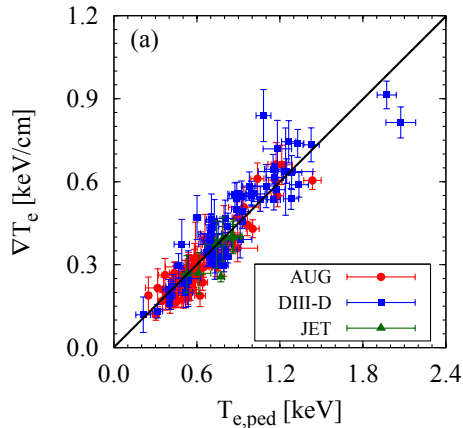


Figure 0.1 – Database of pedestal from AUG, DIII-D, and JET showing the correlation between $\langle \nabla T_e \rangle$ and $T_{e,ped}$ [6].

The pedestal transport model is based on the experimental observation illustrated in figure 0.1, which shows that the ratio of the average gradient of the electron temperature in the pedestal region to the pedestal top temperature $\langle \nabla T_e \rangle / T_{e,ped}$ is approximately constant and equal to $-0.5 [\text{cm}^{-1}]$ in a multi-device analysis [6]. This observation gives a new transport constraint for the pedestal evolution in the inter-ELM recovery phase, which is different from the usual technique adopted by the EPED model [7] ($\Delta\psi_N \propto \sqrt{\beta_{p,ped}}$). The inclusion of this constraint into the ASTRA transport code allows us, for a given pedestal width, to find the electron heat conductivity ($\chi_{e,ped}$) that fulfills the condition $\langle \nabla T_e \rangle / T_{e,ped} \approx \text{const} = -0.5 [\text{cm}^{-1}]$. We assume that the ion heat conductivity and the particle diffusivity are proportional to the value of $\chi_{e,ped}$ which is consistently determined in the ASTRA simulation.

The ASTRA simulations combine the pedestal transport coefficients, obtained through this technique, with the transport coefficients calculated with the TGLF and NCLASS models to give a complete description of transport over the whole radial profile. This allows the simulation of the kinetic profiles, namely the electron and ion temperature and density (T_e, T_i, n_e, n_i), and the current density (j) profiles from the magnetic axis to the separatrix.

The modeling of the toroidal rotation is also included in the ASTRA simulations. An analytical formula for the residual toroidal stress at the edge [8] calculates the toroidal rotation at the pedestal top, and the core rotation profile is obtained assuming a Prandtl number $P_r = 1$, which means that we assume a momentum diffusivity equal to the ion heat diffusivity. The torque provided by the NBI is

calculated by the ASTRA NBI module. By doing this we calculate all the components of the radial electric field core profile, which is used by TGLF to calculate the effect of the $\mathbf{E} \times \mathbf{B}$ shear on turbulent transport, without the need of using any experimental information from profile measurements.

The SOL model consists of a set of analytical formulas, obtained through an extension of the two point model [9], which calculate $n_{e,sep}$, $T_{e,sep}$, $T_{i,sep}$, and the source of neutrals at the separatrix, and has proven to robustly describe the effect of the fueling rate on $n_{e,sep}$ for the AUG cases considered. An important input parameter to the formula evaluating $n_{e,sep}$ is the divertor neutral pressure p_0 . To estimate this quantity, a scaling has been derived using AUG experimental data. We have shown that a self-consistent treatment of the boundary conditions is a key element of this approach, and is necessary to capture the dependence of the pedestal pressure on the separatrix density, and therefore on the fueling rate, increasing the detail of the physics describing pedestal and global confinement.

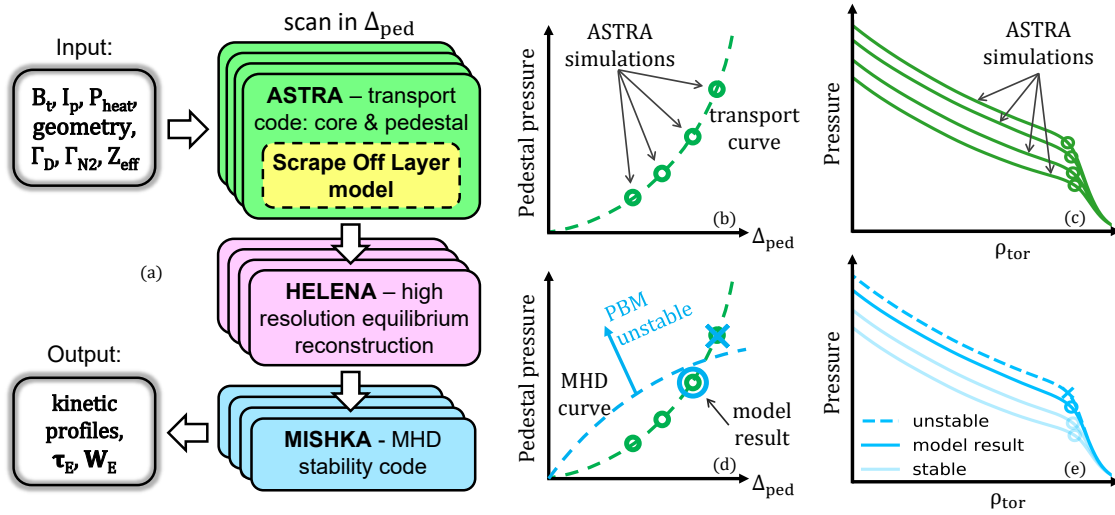


Figure 0.2 – Chart representation of the modeling workflow (a). Multiple parallel ASTRA simulations calculate the kinetic profiles for different values of the pedestal width (c). The pedestal model integrated in ASTRA gives a transport constraint which determines the pedestal pressure for a given pedestal width (b). MISHKA tests the stability of the resulting profiles to find the highest stable pedestal pressure (d,e).

Figure 0.2 (a) depicts the modeling workflow, which is based on the approach of performing multiple simulations in parallel, represented by the multiple ASTRA blocks (green) in the workflow, each with a different value of the pedestal width, where the kinetic profiles are evolved until stationary conditions are reached. The inputs of the model are the magnetic field, the total plasma current, the engineering parameters determining the auxiliary heating powers, the deuterium fueling rate, the nitrogen seeding rate, the plasma boundary, and the effective charge Z_{eff} . As

a result of the imposition of the condition $\langle \nabla T_e \rangle / T_{e,ped} \approx const = -0.5 [cm^{-1}]$, by increasing the pedestal width the pedestal top temperature increases, and also the total pressure. Therefore, a scan in pedestal width allows us to obtain a scan in pedestal top pressure, as sketched in figure 0.2 (b). Figure 0.2 (c) shows the corresponding pressure profiles calculated by ASTRA (from the magnetic axis to the separatrix, although here shown only from $\rho_{tor} = 0.5$ to better highlight the pedestal) for different values of the pedestal width. The MISHKA code is then used to calculate the peeling-ballooning mode (PBM) stability of the pedestals corresponding to the different values of the pedestal width, as in figure 0.2 (d). The final pressure profile, illustrated in figure 0.2 (e), providing the result of the modeling workflow, is the one with the highest stable pedestal pressure, corresponding to pre-ELM conditions.

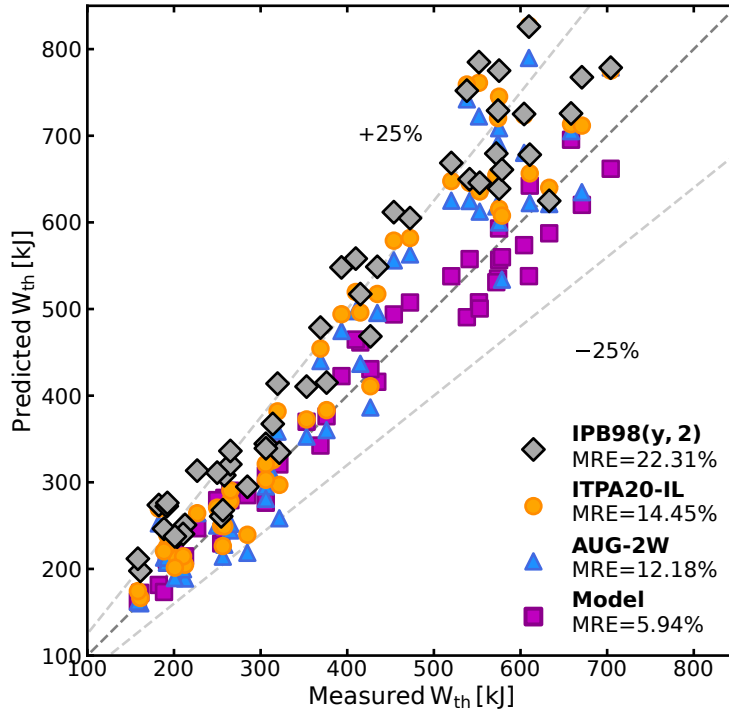


Figure 0.3 – Comparison of the measured thermal energy with the prediction of the model (purple squares), IPB98(y,2) (gray diamonds), ITPA20-IL (orange circles), and AUG-2W (blue triangles) scaling laws.

The model has been extensively validated, testing it on a database of 50 experimental cases covering the strongest possible AUG operational parameter variations. This results in a variation across the database in plasma current $I_p = 0.6 - 1.2$ MA, magnetic field $B_t = 1.5 - 2.85$ T, safety factor $q_{95} = 3 - 8$, heating power $P_{heat} = 2 - 14$ MW, triangularity $\delta = 0.19 - 0.42$, fueling rate $\Gamma_D = 0 - 8 \times 10^{22}$ e/s. The prediction of the model is compared with experimental measurements and with the

scaling law of the ITER physics basis IPB98(y,2), regularly applied over the last two decades to qualify confinement in present experiments. Comparisons are also performed with the most recently derived scaling law ITPA20-IL from the international multi-device tokamak confinement database specific for ITER like plasmas, and with AUG specific regressions, made on the AUG confinement database only. Figure 0.3 shows that the prediction of the model (purple squares) is very accurate and robust across the database, with a significantly lower mean relative error with respect to each of the scaling laws considered. This shows that indeed a sophisticated model which contains a description of the physics regulating plasma confinement can capture important dependencies beyond the possibilities of a log-linear regression of experimental data. In particular we have noticed that, for the AUG experimental cases considered, both the IPB98(y,2) and the ITPA20-IL scaling laws tend to be less accurate at higher values of the fueling rate (Γ_D), as they do not capture the confinement degradation caused by this parameter. The fact that the model is instead capable of capturing the effect of fueling correctly is a very important aspect for the study of the scenarios for ITER and future fusion reactors. Power exhaust sets constraints on the possible variation of the fueling rate, therefore it is important to take into account the effect that the operating conditions have on the fusion performance, by including it in the simulations.

Overall, the analysis carried out in this work shows that the model can accurately reproduce the change in confinement caused by a change in plasma current, heating power, fueling rate, triangularity, and magnetic field. Some important experimental cases have been included in the data set, which has been considered in this thesis to provide specific stringent tests for the model. In particular, the model has proven to reliably capture the effect of different heating mixes (e.g. correctly predicting the effect on confinement caused by a change in T_e/T_i), and of different NBI voltage (i.e. the effect of a change in the core particle source). This modeling framework has proven to also correctly describe plasma confinement for two particular operating regimes, such as the ITER baseline scenarios, and the small ELMs scenario. This shows that plasmas in the small ELMs regime are not far from the peeling-ballooning limit provided by linear MHD stability codes, such as MISHKA, allowing accurate predictions also in this plasma regime, at least for the cases taken into account.

The new pedestal transport model we presented can robustly capture the effect of the different plasma parameters on the pedestal pressure. It also brings important advantages, as it can accurately predict the pedestal top density with no need of experimental information, as opposed to the widely applied EPED model where this must be given as input, increasing the predictive capabilities of previous integrated models. A comparison between the predicted and measured values of n_e at the pedestal top (blue) and n_e at the center of the plasma (red) is illustrated in figure 0.4. The model also brings for the first time (to our knowledge) the capabilities of modeling separately the electron temperature and the ion temperature profiles in the pedestal region. Even though this is obtained with quite rough assumptions, i.e. considering that the pedestal ion heat diffusivity is equal to that of the electrons

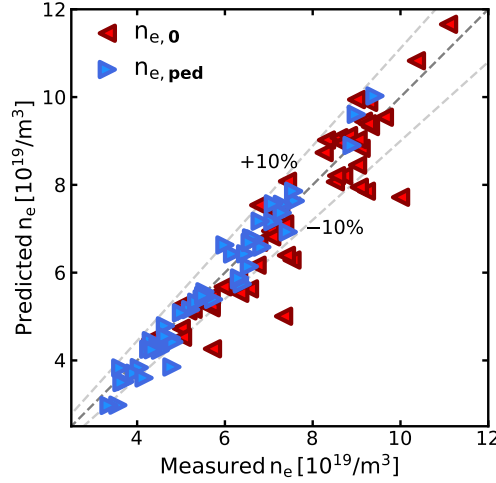


Figure 0.4 – Comparison between the predicted and measured values of n_e at the pedestal top (blue) and n_e at the center of the plasma (red).

summed with the ion neoclassical diffusivity $\chi_{i, \text{ped}} = \chi_{e, \text{ped}} + \chi_{i, \text{neo}}$, it allows the determination of the pedestal top ion and electron temperature separately (without assuming $T_{e, \text{ped}} = T_{i, \text{ped}}$). Thereby, the modeling approach is completely general and flexible and able to include more sophisticated, theoretical pedestal transport models when these will become available.

The capability of simulating the kinetic profiles of the confined plasma increases the accuracy and the reliability in the prediction of energy confinement with respect to 0D scaling laws, as a 1D model can include the description of the physics phenomena which are strongly dependent on the gradients of the kinetic quantities, both in the core and in the pedestal regions. In particular, the density profile affects the shapes of the pressure gradients, which has a strong impact on the pedestal stability. Also, the prediction of 1D profiles is important for a reactor, since the shape of the kinetic profiles can influence the design and the prediction of the operation of a reactor at the same total stored energy, and therefore this is a great advantage that the integrated model provides over 0D approaches.

Comparing the quality of the prediction on the pedestal and core thermal energy components, as illustrated in figure 0.5, we found that the larger error is associated to the core. This could be surprising, as core transport is considered to be better understood and reproduced than pedestal confinement. This does not mean that the description of core transport is performing worse than expected (the error of the predicted core energy is small), but rather that the new pedestal modeling included in this work is robust and accurate. The successful application of the empirical pedestal model could therefore give guidelines in the understanding of the actual physical properties of transport in the pedestal. We have seen that TGLF tends to overestimate transport for cases with a relatively large fast ions density (at high NBI power), for which the turbulence stabilization can be important (but is not

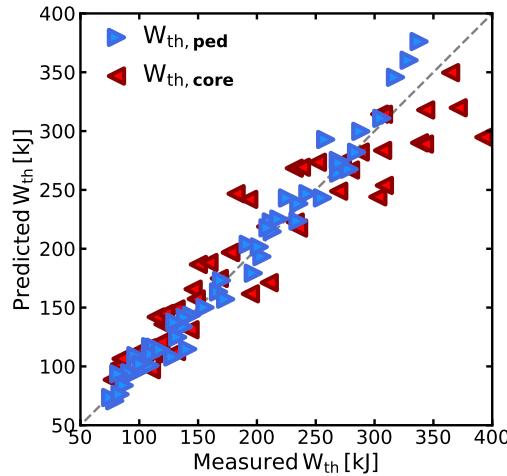


Figure 0.5 – Comparison between predicted and measured thermal energy separated in the pedestal (blue) and core (red) components.

reproduced by TGLF), and for cases at high β . We have noticed that TGLF can underestimate the reduction of the ITGs growth rates when increasing β compared to linear gyrokinetic simulations, and it also does not include the nonlinear effect, which is usually considerably larger.

The identification and the discussion of the analogies and the differences between the present integrated model and the traditional 0D scaling laws, like the IPB98(y,2), reveal interesting aspects. The integrated model and the IPB98(y,2) scaling law make use of the same input parameters, with the exception of the line averaged density which is required by the IPB98(y,2). The model is instead capable of predicting the plasma density profile, but contains supplementary information and other elements in order to calculate it. Additional inputs are the effective charge Z_{eff} , the fueling rate, and the engineering parameters of the heating systems (e.g. power, angles, voltage of the beams, frequency of the gyrotrons, etc.). The result of the model is very little sensitive to the effective charge in this range of values relatively close to $Z_{eff} = 1$, therefore this is not an essential parameter. Another important aspect is that the model relies on empirical elements (in particular for the description of the pedestal and SOL) and a set of device specific coefficients which increase the accuracy of its prediction, that the scaling law can not benefit of.

Parts of such components of the integrated modeling workflow could be specific and applicable only to AUG, while scaling laws can readily be used for many different machines. In particular the pedestal transport model is based on experimental observations that we expect to be applicable to other devices since it relies on a multi-machine analysis which has identified a common parameter. However, because such common parameter is dimensional, the validity of this assumption needs to be tested for machines with a different size than AUG. An interesting consideration is that the application of the pedestal model to smaller machines could be limited

by the locality of the description of pedestal transport, which in contrast becomes increasingly applicable towards a reactor, since the relative gyro-radius $\rho_* = \rho_s/a$ becomes smaller at increasing size a of the device. Of course this modeling of the pedestal can be easily and readily replaced by a theory-based model in case this becomes available.

The main aspects which produce a strong machine dependency are the geometry of the divertor and its baffles, the location of the gas valves, and the materials of the walls and the plasma facing components, which would probably make the estimation of the divertor neutral pressure not valid for different machines or divertors. A new scaling should be then derived for the tokamak of interest, using either experimental measurements if available, and/or synthetic data from simulations, particularly for non existing devices. Codes for the simulation of the SOL profiles are capable of predicting the divertor neutral pressure, therefore it would be interesting to study if a small database of such simulations would be sufficient to obtain a scaling for divertor neutral pressure p_0 , based on synthetic data rather than experimental measurements. If this approach results successful, leading to a similar accuracy of the prediction for AUG cases, the validation of the integrated model could be extended to other tokamaks. Testing the model on a larger device, such as JET, and on a smaller one, e.g. TCV, would allow us to obtain also a scan in the size of the device, which, if successful, would increase the confidence in the prediction for ITER, for which a database of SOL simulations is already available, and therefore a dependence of p_0 on the main engineering parameters could be extracted.

In conclusion, this thesis clearly demonstrates that it is possible to combine together many different components for the description of plasma confinement into an integrated modeling workflow, which simulates the entire confined plasma from the magnetic axis to the last closed flux surface and which produces very realistic results. For the first time it has been proved that a 1D modeling approach can reproduce experimental results over the largest parameter variations allowed by a single device, with a higher accuracy than any statistical regression, even those performed on the device itself only. The approach of integrated models, like the one presented in this work, has therefore the potential to improve the prediction of the fusion performance in future tokamak reactors.

Moreover, even if some elements in the modeling are not completely based on theory, the integration of the different modules can provide important insights to better understand other nonlinear interdependencies, particularly between different plasma regions, which are not possible to explore otherwise. Thereby, in addition to the increased predictive capabilities, which are promising also for applications to other devices, this approach has proven very helpful in the identification of hidden dependencies, specifically those resulting from effects that connect the different plasma regions (from SOL to core) and cannot be identified in 0D statistical studies nor in physics studies focusing on specific plasma regions.

Contents

Résumé	6
Abstract	8
Summary	10
Contents	20
List of Figures	23
List of Tables	25
1 Introduction	26
1.1 Challenge of Energy Supply	26
1.2 Nuclear Fusion	27
1.3 Magnetic Confinement and the Tokamak	31
1.3.1 Limiter and divertor configurations	34
1.3.2 Confinement regimes of tokamak plasmas	36
1.3.3 Heating systems	37
1.4 Plasma Performance	38
1.5 Thesis Objectives and Outline	42
2 ASDEX Upgrade Experiment	44
2.1 ASDEX Upgrade tokamak	44
2.2 Diagnostics	45
2.2.1 Magnetic Probes	46
2.2.2 Thomson Scattering	46
2.2.3 Lithium Beam	47
2.2.4 Interferometer	47
2.2.5 Electron Cyclotron Emission	48
2.2.6 Charge Exchange Recombination Spectroscopy	48
2.3 Tools for profile fitting	49
2.3.1 Integrated Data Analysis	49
2.3.2 Gaussian Process Regression	50
2.3.3 AUGPED	50
2.3.4 Summary	52

3	H-mode plasmas simulations: Transport and Stability	53
3.1	Transport in tokamak plasmas	53
3.1.1	Collisional transport	55
3.1.2	Turbulent transport	58
3.1.3	Prediction of pedestal profiles	62
3.1.4	Pedestal MHD stability	64
3.1.5	SOL transport	66
3.2	Simulation of plasma profiles with transport codes	69
4	Description of the Integrated Modeling Workflow	72
4.1	Introduction	72
4.2	Transport simulations	76
4.2.1	Scrape-off layer model	76
4.2.2	Pedestal transport	82
4.2.3	Core transport	86
4.2.4	Integration of the different components	87
4.3	Pedestal MHD stability	91
4.4	Assumptions	93
5	First model validation on main confinement time dependencies, current, power, and density	96
5.1	Introduction	96
5.2	Experimental results considered for the first application of the model	97
5.3	Results from the first application of the model	98
5.3.1	Fuelling scan	102
5.3.2	Power scan at high fueling	106
5.3.3	Power scan at fixed line averaged density	109
5.3.4	Current scan	114
6	Extensive validation of the model	117
6.1	Introduction	117
6.2	Experimental results considered for the extended validation of the model	118
6.3	Results from model application	119
6.3.1	Comparison with recent scaling laws	123
6.3.2	Accuracy of kinetic profiles prediction	125
6.4	Analysis of specific dependencies	128
6.4.1	Triangularity scan	128
6.4.2	Magnetic field scan	130
6.4.3	NBI voltage scan	135
6.4.4	Current scan at similar line averaged density	140
7	Conclusion	142

Contents

Bibliography

149

List of Figures

0.1	Multi-machine pedestals analysis	13
0.2	Chart representation of the modeling workflow	14
0.3	Prediction of more recent scaling laws	15
0.4	Prediction of plasma density	17
0.5	Comparison between core and pedestal energies	18
1.1	Binding energy	27
1.2	Fusion reactions cross sections	29
1.3	Velocity averaged cross sections	30
1.4	Tokamak principle	32
1.5	Geometry of the magnetic field lines, coordinated definition, and particle orbit	33
1.6	Limiter and divertor configurations	35
1.7	H-mode and L-mode plasma pressure profiles	36
1.8	Tokamak heating systems	38
1.9	IPB98(y,2) scaling law	40
2.1	ASDEX Upgrade tokamak	44
2.2	AUG diagnostics	46
2.3	AUGPED GUI	51
2.4	AUGPED fits	52
3.1	Banana orbits	56
3.2	ITG mode	59
3.3	EPED pedestal model	63
4.1	Chart representation of the modeling workflow	73
4.2	Multi-machine pedestals analysis	74
4.3	Regression plot for the scaling of the divertor neutral pressure	77
4.4	Composition of the database used for the scaling of the divertor neutral pressure	78
4.5	Location of the baratron in the AUG divertor	79
4.6	SOL profiles for the decay of the neutral density	81
4.7	Pedestal profiles from width scan	83
4.8	Relation between $T_{e,top}$ and Δ_{ped}	85
4.9	Example of electron and ion heat diffusion coefficients	89
4.10	Time evolution of pedestal quantities	91
4.11	Automatic pedestal width solver	92

List of Figures

5.1	Comparison between measured and predicted thermal energies	99
5.2	Comparison between predicted and measured values of T_i/T_e	100
5.3	Comparison between the predicted and measured values of T and n	101
5.4	Fueling scan: pedestal analysis	102
5.5	Fueling scan: comparison of thermal energies	104
5.6	Fueling scan: comparison between profiles and measurements	105
5.7	Power scan: pedestal width scans	106
5.8	Power scan: comparison of thermal energies	107
5.9	Power scan: comparison between profiles and measurements	108
5.10	Power scan at fixed density: thermal energies	109
5.11	Power scan at fixed density: profiles and measurements	111
5.12	Power scan at fixed density: diffusion coefficients	112
5.13	Power scan: diffusion coefficients	113
5.14	Dependence of pedestal logarithmic density gradient on the heating power	114
5.15	Current scan: thermal energies	115
5.16	Current scan: profiles and measurements	116
6.1	Model results from extended database	119
6.2	Color-maps of thermal energies	121
6.3	Prediction of more recent scaling laws	124
6.4	Color-maps of more recent scaling law prediction	125
6.5	Accuracy of profiles prediction	126
6.6	Comparison between predicted and measured toroidal rotation	127
6.7	Triangularity scan: modes growth rates	129
6.8	Triangularity scan: thermal energies	130
6.9	Triangularity scan: profiles and measurements	131
6.10	Magnetic field scan: thermal energies and profiles	132
6.11	Magnetic field scan: ITG spectra	133
6.12	Magnetic field scan: profiles and measurements	134
6.13	NBI voltage scan: pedestal analysis	136
6.14	NBI voltage scan: fluxes, power, and particle source densities	138
6.15	NBI voltage scan: thermal energies	139
6.16	Current scan at similar line averaged density: thermal energies	140

List of Tables

2.1	ASDEX Upgrade typical parameters	45
3.1	Microinstabilities	61
4.1	Assumptions taken into the model	94
5.1	Summary of the experimental cases considered for the first application of the model	98

1 Introduction

Summary

1.1	Challenge of Energy Supply	26
1.2	Nuclear Fusion	27
1.3	Magnetic Confinement and the Tokamak	31
1.3.1	Limiter and divertor configurations	34
1.3.2	Confinement regimes of tokamak plasmas	36
1.3.3	Heating systems	37
1.4	Plasma Performance	38
1.5	Thesis Objectives and Outline	42

1.1 Challenge of Energy Supply

The world population and economic growth, and the technological advancements of the last centuries have been strongly increasing the demand for energy. The energy production relies mainly on the exploitation of fossil fuels. However, global warming and the receding amounts of fossil fuels require the transition to different energy sources. This makes energy production one of the most substantial challenges for humanity at present.

Renewable sources, such as wind, water, solar, and geothermal energy sources, seem good candidates for solving this problem, since they provide a virtually unlimited source of clean energy. However, due to the high costs, low power density, and inefficient distribution of energy to areas with restricted production opportunities these sources are not suitable for producing energy on the enormous scale necessary to replace fossil fuels. Additionally, discontinuous energy production caused by the weather, the day cycle, and the seasons put under severe stress backup power sources and storage capacities.

Another feasible option is represented by nuclear fission, as it produces energy without emission of substances contributing to global warming. However, it produces long-lived radioactive waste, and fission reactors are prone to accidents. Recent technological developments have significantly reduced the risk of nuclear disasters, but at the expense of a much higher cost of the installation of power plants. The exploitation of energy from nuclear fission is currently hampered by the high investment costs and by the negative public and political opinion, influenced by serious accidents in Chernobyl, Three Mile Island, and Fukushima.

Although these technologies do not represent a long term solution for energy production, renewable sources and fission power plants are important components of the world energy mix, and play a fundamental role in mitigating global warming and environmental pollution. Harnessing the atomic energy is extremely attractive, due to its vast energy yield per reaction. This energy can also be accessed by combining very light nuclei, which is called nuclear fusion. Compared to nuclear fission, it is the more technically challenging solution. Solving this challenge would guarantee a safe and clean source of energy fueled by an almost unlimited amount of natural resources. The principles of fusion reactors make an uncontrolled chain reaction impossible, in contrast to fission power plants. This is because the core of a fission reactor contains during its operation a quantity of fuel sufficient to produce energy for tens of years. An uncontrolled instability which causes an increase of reactivity can potentially burn a large fraction of the stored fuel in a short amount of time, producing an extremely large amount of power, potentially destroying the reactor and causing catastrophic release of radioactive material. In fusion power plants instead, fuel needs to be constantly introduced into the reactor in a quantity that is just sufficient to sustain the reaction. Furthermore, any instability leads to the immediate interruption of the fusion reaction. The material necessary for the fuel production, deuterium and lithium, are equally distributed over the world and their supplies are sufficient for millions of years of energy production, given today's consumption.

1.2 Nuclear Fusion

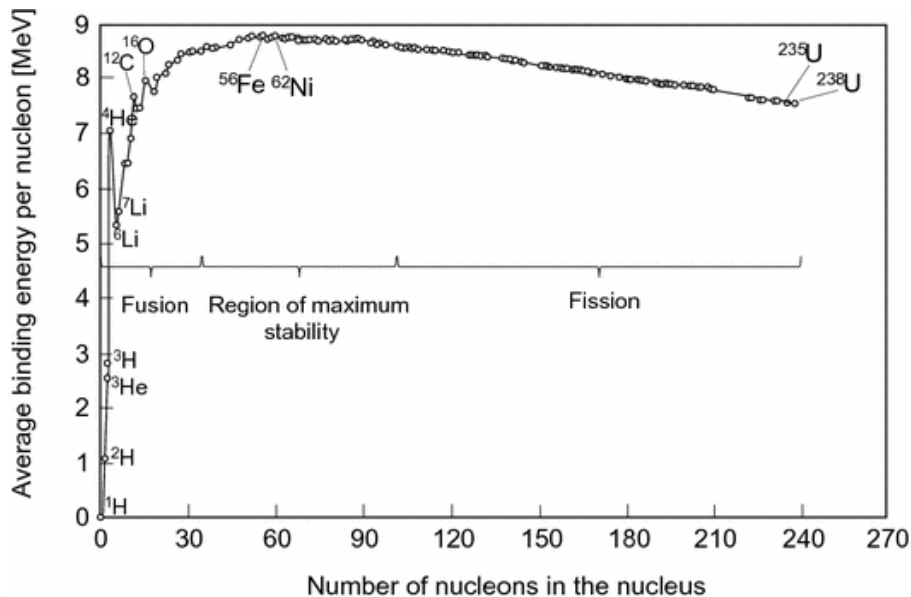


Figure 1.1 – Average binding energy per nucleon as a function of their mass number [10].

1 Introduction

As anticipated, nuclear fusion is the nuclear reaction which involves the combination of two light nuclei into an heavier one, releasing other products like neutrons or ions. This process is releasing energy, since the reactants in a nuclear fusion reaction are evolving into a more stable state. In fact, the products of a fusion reaction have a mass defect Δm with respect to the reactants, which, according to Einstein relationship $E = \Delta mc^2$ (where $c \sim 3 \times 10^8 m/s$ is the speed of light), results in a release of energy. If we take for example the deuterium-tritium (D-T) reaction



where α is a nucleus of ${}^4\text{He}$, and we evaluate the mass difference between the products and reactants, it appears that there is a mass defect of $\Delta m = (m_n + m_\alpha) - (m_D + m_T) = (1.67 \times 10^{-27} + 6.65 \times 10^{-27}) - (3.34 \times 10^{-27} + 5.01 \times 10^{-27}) = 8.32 \times 10^{-27} - 8.35 \times 10^{-27} = -3.13 \times 10^{-29} \text{ kg}$, which corresponds to an energy release of $2.82 \times 10^{-12} \text{ J}$, or 17.6 MeV ($1 \text{ eV} = 1.602 \times 10^{-19} \text{ J}$). This energy difference is due to the different binding energies, which hold the nuclei together, of the ions involved in the reactions. As we can see in figure 1.1 light elements (with a low number of nucleons, or mass number) have a small binding energy, which means that they are less stable than a heavier one which has a larger binding energy. So, merging two elements into a heavier one, will produce an amount of energy proportional to the difference between the binding energies of the heavier and the lighter elements. The most stable chemical element is ${}^{56}\text{Fe}$. At the other end of the spectrum we have that energy is released when a heavy nuclei (e.g. ${}^{235}\text{U}$) is split into two lighter elements, creating thus a nuclear fission reaction.

Together with the D-T reaction there are many other fusion reactions, and studies of the nuclear properties of light elements indicate that three such reactions may be attractive for the production of energy. These are, besides the D-T reaction, the deuterium-deuterium (D-D) and the deuterium-helium-3 (D- ${}^3\text{He}$) reactions. One would think that the D-D reaction is the most convenient one since it does not involve tritium, but only deuterium which is not radioactive and largely abundant in nature. However, the D-D reaction is harder to initiate than the D-T reaction, which poses already several challenges to be achieved.

To ensure that a fusion reaction can occur, the reacting positively charged nuclei must get sufficiently close to allow the nuclear force to overcome the Coulomb repulsion. In nature this repulsive force can only be overcome in the core of stars where the massive gravitational force provides the pressure necessary for the fusion reaction. The probability of the reaction to occur, when the two nuclei are colliding, depends on their relative kinetic energy and is provided by the cross section $\sigma(E)$. Figure 1.2 shows the cross sections for the reactions mentioned above as a function of the deuteron kinetic energy expressed in keV.

As we can see, the D-T reaction is the most probable at lower kinetic energy. Its cross section indicates that the maximum probability is at $\sim 100 \text{ keV}$, which means that the reacting particles must have a high kinetic energy in order to have a good probability for the fusion reaction to occur. A gas mixture of D-T must have

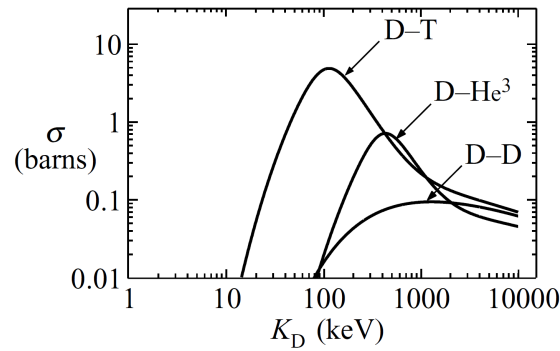


Figure 1.2 – Experimentally measured cross sections for the D-T, D- ^3He , and D-D fusion reactions as a function of deuteron energy $K_D = m_D v_D^2/2$ [11].

therefore a temperature of over $T > 2 \times 10^8$ °C, which is more than ten times the temperature of the core of the sun. In this condition the gas becomes fully ionized and enters in the so called *plasma* state.

The plasma is a partially or fully ionized gas whose behavior is dominated by long range electromagnetic collective effects rather than interactions of single close particles. It is an excellent electricity conductor, and exhibits local quasineutrality property, which means that the electron density is locally equal to the ion density. Consequently, no static electric fields are present due to charge imbalance.

Not all the plasma particles need to be at the energy corresponding to the maximum cross section ($E = 120$ keV) for producing a significant amount of energy. In fact, ions inside the plasma have different kinetic energy characterized by a distribution function. It is sufficient that only a fraction of particles undergo fusion reactions. These particles can be in the tail of the distribution function that is at a higher kinetic energy than the mean one. The reaction rate, i.e. the number of reactions per unit time and volume, can be evaluated as a function of particles mean energy by averaging the product of the cross section and particles velocity for the distribution function $\langle \sigma v \rangle$. This is the relevant parameter when we are interested in a sustained fusion reaction inside the plasma, i.e. thermonuclear fusion, rather than the single fusion of the nuclei event. The velocity averaged cross section is showed in figure 1.3 as a function of the plasma temperature and presents a maximum for the D-T reaction at $T_{max} \sim 70$ keV.

The 17.6 MeV generated in the D-T fusion reaction are released in the form of kinetic energy, and are divided between the neutron and the alpha particle produced according to their masses (from conservation of energy and momentum relations). Therefore, the kinetic energy of the neutron is 14.1 MeV, while that of the alpha particle is 3.5 MeV. In a thermonuclear fusion reactor the alpha particles produced by the reaction remain inside the plasma, heating the mixture and helping therefore in sustaining the reaction, while the heat produced by slowing down the neutrons will be used to produce electricity.

The natural abundance of deuterium in Hydrogen is one part in 6700, so, since

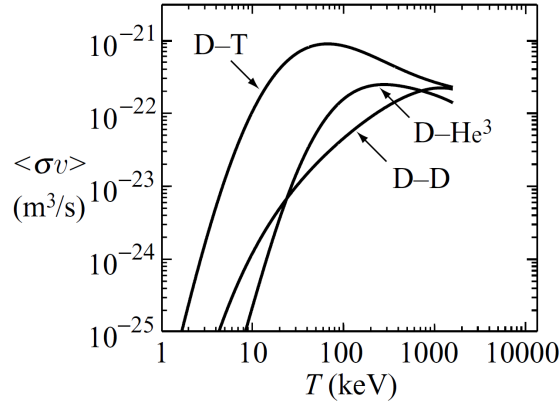


Figure 1.3 – Velocity averaged cross section $\langle \sigma v \rangle$ for the D-T, D- ^3He , and D-D fusion reactions as a function of temperature [11].

the mass of water in the oceans is 1.4×10^{21} kg, the mass of deuterium is 4×10^{16} kg. In D-T fusion reactors utilizing a standard steam cycle this would allow to produce 10^{22} GJ of electric energy, which is more than 10^{10} times the world's annual primary energy consumption. Clearly there is no problem with deuterium resources. However, tritium is a radioactive isotope with a decay time of 12 years and is practically non-existent in nature, but it can be produced by the following reactions.



The tritium supply for the D-T reaction can be created directly in the blanket surrounding the region where the fusion reaction takes place, exploiting the neutrons produced by the D-T reactions, as shown below. Natural lithium comprises 7.4% ${}^6\text{Li}$ and 92.6% ${}^7\text{Li}$. Even though there is a much larger fraction of ${}^7\text{Li}$, ${}^6\text{Li}$ reaction is much easier to initiate and as a result it is this reaction that dominates in the breeding of tritium. The estimated world energy resources of land-based ${}^6\text{Li}$ is around 10^{12} kg and this would provide 10,000 years of power at the present world level energy consumption. Lithium and deuterium are cheap and widely spread on the earth avoiding political issues for supply. Fusion seems then to have the potential to critically contribute in solving the world energy problem, being able to provide a long-term energy supply in a safe way, and with minimal damage to the environment. In fact, neither greenhouse gases nor long-term radioactive wastes are produced. The D-T reaction itself does not produce any radioactive products and tritium has a very fast decay time, so the only mid-long radioactive waste will be the reactor materials activated by the produced neutrons. These will have to be stored for only about 100 years to become harmless [12].

1.3 Magnetic Confinement and the Tokamak

The high temperature needed to sustain the thermonuclear reaction requires to confine the plasma avoiding contact with the reactor walls. Since the plasma is ionized, the presence of a magnetic field constrains the particles to move in a spiral around the magnetic field lines, as a consequence of the Lorentz force $\mathbf{F} = q\mathbf{v} \times \mathbf{B}$, where q is the particle charge, \mathbf{v} is its velocity and \mathbf{B} is the magnetic field. One of the possible strategies to confine the plasma is therefore to use an appropriate magnetic field. This approach is the usually called *magnetic confinement*.

The *tokamak* is a toroidal shaped device which uses this strategy. 'Tokamak' is a transliteration of the Russian words **t**oroidalnaya **k**amera and **m**agnitnaya **k**atushka, which stand for toroidal chamber and magnetic coil [13]. This type of machine has been the most studied in the field of magnetic confinement and is currently considered to be the most promising solution for building a fusion power plant in the future.

Providing a magnetic configuration with closed field lines should constrain the plasma particles to follow \mathbf{B} , rotating around the field lines. The most simple geometrical configuration with this property is the torus. Figure 1.4 illustrates the configuration of the coils generating the magnetic field in a tokamak. The field has two different components: the *poloidal* and the *toroidal* magnetic field. A set of coils arranged periodically around the torus (blue) creates the toroidal magnetic field (blue arrow). By continuously increasing or decreasing the current in the central solenoid (green discs in the center) the toroidal *plasma current* (light green arrow) is driven inductively. The poloidal magnetic field (dark green arrows) is then generated by this plasma current. During the revolution in the toroidal direction, particles undergo a drifting vertical motion together with the spiral motion around the magnetic field line. The poloidal magnetic field is an essential component of a tokamak because it counteracts this effect, that would otherwise cause loss of the particle confinement. Beside the central solenoid and the toroidal magnetic field coils there are also large poloidal coils located at the outer side of the torus (gray in figure 1.4). These coils are used to control the position and the shape of the plasma.

It is useful to define some geometrical quantities that will be extensively used in this work, by looking at figure 1.5 (a) : R, z are the radial and vertical coordinates of the torus; R_0 is the major radius and a the minor radius; the plasma section plane parallel to the R, z plane is called the *poloidal* plane and the angle θ , taken R_0 as the origin, is the poloidal angle; the angle φ (or ϕ) in the direction of the torus symmetry is called the toroidal angle. A typical resulting magnetic field line is displayed in figure 1.5 (b) (continuous line). It winds along the toroidal direction and the particle moves in spiral around it.

In a tokamak, the equilibrium between the pressure of the plasma (that tends to expand the plasma) and the magnetic field (that tries to confine it), is described by the Grad-Shafranov equation [14]. Such equation is derived from the equilibrium equation in ideal magnetohydrodynamics (MHD) under the assumption of toroidal symmetry, and couples the poloidal magnetic flux, plasma pressure (p) and current

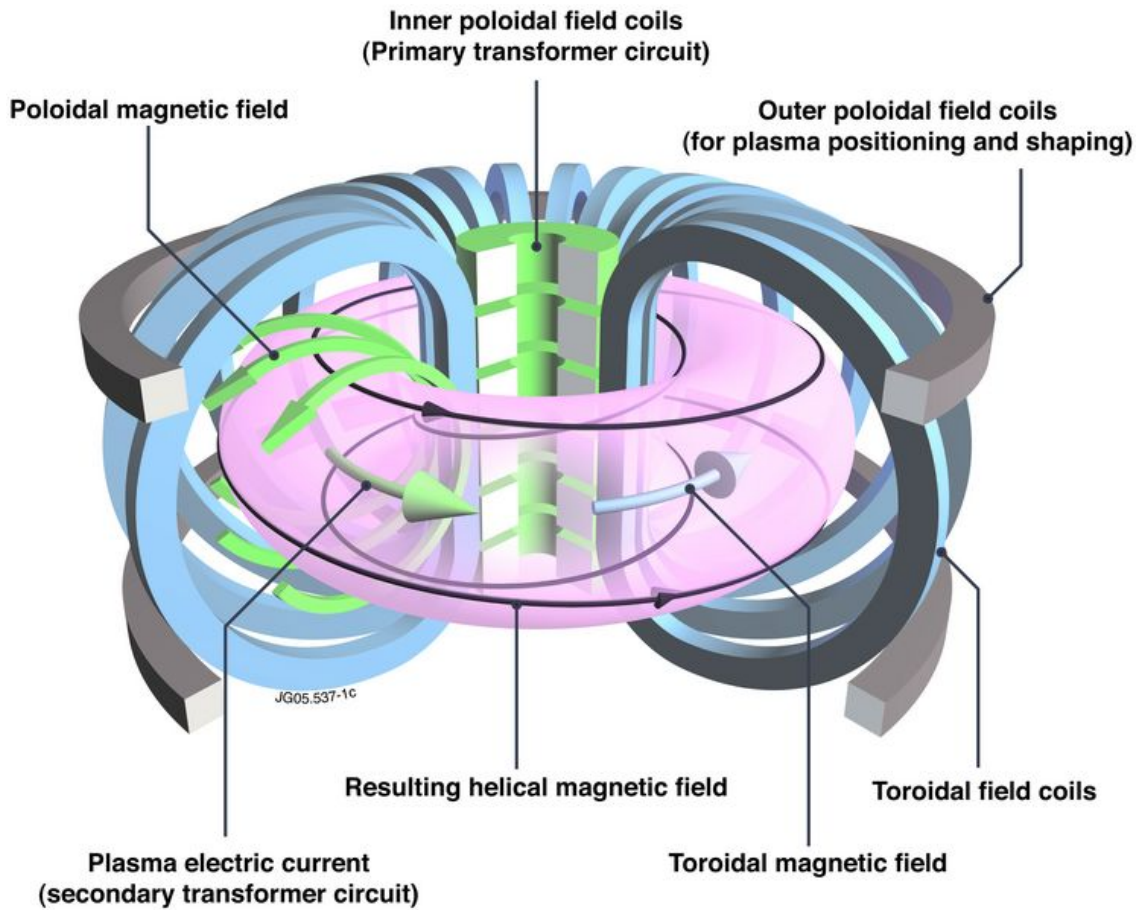


Figure 1.4 – Illustration of the coils and the resulting magnetic field in a tokamak. The central solenoid, the plasma current, and the poloidal magnetic field are indicated in green. The toroidal field coils and the toroidal magnetic field are shown in blue. The outer poloidal field coils are displayed in gray. The confined plasma is represented by the magenta torus.

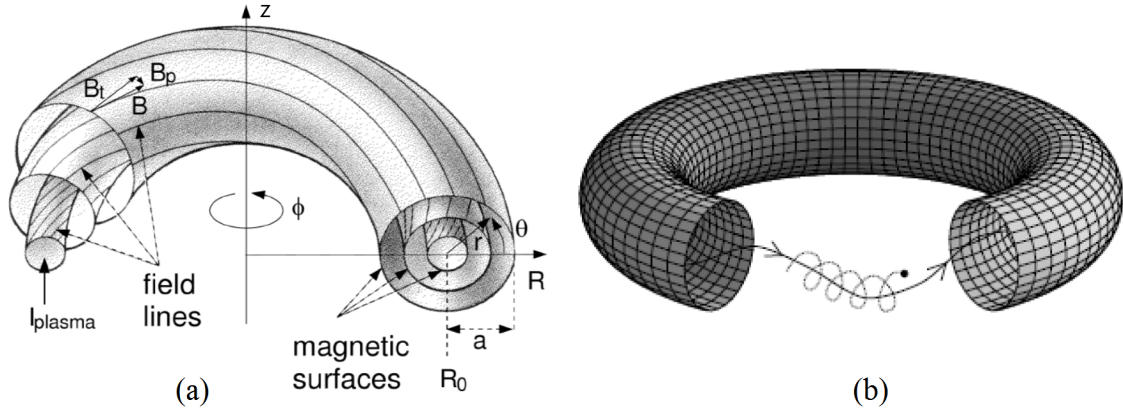


Figure 1.5 – (a) Geometry of the magnetic field lines, coordinates definition, and nested flux surfaces. (b) Charged particle orbit (dashed line) in a tokamak magnetic field (continuous line).

(j). An equilibrium requires zero net forces acting on the plasma. This leads to the force-balance equation:

$$\mathbf{j} \times \mathbf{B} = \nabla p. \quad (1.4)$$

This implies that no pressure gradient is present along the magnetic field lines ($\mathbf{B} \cdot \nabla p = 0$) and there is no radial current. The magnetic field lines are embedded into concentric magnetic surfaces with constant pressure. The nested flux surfaces are illustrated in figure 1.5 (a). Since parallel transport is very large compared to the perpendicular one, it can be assumed that on a flux surface not only the pressure is constant $p = nT$, but also the temperature T and the density n of the plasma are constant on each flux surface. Therefore, these quantities are often represented by one-dimensional profiles, labeled by a normalized flux coordinate, such as:

$$\rho_{\Psi} = \sqrt{\frac{\Psi - \Psi_{\text{axis}}}{\Psi_{\text{LCFS}} - \Psi_{\text{axis}}}}, \quad (1.5)$$

$$\rho_{\Phi} = \sqrt{\frac{\Phi - \Phi_{\text{axis}}}{\Phi_{\text{LCFS}} - \Phi_{\text{axis}}}}, \quad (1.6)$$

where Ψ is the poloidal magnetic flux and Φ is the toroidal magnetic flux. The coordinate ρ is defined such that it is null at the magnetic axis, which is the innermost magnetic surface (it is actually a line), and it assumes the value of $\rho = 1$ at the last closed flux surface (LCFS). The radial coordinate is more commonly referred as ρ_{pol} (corresponding to the poloidal flux) or ρ_{tor} (corresponding to the toroidal flux).

Given that the magnets are a dominant factor in the design of a reactor (they are one of the most expensive components), the ratio between the pressure of the plasma and the magnetic energy density

$$\beta = \frac{p}{p_{\text{mag}}} = \frac{nk_B T}{B^2/2\mu_0}, \quad (1.7)$$

1 Introduction

is an important figure of merit in tokamak physics, since it illustrates how efficiently a device confines its plasma. In the formula k_B is the Boltzmann constant and μ_0 is the vacuum permeability.

The ratio between the toroidal magnetic field B_t and the poloidal magnetic field B_p defines how many poloidal turns i a magnetic field line does per toroidal turn. This is expressed by the safety factor

$$q = \frac{1}{i} = \frac{d\Phi}{d\Psi}. \quad (1.8)$$

In a circular tokamak (creating plasmas with a circular cross section), q can be approximated as

$$q = \frac{2\pi}{\Delta\theta} = \frac{d\phi}{d\theta} \approx \frac{rB_t}{RB_p}, \quad (1.9)$$

where $\Delta\theta$ is the angle traveled by a field line in the poloidal direction for one turn in the toroidal direction $\Delta\phi = 2\pi$. The safety factor can be expressed as the rate of change of toroidal flux with poloidal flux, as in eq. 1.8. If a field line closes itself after a finite number of helical turns, its q value is rational and can be expressed as the ratio between the number of toroidal turns m and poloidal turns n , $q = m/n$. Flux surfaces with a rational value of q are the more unstable ones as non-axisymmetric deformations of flux surfaces can be produced without bending the field lines. The term 'safety' refers to the stability of the plasma. This is because q is inversely proportional to the plasma current I_p (which is proportional to B_p), and plasmas with a relatively smaller current are more stable to current-driven (kink) instabilities. An important parameter for the stability of the plasma is the safety factor at 95% of the magnetic flux q_{95} , which usually denotes an unstable plasma for $q_{95} \leq 2$.

1.3.1 Limiter and divertor configurations

The plasma is surrounded by a vacuum vessel and, depending on the geometry of the magnetic flux surfaces, there can be two different types of configurations in which the plasma comes in contact with the wall of the vessel. These are known as the *limiter* and the *divertor*, sketched in figure 1.6. The limiter (a) consists in a protruding element that limits the plasma-wall interaction to a small area, while protecting the vessel. Due to its high temperatures, the plasma erodes the limiter material, causing an increase in the number of impurities diffusing into the plasma. These impurities can radiate a large fraction of the plasma energy, leading to a cooling of the plasma and, in the worst case, to a disruption of the plasma current. The divertor configuration (b) has extra magnetic coils that create a null point (called *X-point*) in the poloidal magnetic field near the edge of the plasma. As plasma diffuses from the confined region across the LCFS, also called separatrix, to the region of open field lines, there is a rapid loss of particles and energy along the field lines, which reaches the divertor targets. Due to the high ratio of parallel to perpendicular transport, only a narrow layer of plasma, called *Scrape*

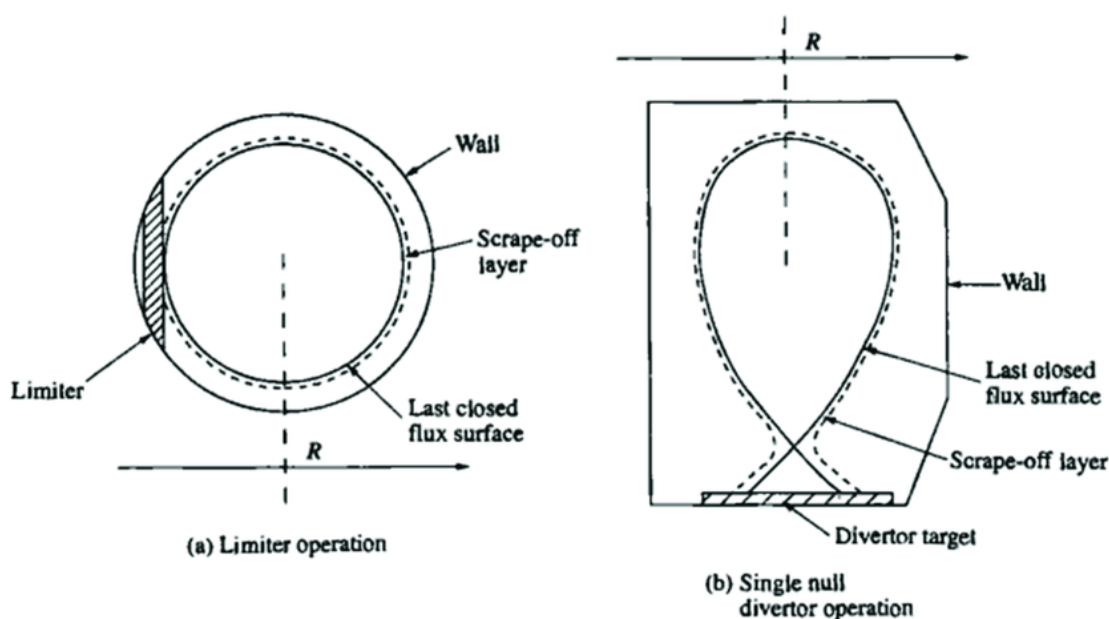


Figure 1.6 – Schematic diagram of poloidal cross-sections of a tokamak in the limiter (a) and in the divertor (b) configurations [13].

Off Layer (SOL), connects the separatrix to the divertor targets, as shown in the diagram. Because of the distance between the divertor and the confined plasma, this configuration provides a better isolation from impurities. The negative aspects of the divertor are that it requires a larger volume of the vacuum chamber, and tends to focus the heat load on a narrow region of the divertor target. The exhaust of the extremely large heat flux that is expected in future fusion reactors represents one of the greatest challenges in the field of magnetic confinement fusion. New innovative solutions are being studied to handle the heat fluxes of several MW/m^2 [15], which are at the limit of present technologies.

Together with preventing impurities to reach the core of the plasma, the divertor has other key advantages over the limiter. The structure of the divertor can be optimized to achieve a high neutral pressure, which allows for more efficient pumping of particles than in a limiter configuration. Pumps, located near the divertor plates [16], help to control the plasma density, and will be an essential element of future fusion reactors as they remove the helium ash produced by the D-T fusion reactions, which otherwise dilute the plasma deteriorating the performance of the device. Also, the divertor helps reducing the power loads by radiation, decreasing the temperature of the plasma. When the temperature becomes lower than about 5 eV, the divertor reaches a state called *detachment* [5]. In this conditions atomic processes reduce the particle flux to the divertor targets. Detachment is a favorable regime compared to the *attached* regime since the reduced power and particle loads can extend the life time of the materials constituting the divertor. Finally, the divertor allows the plasma to access more easily the H-mode regime, presented in section 1.3.2.

1.3.2 Confinement regimes of tokamak plasmas

The *high confinement mode (H-mode)* is a regime in which the energy confinement of the plasma is strongly increased with respect to the standard *low confinement mode (L-mode)*. The H-mode was discovered on the ASDEX tokamak [17]. To access this regime, the plasma needs to be heated with a sufficient amount of power [18, 19]. The increased confinement stems from the edge of the confined plasma, in the proximity of the separatrix. A layer of plasma in this region (of the extent of a few centimeters) exhibits strongly reduced perpendicular transport by means of an edge transport barrier (ETB), and consequent development of steep gradients of both temperature and density. This steep gradient region is called *pedestal*, as it looks like a structure elevating the core profiles. Figure 1.7 (a) shows the pressure

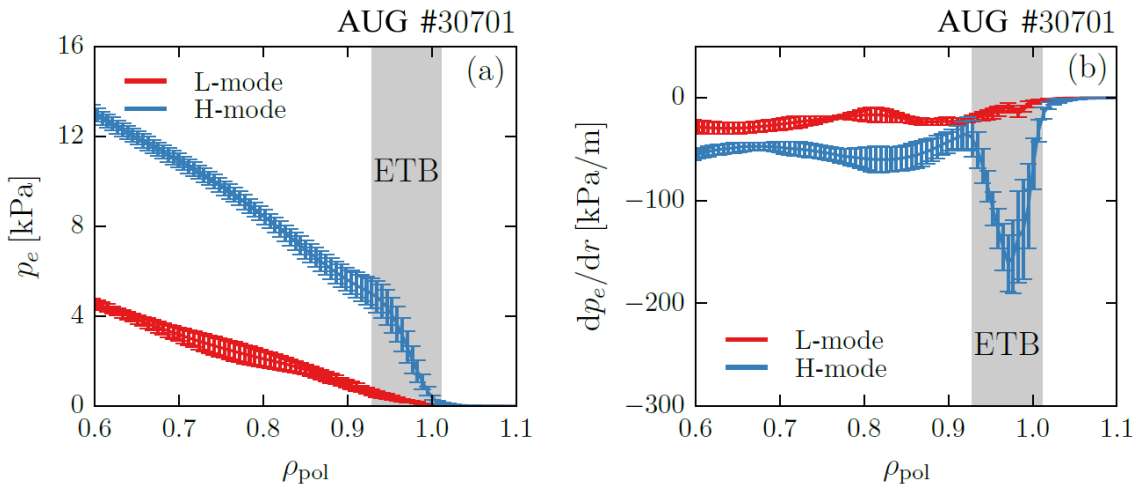


Figure 1.7 – Profiles of the electron pressure (a) and its gradient (b) in the L-mode (red) and H-mode (blue) phases of a plasma in the ASDEX Upgrade (AUG) tokamak [20].

profiles of a plasma in L-mode (red) and in H-mode (blue), where the feature of the pedestal can be identified. The mechanism behind the creation of the ETB is not yet fully understood, but the most agreed explanation is based on the suppression of turbulence induced transport by a plasma flow velocity shear [21]. Such flow originates from a radially varying electric field E_r , that creates a $\mathbf{E} \times \mathbf{B}$ drift which ultimately decorrelates the turbulence structures. Neoclassical theory suggests that the poloidal rotation in the edge is small, therefore the main terms contributing to this edge E_r are the toroidal rotation and the pressure gradient [22]. A comparison of pressure gradient profiles in L-mode and in H-mode is illustrated in figure 1.7 (b). Because the edge pressure gradient steepens due to the reduced transport it is difficult to identify the causality in the L-H transition. What increases first, the velocity shear or the pressure gradient?

The strong pressure gradients arising from the turbulent transport suppression constitute the drive for MHD instabilities in the pedestal region, called *Edge Localized*

Modes (ELMs) [23]. The ELMs are periodic events that cause strong plasma transport, causing a relaxation of the edge pressure profile and limiting the growth of the pedestal. Given the large amount of power that is released by the ELMs, they represent a serious concern for the wall and divertor materials of future fusion reactors [24]. A high pedestal pressure on the one hand increases the plasma confinement and therefore the fusion performance of a future reactor, on the other hand it leads to larger heat loads on the materials due to the ELMs. The H-mode is the operational regime foreseen for a future fusion reactor given its good confinement properties, but a special attention will be required to satisfy the limits imposed by power exhaust. Due to its importance for the next tokamaks generations, the ELMy H-mode regime is the one considered in this PhD thesis.

The current generation of tokamaks can rely on heating systems delivering large amounts of heating power to the plasma. This makes the H-mode easily accessible, and is therefore the present more regular confinement regime, also because of the high research interest it represents. However, due to the already mentioned large heat loads, ELMs will have to be controlled or even suppressed in future reactors to preserve the integrity of the machine. In recent years, a large effort has been made to develop operational regimes that maintain the good confinement performance of the H-mode while suppressing and mitigating ELMs. Many natural ELM-free and small-ELM regimes, such as the *quiescent H-mode*, the *improved confinement mode (I-mode)*, the *type-II*, and the *grassy ELM-regime*, have been obtained in various tokamaks. The current research on these regimes focuses on understanding and extending their access and sustainment, since it is not yet clear if they can be obtained in future reactors and if they can provide good confinement properties while causing tolerable heat loads on the plasma facing components. In this thesis also this aspect has been considered, including in the analysis experimental stationary phases in the small-ELMs regime, in addition to the standard type-I ELMs.

1.3.3 Heating systems

In order to heat the plasma in a tokamak, several technologies exploiting different physics mechanisms are used, as depicted in figure 1.8:

- **Ohmic heating** is naturally generated in a tokamak due to the resistivity of the plasma. The Ohmic heating power is proportional to I_p^2 . Because the resistivity decreases as $T^{-3/2}$, there is a limit on the maximum temperature the plasma can reach using this method only.
- **Electromagnetic waves** injected into the plasma can be absorbed and heat the different species. Depending on their frequencies these waves resonate with the ion or electron cyclotron frequencies, which is the frequency at which particles gyrate around the magnetic field lines. These frequencies lie in the radio-frequency range for ions and in the microwave range for electrons. The different heating systems are therefore called *Electron Cyclotron Resonance Heating (ECRH)* and *Ion Cyclotron Resonance Heating (ICRH)*. The plasma

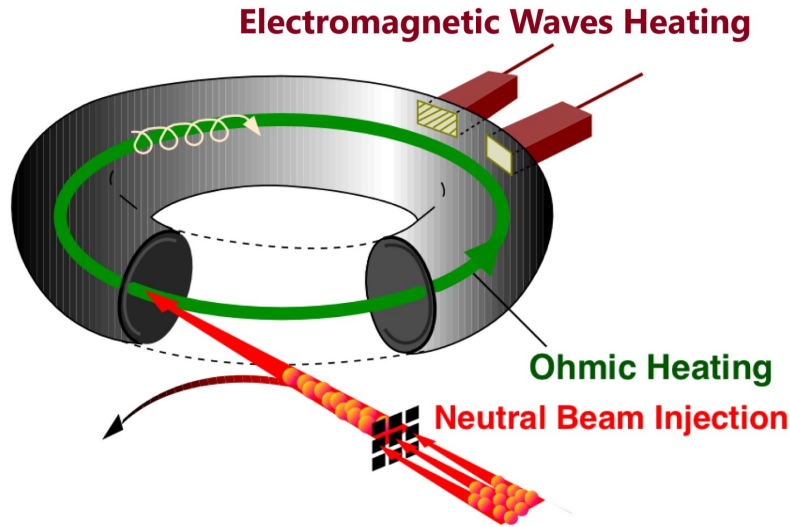


Figure 1.8 – Artistic representation of the different heating systems in a tokamak.

can also be heated by means of waves at the *lower hybrid* frequency (generated by dedicated systems), so called because it is a "hybrid", or mixture, of two frequencies.

- **Neutral Beam Injection (NBI)** consists in a highly energetic beam of neutral hydrogen or deuterium atoms which, by not being charged, are not deflected by the magnetic field and can be injected into the plasma. These particles get ionized and transfer their kinetic energy to the plasma by collisions.
- **α -particles** produced by the fusion reaction (carrying 3.5 MeV of energy) will provide self-heating of the plasma in future reactors [25–27].

1.4 Plasma Performance

From the plasma physics standpoint, the main reason nuclear fusion has not yet succeeded to produce electricity is the low energy confinement. In order to become a viable and economically attractive source of energy, it is necessary that the power produced by the fusion reactions P_{fus} is significantly larger than the auxiliary heating power P_{aux} , applied by external heating sources. The ratio between these two quantities defines the fusion power multiplication factor $Q = P_{fus}/P_{aux}$. The total power that heats the plasma P_{heat} is the sum of the auxiliary heating power P_{aux} and the fraction of the power produced by the fusion reactions carried by the α -particles $\frac{1}{5}P_{fus}$:

$$P_{heat} = P_{aux} + \frac{1}{5}P_{fus}. \quad (1.10)$$

In stationary conditions, P_{heat} is equal to the power lost due to transport through the LCFS P_{loss} :

$$P_{heat} = P_{loss}, \quad (1.11)$$

and therefore the auxiliary heating power can be expressed as

$$P_{aux} = P_{loss} - \frac{1}{5}P_{fus}. \quad (1.12)$$

The problem is that the confinement of the energy of the plasma is rather weak in present tokamaks, leading to a large P_{loss} . This leads to the requirement of a large heating power to sustain a certain plasma energy, which makes the problem of obtaining a high value of Q extremely challenging. The recognized cause of the observed large transport is plasma turbulence. So far the record for the largest fusion gain has been obtained in the Joint European Torus (JET) during a D-T experiment, where a $Q = 0.6$ was achieved [28].

The energy of the plasma can be divided in two different components, the energy carried by the particles in a thermal distribution W_{th} , and the energy carried by the fast (supra-thermal) particles W_{fast} . In a reactor, the thermal particles will give the major contribution to the fusion reactions, therefore we will focus on the corresponding term W_{th} . The thermal energy confinement time τ_{th} is the ratio between the thermal energy stored in the plasma W_{th} and P_{loss} :

$$\tau_{th} = \frac{W_{th}}{P_{loss}}. \quad (1.13)$$

In practice, it represents the time it takes for the plasma to lose its energy if the heating sources are removed (including the α -particles). The two most effective ways of increasing τ_{th} , to obtain a sufficiently high Q , are increasing the plasma current, and increasing the size of the device. To increase I_p , also B_t has to be increased, as the two are coupled by the safety factor, which should be high enough to avoid plasmas instabilities (kink instabilities, presented in section 3.1.4). The maximum achievable B_t (and therefore I_p) is limited by the technology used for the coils generating the magnetic field. The size of the device instead is more a matter of economical budget rather than technological limit, with the cost of the device being proportional to the volume of the machine. The energy confinement time increases with the size of the device because the dependence on this parameter is stronger for the plasma energy than for the losses due to transport.

This means that to progress in the challenge of producing energy by nuclear fusion, larger devices need to be built. This is the philosophy of the ITER tokamak under construction in Cadarache (France), which has the aim of reaching a $Q = 10$, which corresponds to sustain a plasma predominantly heated by α particles, demonstrating the technological feasibility of magnetic confinement fusion.

The prediction of the ITER energy confinement time, on which is based the design of the reactor, has been obtained by the use of scaling laws, which are based on statistical analyses performed on large databases of experimental data. These scaling laws for the global plasma confinement are very valuable and useful tools for zero dimensional (0D) predictions, and even in providing a scaling factor in (semi-)empirical modeling for the prediction of the radial kinetic profiles (i.e. the

1 Introduction

plasma quantities, such as temperature, density). They translate the complexity of the entire physical system of the plasma into a relatively simple log-linear regression based on reduced essential sets of engineering parameters, most commonly the plasma size, the plasma current, the magnetic field, the heating power, the plasma density and the plasma composition. In particular, for ITER the IPB98(y,2) scaling law has been created [29], using a database containing the measured thermal energy confinement time for 9 different tokamaks from plasma phases with NBI heating only, except for one device (Alcator C-Mod) with ICRH only:

$$\tau_{th}^{IPB98(y,2)} = 0.0562 \times I_p^{0.93} B_T^{0.15} P^{-0.69} n_e^{0.41} M^{0.19} R^{1.97} \epsilon^{0.58} \kappa^{0.78} \quad (1.14)$$

where P is the loss power, n_e is the line averaged density, M is the average mass number, R is the major radius, ϵ is the aspect ratio, and κ is the elongation of the plasma. Figure 1.9 shows a comparison between the measured and predicted thermal energy confinement time.

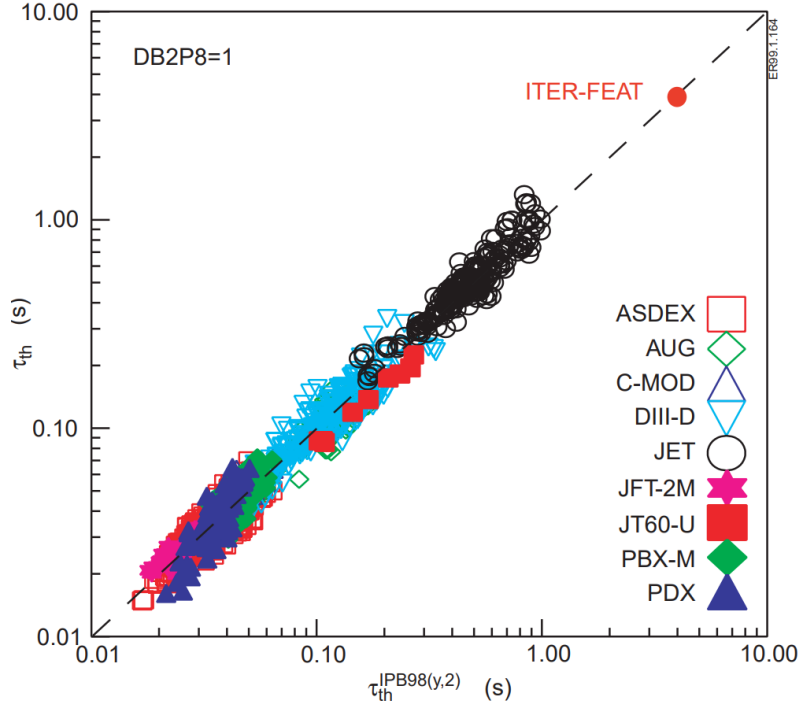


Figure 1.9 – Comparison between the measured thermal energy confinement time and the one predicted by the IPB98(y,2) scaling law for 9 different tokamaks and for ITER [30].

In the design of the ITER reactor the maximum magnetic field in the innermost region of the plasma is fixed by the engineering constraints, leading to a $B_0 = 5.3$ T. The energy confinement time that is expected to provide a $Q = 10$ is $\tau_{th} = 3.62$ s [31]. Such τ_{th} determines, thanks to the IPB98(y,2) scaling law, the plasma dimensions, leading to a major radius of $R_0 = 6.2$ m, a minor radius of $a = 2$ m, and a resulting

aspect ratio of $R_0/a = 3.1$. The plasma volume is then $V_p = 837m^3$, and the surface to volume ratio will be small to improve the plasma confinement. With those discussed dimensions ITER is close to being a full-scale prototype fusion reactor both in term of size and performance. However, it still remains an experimental facility since all the devices to convert the heat into electricity will not be present in the machine. Also, the elements for the breeding of tritium will not be like that required in a reactor.

The large experience with the operation of tokamaks has shown that these scaling laws can robustly capture some dominant dependencies on critical engineering parameters, for instance that on the plasma current and to some extent on the plasma size, but at the same time has revealed that some of the other dependencies, like those on the density and the heating power, are connected to a complex combination of various physical effects which depend on several other variables and can be hardly described within a zero-dimensional approach for all domains of operation [32–34]. Moreover, since these statistical approaches do not contain any (or little) element of the physics which is behind these dependencies, their predictive reliability has to be considered with care, as the extrapolation to reactor conditions requires to move largely outside of the multi-dimensional domain of data over which the statistical analysis has been performed. This means that the energy confinement time predicted for ITER contains large uncertainties.

Another way of estimating the energy confinement time, is by predicting the plasma kinetic profiles by means of one dimensional (1D) approaches which combine different modules describing plasma transport and sources at various levels of integration, and various levels of realism. This can imply the coupling of different modules to describe various transport mechanisms and sources [35–44], while adopting boundary conditions from measurements inside the confined plasma, but also the connection between core and edge, including a description of the pedestal [45–54]. Today these integrated modeling workflows can rely on increasingly sophisticated theory-based models for turbulent transport, particularly applicable in the core of the confined plasma [1, 55–57]. Here the completeness and realism of the physics description is naturally limited by requirements in computational time, which is particularly severe when simulating the dynamical evolution of entire discharges. Moreover, since at least in this context no single model for plasma transport exists which can be applied over the entire plasma cross section, predictions unavoidably rely on a set of empirical elements, which usually consist in the definition of boundary conditions which are taken from experimental measurements outside the radial simulation domain. Obviously the use of experimental measurements as boundary conditions strongly limits the possibilities of this approach to the prediction of non-existing devices. This limitation is particularly severe in the H-mode confinement regime and the related operational scenarios which are foreseen for ITER [58], and which could be also considered for a future fusion reactor, since in this regime the physics regulating the different plasma regions becomes even more complex to describe. To overcome this limitation, simulations for ITER have been performed with integrated

models which take the boundary conditions at the separatrix (as a fixed value) from SOL simulations [59], or are directly including a self-consistent description of the boundary conditions, using scalings obtained from a database of SOL simulations [60–62]. Such approach provides important insights to understand the behavior of ITER plasmas, clarifying the effects of the divertor and SOL conditions on pedestal and global confinement. However, these models have never been systematically validated on a database of experiments from existing devices, therefore, the accuracy of such predictions is uncertain.

As already mentioned, the maximum achievable pressure of the H-mode pedestal is limited by the ELMs. The trigger of these instabilities turns out to be sufficiently well described by magneto-hydrodynamic (MHD) models based on linear physics. This, combined with particle and energy transport levels, result in a determination of the pedestal height and width. The linear stability of these modes also depends on the parameters of the core, particularly through the plasma pressure and the consequent impact on the Shafranov shift of the magnetic equilibrium, while, at the same time, the core profiles depend on the boundary conditions set by the pedestal stability. Such a strong coupling clearly requires a modeling framework which describes both core and edge self-consistently [52–54]. The pedestal stability is also critically affected by the actual shape of the pressure profiles, which are influenced by the radial transport and also by the pressure values at the separatrix, directly connecting pedestal stability with the properties of the scrape-off layer (SOL). In tokamak operation, and particularly in a reactor, SOL parameters have to respect the constraints imposed by power exhaust and thereby an interesting and highly relevant problem becomes the study and the prediction of how the plasma confinement is affected by the SOL and the divertor conditions. This also implies that a complete model for plasma confinement cannot exclude the SOL, which is usually modeled by highly sophisticated and computationally expensive 2D or 3D edge codes. These codes, however, are not practical to be coupled with a 1D transport solver.

1.5 Thesis Objectives and Outline

The aim of this PhD thesis is to develop an integrated modeling tool, based on a 1D transport solver, which combines realistic modules to give a self-consistent and complete description of the different plasma regions, so that the only necessary inputs are the plasma engineering parameters and the external actuators. This approach is carried out with the goal of keeping the amount of empirical and device specific elements to a minimum. It is then interesting to see whether such a model would have the possibility of correctly predicting critical dependencies on various hidden parameters which cannot be captured by 0D scaling laws, offering the possibility to obtain more reliable predictions of the plasma confinement also for future devices.

Also, the prediction of the pedestal performance for ITER is based on models, such as EPED [7], which contain many assumptions on the input parameters and

the boundary conditions. As an example the pedestal top density must be given as input, and the temperature and density values at the separatrix are given by simple assumptions (e.g. $n_{e,sep} = n_{e,top}/4$). This poses two limitations: first, different assumptions on the pedestal density profile and its gradients can have a strong impact on the result of the pedestal stability calculation (as observed on multiple devices such as AUG, JET-ILW (ITER-like wall) and TCV [63–65]), and second, it is important to take into account the effects of the SOL and divertor conditions on the separatrix conditions. Therefore another important point for this PhD thesis is to identify a way to include into the integrated model a description of the pedestal which is capable of accurately predicting the pedestal top density, and capture the effects of the SOL and divertor conditions on the pedestal pressure.

Finally, not only it is important to develop a model which has increased predictive capabilities over the currently present solutions, but it is important to perform an extensive validation of the model on a large experimental database to address its reliability. A test of the model on a large database also gives important information about which range of parameters the model is trustworthy on, and which kind of effects or phenomena it is able to replicate.

This thesis is organized in different chapters. Chapter 2 contains a description of the machine, the diagnostics, and the method used to obtain the experimental data. Chapter 3 gives a brief overview on the transport mechanisms determining the plasma profiles, with specific emphasis on how these can be modeled within a transport code. Chapter 4 describes the integrated modeling workflow explaining the details of the different components constituting it. Chapter 5 presents the results obtained from the first application of the model to a restricted selection of experimental cases. Chapter 6 describes the extensive validation of the model carried out on a large database covering a wide variation of operational parameters, and discusses the outcome of this project. Finally, chapter 7 contains the discussions and outlook.

2 ASDEX Upgrade Experiment

Summary

2.1	ASDEX Upgrade tokamak	44
2.2	Diagnostics	45
2.2.1	Magnetic Probes	46
2.2.2	Thomson Scattering	46
2.2.3	Lithium Beam	47
2.2.4	Interferometer	47
2.2.5	Electron Cyclotron Emission	48
2.2.6	Charge Exchange Recombination Spectroscopy	48
2.3	Tools for profile fitting	49
2.3.1	Integrated Data Analysis	49
2.3.2	Gaussian Process Regression	50
2.3.3	AUGPED	50
2.3.4	Summary	52

2.1 ASDEX Upgrade tokamak



Figure 2.1 – Interior view of the ASDEX Upgrade tokamak during installation of the tungsten plasma facing components (source: IPP web-page).

ASDEX Upgrade (AUG) is a medium-sized metallic-walled divertor tokamak (figure 2.1) located at the Max-Planck-Institute for Plasma Physics in Garching (Germany). The experimental results considered in this work were obtained on this tokamak. AUG entered into operation in 1991, and is the follow-up experiment of the ASDEX (Axial Symmetric Divertor EXperiment) tokamak, which was operated from 1980 to 1990. Some typical AUG operational parameters are listed in table 2.1. The AUG tokamak has currently the highest ratio of the heating power to the size

Parameter	Value
Major radius R_0	1.65 <i>m</i>
Minor radius a	0.5 <i>m</i>
Plasma volume V	$\sim 12 \text{ m}^3$
Plasma current I_p	0.6-1.2 <i>MA</i>
Toroidal magnetic field B_t	1.5-3.2 <i>T</i>
Maximum NBI heating power	20 <i>MW</i>
Maximum ECRH power	5 <i>MW</i>
Maximum ICRH power	4 <i>MW</i>

Table 2.1 – Typical operational parameters of the ASDEX Upgrade tokamak.

of the machine, which makes it particularly suited for exhaust studies and plasma scenario development for future reactors [66–68]. The available heating systems consist of 8 NBI sources, providing up to 2.5 MW each for a total of 20 MW of heating power, 8 ECRH gyrotrons, each delivering ~ 0.6 MW of heating power for a total of ~ 5 MW, and 4 ICRH generators, heating the plasma with 1 MW each for a total of 4 MW. The maximal acceleration voltage of the NBI heating system is 60 kV for 4 of the sources, and 93 kV for the other 4. The NBI sources have a different orientation, leading to a deposition of the power which can be more central or more peripheric (4 beams are more aligned to the magnetic axis while the other 4 are pointing more off-axis). The ECRH system makes use of metallic mirrors which can be tilted to deflect the beam at the desired angle and change the heating position. The position of the ICRH antennas is fixed so it is not possible to change the location of the heating power by means of mechanical movements of the system. The resonance position of the ion cyclotron waves is determined by the intensity of the toroidal magnetic field and by the frequency of the generator.

2.2 Diagnostics

AUG is equipped with an extensive set of diagnostics that can accurately monitor the plasma behavior. Their high time and spatial resolution enables a precise evaluation of many plasma quantities (e.g. the most relevant in the framework of this thesis are temperature, density, and rotation). This section presents an overview of the diagnostics used to collect the experimental results considered for this work.

Figure 2.2 illustrates the location and the lines of sight of these diagnostics on poloidal and toroidal cross sections of the AUG vessel.

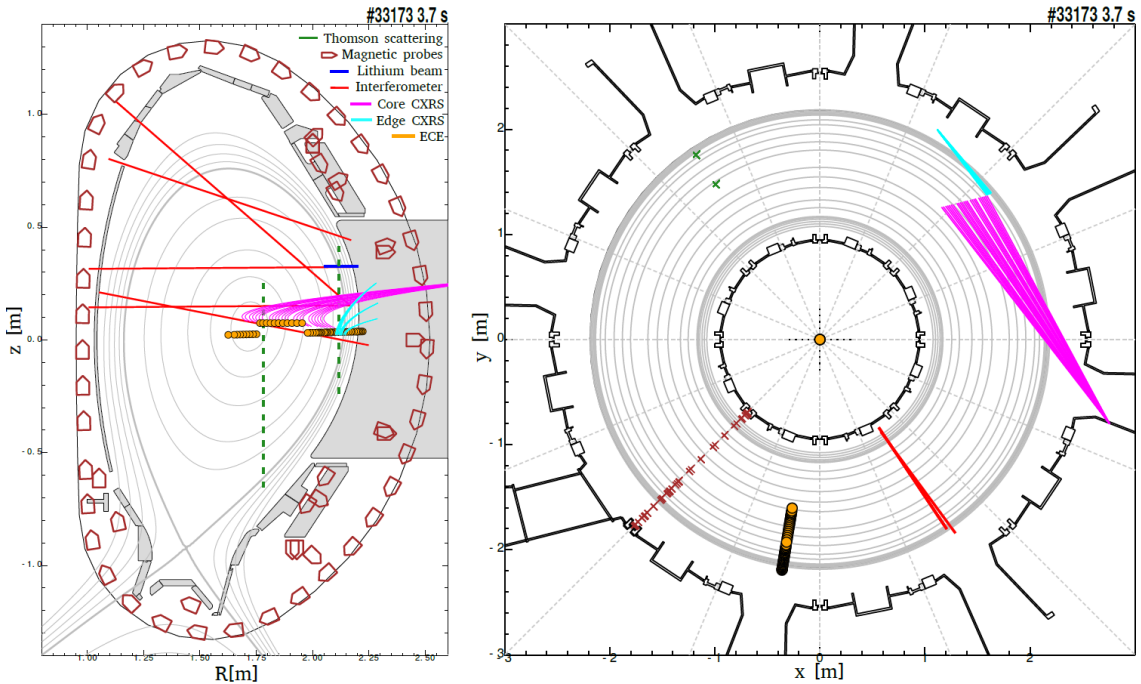


Figure 2.2 – Poloidal (left) and toroidal (right) cross sections of the AUG vessel with the location and the lines of sight of the main diagnostics.

2.2.1 Magnetic Probes

Magnetic coils are fundamental diagnostics of tokamaks, as they provide information on the magnetic field from which it is possible to reconstruct the magnetic flux surfaces. The poloidal flux function $\psi(R, z)$ can be evaluated by solving the previously mentioned Grad-Shafranov equation using equilibrium codes (such as CLISTE [69]), which use as input the measurements of the magnetic probes located in the vacuum vessel surrounding the plasma. This technique provides also information on other quantities, like the plasma current and the plasma stored energy (W_{MHD}). The latter is an experimental information that will be extensively used in this work.

2.2.2 Thomson Scattering

The Thomson scattering (TS) diagnostic measures simultaneously the temperature and the density of the electrons. The principle of this diagnostic is the scattering of electromagnetic waves (in this case emitted by a laser) on charged particles (in case of a plasma the electrons since $m_e \ll m_i$) [70]. The scattered radiation is frequency shifted due to double Doppler effects, one for the photon incoming and one

for the outgoing photon emitted by the electron. The Doppler width of the measured scattered radiation gives the information on T_e while the intensity is proportional to n_e . This implies that at low plasma density the measurements can result inaccurate due to a low intensity of the signal.

AUG makes use of two vertical TS systems [71], one for probing the core region and the other for the edge region of the plasma. This diagnostic relies on a cluster of four (for the core) and six (for the edge) Nd-YAG lasers with pulse energies of 1 J and pulse duration of 15 ns, and repetition rate of 20 Hz. The scattered light is detected by 16 channels for the core and 10 channels for the edge, with a spatial resolution of 25 mm and 3 mm respectively. Since the TS is the only diagnostic that measures the electron temperature and density simultaneously at the same location, it can be used for the alignment (i.e. radial mapping) of profiles relative to each other when combining the measurements from multiple diagnostics.

2.2.3 Lithium Beam

The lithium beam diagnostic provides information on the electron density at the edge of the plasma. The basis of this diagnostic is the interaction between the plasma and an injected neutral lithium beam. The Li atoms are excited or ionized due to the collisions between the lithium atoms and electrons and main ions. The emitted radiation can then be measured and corresponds to radiative de-excitation of the Li_{2p} state, which is the most abundant excited state. The characteristic line intensity is measured along the lithium beam in the plasma. The spatial distribution of the emission line together with the collisional-radiative model allows for the determination of n_e . Because the Li beam injected into the plasma gets quickly attenuated due to atomic processes, only measurements in the edge of the plasma are possible with this technique. At higher density of the plasma the beam penetrates less into the plasma due to a higher attenuation, decreasing the radial extent in which the measurements are reliable.

The lithium beam in AUG is injected from the low field side (LFS) with an energy of 60 keV. The emission profile is viewed by two different optical systems with 35 and 26 chords with 5 to 6 mm spatial resolution respectively. The maximum time resolution achievable is at a frequency of 200 kHz, although profile measurements are usually acquired averaging over $100\mu\text{s}$ to reduce noise level.

2.2.4 Interferometer

Interferometry allows the measurement of the line integrated density along a line of sight. A Mach-Zehnder interferometer is used for this purpose, consisting of a light beam in the far infrared range which is split into a reference beam bypassing the plasma, and a second beam passing through the plasma. The phase speed of electromagnetic waves in the plasma is proportional to the plasma density. It is therefore possible to evaluate the line averaged density of the plasma by looking at the phase shift between the two beams.

AUG is equipped with five lines of sight of the deuterium-cyanide-nitrogen (DCN) laser interferometer, operating at $195 \mu\text{m}$. This system gives an extremely accurate evaluation of the line averaged density at the different channels. Although the information provided is a line integrated quantity and not a local measurement, it is still very valuable as the only other diagnostic probing the core electron density of the plasma is the TS system, which is not as accurate and can be affected by the accuracy of its calibration. Thereby DCN integrated signals can be used for the overall calibration of TS (which provide local density measurements).

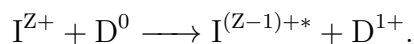
2.2.5 Electron Cyclotron Emission

The electron cyclotron emission (ECE) diagnostic measures the electron temperature. The gyrating electrons on their orbits emit photons due to the cyclotron radiation at their gyro-frequency and higher harmonics. If the density of the plasma is high enough, the plasma can be considered as optically thick at these frequencies, radiating as a black-body. In this case, the intensity of the radiation is proportional to the electron temperature, independent of the density.

AUG is equipped with a 1D ECE Heterodyne radiometer operating in X-mode at the second harmonic [72, 73]. This radiometer has 60 channels which are sampled at 1 MHz rate on different consecutive frequency bands, allowing measurements of the electron temperature with a high spatial and temporal resolution. Due to calibration uncertainty, limited amplifier stability, non-linearity, and other issues, the accuracy of the measurements is expected to be around 7% in the absolute value of the temperature. The uncertainties in the location of these measurements is about 1 cm, but it can be reduced by using a newly developed model for the position of the warm resonances and ray tracing [73]. The ECE is the diagnostic usually providing the most accurate evaluation of the electron temperature on AUG, but only for large enough plasma densities, which make it not reliable at the edge of the plasma. Forward modeling of the electron cyclotron radiation transport is used in the Integrated Data Analysis technique (presented in section 2.3.1) to overcome this limitation [72].

2.2.6 Charge Exchange Recombination Spectroscopy

The charge exchange recombination spectroscopy (CXRS) system measures the temperature, the rotation, and the density of light impurities. This diagnostic is based on the charge exchange processes between neutral atoms D^0 (injected by NBI or gas-puff) and ions of impurities I^{Z+} present in the plasma:



The electron captured by the impurity stays for a short time in the excited state and then experiences a radiative decay leading to a cascade of transitions to the ground level. The light emitted during specific transitions is analyzed spectroscopically, and

the impurity velocity and temperature with the corresponding statistical uncertainty can be evaluated from the Doppler shift and broadening of the measured spectral line. Due to significant energy exchange caused by collisions, the temperature of the impurities can be assumed to be equal to that of the main ions. This assumption might not be valid for low density, high power discharges, where the ion-impurity temperature differences can approach a value of 10% [74]. This can lead to a not always negligible effect on the estimate of fusion reaction rates, although generally small, since it is a function of the main ion temperature.

On AUG several CXRS systems are installed, probing both the core and the edge of the plasma, and with different lines of sight measuring the toroidal and the poloidal rotation. Recent upgrades improved the temporal and spatial resolution of the edge CXRS system [75].

2.3 Tools for profile fitting

The experimental measurements of the previously described diagnostics can be combined and processed in different ways to obtain radial profiles of the plasma quantities of interest. The used technique largely depends on the kind of application. For this work we used three different techniques, presented in this section.

2.3.1 Integrated Data Analysis

The integrated data analysis (IDA) is a computational tool based on a Bayesian probability approach which provides profiles of the electron temperature and electron density [76]. The diagnostics used by this technique are the Thomson scattering, the interferometer, the lithium beam, and the ECE, which are all mapped to the normalized poloidal flux coordinate ρ_{pol} . The IDA approach combines forward models for the different diagnostics to compute the probability distribution resulting from the uncertainties and the priors considered (e.g. smoothness, monotonicity, non-negativity constraints). Together with the profiles of electron temperature and density, this technique also provide an estimation of their errors. Since recently, the IDA profiles are automatically evaluated after every AUG discharge. The access to a rapid and robust analysis of the electron temperature and density of the plasma greatly accelerates the experimental operations and their study. In the context of this work, the IDA provides additional information which helps reducing the uncertainties when estimating the plasma kinetic quantities. Also, when studying core phenomena with turbulent transport models, a high level of confidence in the experimental gradients of the electron temperature and density is required. The IDA is a preferable option for this task, due to its accurate evaluation of core profiles gradients.

2.3.2 Gaussian Process Regression

The gaussian process regression (GPR) technique [77] has been used in this work to fit the CXRS measurements in order to obtain accurate core profiles of the ion temperature and rotation, and their gradients. The GPR algorithm is based on Bayesian statistical principles, with the assumption that the input noise is described by Gaussian probability distribution functions. This tool has the advantage, over other common fitting techniques (such as spline fits), that it provides statistically rigorous uncertainties of the fit and its derivatives, based on the errors of the measurements provided as input. A common issue when fitting H-mode plasma profiles is that it is difficult to obtain an accurate fit both in the core and in the pedestal region, due to their dramatic difference in gradients. The GPR methodology provides a potential solution to this problem by using sophisticated kernel functions (or covariance functions), which can rely on different warping functions based on the desired behavior of the length scale of the fit. The fit can thus be optimized using some tuning parameters, based on the a priori knowledge that in the core and in the pedestal regions different scale lengths of the profiles are expected.

This technique has proved very robust to provide accurate fits and derivatives estimation of the core ion temperature and rotation, together with uncertainties of these quantities. For these reasons, this tool has been used to create the inputs for turbulent transport simulations when performing core studies. For pedestal analysis instead (e.g. to evaluate the pedestal pressure), other techniques are preferable since obtaining accurate fits in the pedestal region requires fine tuning the parameters of the algorithm or significantly increasing the computational time, aspects which are not practical when analyzing large experimental database.

2.3.3 AUGPED

AUGPED is a code that allows users to combine the measurements from different diagnostics and process them to obtain fits of the main plasma kinetic quantities, through the use of a graphic user interface (GUI). As an example, figure 2.3 (a) shows the T_e data obtained by combining the ECE (blue), and the core (green) and edge (red) TS systems for a stationary phase (between 5 and 5.5 seconds) of the AUG discharge #33616. The raw data is mapped on ρ_{pol} , and a time filter is applied to remove the time points corresponding to the ELM crashes and the ELM recovery phases, retaining only the steady-state phases prior to the ELM crash. Focusing on the pedestal region, figure 2.3 (b) shows a vertical blue line indicating that the ECE data outside of $\rho_{pol} > 0.96$ is discarded. This is because, as we already mentioned, at low density the plasma is not optically thick and the ECE measurements are not reliable (as can be seen by the 'bump' at $\rho_{pol} \sim 1.02$). The measurements of different diagnostics are usually not naturally aligned to each other, and this is particularly evident in the pedestal region due to the steep gradients. The reason for this is currently under investigation, so far no evident reasons have been found [78]. To solve this problem the electron temperature measured by the edge TS is

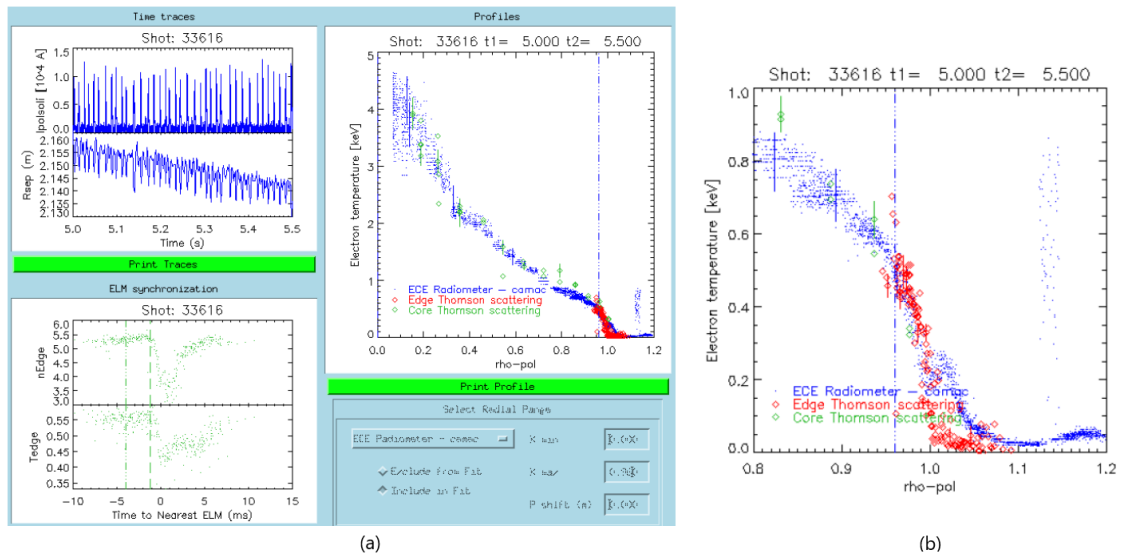


Figure 2.3 – (a) Illustration of the AUGPED GUI, which allows to combine the measurements from different diagnostics (in this case for T_e), map them to the preferred radial coordinate, filter the data relative to ELMs, and align the profiles to each other. (b) The edge TS data is shifted such that the separatrix electron temperature is ~ 100 eV, and the other diagnostics are aligned to it. The ECE data is discarded in the pedestal region ($\rho_{pol} > 0.96$).

shifted such that the separatrix electron temperature is ~ 100 eV, as typical of AUG [79]. All the other diagnostics are then aligned to the edge TS. Since this diagnostic measures the electron temperature and density simultaneously, for consistency also the density profile is shifted by the same amount as the temperature. The lithium beam is then also aligned to it. For the CXRS diagnostic this alignment is a more delicate process because there is no typical value of T_i at the separatrix, and the uncertainties of the measurements of this diagnostic become larger at the edge of the plasma (especially at the separatrix), due to a usually weak signal. Therefore, the CXRS data is usually fitted as it is, without performing any radial shift.

Finally, figure 2.4 shows the fits (magenta lines) of T_e , n_e , and T_i obtained with AUGPED using the modified hyperbolic tangent function. As one can see these fits reproduce very accurately the pedestal top measurements. The fit of the electron density also reproduces well the integral measurements of the interferometer, illustrated by the overlap between the magenta crosses (fit) the cyan dots (measurements). Due to the low radial resolution of the core TS diagnostic and its low accuracy in the pedestal top region, the core density gradient evaluated with this method is not very reliable. When looking at the core density gradients, the IDA technique is preferable. Also, the fitting tools available in AUGPED do not take into account of the measurements errors.

2 ASDEX Upgrade Experiment

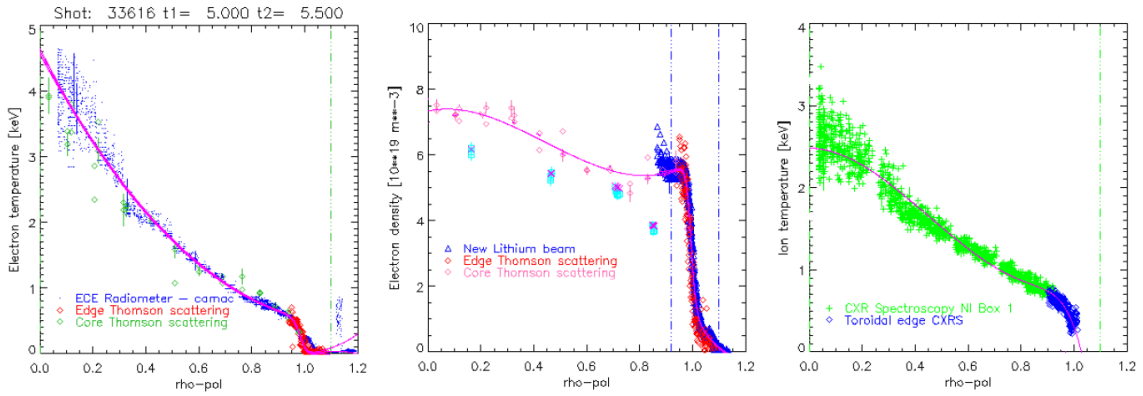


Figure 2.4 – Final fits (magenta lines) of T_e , n_e , and T_i obtained with AUGPED using the modified hyperbolic tangent function.

2.3.4 Summary

In summary, when performing turbulent transport simulation for core studies (using gyrokinetic codes or quasilinear turbulent transport models) a high confidence on the gradients is required, therefore for these purposes we used the information provided by the IDA (for T_e and n_e) and the GPR (for T_i and v_{tor}) techniques. To evaluate the experimental pedestal top parameters (pressure, temperature, density, and rotation) we made use of the AUGPED tool, since a manual alignment of the different diagnostic is required. Also, the modified hyperbolic tangent fitting method was found to be more accurate and robust when fitting pedestal profiles.

3 H-mode plasmas simulations: Transport and Stability

Summary

3.1	Transport in tokamak plasmas	53
3.1.1	Collisional transport	55
3.1.2	Turbulent transport	58
3.1.3	Prediction of pedestal profiles	62
3.1.4	Pedestal MHD stability	64
3.1.5	SOL transport	66
3.2	Simulation of plasma profiles with transport codes	69

3.1 Transport in tokamak plasmas

Transport physics aims at describing the mechanical and thermodynamical evolution of a system. The theory of transport in magnetized plasmas can be used to simulate the kinetic profiles by including a description of the gains (due to sources) and losses (due to sinks and outward transport). This requires to correctly predict the capability of the plasma to retain or evacuate energy, particles, and momentum for different operating conditions of the tokamak. Since the early studies of transport in tokamaks, physicist noticed that energy, particle, and momentum transport are regulated by different mechanisms. In particular it was predicted that cross-field collisional transport was an important cause for radial transport in the plasma, where collisions are produced by Coulomb scattering between charged particles. It was also noticed however, that collisional transport in tokamaks is responsible for far lower levels of transport than that measured experimentally in the plasma core. The experimentally inferred plasma heat and particle diffusivities are usually one or two orders of magnitude larger than the ones resulting from collisional transport model predictions. The phenomena accounting for the missing amount of transport arising from this comparison has been referred as anomalous transport, which today has been conclusively identified to be produced by micro-turbulence.

Fluid dynamics theory is capable of describing instabilities that can form in unfavorable regions of a dynamical system, such as the Rayleigh-Taylor instability, which amplifies small perturbations of an interface between two fluids of different densities, occurring when the lighter fluid is pushing the heavier fluid. In tokamak

plasmas, instabilities can develop according to a similar principle, i.e. due to the presence of finite gradients of the plasma temperature and density [80]. The presence of plasma microinstabilities leads to a turbulent state that in tokamaks produces the largest part of the radial cross-field transport of energy, particles, and momentum. The description of turbulent transport determining the plasma profiles is highly non-trivial due to the nonlinear dependence of the amplitude of radial diffusion on the plasma equilibrium quantities and the magnetic geometry. Also, the properties of turbulent transport can change significantly from the core to the edge of the plasma, not only in H-mode but also in L-mode (that is without the additional effects of the ETB on turbulence), due to strong changes in the plasma parameters, e.g. collisionality, the electron to magnetic pressure ratio, the safety factor and its shear. While core turbulent transport is quite well understood at present days, the description of turbulent transport in the edge of L-mode plasmas still presents several challenges [81–84]. The properties of turbulent transport in the edge of the plasma dramatically change in the different confinement regimes (L-mode, ELM-free improved regimes like the I-mode, and H-mode).

In principle, the description of transport in ELMy H-mode is even more challenging due to the transport caused by the ELMs. While in L-mode neoclassical and turbulent transport are sufficient ingredients to describe the plasma, which reaches stationary conditions, in ELMy H-mode also a description of the transport caused by the ELMs has to be included, as the profiles continuously evolve according to the ELM cycle. In practice however, it is not necessary to describe the dynamical behavior of the kinetic profiles, but it is sufficient, for our purposes, to estimate the plasma conditions right before the ELM crash. Also, the thermal energy of the plasma before the ELM crash is usually not too different from the thermal energy averaged over the ELM cycle. This approach for the prediction of the plasma profiles in ELMy H-mode conditions requires a description of the transport regulating the pedestal width and height (which is a measure of the pressure at the top of the pedestal) and also a description of the MHD stability of the pedestal to take into account the ELM onset. The description of pedestal transport in the inter ELM phase is extremely complicated due to the fact that many phenomena are competing in the determination of the radial diffusion. It is difficult to estimate the residual amount of turbulent transport, suppressed by the ETB, and the radial extent of the region of reduced transport. Empirical models can then be used to describe the pedestal transport, which are for example based on experimental observations. Such models, such as EPED [7], usually allow the determination of the pedestal profiles for a given value of the pedestal width, so that by scanning the pedestal width one can scan the pedestal pressure. The stability of such pedestal profiles is tested with linear ideal MHD codes to find the highest stable pressure, corresponding to pre-ELMs condition. This is also the approach adopted in the work of this thesis.

Finally, the boundary conditions of the confined plasma (at the separatrix) depend on the divertor parameters and on the transport in the SOL. This can be approximated by a one-dimensional model describing the SOL with 2 points, at its

boundary: the divertor and the separatrix at the outer midplane (two point model [4, 5]).

This chapter is organized in sections describing the different transport mechanisms. Section 3.1.1 introduces the general aspects of collisional transport, then section 3.1.2 gives an overview on turbulent transport and how this can be modeled. Section 3.1.4 explains the theoretical framework describing the pedestal MHD stability, regulating the ELM onset. Section 3.1.5 presents the derivation of the two point model, discussing why it has been preferred over more sophisticated and computationally expensive codes, to include into the integrated model the effect of SOL transport on the separatrix conditions. Finally, section 3.2 illustrates how the kinetic plasma profiles are simulated with a transport code, taking into account the aforementioned transport mechanisms, in particular for the application of the work of this thesis.

3.1.1 Collisional transport

Coulomb collisions constitute the most general mechanism of radial transport in plasmas. Collisional transport arising from collisions which affect the charged particles gyromotion around the field lines is referred to as classical transport. This transport mechanism can be described by a random walk diffusion process, where the characteristic radial step length (i.e. the displacement of particle after a collision) is given by the gyro-radius (or Larmor radius $r_L = mv_{\perp}/(qB)$), and the stepping frequency is given by the collision frequency ν . Thus, a diffusion coefficient can be written as

$$D_{classical} = r_L^2 \nu. \quad (3.1)$$

A non-zero density gradient can generate a flux from this diffusion. Also, a net particle flux can only arise from collisions between particles of different type, since otherwise they would simply switch places. For heat transport instead, it is sufficient that a temperature gradient is present to generate a flux, even between particles of the same type. The heat conductivity is $\chi = r_{L,s}^2 \nu$, and the Larmor radius for a given species of particles s is $r_{L,s} = m_s v_{\perp}/(q_s B)$. Because the perpendicular velocity is proportional to $v_{\perp} \propto \sqrt{T/m}$, it follows that $r_{L,s}^2 \propto m_s$. The collision frequency between species a and species b is proportional to

$$\nu_{ab} \propto \frac{\sqrt{m_{ab}}}{m_a} Z_a^2 Z_b^2, \quad (3.2)$$

where Z is the charge of the different species, and $m_{ab} = (m_a m_b)/(m_a + m_b)$ is the reduced mass, that is $m_{ie} = m_{ei} \approx m_e$, whereas $m_{ii} = m_i/2$. Thus, $\nu_{ii} \propto 1/\sqrt{m_i}$ and $\nu_{ei} \propto 1/\sqrt{m_e}$. The classical heat conductivity is therefore much higher for ion-ion collisions due to their much higher mass:

$$\chi_{ee} \approx \chi_{ei,ie} \approx \sqrt{\frac{m_e}{m_i}} \chi_{ii}. \quad (3.3)$$

3 H-mode plasmas simulations: Transport and Stability

Instead, particle transport is ambipolar, which means that the particle diffusivity D is the same for electrons and ions in absence of impurities.

Neoclassical transport describes an additional component of collisional transport produced by the presence of the toroidal magnetic confinement geometry. The toroidal geometry leads to the possibility of particles to get trapped in a magnetic mirror due to the gradient of the magnetic field along the field lines (the magnetic field is stronger at the center of the torus). The orbits of the trapped particles are called banana orbits due to their shape on the poloidal plane, as can be seen in figure 3.1. The characteristic step of the perpendicular neoclassical transport is

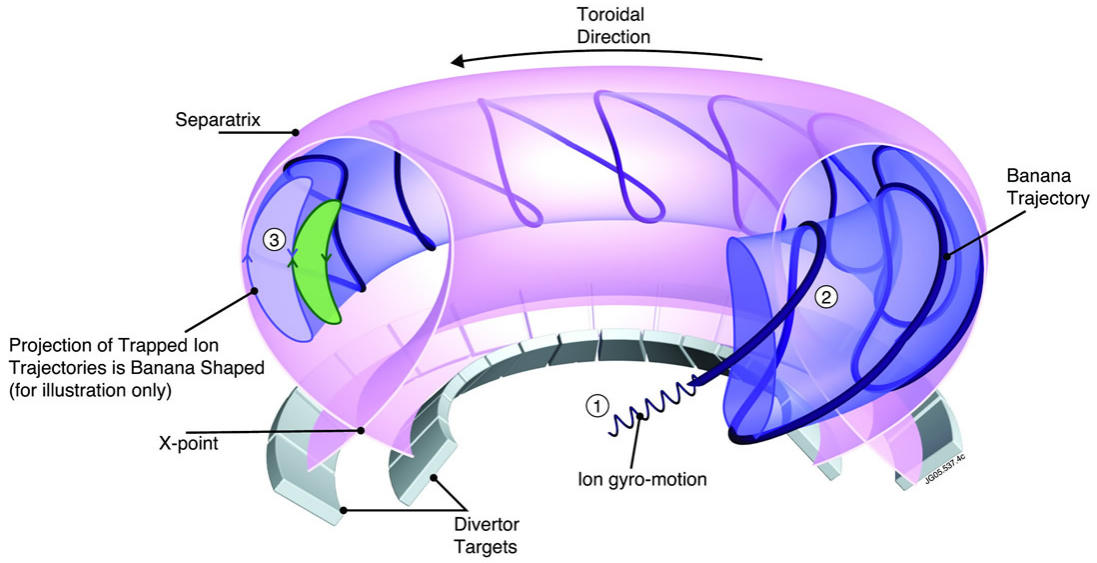


Figure 3.1 – Illustration of the banana orbits in a tokamak.

provided by the radial excursion of the guiding center orbits (trapped and passing) which are affected by collisions. Therefore, for trapped particles, the width of the banana orbit $w_B \approx r_L q / \sqrt{\epsilon}$ (here $\epsilon = r/R$ is the inverse of the aspect ratio), which is significantly larger than the Larmor radius, can be used to estimate the neoclassical diffusivity in a similar way as done for the classical diffusivity. Not only the step size is larger, but also the collision frequency increases to the effective collision frequency $\nu_{\text{eff}} = \nu/2\epsilon$. The larger collision frequency with respect to classical transport is related to the fact that collisions need to produce a smaller diffusion in the velocity space, that is only the reversal of the direction of the parallel velocity, to move the trapped particle orbit by one banana width. The neoclassical diffusion coefficient for the trapped particles can then be expressed as

$$D_{\text{banana}} = w_B^2 \nu_{\text{eff}} \frac{n_t}{n} = r_L^2 \frac{q^2 \nu}{2\epsilon^2} \sqrt{2\epsilon} \approx \frac{q^2}{\epsilon^{3/2}} D_{\text{classical}}, \quad (3.4)$$

where n_t/n is the trapped particle fraction, which can be expressed as $n_t/n = \sqrt{2\epsilon}$.

For typical plasma parameters at mid-radius one gets $D_{banana} \approx 100D_{classical}$.

Different neoclassical transport regimes exist, depending on the collisional frequency and the type of orbits that can still survive and are perturbed by collisions. The following normalized collisionality parameter allows the different regimes to be properly identified:

$$\nu_* = \frac{\nu_{\text{eff}}}{\omega_b} = \frac{\nu qR}{2\epsilon^{3/2}v_{th}}, \quad (3.5)$$

where ω_b is the trapped particle bounce frequency. Collisionality ν_* represents the inverse of the number of complete banana orbits which can be performed before a detrapping scattering. Three different regimes can be distinguished: the banana regime at low collisionality ($\nu_* < 1$), the Pfirsch-Schlüter regime at high collisionality ($\nu_* > \epsilon^{3/2}$, or better $\nu > v_{th}/(qR)$), and the plateau regime at intermediate collisionality ($1 < \nu_* < \epsilon^{3/2}$).

We notice that the Pfirsch-Schlüter regime is better described by the condition $\nu > v_{th}/(qR)$, that is, collision frequency higher than the inverse of the characteristic time to cover one connection length qR at the thermal velocity v_{th} . The diffusion of the plasma due to neoclassical transport changes at the different regimes. It increases with collisionality in the banana regime, then there is a transition in the plateau regime, where the increase in transport with increasing collisionality is compensated by a decrease in the effective trapped particle fraction. As a result, in this regime transport becomes weakly dependent on collisionality, hence the name plateau. Finally, transport increases again with collisionality in the Pfirsch-Schlüter regime, although with a weaker rate as compared to the banana regime.

Although turbulent transport usually constitutes the dominant component of radial transport, transport parallel to the magnetic field lines is found to be well described by neoclassical theory. Neoclassical transport is also particularly important in regions and conditions of the plasma in which turbulence is strongly reduced by means of transport barriers (not only in the edge but also in the core of the plasma). In such cases neoclassical transport, in particular in the ion heat channel, can become responsible for the largest portion of the radial transport. Since the neoclassical heat diffusivity is much larger for the ions than for the electrons, electron heat transport is practically never at the neoclassical level. Also, because the collision frequency is proportional to the charge squared $\nu \propto Z^2$ of the colliding particle species, neoclassical transport can be very important for highly charged (heavy) impurities. Neoclassical codes, such as NCLASS [2], can be used to calculate the transport coefficients, as well as the plasma resistivity and the bootstrap current [85–88], a component of the plasma current self-generated in the presence of inhomogeneities of the density and temperature profiles. The bootstrap current can be expressed as [89, 90]

$$\langle j_{bs}B \rangle = -I(\psi)p_e \left[\mathcal{L}_{31} \frac{p_e}{p} \frac{\partial \ln p}{\partial \psi} + \mathcal{L}_{32} \frac{\partial \ln T_e}{\partial \psi} + \mathcal{L}_{34} \alpha \frac{1 - R_{pe}}{R_{pe}} \frac{\partial \ln T_i}{\partial \psi} \right], \quad (3.6)$$

where $R_{pe} = p_e/p$ is the ratio of electron pressure to total pressure. The factors

\mathcal{L}_{xx} and α depend on the plasma parameters and can change by up to an order of magnitude, where \mathcal{L}_{32} and α can also change their sign, reversing the effects of the temperature gradients. Their exact expressions are given in Refs. [89, 90], including some typical values: $\mathcal{L}_{31} \approx \mathcal{L}_{34} \approx 0.5$, $\mathcal{L}_{32} \approx -0.2$, $\alpha \approx -0.5$, $R_{pe} \approx 0.5$. By assuming similar scale lengths for the different species and by introducing $\eta = \partial \ln T / \partial \ln n$ the bootstrap current can be expressed in a way that illustrates the relative contribution due to the density, electron temperature, and ion temperature gradients respectively

$$\langle j_{bs} B \rangle = -I(\psi) \frac{\partial p}{\partial \psi} \frac{\eta}{\eta + 1} \left[\frac{\mathcal{L}_{31}}{\eta} + R_{pe}(\mathcal{L}_{31} + \mathcal{L}_{32}) + (1 - R_{pe})(1 + \alpha)\mathcal{L}_{31} \right]. \quad (3.7)$$

For similar temperature and density scale lengths ($\eta \sim 1$) it can be noticed that the largest contribution to the bootstrap current is given by the density gradient (first term in eq. 3.7). This is in principle also true for typical H-mode pedestal parameters ($\eta \sim 2$), although different operating conditions could lead to a significantly smaller contribution of the density gradient.

3.1.2 Turbulent transport

The geometry of the magnetic equilibrium and the plasma kinetic profiles are such that electrostatic (and electromagnetic) microinstabilities can develop, leading to a turbulent state that causes large energy, particle, and momentum transport. Plasma microinstabilities can be destabilized for example by the interplay between the unfavorable magnetic curvature in the low field side of the tokamak and the presence of temperature and density gradients. An example is provided by figure 3.2, illustrating the mechanism leading to the ion temperature gradient (ITG) mode in the poloidal cross-section of a plasma. The presence of a temperature perturbation \hat{T} on a flux surface generates inhomogeneities in the drift velocity of the local ions: hotter ions with a higher drift velocity move ahead, while colder ions with a lower drift velocity fall behind. This leads to an aggregation and rarefaction of ions along the flux surface in the poloidal direction. This generates a perturbation in the ion density, which, assuming an adiabatic response of the electrons, leads to an electron density perturbation so that quasi-neutrality is conserved. Parallel force balance implies the existence of an electrostatic potential ϕ proportional to and in phase with the density perturbation. The electric field $\mathbf{E} = -\nabla\phi$ results in an $\mathbf{E} \times \mathbf{B}$ flow that amplifies the original perturbation: colder plasma from the outside is pulled inwards, while hot plasma from the inside is pushed outwards, increasing the initial perturbation and reducing the background temperature gradient. This only happens in the low field (unstable) side of the tokamak, where the gradient of the magnetic field ∇B and the gradient of the temperature ∇T point in the same direction. In the high field side instead, since ∇B and ∇T point in the opposite direction, the $\mathbf{E} \times \mathbf{B}$ flow has a stabilizing effect. The name of this instability is given by the fact that it is driven by an ion temperature gradient, and is often the dominant mode in

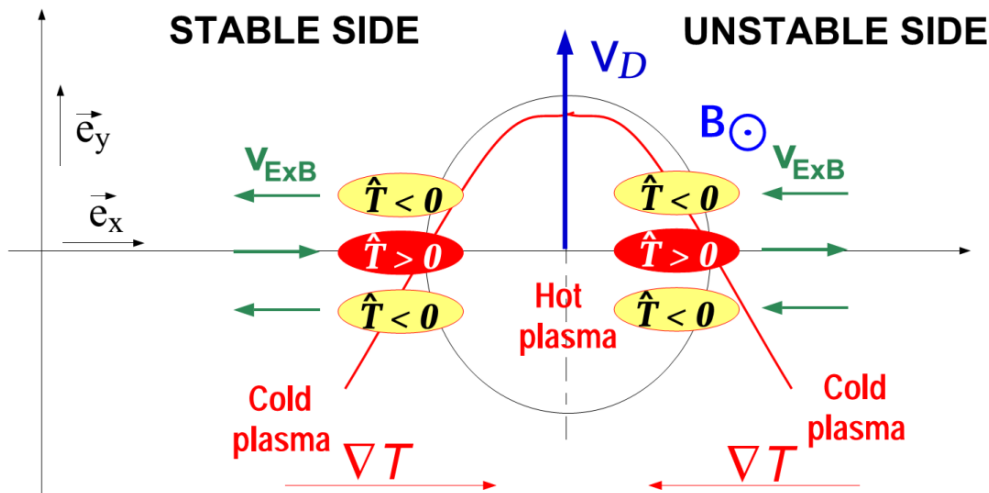


Figure 3.2 – Illustration of the mechanism leading to the ITG mode in the poloidal cross-section of a plasma. A temperature perturbation \hat{T} causes inhomogeneities in the drift velocity \mathbf{v}_D of the local ions, which leads to the creation of an electric field that results in an $\mathbf{E} \times \mathbf{B}$ flow ($\mathbf{v}_{\mathbf{E} \times \mathbf{B}}$) that amplifies the original perturbation. Figure from C. Angioni 2018, private communication from Advanced Courses on Fusion Plasma Physics.

the core of the plasma.

The heat flux associated to the ITG does not have a linear dependence on the temperature gradient. The mode is stable for values of the normalized ion temperature gradient $R/L_{T_i} = R\nabla T_i/T_i$ smaller than a threshold value, which is a function of the plasma parameters, and in particular decreases with increasing T_e/T_i . Above such threshold this instability grows very strongly with small increases in R/L_{T_i} . This limits the possibility of increasing the slope of the core ion temperature profile, with a normalized logarithmic temperature gradient R/L_{T_i} which can exceed the critical value only by a relatively limited amount. This phenomenon is known as profile stiffness. This implies that the maximum achievable temperature at the center of the plasma strongly depends on the edge temperature, highlighting how H-mode plasma confinement is strongly dependent on the pedestal performance. Similar considerations can be done for the trapped electron modes (TEM) and the electron temperature gradient (ETG) modes, which are driven by the electron temperature gradients R/L_{T_e} (as well as by density gradients R/L_n for TEMs).

These microinstabilities feature fast time scale ($\sim R/v_{th}^i$ the ion sound transit time) and short length scale ($\sim \rho_i$ the ion gyro-radius) compared to the confinement time ($\sim \tau_E$) and the length scale ($\sim R$). However, the time scale $\tau_{turb} \sim R/v_{th}^i$ is much longer than the cyclotron time scale $\tau_{turb} \gg (m_i, m_e)/(eB)$, allowing to average over the faster gyro-motion. The theoretical framework developed from first principle (statistical) kinetic equations, introducing these characteristic time and length scales separation, but at the same time allowing the finite Larmor radius

effects to be consistently taken into account, is called the *gyrokinetic theory*. If a fluid closure is introduced to represent the plasma, considering a set of fluid moments of the gyrokinetic equation over the phase space, then the theory is called *gyrofluid*. The ultimate goal of these two paradigms is to describe plasma turbulence such that a reliable calculation of transport fluxes is possible. In principle the gyrokinetic theory is more complete as it contains single-particle kinetic effects. However, as done in fluid dynamics for example, to shorten calculation time it is easier to apply a fluid model (gyrofluid in the case of magnetized plasma), whose drawback is the loss of kinetic effects and the requirement of the choice of the fluid closure.

The prediction of the heat, particle and momentum fluxes caused by turbulent transport requires to take into account the nonlinear coupling and saturation of the different modes. However, such nonlinear calculations are highly computationally expensive, and even more when considering a wide range of binormal wave numbers k_y , to include the instabilities that develop at the electron and ion scales simultaneously (multiscale). Therefore, the simulation of the plasma profiles with gyrokinetic codes would require a staggering amount of computational resources, making this task impractical with present day computing facilities. For this purpose reduced quasilinear models can be used. A quasi-linear transport model solves a set of linearized equations describing the plasma micro-instabilities, and from the eigenvalues and eigenvectors of the solution it computes the turbulent fluxes by means of a quasi-linear approach, which is based on the adoption of a saturation rule. An example of such reduced quasilinear models are the Trapped-Gyro-Landau-Fluid TGLF code [1] and the QuaLiKiz code [56]. The former has been applied in this work to simulate core turbulent transport. The terminology 'Trapped-Gyro-Landau-Fluid' means that TGLF employs a gyro-averaged fluid paradigm that allows a very fast calculation of turbulence in the linear regime, using a mixing-length rule to emulate the non-linear saturation phase, but it retains kinetic Landau damping in the fluid closure in the form of a dissipative heat flux and an accurate description of the trapped particles.

The saturation rule assumes that the nonlinear saturation amplitude of the electrostatic potential fluctuations $|\tilde{\phi}_k|^2$ is proportional to the growth rate of the instabilities in the linear phase $\gamma / \langle k_\perp^2 \rangle$ where γ is a characteristic inverse linear time scale and $\langle k_\perp \rangle$ is a characteristic perpendicular wave number. The actual proportionality factor for the saturation rule adopted by TGLF is obtained by a fit of nonlinear gyrokinetic simulations. As already mentioned, the turbulent fluxes are caused by a fluctuating potential $\tilde{\phi}$ (and corresponding fluctuating electric field) which produces a radial component of the $\mathbf{E} \times \mathbf{B}$ drift due to the equilibrium magnetic field. The fluxes of heat Q and particle Γ are given by

$$\Gamma = \left\langle \int d^3v \tilde{f} \frac{\mathbf{b} \times \nabla \tilde{\phi}}{B} \cdot \mathbf{r} \right\rangle, \quad (3.8)$$

$$Q = \left\langle \int d^3v E \tilde{f} \frac{\mathbf{b} \times \nabla \tilde{\phi}}{B} \cdot \mathbf{r} \right\rangle, \quad (3.9)$$

where \tilde{f} is the perturbed distribution function. By averaging over time and spatial scales larger than those characteristic of the fluctuations it is possible to express the radial fluxes in Fourier space

$$\Gamma = \left\langle \sum_{k\omega} \text{Re} \left[\frac{ik_y \tilde{n}_{k\omega} \tilde{\phi}_{k\omega}^*}{B |\tilde{\phi}_{k\omega}|^2} \right] |\tilde{\phi}_{k\omega}|^2 \right\rangle, \quad (3.10)$$

$$Q = \left\langle \sum_{k\omega} \text{Re} \left[\frac{3}{2} \frac{ik_y \tilde{p}_{k\omega} \tilde{\phi}_{k\omega}^*}{B |\tilde{\phi}_{k\omega}|^2} \right] |\tilde{\phi}_{k\omega}|^2 \right\rangle, \quad (3.11)$$

where k is the wave number and ω is the frequency. The terms in the square brackets are often called quasilinear weights, and represent the phase relations between the density/pressure fluctuations and the electrostatic potential fluctuations.

To summarize, in TGLF a linear fluid description gives the relationship between the dynamical responses of the fluctuating kinetic fields (density and pressure fluctuations) and those of the electromagnetic potentials. The quasilinear fluxes are then calculated considering three assumptions, one for the frequency spectrum, one for the binormal wave number spectrum, and one for the amplitude of the fluctuations of the potential in the saturated nonlinear phase (saturation rule). The local fluxes can be calculated by TGLF by supplying the plasma parameters at a certain radial location, e.g. the normalized gradients, the magnetic geometry, the equilibrium quantities, the temperature and density ratios among the different species, collisionality, and other parameters which can affect turbulent transport.

Instability	Drive
ITG	R/L_{T_i}
TEM	$R/L_{T_e}, R/L_n$
ETG	R/L_{T_e}
MTM	$R/L_{T_e}, \beta_e$
KBM	$q^2 \beta_e, \beta'(R/L_T, R/L_n)$

Table 3.1 – Types of microinstabilities causing turbulent transport and their drives.

In the plasma different types of microinstabilities can be present, and are categorized as a function of their drive, as illustrated by table 3.1. TEMs can be stabilized by electron-ion collisions. ETGs can be stabilized by the density gradient. ITG and ETG modes are weakly affected by collisions. ITGs and TEMs are destabilized by the electron to ion temperature ratio T_e/T_i , while ETGs are stabilized by T_e/T_i . The micro tearing modes (MTM) and the kinetic ballooning modes (KBM) are electromagnetic instabilities, caused by fluctuations of the magnetic potential, driven by the electron to magnetic pressure ratio β_e . Specifically, MTMs are destabilized by R/L_{T_e} and β_e , while KBMs are destabilized by $q^2 \beta_e$ and β' , with a dependence on the temperature and density gradients. Another important feature that differentiates these instabilities is their spatial scale. ITG, TEM, MTM, and KBM develop at

binormal wave numbers $k_y \rho_i < 1$ (ion scales), whereas ETG develop at binormal wave numbers $k_y \rho_e < 1$ (electron scales).

The main instabilities present in the core of the plasma are ITG, TEM, and ETG. Which instability is dominant depends on the plasma conditions, that can for example, be altered by different heating mixture (changing the location and ratio of ion to electron heating), the fueling (affecting the density), the magnetic configuration (i.e. plasma shape), the plasma current and the magnetic field (changing β and q). In the edge of the plasma instead (in the pedestal region), the H-mode ETB stabilizes such instabilities, especially the ones featuring the largest spatial scale (ITG). The instabilities that are more likely to survive the strong $\mathbf{E} \times \mathbf{B}$ flows in this region are the ones associated to the smaller spatial scales (ETG, TEM, MTM), and the ones driven by the strong pressure gradients (KBM) typical of this region. Other types of instabilities that can be present in the pedestal region are resistive ballooning modes and drift resistive and Alfvén wave turbulence [82]. Quasi-linear models like TGLF cannot be expected to reproduce turbulent transport in the pedestal and therefore cannot be used for this purpose.

The study of the turbulence properties in the pedestal region with gyrokinetic codes is very challenging. The geometry of the field lines require a high resolution in the direction parallel and perpendicular to the magnetic field, and nonlinear simulations are required to clarify the relevant transport mechanisms. These aspects, together with the fact that a large number of instabilities has to be taken into account in this type of analysis, make these kind of simulations very expensive in terms of required computational resources. Different confinement regimes are characterized by different behavior of turbulent transport in the edge of the plasma. So far no clear and unified picture has emerged regarding the relative role of the different instabilities with respect to turbulent transport in the pedestal of ELMy H-mode plasmas. Experimental measurements of the fluctuations have been diagnosed that are consistent with MTM [91–93], KBM [91, 93–95], and TEM [91]. Linear gyrokinetic simulations have identified MTM [96–100], TEM [100, 101], ETG [99, 100, 102, 103], and KBM [95, 96, 98–100, 104]. Recent nonlinear simulations [105, 106] show that MTM is the main ingredient for turbulent transport which can quantitatively reproduce the experimental transport levels in the pedestal of JET discharges.

3.1.3 Prediction of pedestal profiles

Given the complexity of estimating the pedestal transport in the pre-ELM phase, where not only turbulence but also MHD modes can play an important role, it is not possible at present to use theory based models to simulate the pedestal profiles within the usual transport modeling approach. Instead pedestal models which describe pedestal transport with simple assumptions, derived from experimental observations and/or theoretical considerations, can be used to describe the pedestal evolution. The EPED1 model [7] for example, assumes a pedestal transport constraint which relates the width of the pedestal (Δ_{ψ_N}) to the poloidal beta at the top of the pedestal

($\beta_{p,ped}$) as $\Delta\psi_N = G\sqrt{\beta_{p,ped}}$, where G is a function of collisionality and geometry. EPED combines this dependence, which describes transport, with a MHD stability code to predict the pedestal profiles before the ELM onset. This approach allows EPED to be applied in a stand-alone manner, not requiring the use of a transport code. This is possible since it takes the pedestal top electron density as input, and then assumes the same value for the electron and ion temperatures at the pedestal top $T_{e,top} = T_{i,top}$, giving all the elements required to define the pedestal pressure. The boundary conditions at the separatrix are given by simple assumptions (e.g. $n_{e,sep} = n_{e,top}/4$). With such a transport constraint it is then possible to do a scan

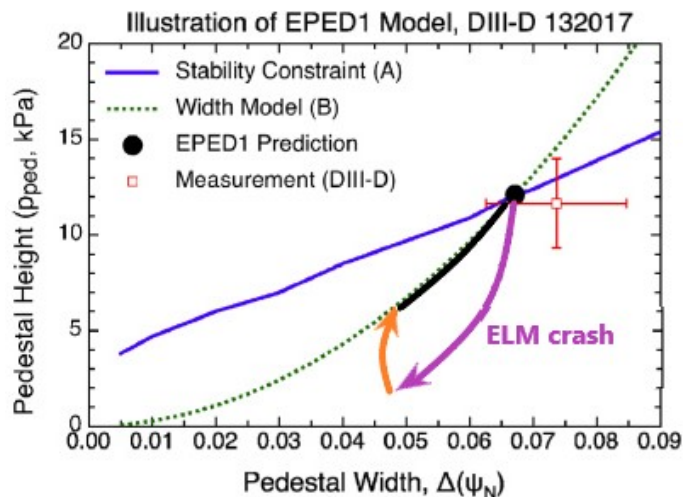


Figure 3.3 – Illustration of the ELM cycle according to the EPED model for a DIII-D discharge. The green line represents the transport constraint for the pedestal evolution in the inter-ELM recovery phase (black line). The blue line defines the MHD stability constraint above which the ELM crash is triggered (magenta line). The orange line represents the short pedestal recovery phase after the ELM crash. Figure modified from [107].

in pedestal pressure by calculating the pedestal profiles corresponding to different pedestal widths, as illustrated in figure 3.3 by the green dotted line. The stability of these pedestal profiles is then tested with MHD codes, such as ELITE [108–111] in the case of EPED, to find the highest stable pedestal, corresponding to pre-ELM conditions. The points below the blue line in the figure represents the pedestals that are stable to peeling-ballooning modes (PBM). The final result of the EPED model is the point at the intersection between the two lines representing the transport (green) and the stability (blue) constraints.

The EPED model has been used to reproduce the experimental pedestals in DIII-D, as well as in other tokamaks [112]. In particular it reproduces general trends like the change in pedestal pressure with the plasma current I_p and the size scaling. This makes the approach adopted by EPED to predict the pedestal pressure realistic and very useful for plasma confinement studies. However, EPED

does not reproduce all detailed effects of pedestal confinement, like, for example the confinement degradation due to fueling [65]. It also lacks the capability of predicting the pedestal top density. In the work of this PhD thesis a new pedestal transport model has been developed, presented in the next chapter, which follows the main concept of EPED, but uses a different approach to describe the effect of transport. The different pedestal transport constraint opens the possibility to predict the pedestal top density, and the pedestal top electron and ion temperatures separately (i.e. without assuming $T_{e,top} = T_{i,top}$), and therefore to also describe effects which go beyond the possibilities of EPED.

3.1.4 Pedestal MHD stability

The onset of ELMs has been demonstrated to be well reproduced by the destabilization of peeling-ballooning modes [110, 113], described by ideal MHD equations. Linear MHD theory, and codes solving its corresponding equations, can determine the PBM stability and therefore the plasma conditions corresponding to the onset of the ELM crash. Nonlinear magnetohydrodynamics can describe the coupling between different modes, evaluating their amplitude and the levels of transport caused by them, as well as the detailed dynamics of the ELM crash. Linear ideal MHD codes are therefore sufficient to predict the pedestal pressure when combined with a pedestal transport model.

MHD theory describes the equilibrium of the plasma with macroscopic quantities (mass density ρ , macroscopic velocity \mathbf{v} , current density \mathbf{j} , and pressure p), treating it as a fluid. By restricting attention to long-wavelength, low-frequency phenomena (as opposed to the scales of microinstabilities leading to turbulent transport), the electrons and ions can be considered as a single fluid within the MHD picture. The motion of the plasma is described with hydrodynamic equations coupled to Maxwell's equations:

$$\frac{\partial \rho}{\partial t} + \nabla \cdot (\rho \mathbf{v}) = 0 \quad (3.12)$$

$$\rho \frac{d\mathbf{v}}{dt} = \mathbf{j} \times \mathbf{B} - \nabla p \quad (3.13)$$

$$\mathbf{E} + \mathbf{v} \times \mathbf{B} = \eta_{\parallel} \mathbf{j} \quad (3.14)$$

$$\frac{d}{dt} \left(\frac{p}{\rho^{\gamma}} \right) = 0 \quad (3.15)$$

$$\nabla \times \mathbf{E} = -\frac{\partial \mathbf{B}}{\partial t} \quad (3.16)$$

$$\nabla \times \mathbf{B} = \mu_0 \mathbf{j} \quad (3.17)$$

$$\nabla \cdot \mathbf{B} = 0 \quad (3.18)$$

The ideal MHD equations are obtained by assuming that the plasma has zero

resistivity $\eta = 0$, which makes eq. 3.14 become

$$\mathbf{E} + \mathbf{v} \times \mathbf{B} = 0. \quad (3.19)$$

In ideal MHD the formation of magnetic islands is prohibited, i.e. flux is conserved. Other assumptions like a toroidal geometry with dominant, time-independent toroidal magnetic field lead to the so-called reduced MHD equations.

By solving these equations it is possible to describe the equilibrium of the plasma, where the forces acting upon it are balanced. Perturbations of this equilibrium will cause the system to oscillate, and if such perturbations are damped or amplified, the equilibrium will be stable or unstable. The interplay between the pressure gradient forces ∇p and the forces caused by the current density \mathbf{j} and the magnetic field \mathbf{B} in an equilibrium state ($d/dt \rightarrow 0$) is described by the force balance, eq. 3.13. The equilibrium state of the pedestal is therefore determined by the topology of the magnetic field, the achievable pressure gradient, and the currents in the pedestal. In order to investigate whether a certain combination of ∇p , \mathbf{j} , and \mathbf{B} can lead to instabilities the energy principle can be applied to the linearized MHD equations. This consists in performing a linear stability analysis of the system when a small displacement ξ is introduced. If the potential energy of the system W is decreased by the perturbation, the system is unstable. The change in the energy of the system δW caused by a displacement ξ of the equilibrium is described by

$$\begin{aligned} \delta W_F = \frac{1}{2} \int_F & \left(\frac{|B_{1\perp}|^2}{\mu_0} + \frac{B_0^2}{\mu_0} |\nabla \cdot \xi_{\perp} + 2\xi_{\perp} \cdot \kappa|^2 \right) + \gamma p_0 |\nabla \cdot \xi|^2 \\ & - \underbrace{2(\xi_{\perp} \cdot \nabla p_0)(\kappa \cdot \xi_{\perp}^*)}_{\text{pressure}} - \underbrace{\frac{j_{0\parallel}}{B_0} (\xi_{\perp}^* \times \mathbf{B}_0) \cdot \mathbf{B}_1}_{\text{current}} dV, \end{aligned} \quad (3.20)$$

where 0 and 1 denotes the equilibrium and the perturbed values respectively, κ is the curvature vector of the equilibrium magnetic field and ξ^* the complex conjugate of the displacement ξ . Parallel and perpendicular refer to the direction relative to the magnetic field. The index F denotes that only the fluid (plasma) component of the energy change is considered, as the vacuum part is usually stabilizing. This equation highlights the main drives of instabilities. The first three terms are all positive and give rise to stabilizing Alfvén and sound waves [114]. The last two terms can be negative and therefore drive pressure and current instabilities.

The pressure term is unstable if the pressure gradient ∇p and the curvature κ are parallel, while this term is stabilizing if they are anti parallel. As already mentioned, the pressure gradient is perpendicular to the magnetic flux surfaces, pointing towards the center of the plasma. The toroidal field curvature points towards the center of the torus. Similarly as described for the ITG modes, there are therefore an unstable (bad curvature) and a stable (good curvature) region, which are respectively on the outboard and inboard side of the tokamak. This kind of instability is similar to the aforementioned Rayleigh-Taylor and ITG instabilities, and are called interchange

instabilities due to the fact that the plasma tries to interchange position with the magnetic field. This effect is particularly important on the outboard side, causing the plasma to expand in this region, similarly to a balloon. For this reason these type of instabilities are usually called *ballooning modes*.

The current term is proportional to the current density parallel to the magnetic field $j_{0\parallel}$. Current driven instabilities lead to a kink of the magnetic surfaces. As a result, the field lines are elongated by the kinked flux surfaces, although the kink can also locally reduce the length, minimizing the plasma energy. This phenomenon can be visualized with the mechanical analogy of the kinking of a towel when twisting it. The main contributor for the current responsible for these instabilities in H-mode is usually the bootstrap current rather than the ohmic current, since it is proportional to the density and temperature gradients, typically large in the pedestal region. These instabilities are usually called *peeling modes* due to the fact that the plasma surface looks like 'peeled off' by such kink.

The MHD stability of the pedestal can be described by the coupling of these two instabilities, hence the name peeling-ballooning modes (PBM). Linear ideal MHD codes scanning a range of possible finite mode numbers like MISHKA [3] and ELITE can then be used to calculate the PBM stability of a pedestal, taking as input the pressure, the current density, and the magnetic flux profiles, and the geometry of the LCFS. Instead of using the energy principle, an eigenvalue equation is solved, yielding a growth rate and mode structure of the perturbation.

3.1.5 SOL transport

The boundary conditions of the confined plasma, at the separatrix, are determined by the transport in the SOL and the conditions of the divertor and the wall of the tokamak. This section gives an overview of how the SOL transport can be described by physics based models.

First of all, it is important to describe the particle balance in a tokamak. Plasma particles flow mainly to the divertor targets, but also to the first wall, resulting in particle flux densities Γ_t (at the target) and Γ_w (at the wall). Most of the incoming ions recombine to neutrals at the surface of the plasma facing components, which can then reach again the plasma, leading to a flux Γ_{rec} of recycled neutrals. At steady state the recombination rate equals the neutrals flux towards the plasma, which is then ionized and constitute a large particle source. This process is called *particle recycling*, and allows the plasma to maintain a certain density without the need of providing an external particle source. Cryopumps located in the proximity of the divertor region can be used to control the particle content by removing a part Γ_{pump} of the neutrals inventory. Also, to reach higher density values, the plasma can be fueled by gas valves which provide an external source of neutrals Γ_{fuel} .

Transport in the SOL can be described by analytical one-dimensional models which treat the plasma as a fluid, neglecting volumetric sources and sinks of particles, momentum, and energy, as well as cross field transport. The starting point of such

models are the equations for the conservation of particles, momentum, and energy:

$$\Gamma_p = nv = \text{const} \quad (3.21)$$

$$p_{tot} = m_i n v^2 + p_{stat} = \text{const} \quad (3.22)$$

$$q_{\parallel} = \text{const} \quad (3.23)$$

where n is the plasma density, v is the plasma fluid velocity parallel to the magnetic field lines and m_i is the ion mass. These equations state that the parallel particle flux Γ_p , the total pressure p_{tot} and the heat flux q_{\parallel} are conserved along the field lines in the SOL. The static pressure is defined as $p_{stat} = n(T_e + T_i)$.

The electrons coming from the confined plasma reach the target more rapidly than the ions due to their much lower mass, if the ion and electron temperatures are similar. As a result the surface of the target charges negatively and a negative electric field is created in front of the target, which repels the electrons. This causes the electrostatic potential from the plasma to the target to drop. The region corresponding to this drop of the electrostatic potential is called *sheath*. The parallel heat flux at the sheath entrance q_{se} can be expressed as

$$q_{se} = (\gamma_i T_i + \gamma_e T_e) \Gamma_{se}, \quad (3.24)$$

where Γ_{se} is the particle flux at the sheath entrance, and γ_i and γ_e are the ion and electron *sheath heat transmission factors*. This equation can be simplified by assuming $T_e = T_i = T$, and introducing a total sheath heat transmission factor γ

$$q_{se} = \gamma T \Gamma_t. \quad (3.25)$$

A relation between the upstream (u) static pressure, that is the pressure at the outer midplane, and the target (t) static pressure can be derived from eq. 3.21, assuming that the velocity reaches the sound speed and that $T_e = T_i$

$$p_u = n_u T_u = 2n_t T_t. \quad (3.26)$$

The parallel heat flux q_{\parallel} can be decomposed into conductive and convective terms

$$q = q_i^{conv} + q_e^{conv} + q_i^{cond} + q_e^{cond}, \quad (3.27)$$

where $q_{e,i}^{conv}$ are the electron and ion convective heat fluxes and $q_{e,i}^{cond}$ the electron and ion conductive heat fluxes. The convective heat fluxes can be expressed as

$$q_{e,i}^{conv} = \left(\frac{1}{2} m_{e,i} v_{e,i}^2 + \frac{5}{2} k T_{e,i} \right) n v_{e,i}, \quad (3.28)$$

where $v_{e,i}$ are the electron and ion fluid velocities. The conductive heat fluxes are

3 H-mode plasmas simulations: Transport and Stability

given by Spitzer-Härm conductivity [115]

$$q_{e,i}^{cond} = -\kappa_{e,i} T_{e,i}^{5/2} \frac{dT_{e,i}}{dx}, \quad (3.29)$$

where $\kappa_i \approx 60 \text{ W}/(\text{eV})^{7/2}\text{m}$ and $\kappa_e \approx 2300 \text{ W}/(\text{eV})^{7/2}\text{m}$.

At sufficiently high plasma density a large ionization front of the neutrals exist in front of the divertor target. As a simplification it can be assumed a zero upstream particle flux $\Gamma_u = 0$, which implies that the entire heat flux has to be carried by conduction to the target. In this case the upstream temperature T_u and the target temperature T_t can be related by integrating eq. 3.29 from the target to the upstream location:

$$q_{\parallel} L = -\kappa_e \frac{7}{2} (T_u^{7/2} - T_t^{7/2}) \rightarrow T_u^{7/2} = T_t^{7/2} + \frac{2}{7} \frac{q_{\parallel}}{\kappa_e} L, \quad (3.30)$$

where L is the field line length. The conductive ion heat flux is neglected due to $\kappa_i \ll \kappa_e$. The combination of eq. 3.25, the momentum conservation equation 3.26, and eq. 3.30 constitute the so called two point model [4, 5]. It can often be assumed that $T_u^{7/2} \gg T_t^{7/2}$, and therefore the target temperature can be neglected in eq. 3.30, which can then be expressed as

$$T_u = \left(\frac{7q_{\parallel} L}{2\kappa_e} \right)^{2/7}. \quad (3.31)$$

The upstream temperature T_u has a weak dependence on the parallel heat flux q_{\parallel} and the connection length L . For this reason, as it is observed from experiments and simulation results, the upstream temperature changes very little with different operating conditions. Typical AUG upstream separatrix temperatures are in the order of $T_{e,sep} \sim 100 \text{ eV}$ for plasmas in H-mode, and $T_{e,sep} \sim 50 \text{ eV}$ in L-mode.

The discussion on the treatment of the separatrix ion temperature $T_{i,sep}$ is given in section 4.2.1.

It is possible to estimate the separatrix density $n_{e,sep}$ through an extension of the two point model, presented in Ref. [9] (eq. 8)

$$n_{e,sep} = 0.35 \frac{2}{e} \left(\frac{2\kappa_0 \kappa_z}{7\pi q_{cyl}} \right)^{2/7} \left(\frac{m_D}{2} \right)^{0.5} R^{-0.5} \left(\frac{P_{sep} B}{3\pi \langle \lambda_{q,HD} \rangle \langle B_p \rangle} \right)^{3/14} (\gamma \sin(\alpha))^{-0.5} (1.5 \cdot 10^{23} Pa / (at m^{-2} s^{-1}))^{0.5} p_0^{1/4}, \quad (3.32)$$

where $\kappa_z = (0.672 + 0.076 Z_{eff}^{1/2} + 0.252 Z_{eff})^{-1}$ is the finite-Z correction of the electron parallel conductivity [116], q_{cyl} is the cylindrical safety factor, P_{sep} is the power crossing the separatrix, m_D is the main ion mass, $\langle \lambda_{q,HD} \rangle$ is the power decay length from the Heuristic Drift model [116], $\langle B_p \rangle$ is the poloidally averaged value of B_p , α is the impact angle of the field line at the outer target, and p_0 is the divertor neutral pressure, which is the main term of the formula. The divertor neutral pressure p_0 can be regarded as an engineering parameter, since it is determined by the balance between gas puffing and pumping.

The two point model contains several simplifications in the description of the physics regulating the SOL transport. More sophisticated models exist, which give a 2D or 3D description of the SOL that allow them to capture the effects of the geometry of the tokamak. Perpendicular transport can be simulated by turbulence codes specifically developed for the SOL. However, these models are very expensive in terms of computational resources, and therefore their coupling with core and pedestal transport codes for the simulation of the whole plasma is impractical. The goal of this PhD thesis is to provide a tool that can describe plasma confinement within a certain level of accuracy and realism, while maintaining a low computational time, so that the approach can be applied to a sufficiently large number of experimental cases to validate it. In this context, a simplified description of the SOL has been preferred, instead of developing a highly complex modeling workflow which then can be only tested on a restricted number of cases due to the high computational cost, which does not allow a validation over an extended number of cases, covering a sufficiently broad range of operational parameters. Also, the level of accuracy provided by the two point model can be expected to be sufficient to describe the main effects of the divertor and SOL conditions on the separatrix conditions, and ultimately on the pedestal and global confinement. The use of more sophisticated codes to capture such dependencies is therefore not efficient in the framework of this project, while it is certainly important when addressing different problems, such as power exhaust studies.

3.2 Simulation of plasma profiles with transport codes

The elements discussed in this chapter describing the different transport phenomena can be combined together in a transport code to simulate the plasma profiles from the magnetic axis to the separatrix. In this work the ASTRA transport code [117, 118] has been used for this purpose. ASTRA is a 1.5D code, in the sense that it maintains a 2D equilibrium description, but the transport equations are treated as 1D, corresponding to the radial coordinate.

One of the strengths of ASTRA consists in its flexibility, as it allows the user to define which equations should be used to simulate the plasma, which quantities should be evolved with the underlying equations and which should be kept fixed with a prescribed value, how many species (i.e. impurities) should be considered, and which boundary conditions should be adopted. For our purpose we included the equations of heat transport for electrons and ions, the particle transport equation for the electrons, calculating the ion density via quasineutrality, imposing as boundary conditions the electron and ion temperature and electron density at the separatrix. An equation for momentum transport allows the calculation of the toroidal rotation, and we impose the boundary condition at the pedestal top, as discussed in the next chapter, which describes the details of the integrated model.

3 H-mode plasmas simulations: Transport and Stability

The following part of this section illustrates the main equations adopted by ASTRA to simulate the radial plasma profiles. A more detailed description of the equations and elements constituting the ASTRA transport code can be found in Ref. [117]. We consider here a simplified form of the ASTRA equations, assuming that the toroidal magnetic field is constant in time, as in this work only stationary phases have been considered. The radial coordinate adopted by ASTRA is an effective minor radius that has the units of ρ [m], and $V' = \partial V / \partial \rho$ is the radial derivative of the volume enclosed in a flux-surface. The equation of the poloidal magnetic flux

$$\sigma_{\parallel} \frac{\partial \Psi}{\partial t} = \frac{J^2 R_0}{\mu_0 \rho} \frac{\partial}{\partial \rho} \left(\frac{g_2}{J} \frac{\partial \Psi}{\partial \rho} \right) - \frac{V'}{2\pi \rho} (j_{bs} + j_{cd}), \quad (3.33)$$

where $g_2 = \langle |\nabla \rho / r|^2 \rangle V' / (4\pi^2)$ is a metric coefficient and $J = I_p / (R_0 B_0)$ is a dimensionless quantity close to unity, allows the evolution of the total plasma current density j_{\parallel} . This is calculated as the sum of the resistive inductive contribution $\sigma_{\parallel} E_{\parallel}$, the bootstrap current j_{bs} , and the external non-inductive current drive j_{cd}

$$j_{\parallel} = \sigma_{\parallel} E_{\parallel} + j_{bs} + j_{cd}. \quad (3.34)$$

The neoclassical conductivity σ_{\parallel} and the bootstrap current are calculated with the aforementioned NCLASS code. To compute the heat and particle sources, and the non-inductive current drive, ASTRA includes TORBEAM [119], and NBI and neutrals modules. The TORBEAM and NBI modules require as input all the engineering parameters of the heating systems (e.g. power, injection angles, voltage of the beams, frequency of the gyrotrons, etc.), as well as the plasma kinetic profiles, and can predict the radial profiles of the heating power densities. The radial derivatives of the total pressure profile and of the toroidal covariant component of the magnetic field are used as source terms in the Grad-Shafranov equation, solved in ASTRA by the 2D coupled equilibrium solver SPIDER [120], which uses an adaptive grid method that allows a high resolution and small computational cost. SPIDER calculates the plasma magnetic equilibrium for a fixed plasma boundary (LCFS) at each time step, allowing the calculation of all the metric functions needed in the transport equations.

Particle transport is described by the 1D flux-surface averaged continuity equation

$$\frac{1}{V'} \frac{\partial V' n_j}{\partial t} + \frac{1}{V'} \frac{\partial}{\partial \rho} (\Gamma_j) = S_j, \quad (3.35)$$

where the index j refers to the different species in the plasma (i.e. electrons and ions), S_j is the particle source, and Γ_j is the particle flux, which can be expressed as

$$\Gamma_j = -n_j V' g_1 \left(D_j \frac{\partial n_j}{n_j \partial \rho} - C_j \right), \quad (3.36)$$

where $g_1 = \langle |\nabla \rho|^2 \rangle$ is another metric coefficient, the first term $D_j \frac{\partial n_j}{n_j \partial \rho}$ represents

3.2 Simulation of plasma profiles with transport codes

diffusion, and the second term C_j represents convection.

Heat transport is described by the equation

$$\frac{3}{2}(V')^{-5/3} \frac{\partial(V')^{5/3} n_j T_j}{\partial t} + \frac{1}{V'} \frac{\partial}{\partial \rho} (q_j + \frac{5}{2} T_j \Gamma_j) = P_j, \quad (3.37)$$

where q_j is the local heat flux, and P_j is the source term of local power density. The heat flux q_j can be expressed as

$$q_j = -n_j T_j V' g_1 \sum_i \chi_j^i F_j^i, \quad (3.38)$$

where χ_j^i is the heat transport coefficient for species j , relative to the thermodynamical quantity i , given by

$$F_j^i = \left(\frac{\partial T_j}{T_j \partial \rho}, \frac{\partial n_j}{n_j \partial \rho}, \dots \right). \quad (3.39)$$

For our purposes energy convection and the off-diagonal terms of the transport matrix appearing in eq. 3.38 (the so called heat pinch) are directly included in the description through effective heat conductivities, defined by the ratio between the turbulent heat flux and the corresponding (diagonal) gradient. By this way only the diagonal terms are retained, leading to:

$$q_j = -n_j V' g_1 \chi_j \frac{\partial T_j}{\partial \rho}. \quad (3.40)$$

The transport coefficients (the heat and particle diffusivities, and the pinch velocity) are given by the sum of the neoclassical (calculated with NCLASS), and the turbulent components (calculated with TGLF in the core, and with the empirical model in the pedestal, as discussed in the next chapter). The external power and particle sources are self-consistently calculated by the corresponding modules included in ASTRA. The simulations are run until stationary conditions are reached.

The new integrated model presented in this thesis has been developed within the highly flexible modeling framework enabled by the ASTRA transport code, based on a workflow which allows the description of the coupling between SOL, pedestal and core, with a self-consistent treatment of the boundary conditions. The workflow combines theory-based components (like the quasi-linear TGLF model for core turbulent transport, the NCLASS model for neoclassical transport, the MHD code MISHKA for the pedestal stability and the two-point model for the SOL) with semi-empirical elements, in particular for the description of the transport in the pedestal region and for the connection between divertor and SOL parameters. Chapter 4 describes in details all the physics based and empirical elements constituting the modeling workflow, with an explanation on the integration of the different components.

4 Description of the Integrated Modeling Workflow

Summary

4.1	Introduction	72
4.2	Transport simulations	76
4.2.1	Scrape-off layer model	76
4.2.2	Pedestal transport	82
4.2.3	Core transport	86
4.2.4	Integration of the different components	87
4.3	Pedestal MHD stability	91
4.4	Assumptions	93

4.1 Introduction

This chapter provides a detailed description of the modeling framework and of the transport models which are applied in the different regions of the plasma. We developed a tokamak plasma simulation tool which takes as inputs global plasma parameters like the magnetic field B_t , the plasma current I_p , the deuterium fueling rate Γ_D , the nitrogen seeding rate Γ_{N_2} , as well as the auxiliary heating powers P_{heat} and the plasma boundary. Another input parameter required by the model is the effective charge Z_{eff} . The model is capable of predicting the radial profiles of temperatures and densities until the last closed flux surface (LCFS) and, consequently, also the total stored energy and the confinement time, for ELMy H-mode conditions.

Figure 4.1 (a) depicts the modeling workflow, which is based on the approach of performing multiple simulations in parallel, represented by the multiple ASTRA blocks in the workflow. In each of these multiple simulations, a different value of the pedestal width Δ_{ped} is assumed, in order to scan the pedestal pressure. A SOL model is also included to predict the boundary conditions for the temperature and density profiles at the LCFS. All of these transport components are simultaneously included in the simulations, which therefore provide predictions of the entire plasma radial profiles. However, particularly in H-mode, the different regions of the plasma, the core, the pedestal and the SOL, require different models that have to be combined in the integrated modeling framework. In this section we first provide a general description of the modeling workflow, introducing the various numerical tools which

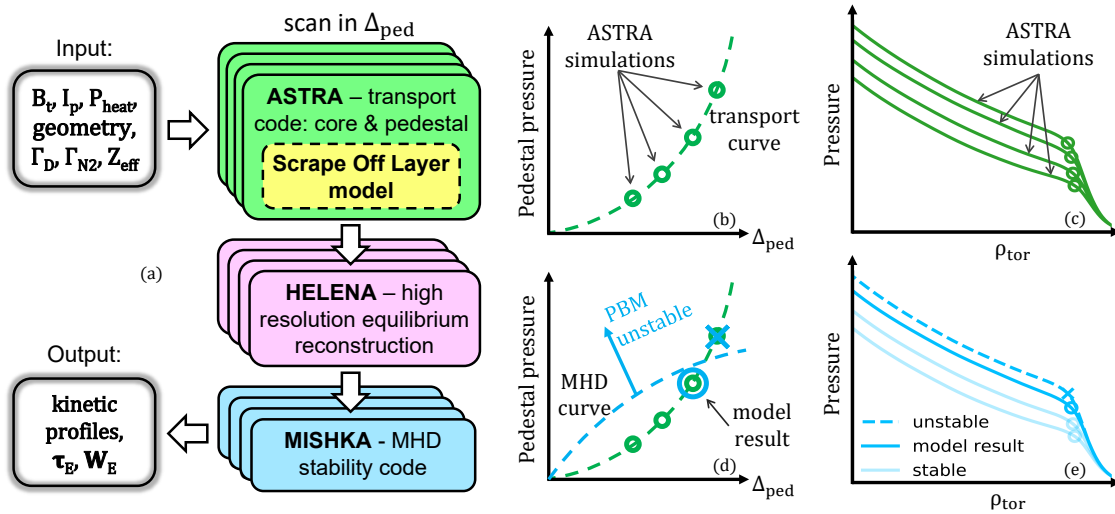


Figure 4.1 – Chart representation of the modeling workflow (a). Multiple parallel ASTRA simulations calculate the kinetic profiles for different values of the pedestal width (c). The pedestal model integrated in ASTRA gives a transport constraint which determines the pedestal pressure for a given pedestal width (b). MISHKA tests the stability of the resulting profiles to find the highest stable pedestal pressure (d,e).

are included and how these are applied to obtain the final prediction of the plasma profiles from the magnetic axis to the LCFS. Section 4.2 illustrates all the elements constituting the ASTRA transport simulations, and is divided into four parts describing: how the SOL model sets the boundary conditions of the simulation in subsection 4.2.1, how transport is modeled in the pedestal in subsection 4.2.2 and in the core in subsection 4.2.3, and finally the methodology which is applied for the integration of the different transport components in the different plasma regions in subsection 4.2.4. Section 4.3 provides information on the calculations of the MHD stability of the pedestals predicted in each one of the multiple ASTRA simulations. Section 4.4 summarizes the assumptions introduced into the model and discusses their applicability to other experimental conditions and the sensitivity of the model result to the values of the free parameters which are present in the model.

As already mentioned, while many different models can describe core transport, no theory based numerical model exists to provide a robust determination of transport in the pedestal region for applications in transport modeling. To overcome this limitation we developed a new pedestal transport model based on empirical observations. In Ref. [6] (figure 4.2, left) it is shown that the pedestals of different machines all exhibit a similar feature: a constant ratio between the averaged pedestal electron temperature gradient (in real space units, calculated over the minor radius at the outer midplane) and the pedestal top temperature $\langle \nabla T_e \rangle / T_{e,\text{top}} \approx \text{const} = -0.5 [\text{cm}^{-1}]$. This condition has been implemented in ASTRA, so that by fixing a value of the

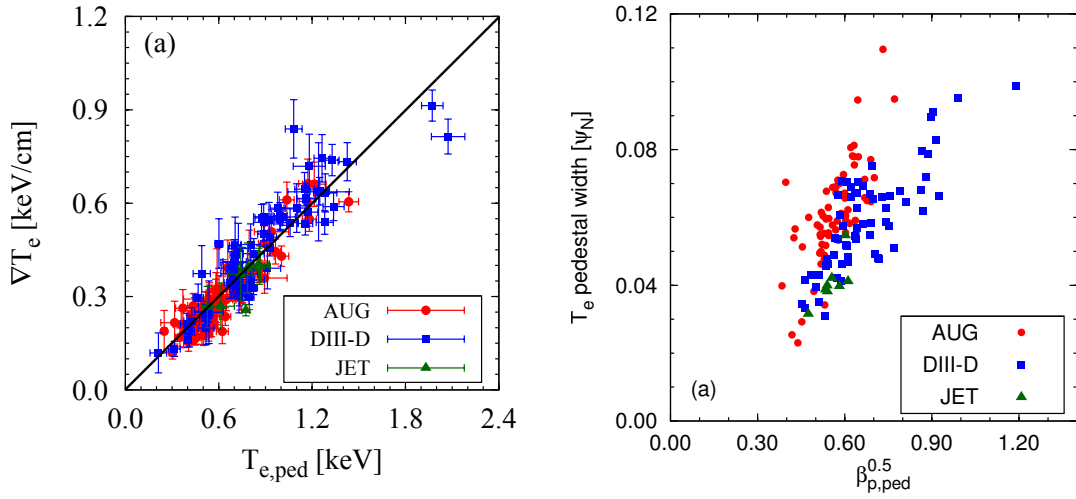


Figure 4.2 – Database of pedestal from AUG, DIII-D, and JET showing the correlation between $\langle \nabla T_e \rangle$ and $T_{e,ped}$ (left) [6], and between $\Delta\psi_N$ and $\sqrt{\beta_{p,ped}}$ (right) [121].

pedestal width, the electron heat conductivity $\chi_{e,ped}$ that fulfills this condition is found. We then consider the ion heat conductivity $\chi_{i,ped}$ and the particle diffusivity $D_{n,ped}$ as given by the sum of neoclassical transport (calculated with NCLASS) and terms proportional to $\chi_{e,ped}$, as described in Sec. 4.2.2. The application of this empirical condition results in a pedestal transport constraint, which gives a relation between the pedestal width and height. Thereby, for a certain value of the pedestal width, we obtain the pedestal height and the pedestal gradient.

With such a transport constraint the pedestal pressure increases with increasing width, as sketched in figure 4.1 (b), until the MHD stability limit is reached, as in figure 4.1 (d). The way the pedestal transport model is implemented in ASTRA, as discussed later on, requires to reach stationary conditions of the kinetic profiles for a given value of the pedestal width. Therefore many different ASTRA simulations with different values of the pedestal width need to be run in parallel in order to obtain a scan of the pedestal pressure. Figure 4.1 (c) shows the pressure profiles calculated by ASTRA (from the magnetic axis to the separatrix, although here shown only from $\rho_{tor} = 0.5$ to better highlight the pedestal) for different values of the pedestal width. The MISHKA MHD stability code is then run on each ASTRA simulation results to find the highest pedestal pressure that is stable to peeling-ballooning modes (PBM), corresponding to pre-ELM conditions. Figure 4.1 (e) shows the pressure profile which is the final result of the modeling workflow, from which we can also calculate the stored energy and the energy confinement time.

The SOL model consists of a set of analytical formulas that we included in ASTRA as an additional external module. The formulas allow us to set the boundary conditions (at the separatrix) for the transport simulation. To compute the heat and

particle sources, and the non-inductive current drive ASTRA includes TORBEAM [119], and NBI [122] and neutrals modules. The TORBEAM and NBI modules require as input all the engineering parameters of the heating systems (e.g. power, angles, voltage of the beams, frequency of the gyrotrons, etc.), as well as the plasma kinetic profiles, and can predict the power distribution.

The main source of radiation in AUG confined plasmas, for cases without seeding of impurities (e.g. nitrogen), is given by tungsten, which is present in the plasma in low concentrations. We noticed that the measured radiated power in the database of experimental cases considered in this work, which does not include impurity seeded discharges, followed robustly a linear dependence on the heating power. Physically, this could be connected to the increase of the divertor temperature with increasing heating power and the consequent increased W sputtering yield. Therefore we adopted the simplified solution of capturing this behaviour by assuming a radially constant tungsten concentration, and scale its value to obtain a total radiated power of $P_{rad} = 0.25(P_{net} - 2)$ [MW], obtained from a regression on experimental data. It is important to point out that this relation has been derived on stationary H-mode phases of AUG discharges, therefore it might not be applicable to other plasma regimes or other machines. This also allows us to be independent from assuming the tungsten concentration. This assumption can be substituted in the future with theory based impurity transport modeling, however this element goes beyond the goals of this PhD thesis and has been left for future work in which the tungsten concentration is also predicted through a combination of models for the tungsten sources and transport.

To calculate the densities of the ions species we simply impose quasineutrality assuming boron as light impurity, which is present in the machine due to wall conditioning, and that Z_{eff} is constant over the plasma radius. The SPIDER equilibrium code [120] is also coupled to ASTRA to calculate the plasma equilibrium with a prescribed plasma boundary. To calculate core turbulent and neoclassical transport the TGLF quasilinear transport model [1] and the NCLASS model [2] are used respectively.

With the inclusion of the empirical pedestal transport model, ASTRA provides a complete description of the transport coefficients in the whole radial domain of the confined plasma, allowing us to simulate the kinetic profiles, namely the electron and ion temperature and density (T_e, T_i, n_e, n_i) , and the current density (j) profiles from the magnetic axis to the separatrix. We also simulate the toroidal rotation (v_{tor}) , but only from the magnetic axis to the pedestal top, since its only purpose is to self-consistently calculate the radial electric field in the core region, and no simply applicable model exist to predict the toroidal rotation profile in the pedestal region. The inputs of the model are the magnetic field, the total plasma current, the engineering parameters determining the auxiliary heating powers, the deuterium fueling rate, the nitrogen seeding rate, the plasma boundary, and the effective charge Z_{eff} . The value of the effective charge is taken from the Integrated Data Analysis (IDA) [123] if available, otherwise is assumed equal to $Z_{eff} = 1.2$ (typical AUG value

for experiments without seeding of impurities, in the intermediate to high density range). The result of the model is anyway very little sensitive to the effective charge in this range of values relatively close to $Z_{eff} = 1$.

4.2 Transport simulations

4.2.1 Scrape-off layer model

A simple SOL model, consisting of a set of analytical formulas, has been included in ASTRA to provide the boundary conditions of the neutral density, and of the electron temperature and electron density at the last closed flux surface. We use the formulas for the separatrix electron temperature $T_{e,sep}$ and density $n_{e,sep}$ from Ref. [9] (equations 5 and 8 respectively), as already presented in section 3.1.5, obtained through an extension of the two point model.

For the boundary condition of the ion temperature we simply assume $T_{i,sep} = 2T_{e,sep}$. This is regularly observed in AUG experiments, and can be justified by the fact that the parallel heat conductivity in the SOL is smaller for the ions than for the electrons. This assumption might not be valid for pronounced detached divertor conditions, where one would expect that the difference between $T_{i,sep}$ and $T_{e,sep}$ becomes smaller. The experimental cases considered in this thesis are all in attached divertor conditions. In order to also take into account cases in fully detached conditions this assumption will have to be replaced with a more complete and appropriate one, this could be done as part of future work.

The $n_{e,sep}$ formula, as already presented in section 3.1.5 (eq. 3.32), couples the plasma parameters in the divertor and midplane (at the separatrix), by assuming pressure balance. The formula also assumes that momentum losses, power losses, and divertor heat flux broadening can be combined into a coefficient, which is found by regression analysis on AUG to depend mainly on the divertor neutral pressure. For fully detached divertor conditions, which are relevant for future fusion reactors (e.g. DEMO), the hypothesis of pressure balance would not hold anymore due to significant momentum losses, so the formula should be modified to include also convective flows (as done in Ref. [124]), which become important at low temperatures (i.e. detached conditions) [125]. The midplane parameters required by the formula are the power crossing the separatrix P_{sep} , the major radius, the main ion mass m_D , the magnetic field and the safety factor (also used to calculate the power decay length λ_q [116]), and are calculated by ASTRA. For the divertor parameters we assume constant (not changed among the different cases considered in this work) the total sheath energy transmission factor $\gamma = 6$, the impact angle of the field line at the outer target $\alpha = 3.3^\circ$, and $Z_{eff,div} = 1.3$ (used to calculate κ_z), values of which are typical for AUG [126]. The only remaining unknown parameter is the pressure of the neutrals in the divertor p_0 , which is the main term of the formula. To estimate it, a scaling has been derived using AUG data, obtained with a baratron [127] in the configuration with the divertor DivIII [128]. The regression has been performed

on 116 data-points, using as variables the deuterium fueling rate $\Gamma_D[10^{19}\text{e/s}]$, the nitrogen seeding rate $\Gamma_{N_2}[10^{19}\text{e/s}]$, the NBI power $P_{NBI}[\text{MW}]$ (which represents the fueling provided by the NBI), and (because AUG operates with a cryopump) the pumping speed expressed in relative velocity $v_{pump}[\%]$ (1 if operating on liquid helium, 0.5 if on liquid nitrogen, 0.2 if turned off). The result of this regression reads,

$$p_0 = 0.174 \Gamma_D^{0.63} \Gamma_{N_2}^{-0.057} P_{NBI}^{0.33} v_{pump}^{-0.67}. \quad (4.1)$$

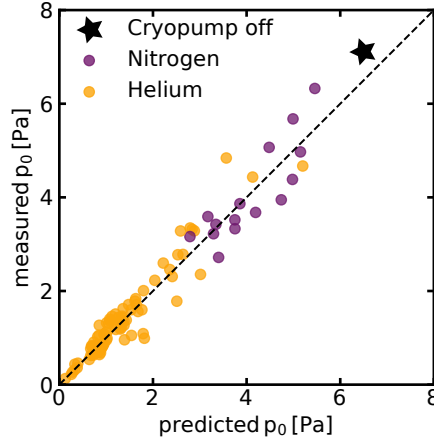


Figure 4.3 – Comparison between the predicted and measured divertor neutral pressure. The color code shows the operation of the cryopump with liquid helium (orange), liquid nitrogen (purple), or turned off (black).

Figure 4.3 shows the measured divertor neutral pressure compared to the one predicted. Remarkably, the coefficient of determination $R^2 = 0.948$ and the root mean squared error $RMSE = 16.8\%$ show the good description of the data by the scaling, allowing a robust evaluation of $n_{e,sep}$. We performed a log–linear regression instead of a linear regression since it provided a better result. For the cases without nitrogen seeding or NBI power the terms Γ_{N_2} or P_{NBI} are simply dropped out of the formula to avoid getting a null value of p_0 . A histogram showing the distribution of the data used to compute the scaling is depicted in figure 4.4. The range of parameters used for the scaling is wide enough to cover the AUG operational space, therefore we expect that it can be robustly applied to predict p_0 for AUG.

Due to the location of the baratron, illustrated in figure 4.5 (figure 3 in Ref. [127]), the measurement of the divertor neutral pressure is influenced by (and is therefore able to capture the effects of) the high-field-side high-density (HFSHD) front (observed in AUG and JET) [129, 130], a region of the HFS SOL where the density of the plasma reaches high values, approximately one order of magnitude higher than at the separatrix. This high density front appears when operating with sufficient levels of gas fueling and heating power. The density of the front is reduced by impurity

4 Description of the Integrated Modeling Workflow

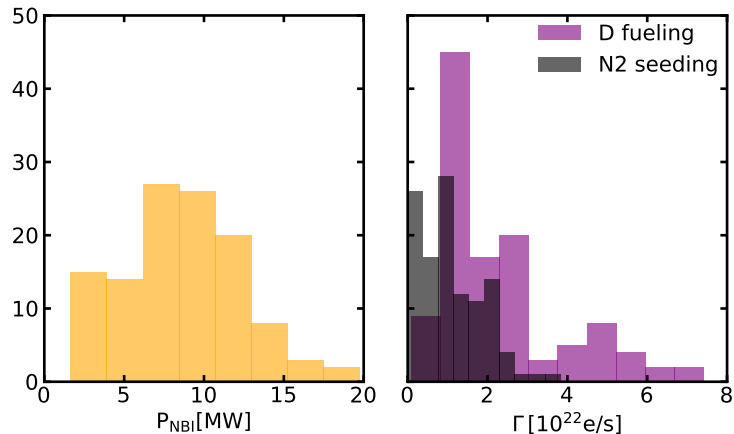


Figure 4.4 – Histograms showing the number of observations in the database used for the regression as a function of the NBI power (left), and deuterium fueling (purple) and nitrogen seeding (black) rates (right). The histograms with deuterium fueling and nitrogen seeding are plotted with transparent colors, the darker region results from their overlap.

seeding since this increases the radiation, causing a decrease of the power exhausted by the confined plasma before reaching the HFS SOL. This reduced amount of power leads to a reduction of the ionization of the particles associated with the HFSHD [130]. The heating power also has a similar effect: if it is reduced, the density of the HFS front decreases. Because of the influence of the HFSHD front on the measurement of divertor neutral pressure, we can include in the scaling the effect of nitrogen seeding (the main impurity used in AUG), and ultimately its effect on the separatrix density. Interestingly, when performing the regression for the scaling the only type of heating source that turns out to have an impact on the divertor neutral pressure is the NBI, while ECRH and ICRH seem to have no correlation. This could be due to the fact that the NBI is not only heating the plasma but it also provides a source of particles. Across the simulations performed on the experimental cases presented in chapter 6, the contribution of the NBI to the total plasma particle source varied from $\sim 5\%$ to $\sim 27\%$, depending on the operating conditions, hinting that this is usually a rather small but non-negligible contribution.

The source of neutrals crossing the separatrix, coming from outside the confined plasma, is an important boundary condition since it is the main contribution to the total plasma particle source. It is important to correctly estimate the source of particles since together with transport it defines the electron density profile in the pedestal region. In the core, in contrast, the density profile is predominantly determined by the turbulent transport convection in a large majority of plasma conditions [44, 131, 132], with the effect of the particle source relatively weaker in this region. The main source of neutrals coming from outside the confined plasma

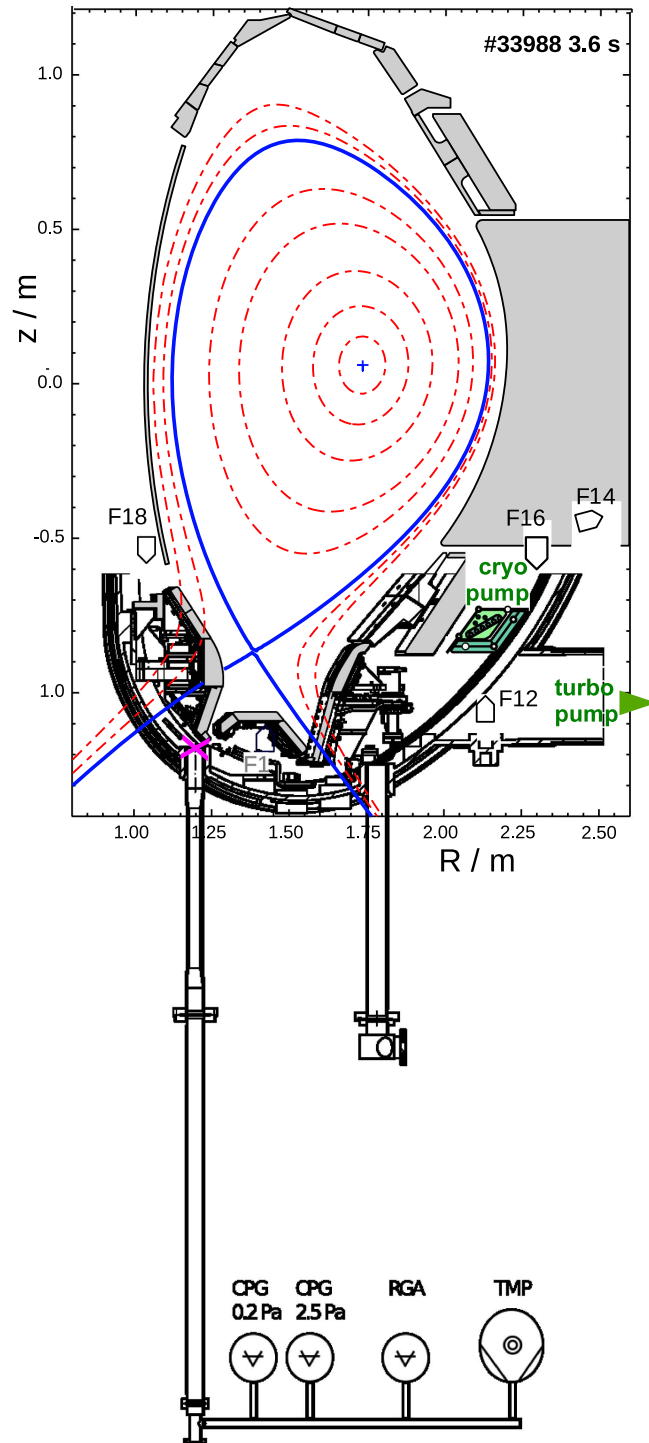


Figure 4.5 – Illustration of the AUG lower divertor, indicating the location of the cryopump, and of the baratron measuring the divertor neutral pressure at the port entrance, marked by a magenta cross. Figure modified from [127].

4 Description of the Integrated Modeling Workflow

is given by the wall gas inventory which is sustained by recycling and gas puffing, which we compute as

$$\Gamma_{0,wall} = f_R \Gamma_{e,sep} + c_{div,wall}(\Gamma_D - \Gamma_{pump}). \quad (4.2)$$

The term $f_R \Gamma_{e,sep}$ represents recycling, where $\Gamma_{e,sep}$ is the electron flux leaving the plasma, and f_R is the recycled fraction. The term $c_{div,wall}(\Gamma_D - \Gamma_{pump})$ represents the fueling given by gas puff valves Γ_D minus the cryopump absorption Γ_{pump} , considering that only a fraction $c_{div,wall}$ diffuses from the valves (in the divertor region) to the SOL (or to the wall). We can then estimate the source of neutrals crossing the LCFS as

$$n_{0,sep} = \alpha_{wall,sep} \frac{\Gamma_{0,wall}}{\nu_0 A_{eff}} = \alpha_{wall,sep} \frac{(f_R \Gamma_{e,sep} + c_{div,wall}(\Gamma_D - \Gamma_{pump}))}{\nu_0 A_{eff}}. \quad (4.3)$$

ASTRA requires the neutral density at the separatrix $n_{0,sep}$ as input, which can be obtained dividing the neutrals flux Γ_0 by the neutrals velocity ν_0 and the surface crossed by the neutrals A_{eff} . We assume that the majority of the neutrals come from the divertor region and the wall at the outer midplane, which roughly correspond to one third of the LCFS $A_{eff} = A_{LCFS}/3$. The term $\alpha_{wall,sep}$ is a parameterization of the decay of the neutrals density caused by the ionization and charge exchange (CX) processes that occur during their flow from the wall to the confined plasma. The formula used to estimate this parameter has been obtained by fitting a database consisting of ~ 1000 values of $\alpha_{wall,sep}$ calculated for different values of the electron temperature and density, and of the distance between the LCFS and the wall. The calculation of $\alpha_{wall,sep}$ has been performed using the rate coefficients for ionization and CX of deuterium as a function of T_e as in [133], assuming a fixed decay length of the plasma density and temperature profiles in the SOL, and considering neutrals with a constant temperature of $T_0 = 5$ eV, representing reflection of sheath accelerated ions and Franck-Condon neutrals

$$\frac{\partial n_0}{\partial x} = -R_{ion} n_e n_0 / \nu_0 - R_{CX} n_i n_0 / \nu_0 \quad (4.4)$$

where x is the radial coordinate. We solve this equation numerically, considering for simplicity $n_e = n_i$ and $T_e = T_i$ since the CX rate coefficient R_{CX} is not very sensitive to the temperature. We ignore line radiation and recombination since they are negligible in the range of temperatures we are considering. We then obtain $\alpha_{wall,sep}$ for different values of $n_{e,sep} = 0.5 - 6 \times 10^{19}/\text{m}^3$, $T_{e,sep} = 70 - 150$ eV, and distance between the wall and the LCFS $d_{wall,sep} = 0.02 - 0.1$ m.

Figure 4.6 (left) shows the SOL profiles of the electron density (blue) and temperature (red), resulting from assuming a fixed decay length (but different for n_e and T_e), normalized to their separatrix value for a distance between the wall and the LCFS $d_{wall,sep} = 0.05$ m, where x is the radial coordinate which goes from the separatrix ($x = 0$) to the wall ($x = 50$ mm). Figure 4.6 (right) illustrates an example

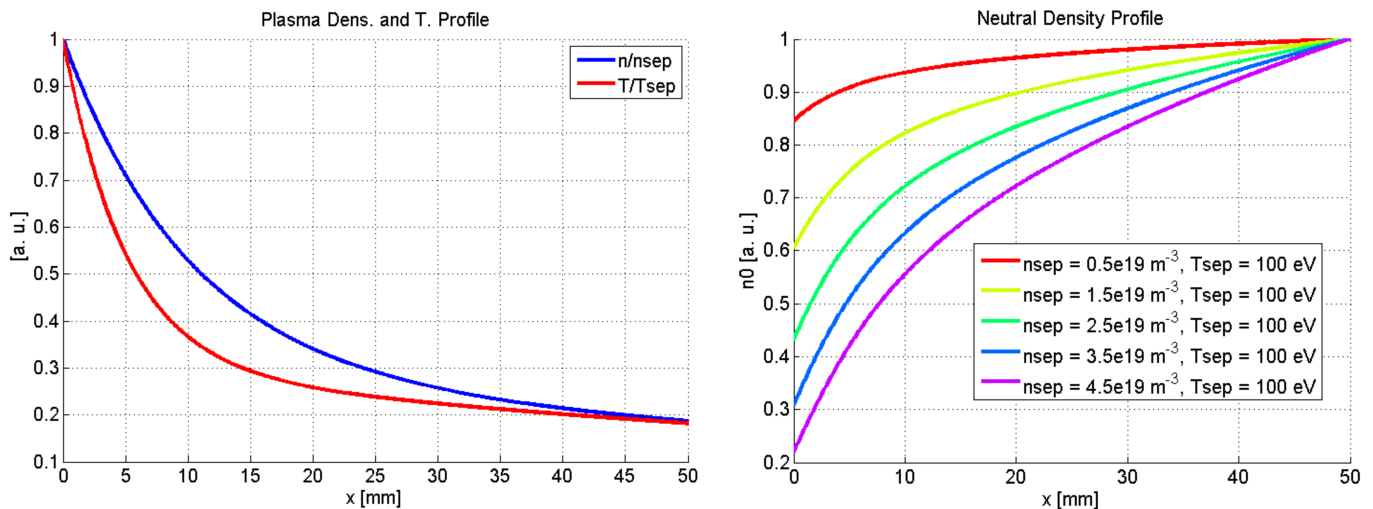


Figure 4.6 – SOL profiles of the electron density (blue) and temperature (red) normalized to their separatrix value, resulting from assuming a fixed decay length (left), and of the neutral density, normalized to their value at the wall, calculated for different values of the separatrix electron density, with constant $T_{e,sep}$ and $d_{wall,sep}$ (right).

of SOL neutral density profiles, normalized to their value at the wall (which is therefore equal, at $x = 0$, to $\alpha_{wall,sep}$), calculated for different values of the separatrix electron density, with a constant separatrix electron temperature $T_{e,sep} = 100$ eV and $d_{wall,sep} = 0.05$ m. As one can see the decay of the neutral density in the SOL $\alpha_{wall,sep}$ is quite sensitive to the plasma density.

The scaling gives then, with a root mean squared error $RMSE < 0.1\%$:

$$\alpha_{wall,sep} = 87.6 - 18.9n_{e,sep}[10^{19}/\text{m}^3]^{0.016} - 67.2T_{e,sep}[\text{eV}]^{0.0027} - 1.284d_{wall,sep}[\text{m}]^{0.939}. \quad (4.5)$$

We then have an incoming source of neutrals with $T_0 = 5$ eV. The energy of the neutrals does not change the result of the simulations since we estimate the incoming neutral particle flux $\Gamma_{0,sep}$, and the neutral density depends then on the temperature since $\nu_0 \propto \sqrt{T_0/m_0}$. So more energetic neutrals penetrate deeper into the confined plasma, but their density will be lower, and overall the effect will be balanced. We performed a sensitivity study of the effect of neutrals temperature ($T_0 = 5, 3, 2$ eV) on the density profile in the pedestal, but the density profile and its gradient were the same in all cases.

Another interesting aspect is that, for the different experimental cases considered (presented in section 5.2), even variations in the fueling rate by more than one order of magnitude produces only a small change in the neutrals density at the separatrix (i.e. an increase in the fueling rate of a factor 10 causes an increase in the neutrals density of less than a factor 2). This is consistent with the observations

from Ref. [134], where the separatrix neutrals density appears to be in the order of $10^{16}/m^3$ for all the different cases analyzed. This can be explained by the fact that when the fueling rate is increased, the separatrix density increases, causing a stronger decay of the neutrals density due to ionization and charge exchange, which partially compensate the stronger source of neutrals.

This simple SOL model allows us to capture the main effects of fueling (and in principle also of nitrogen seeding, although this has not been tested yet) on the boundary conditions of the ASTRA transport simulation, which can affect the pedestal stability and the plasma confinement.

4.2.2 Pedestal transport

As previously described we make use of the experimental observation $\langle \nabla T_e \rangle / T_{e,top} \approx const = -0.5 [cm^{-1}]$ to calculate the transport coefficients in the pedestal region. This condition has been implemented in ASTRA, so that for a given pedestal width the electron heat conductivity $\chi_{e,ped}$ is changed to fulfill this imposed condition. This is done by minimizing the difference between the value of $\langle \nabla T_e \rangle / T_{e,top}$ calculated by ASTRA and the target value, modifying the absolute value of $\chi_{e,ped}$ in a feedback iteration while evolving the kinetic profiles. The final value of $\langle \nabla T_e \rangle / T_{e,top}$ matches the imposed condition with an error $< 1\%$. As previously described, many different ASTRA simulations are run in parallel to perform a scan (with discrete values) in pedestal width, where each simulation calculates the kinetic profiles for a different value of the pedestal width. We assume equal values of the pedestal widths for the electron and ion temperatures and density $\Delta T_e = \Delta T_i = \Delta n_e$. For each of these ASTRA simulations the kinetic profiles are evolved until the condition $\langle \nabla T_e \rangle / T_{e,top} = -0.5 [cm^{-1}]$ is satisfied and stationary conditions are reached. We then define the ion heat diffusion coefficient as $\chi_{i,ped} = \chi_{e,ped} + \chi_{i,neo}$, where $\chi_{i,neo}$ is the neoclassical ion heat diffusivity, calculated with NCLASS, while the neoclassical electron heat diffusivity $\chi_{e,neo}$ is negligible.

The pedestal density profile is determined by the balance between particle transport and sources, and since we do not have a constraint that gives a quantitative estimate of these two components we have a degree of arbitrariness on the coefficients that define them. To describe the pedestal particle transport we assume that the particle diffusion coefficient is equal to $D_{n,ped} = c_{D/\chi} \chi_{e,ped} + D_{n,neo}$, where the term $c_{D/\chi} \chi_{e,ped}$ represents the turbulent component of $D_{n,ped}$, being proportional to $\chi_{e,ped}$ through $c_{D/\chi}$, and $D_{n,neo}$ is the electron neoclassical particle diffusivity. We also assume a fixed pinch velocity $v_{n,ped} = -0.05 m s^{-1}$. The values of these coefficients ($c_{D/\chi} = 0.06 m^2 s^{-1}$, $v_{n,ped} = -0.05 m s^{-1}$) have been obtained through an optimization procedure trying to match a set of different experimental pedestal density profiles. The resulting effective particle diffusion coefficient is consistent with previous observations from AUG experiments [135]. We underline that the electron heat conductivity $\chi_{e,ped}$ is not influenced by these assumptions since it mainly depends on the electron heat source.

To help understanding how this procedure for modeling the pedestal works,

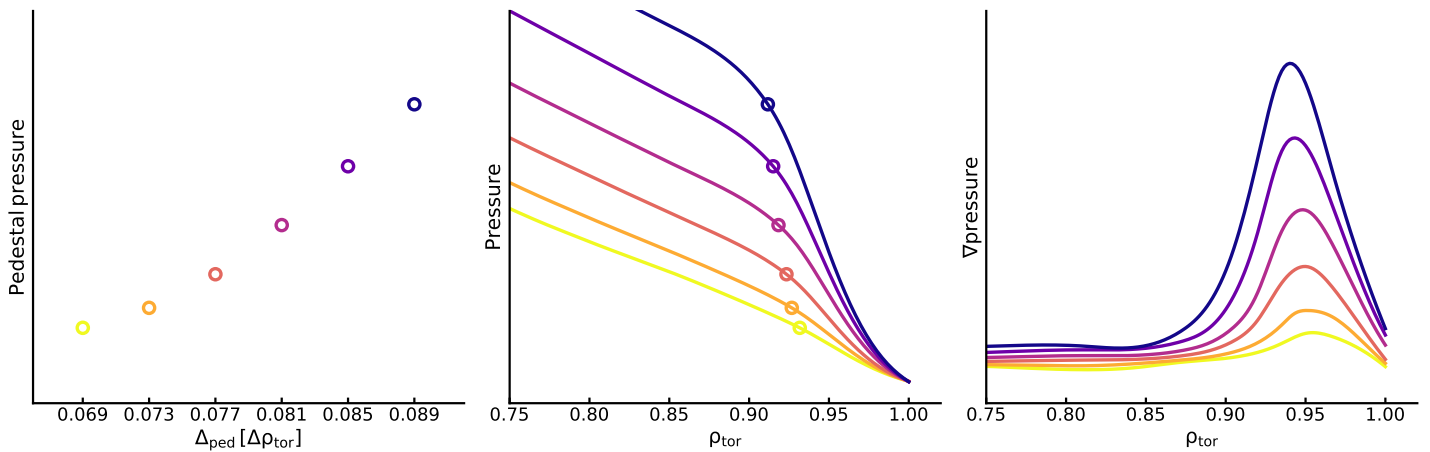


Figure 4.7 – The new pedestal model included in ASTRA gives a transport constraint which determines the pedestal pressure for a given pedestal width (left). Multiple parallel ASTRA simulations calculate the kinetic profiles (we show here the resulting total pressure), from the magnetic axis to the separatrix (we show here the pedestal region only), for different values of the pedestal width (middle). The corresponding pedestal pressure gradients increase with increasing pedestal width (right), as the pressure increases more than linearly with the width.

figure 4.7 shows the resulting pedestal top pressure (left) and pressure profiles (middle) for different values of the pedestal width. By increasing the pedestal width, the pedestal top temperature increases (and therefore also the total pressure), and because the pedestal temperature and its gradient are linked by the constraint $\langle \nabla T_e \rangle / T_{e,top} = -0.5 [\text{cm}^{-1}]$, also the temperature gradient increases with increasing width (and therefore also the pressure gradient), as illustrated in figure 4.7 (right). To sustain stronger temperature gradients with increasing width, $\chi_{e,ped}$ has to decrease in value with increasing width. This is an important feature for understanding the mechanism which allows the model to capture the change in confinement caused by variations in certain operational parameters (e.g. the change in the NBI voltage, as discussed in section 6.4.3).

It can be interesting to point out the main similarities and differences between the approach described in this work and the widely applied EPED pedestal model [7]. Both EPED and the present model scan the pedestal pressure using a transport constraint that relates the pedestal width to its height or gradient, and then use a MHD stability code to find the pedestal structure in the conditions before the ELMs onset, given by PBM instability. The difference between the two models is in the different transport constraint, which in EPED is provided by the relation $\Delta\psi_N = G\sqrt{\beta_{p,ped}}$. As already mentioned in section 3.1.3, this approach allows EPED to be applied in a stand-alone manner, not requiring the use of a transport code. In contrast, the approach developed in this work requires the use of a transport code

4 Description of the Integrated Modeling Workflow

since the adopted constraint does not couple the pedestal width to its height directly, but must solve a system of equations where the variables are the heat source, the heat conductivity, the temperature gradient, and the pedestal top temperature. On the other hand, with a transport code we can separately describe transport in all the different channels, allowing us to also predict the density. A comparison on how the two different transport constraints are representative of experimental data is given by figure 4.2 (right), where the same pedestals database from figure 4.2 (left) is used to show the correlation between the pedestal width Δ_{ψ_N} and the square root of beta poloidal at the pedestal top $\sqrt{\beta_{p,ped}}$. It is interesting to notice that DIII-D and AUG data do not lay on the same region of the graph, perhaps due to the different collisionality regimes between the two different machines, and need a different G coefficient, i.e. steepness of the curve.

Another important aspect is the interpretation of the condition $\langle \nabla T_e \rangle / T_{e,top} = -0.5 [\text{cm}^{-1}]$, and the resulting relationship between the pedestal width and the pedestal top pressure. One might reach the wrong conclusion that $\langle \nabla T_e \rangle = T_{e,top} / \Delta_{ped}$, and therefore $T_{e,top} / \Delta_{ped} / T_{e,top} = 1 / \Delta_{ped} = \text{constant}$. However, this is wrong, because $\langle \nabla T_e \rangle = (T_{e,top} - T_{e,sep}) / \Delta_{ped}$, which does not lead to a constant value of the pedestal width. It is possible to find $T_{e,ped}$, and $\langle \nabla T_e \rangle$, for a given Δ_{ped} and $T_{e,sep}$ by solving a system with 2 equations

$$\langle \nabla T_e \rangle = -0.5 T_{e,top}, \quad (4.6)$$

$$T_{e,top} = T_{e,sep} - \langle \nabla T_e \rangle \Delta_{ped}. \quad (4.7)$$

The solution of this system of equations leads to

$$T_{e,top} = \frac{T_{e,sep}}{(1 - 0.5 \Delta_{ped})}, \quad (4.8)$$

where Δ_{ped} is the fraction of the minor radius at the outer midplane associated to the pedestal width. The relation between $T_{e,top}$ and Δ_{ped} for different values of $T_{e,sep}$ is illustrated in figure 4.8. It can be noticed that the shape of the curves in this figure is similar to that of figure 4.7 (left), showing the pedestal top pressure calculated by the ASTRA simulations for different values of the pedestal width, which is also similar to that obtained from the pedestal width model adopted by EPED ($\Delta_{\psi_N} \propto \sqrt{\beta_{p,ped}}$). A quantitative comparison of the relation between the pedestal height and width resulting from the present pedestal transport model and EPED is given by figure 5.4 (b) in section 5.3.1.

The transport constraint adopted by the EPED model can be thought as a constraint on the pressure gradient and is associated to a representation of kinetic ballooning modes (KBM). The constraint we impose is instead a critical pedestal averaged electron temperature scale length, which can be interpreted as a critical condition for the R/L_{T_e} drive for turbulent transport, and therefore can be associated to electron temperature gradient modes (ETG) or micro tearing modes (MTM). This finds some support from Ref. [105, 106], where MTMs are identified as the

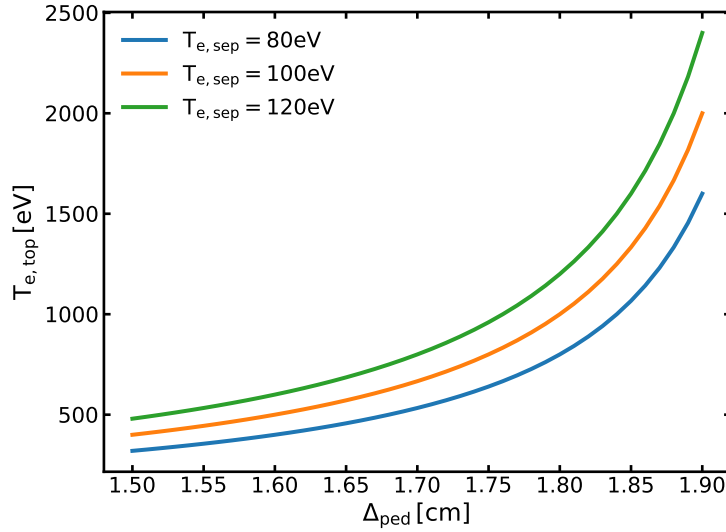


Figure 4.8 – Relation between $T_{e,top}$ and Δ_{ped} for different values of $T_{e,sep}$.

instability limiting transport in the JET-ILW pedestal, as well as from Ref. [100], where ETGs are found to be plausibly responsible for a significant portion of the electron heat flux in the AUG pedestal. Another observation worth pointing out is that MTMs and ETGs cause a particle diffusion coefficient $D_{n,ped}$ that is at least one order of magnitude smaller than the electron heat diffusion coefficient $\chi_{e,ped}$, as opposed to MHD-like instabilities for which these are comparable [136], and the value of its ratio $D_{n,ped}/\chi_{e,ped} \sim 0.02 - 0.06$ (more information is provided in Ref. [137]) is found to be similar to our assumption ($c_{D/\chi} = 0.06$).

For clarification, the relation $\langle \nabla T_e \rangle / T_{e,top} = -0.5 [\text{cm}^{-1}]$ is not exactly a pedestal averaged electron temperature scale length, since the pedestal averaged temperature gradient $\langle \nabla T_e \rangle$, calculated over the minor radius at the outer midplane, is divided by the temperature at the pedestal top $T_{e,top}$, instead of the pedestal averaged temperature $\langle T_e \rangle = (T_{e,top} + T_{e,sep})/2$. However, it is possible to derive an expression for the pedestal averaged normalized gradient $\langle R/L_{T_e} \rangle$ which includes the condition $\langle \nabla T_e \rangle / T_{e,top} = -0.5 [\text{cm}^{-1}]$. The first step is to express the normalized gradient as

$$\left\langle \frac{R}{L_{T_e}} \right\rangle = \frac{R}{\langle T_e \rangle} \frac{\Delta T_e}{\Delta r}, \quad (4.9)$$

where r is the minor radius at the outer midplane. The temperature gradient $\langle \nabla T_e \rangle = \Delta T_e / \Delta r$ can be substituted by the combination of eq. 4.6 and eq. 4.8, leading to

$$\left\langle \frac{R}{L_{T_e}} \right\rangle = \frac{R}{\langle T_e \rangle} \frac{0.5 T_{e,sep}}{(1 - 0.5 \Delta_{ped})}. \quad (4.10)$$

By expressing $\langle T_e \rangle$ as $(T_{e,top} + T_{e,sep})/2$, and after some algebra, where $T_{e,top}$ is

substituted by eq. 4.8, we obtain

$$\left\langle \frac{R}{L_{T_e}} \right\rangle = \frac{R}{(2 - 0.5\Delta_{ped})}. \quad (4.11)$$

This last expression means that, in the present pedestal transport model, $\langle R/L_{T_e} \rangle$ is simply a function of the pedestal width and the major radius. Over the AUG database considered in this work, the value of the pedestal width Δ_{ped} predicted by the integrated model varies from 1.4 cm to 2.2 cm, expressed as minor radius at the outer midplane. Therefore, the normalized gradient has a variation $\langle R/L_{T_e} \rangle = 165 \pm 30$. It is interesting to notice that instead, the ion temperature and the electron density normalized gradients exhibit a much stronger relative variation across the database $\langle R/L_{T_i} \rangle = 112 \pm 50$, $\langle R/L_n \rangle = 150 \pm 76$. The value of $\langle R/L_{T_i} \rangle$ is generally smaller than $\langle R/L_{T_e} \rangle$, since usually at the pedestal top the ion and electron temperatures are similar, while at the separatrix the ion temperature is larger than the electron temperature.

4.2.3 Core transport

To estimate the core turbulent transport fluxes of heat and particles we use the TGLF quasilinear model, with the SAT1 [55] version of the saturation rule. The kinetic profiles are simulated using the diagonal terms of the ASTRA transport matrix, that are heat and particle diffusivities (χ_e, χ_i, D_n) , plus the particle pinch velocity (C_n) . We use the fluxes calculated by TGLF to compute these coefficients in the core region, and in particular for the particle transport we put the complete TGLF particle flux into the pinch velocity. To account for sawteeth, internal kink modes that are triggered when $q < 1$, we consider the transport they cause in an averaged sense, like from a time average over multiple sawtooth periods. We increase by a fixed amount the heat and particle transport coefficients ($\chi_{e,sr} = 0.2 \text{ m}^2/\text{s}$, $\chi_{i,sr} = 1 \text{ m}^2/\text{s}$, $D_{n,sr} = 0.5 \text{ m}^2/\text{s}$) in the plasma region inside of the inversion radius, so that the resulting kinetic profiles are a time averaged profile over the sawtooth period. We also use a model for the sawtooth crash [138], neglecting the effects caused to the temperature and density profiles that are already included with the additional diffusivities, to take into account the effect of internal kink modes on the current density profile.

We include the effect of the dilution due to fast ions in TGLF, by simply removing the fast ion density from the thermal ion density, although not treating the fast ions as a separated species in TGLF. This implies that quasi-neutrality is not respected in TGLF, although it is in ASTRA. We do this to at least take into account the effect of the fast ions on the turbulent fluxes via dilution, although this is a very small effect. This effect has shown to give negligible changes in our cases, probably because of the usually large thermal density values of AUG operation.

The modeling of the toroidal rotation is also included in the ASTRA simulation, allowing us to calculate all the components of the radial electric field core profile,

which is used by TGLF to calculate the effect of the $\mathbf{E} \times \mathbf{B}$ shear on turbulent transport. The TGLF prediction for AUG plasmas is not very sensitive to the $\mathbf{E} \times \mathbf{B}$ shear, but by doing this we self consistently include the effect of the toroidal rotation in our simulations, without the need of using any experimental information from profile measurements. Since we only need the core component of the toroidal rotation, and the modeling of this quantity in the pedestal region is not trivial, we simply simulate it from the magnetic axis to the pedestal top. ASTRA allows us to set the boundary condition directly at this location, while we assume $v_{tor} = 0$ from the pedestal top to the separatrix. The toroidal rotation at the pedestal top is not taken from experimental measurements, but is calculated using the formulas from Ref. [8], which is a theoretical description of the intrinsic rotation based on a transport model that incorporates orbit-loss, transport-driven SOL flows, and turbulence intensity gradient. Such model is able to capture the basic T_i/I_p scaling and X-point-position dependence of experimental observations. We then simulate the core rotation by assuming an effective Prandtl number $P_r = 1$, which means that we assume a momentum diffusivity χ_ϕ equal to the ion heat diffusivity associated to turbulent transport $\chi_{i,turb}$, calculated by TGLF. The torque provided by the NBI is calculated by the ASTRA NBI module. All of the AUG cases considered in this work are heated by means of the NBI system. Therefore, we never face the problem of predicting an intrinsic rotation profile. Thanks to the fact that an external torque is always present, the assumption $P_r = 1$ provides a good qualitative description of the experimentally measured core toroidal rotation.

4.2.4 Integration of the different components

This subsection describes how the transport coefficients in the pedestal and in the core region are combined together. In the ASTRA simulations the extent of the pedestal region is regulated by the value of the pedestal width. In this region the transport coefficients assume the values discussed in section 4.2.2. Conventional core transport modeling of H-mode plasmas applies the boundary condition just inside the pedestal top (usually $\rho_{ped}^{top} \sim \rho_{tor} \simeq 0.9$). Because the boundary values of temperatures and densities are fixed there, oscillations in the transport coefficients in the peripheral region of the simulation have more limited effects in the predicted behavior of the density and temperature profiles in that region. When the simulation domain is extended up to the last closed flux surface, then any oscillation of the transport coefficients has much stronger effects on the simulated kinetic profiles, rendering the simulations much less stable and robust. For this reason, the radial domain within which the TGLF model has been applied has been limited to $\rho_{tor} < 0.85$. The area close to the magnetic axis $\rho_{tor} < 0.1$ is also excluded from the domain of TGLF calculations, as in this region its prediction can become inaccurate and transport is usually dominated by sawteeth and collisions (ion neoclassical transport becomes very large approaching the magnetic axis). The radial domain in which we use TGLF to calculate the turbulent transport fluxes is therefore between $0.1 < \rho_{tor} < 0.85$.

4 Description of the Integrated Modeling Workflow

During the development of the work presented in this thesis, the TGLF transport model has gone through substantial updates and modifications that particularly affected the prediction of the heat fluxes in the edge plasma region, in the proximity of the pedestal top. The results obtained from the first application of the integrated model, presented in Ref. [139] and in chapter 5, still relied on an older version of TGLF (previous to the updated version, released in February 2020, and which includes a more complete description of geometrical effects at the periphery, as well as a new calibration against gyrokinetic nonlinear simulations). We found that the original SAT1 version of TGLF was not reliable in the region outside $\rho_{tor} > 0.78$, systematically overpredicting electron heat transport and underpredicting ion heat transport, as also observed in Refs. [118, 140]. The radial domain in which TGLF was used to calculate the turbulent transport fluxes in the earlier version of the model was therefore between $0.1 < \rho_{tor} < 0.78$.

The new version of TGLF (released in February 2020) turns out to solve this problem, producing electron and ion heat diffusivities in the proximity of the pedestal top which are closer to the values of the diffusivities inferred from experimental measurements. This allowed us to set the TGLF boundary more externally, at $\rho_{tor} = 0.85$, obtaining a more reliable prediction of the heat fluxes, and therefore of the kinetic profiles in this region. Figure 4.9 shows a comparison between the heat diffusivities resulting from the predictions of TGLF (red dashed line), in the old (top) and new (bottom) versions of the model. The lighter dotted red line represents the TGLF solution in the edge region (not considered in the ASTRA simulation), which corresponds to very large electron heat fluxes and practically zero ion heat fluxes for the older TGLF version, and would cause almost flat T_e gradients and too steep T_i gradients. The new TGLF version instead predicts ion and electron heat fluxes closer to each other, leading to similar temperature gradients between electrons and ions.

In the region between the TGLF boundary and the pedestal top location $0.85 < \rho_{tor} < \rho_{ped}^{top}$ we have a transition layer, referred as 'TR' in figure 4.9, in which we include an additional value to the heat and particle transport coefficients ($\chi_{e,tr}$, $\chi_{i,tr}$, $D_{n,tr}$) to ensure smooth gradients, composed of two terms: one that is constant and one that is proportional to the pedestal electron heat diffusion coefficient $\chi_{tr} = c_1 + c_2\chi_{ped}$. The values of c_1 and c_2 have been chosen in order to obtain gradients of the kinetic profiles, in this region, similar to the experimental ones for the experimental cases considered. Their value is kept constant among the different cases. We find that to obtain temperature gradients similar to the experimental ones in this region the ion heat diffusion coefficient $\chi_{i,tr}$ has to be larger than the one obtained by TGLF at $\rho_{tor} = 0.85$, while for the electrons a heat diffusion coefficient $\chi_{e,tr}$ of similar value with respect to the one from TGLF is sufficient. We also find that the ion heat diffusion coefficient $\chi_{i,tr}$ has to be generally larger than the one for the electrons $\chi_{i,tr} > \chi_{e,tr}$. This is in line with the observations reported in Ref. [141], where it is shown that for many AUG cases with different heating schemes, the ion heat flux at the pedestal top was much higher than the electron heat flux. For these

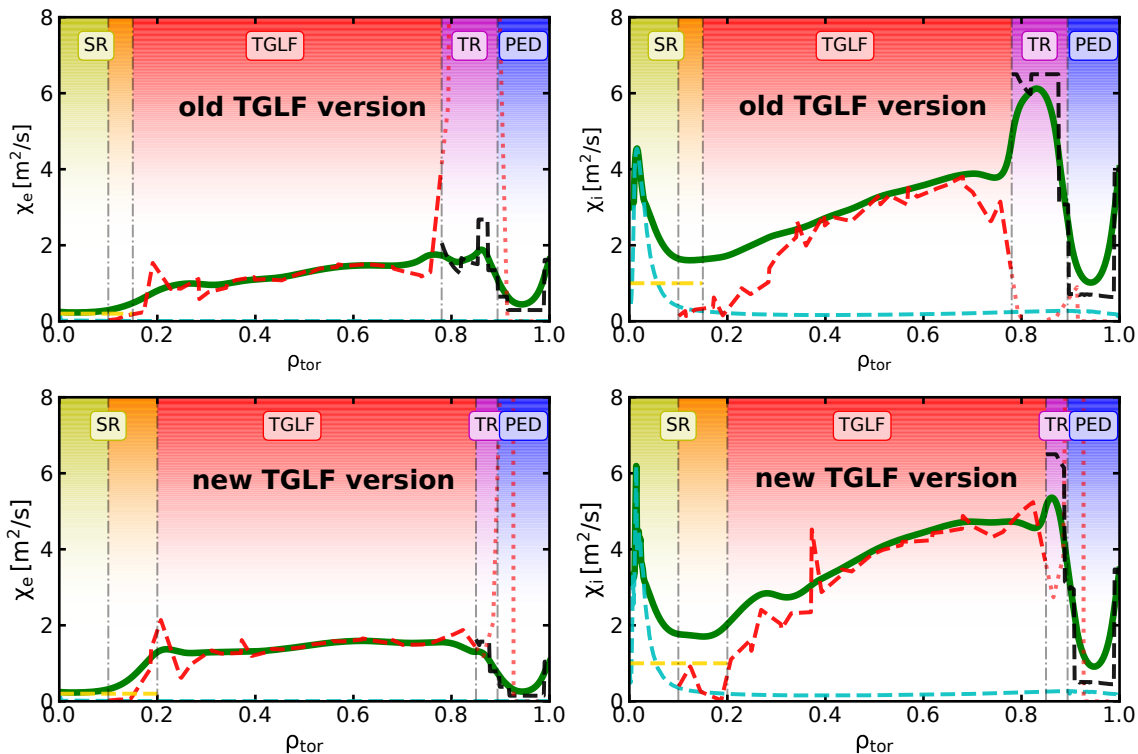


Figure 4.9 – Example of electron and ion heat diffusion coefficients, separated in the components corresponding to the different plasma regions. The figure also illustrates the profiles before (dashed) and after (solid) the smoothing, with an highlight of the components calculated by NCLASS (cyan) and by TGLF (red), and of the component added to account for the transport caused by sawteeth. The lighter dotted red line shows what solution would TGLF give in the edge region. The diffusivities in the upper and lower figures are calculated with the old and the new TGLF versions, respectively.

reasons the coefficients c_1 and c_2 are larger for the ions than for the electrons. For the particle transport we simply assume a fixed diffusion coefficient $D_{n,tr} = 1.5 \text{ m}^2 \text{ s}^{-1}$ to ensure low values of the density gradients, as typical of this transition layer. Finally, we add a fixed term to the diffusion coefficients at the separatrix to ensure continuity with the SOL region, where transport is expected to increase due to the open field lines. This also allows us to obtain more realistic gradients of the kinetic profiles with their peak located around the middle of the pedestal, which otherwise would be placed closer to the separatrix.

The fact that the new TGLF version allows us to set the boundary of its domain of application further outwards, decreases the radial extent of the transition region (TR) between the pedestal and the core (TGLF domain), in which the diffusion coefficients are predetermined in order to get continuously regular profiles from the

4 Description of the Integrated Modeling Workflow

pedestal to the core region (like in the experimental profiles). By this way the extent of the region including ad-hoc diffusivities is reduced, and the theory-based TGLF calculation has more authority on the final prediction of the kinetic profiles.

An important element is the smoothing of the profiles of the transport coefficients, which allows us to obtain smoother and more realistic gradients of the kinetic profiles with respect to the more discontinuous gradients that would result from step-like transport coefficients. This difference is important for the pedestal MHD stability calculation since it uses the profile of the pressure gradients. Figure 4.9 shows an example of the electron and ion heat diffusion coefficients after (solid) and before (dashed) the smoothing, with an highlight of the components calculated by NCLASS (cyan) and by TGLF (red). The yellow dashed line represents the additional transport diffusivity that we use to describe the sawteeth. It also shows the separation between the sawtooth region (yellow), the TGLF computational domain (red), the aforementioned transition region (magenta), and the pedestal region (blue). The orange area highlights the fact that the sawtooth and the TGLF regions overlap.

The ASTRA simulations are performed using a linear radial grid consisting of 601 points. Such a large number of points is necessary to be able to resolve the pedestal with a definition that is large enough to perform a fine scan of the pedestal width, otherwise the final result of the workflow would have a too large uncertainty in the pedestal top pressure and therefore in the stored energy and energy confinement time. The time-step in ASTRA is 2 ms, and TGLF is called every 10 ms, which is a value that finds a good compromise between computational cost and stability of the kinetic profiles due to the aforementioned TGLF oscillations. Every ASTRA simulation requires ~ 2 h of computing time running in parallel on 16 cores on a single CPU. TGLF is run in parallel at 48 radial positions. Such a high number of points is necessary to accurately capture local effects of transport, such as the very localized deposition of the ECRH power. Since we make use of a 16 cores CPU, we can not run all the TGLF calculations in parallel, with the number of serial calls for each core depending on how many radial points need to be computed ($48/16=3$ serial calls). The simulations run for 4 s in the ASTRA real time frame (2000 iterations and 400 TGLF calculations for each of the 48 radial location at which it is called), which we find is a sufficient time to obtain stationary profiles with excellent match between the fluxes and the volume integrals of the sources.

An example of the time evolution of the pedestal quantities in an ASTRA simulation, for a given pedestal width, is illustrated in figure 4.10. The green line represents the value of $\langle \nabla T_e \rangle / T_{e,top}$ calculated by ASTRA, which converges to the target value (0.5, black dashed line). The red line represents the value of $\chi_{e,ped}$ in the middle of the pedestal, scaled by a factor 0.7 for a better rendering of the figure, which acts in feedback to the changes of $\langle \nabla T_e \rangle / T_{e,top}$, and makes it converge to its target. The evolution of the pedestal top electron temperature $T_{e,top}$ and electron density $n_{e,top}$ is illustrated by the blue and orange lines, respectively. As one can see, by the end of the simulation all the pedestal quantities have converged to stationary

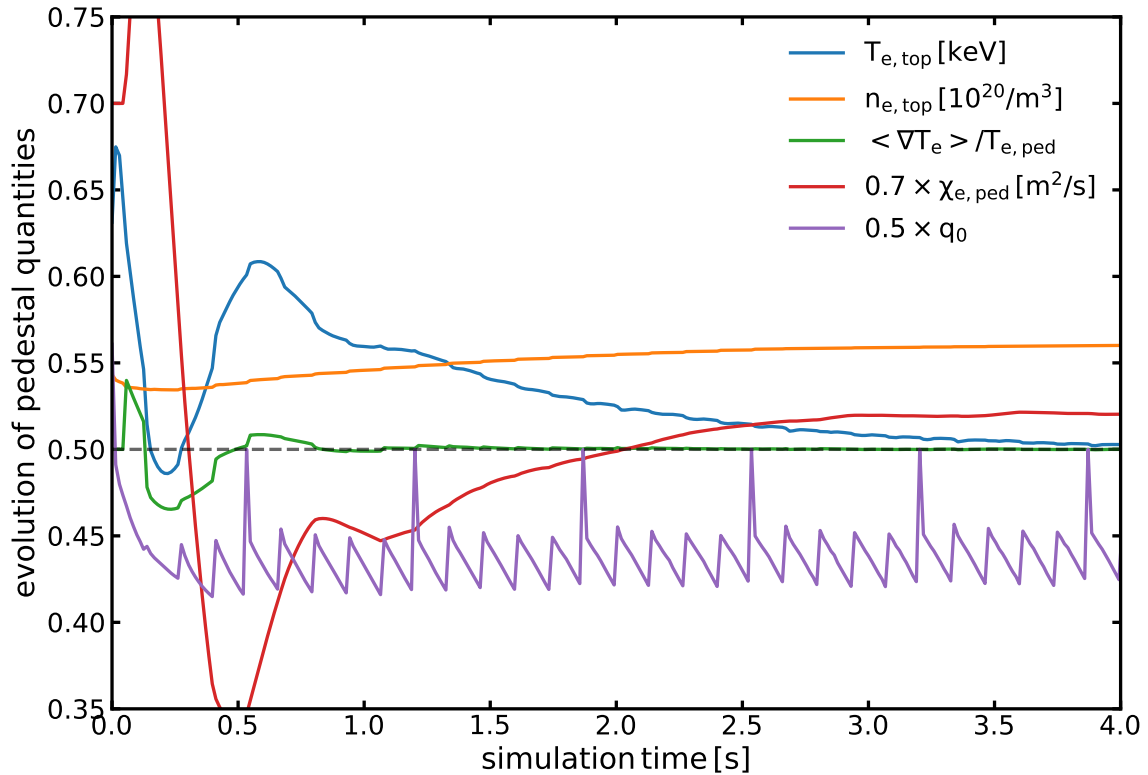


Figure 4.10 – Example of the time evolution of the pedestal quantities in an ASTRA simulation for a given pedestal width. At the end of the simulation the different quantities converge to a stationary state.

conditions. The purple line illustrates the value of the safety factor at the magnetic axis q_0 , scaled by a factor 0.5. It can be observed that the sawteeth (represented by the sudden jumps in q_0) perturb the convergence of the pedestal quantities, causing sudden variations in their values, although this does not have an impact on the final results.

4.3 Pedestal MHD stability

The pressure and current density profiles corresponding to the different values of the pedestal width from the scan are passed to the HELENA high resolution equilibrium solver [142], for a finer calculation of the equilibrium with respect to the faster but lower resolution SPIDER calculation used in ASTRA. The stability of each of these equilibria is tested by using the MISHKA linear MHD stability code for a range of toroidal mode numbers ($1 \leq n \leq 40$). We use the MISHKA-fast variant of the code, which is faster with respect to the standard MISHKA-1 solver [3]. The MISHKA-fast version reduces the computational cost by allowing for a radially varying range of poloidal mode numbers, which can be particularly efficient when analyzing higher toroidal mode numbers. The computing time is usually ~ 0.5 h

4 Description of the Integrated Modeling Workflow

per toroidal mode, running on a single CPU core. All the MISHKA runs, one for every toroidal mode number, are run in parallel. We set a critical growth rate of $\gamma = 0.04\gamma_{Alfven}$ for determining the pedestal stability limit. We select as result of the modeling workflow the point from the scan with the highest pedestal pressure and width that is still PBM stable ($\gamma < 0.04\gamma_{Alfven}$).

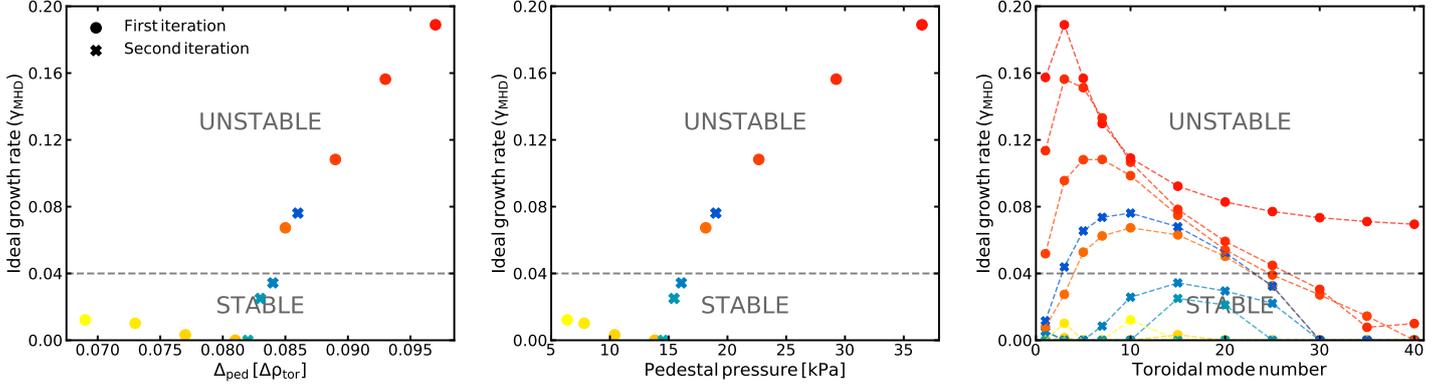


Figure 4.11 – Growth rates of the most unstable modes calculated by MISHKA as a function of the pedestal width (left), of the pedestal pressure (middle), and their spectra as a function of the toroidal mode number (right). Each color corresponds to a certain value of the pedestal width. The different symbols and colors of the points represent the first (circles with warm colors) and second (crosses with cold colors) iterations of the workflow.

Finally, we implemented an automatic solver for the pedestal width, in order to efficiently find the highest stable pedestal width, without the need of running a fine scan on an extended range of pedestal width values. This consists in running first a rougher scan with 8 pedestal width values ($\Delta\rho_{tor} = 0.097, 0.093, 0.089, 0.085, 0.081, 0.077, 0.073, 0.069$), corresponding therefore to 8 different ASTRA simulations. This results in finding a transition point from stable to unstable conditions between two different consecutive pedestal widths. At this point a finer scan in pedestal width is run, launching new ASTRA simulations, with the highest accuracy ($\Delta\rho_{tor} = 0.001$). If 4 consecutive pedestal widths (each with a difference of $\Delta\rho_{tor} = 0.001$ from each other) are found such that the lower ones are both stable and the higher ones are both unstable, the iterative procedure has converged. The highest stable pedestal width is the final one. Otherwise, the procedure continues with a new iteration until this latter condition is satisfied. An example of such procedure is illustrated in Figure 4.11, which depicts the ideal growth rate of the MHD instabilities (γ_{MHD}) and their spectra (for a set of toroidal mode numbers) as a function of the pedestal width (in $\Delta\rho_{tor}$) and pressure. The circles (red) represent the first iteration, which finds a transition from stable to unstable, with a quite large gap in pedestal pressure (from ~ 14 kPa to ~ 18 kPa). This gap is filled by the second iteration, represented by

the crosses (blue), which finds 3 more stable pedestal widths, reducing the gap and finding a pedestal width right below the stability limit ($\gamma = 0.04\gamma_{Alfven}$). Figure 4.11 (right) shows how the most unstable toroidal mode number decreases in value with increasing pedestal width (and pressure). This procedure has proven to be robust when applied on the database of the 50 cases presented in this work, allowing us to efficiently run the whole modeling workflow making the most out of the computing resources available and without requiring human intervention.

If the highest stable pedestal pressure is found within the second iteration of the pedestal width solver, the whole workflow requires ~ 6 h to simulate the plasma profiles corresponding to a time point of a discharge. This is achieved by running in parallel all the different ASTRA simulations, corresponding to different values of the pedestal width, on different nodes (CPUs) of the computing cluster, where every ASTRA simulation requires 16 cores of a node. Once the ASTRA calculations for a certain iteration of the pedestal width solver are finished, all the MISHKA calculations are run simultaneously, where not only the calculations corresponding to different pedestal widths are run in parallel, but a further parallelization is performed over the toroidal mode numbers. This is possible thanks to the large number of computing resources available at the TOK cluster of the Max-Planck-Institute for Plasmaphysics (https://wiki.mpcdf.mpg.de/ipphpc/index.php?title=TOK_batch_cluster_in_Garching&oldid=279), located in Garching (Germany).

4.4 Assumptions

Table 4.1 summarizes all the assumptions introduced into the model. The numerical values listed in the first column are kept constant for all of the simulations performed on the experimental cases considered in this work. The second column describes how the different assumptions were determined, that is, if they are theory based, empirical (derived from regressions on experimental data), or heuristic (assumptions for which we do not have enough constraints, so they were determined trying to reproduce the experiments, while still being compatible with the theory of the underlying physics). The empirical and heuristic elements contained in the model have to be tested and generalized to extend the applicability to different experimental conditions. The third column contains the information on the validity of the assumptions, that is if they are expected to be valid also for other machines or if they are AUG specific (in the configuration with the DivIII divertor), if they are valid only for some particular type of operation (e.g. with deuterium, for attached divertor conditions), or if their validity needs to be investigated. The parameters for which we expect the strongest machine dependency are the parameters related to the divertor and SOL, since the materials and the geometry of the wall and the divertor can change significantly between different machines. These are in particular the scaling of the divertor neutral pressure p_0 , and the coefficients related to the source of neutrals ($f_R, c_{div,wall}, A_{eff}$). For the p_0 scaling a new derivation of the scaling for the tokamak of interest would be needed, and in lack of experimental information, synthetic data from simulations

4 Description of the Integrated Modeling Workflow

assumption	determination	general/machine specific
$T_{e,sep}$ (eq. 5 from [9])	theoretical	general
$n_{e,sep}$ (eq. 8 from [9])	theoretical	attached divertor conditions
$T_{i,sep} = 2T_{e,sep}$	heuristic	to be studied
$\gamma = 6, \alpha = 3.3^\circ, Z_{eff,div} = 1.3$	typical parameters	AUG DivIII specific
p_0 (eq. 4.1)	empirical	AUG DivIII specific
$f_R = 0.8$	heuristic	metallic wall specific
$c_{div,wall} = 0.168$	heuristic	AUG DivIII specific
$A_{eff} = A_{LCFS}/3$	heuristic	to be studied
$\alpha_{wall,sep}$ (eq. 4.5)	theoretical	deuterium specific
$T_0 = 5 \text{ eV}$	heuristic	general
$\langle \nabla T_e \rangle / T_{e,top} = -0.5 [\text{cm}^{-1}]$	empirical	general
$\Delta T_e = \Delta T_i = \Delta n_e$	heuristic	general
$\chi_{i,ped} = \chi_{e,ped} + \chi_{i,neo}$	heuristic	general/to be tested
$D_{n,ped} = c_{D/\chi} \chi_{e,ped} + D_{n,neo}$	heuristic	general/to be tested
$c_{D/\chi,ped} = 0.06$	heuristic	general/to be tested
$v_{n,ped} = -0.05 \text{ m s}^{-1}$	heuristic	general/to be tested
$\chi_{e,sr} = 0.2 \text{ m}^2/\text{s}$	heuristic	general/to be tested
$\chi_{i,sr} = 1 \text{ m}^2/\text{s}$	heuristic	general/to be tested
$D_{n,sr} = 0.5 \text{ m}^2/\text{s}$	heuristic	general/to be tested
$P_{rad} = 0.25(P_{net} - 2) [\text{MW}]$	empirical	to be studied
$v_{tor,top}$ (from [8])	theoretical	general
$\chi_\phi = \chi_{i,turb}$	heuristic	general/to be tested

Table 4.1 – The first column summarizes the assumptions taken into the model. The second column contains the information on how the assumptions were determined. The third column describes the validity of the assumptions.

could be used. This approach could also be applied to future devices. Also the recycling fraction coefficient f_R depends on the material of the wall of the machine, and is expected to be smaller for carbon walled devices. All the other parameters are either derived from theoretical expressions, or are known parameters of the machine.

We performed a sensitivity study on one experimental case to test how a certain variation of the parameters listed in table 4.1 affects the final result of the model. A critical assumption in the model is $\langle \nabla T_e \rangle / T_{e,top} = -0.5 [\text{cm}^{-1}]$, which is derived from experimental data, and can therefore contain uncertainties. The deviation in the database used to obtain $\langle \nabla T_e \rangle / T_{e,top} = -0.5 [\text{cm}^{-1}]$ is around 10%. With a change of 10% ($\langle \nabla T_e \rangle / T_{e,top} = -0.5 \pm 0.05 [\text{cm}^{-1}]$) the change in the plasma thermal energy was $\Delta W_{th} = 3.5\%$, so we conclude that such uncertainties do not have an important impact on the final result of the model. We also tested the effect of a variation of 10% on $T_{e,sep}$, $T_{i,sep}$, $n_{e,sep}$, $n_{0,sep}$, $v_{tor,top}$, $\chi_{i,ped}$, $c_{D/\chi,ped}$, $v_{n,ped}$, P_{rad} , Z_{eff} . The resulting change in the plasma thermal energy was always lower than $\Delta W_{th} < 3.5\%$ for all of these parameters. This small sensitivity on the assumptions

is due to the fact that the pedestal stability calculation is very robust. Small changes caused by variations in the parameters of the model do not cause a significant change in the predicted pedestal top pressure, and consequent small difference in the profiles in the pedestal layer do not significantly affect the core profiles and therefore the stored energy. External actuators, or the inputs of the model (e.g. the heating power) produce much larger changes in the pedestal structure (top pressure and gradients), and result therefore in a substantially different pedestal and global confinement.

It is unfortunately not possible at present to make a quantitative assessment on the sensitivity of each parameter of the model, since the scan in pedestal width is not fine enough to capture changes in pedestal pressure, and therefore in thermal energy, of only a few points percent ($\Delta W_{th} < 3.5\%$). The resolution in the pedestal width scan is limited by the number of radial grid points in ASTRA (601), which currently is not possible to increase due to a memory limitation. By extending the memory usage of the code, it will be possible to give accurate information about how sensitive the results are to each of the assumptions. However, this analysis confirms that the results are not very sensitive to variations in the parameters of the model, otherwise the effect would be evident even with the current resolution in the pedestal width scan.

5 First model validation on main confinement time dependencies, current, power, and density

Summary

5.1	Introduction	96
5.2	Experimental results considered for the first application of the model	97
5.3	Results from the first application of the model	98
5.3.1	Fuelling scan	102
5.3.2	Power scan at high fueling	106
5.3.3	Power scan at fixed line averaged density	109
5.3.4	Current scan	114

5.1 Introduction

As a first step in the assessment of the capabilities of the present integrated model to reproduce the experimental observations, the main dependencies of the scaling law of the confinement time have been considered. According to the IPB98(y,2) scaling law [29] and considering that the dependence on plasma size cannot be tested on a single device, the main parameter dependencies that can be investigated in a single device are current, power and density. For this initial test, also presented in Ref. [139], a first essential version of the model has been used, containing the physics ingredients that can be considered necessary to reproduce those dependencies. In particular, this first version of the model was not yet including the modeling of the toroidal rotation, which was instead taken from the experimental measurements to calculate the $\mathbf{E} \times \mathbf{B}$ shear, required by TGLF. This strategy in the model development and validation follows the logic that any further extension of the modeling workflow (e.g. including also the modeling of rotation) would have not been justified in the event that these dominant dependencies were not correctly reproduced. In this event, some of the essential physics ingredients of the model would have had to be revised. Also, for the experimental cases considered in this first application of the model, the rotation was found to have a negligible impact on the other transport channels, as we have verified by comparing results with measured rotation profiles and assumed flat rotation profiles. This result is consistent with

5.2 Experimental results considered for the first application of the model

usual AUG operation at relatively high density [141]. The results presented in this chapter have been obtained with the previous version of TGLF (TGLF SAT1, before the more recent release in February 2020), as already discussed in section 4.2.4, which led to inaccuracies in the estimation of the turbulent transport fluxes at the proximity of the pedestal top region, and required to set the TGLF boundary more internally (at $\rho_{tor} = 0.78$). Another difference was the estimation of the radiated power, which was calculated by assuming a radially constant tungsten concentration $c_W = 2 \times 10^{-5}$ (arbitrarily chosen), which, for this reduced set of experimental cases, resulted in values of the radiated power in the confined plasma comparable to the ones obtained from the measurements. Furthermore, the pedestal particle diffusion coefficient $D_{n,ped} = c_{D/\chi} \chi_{e,ped} + D_{n,neo}$ was calculated with a different coefficient $c_{D/\chi} = 0.03$ (instead of $c_{D/\chi} = 0.06$), and with the ion neoclassical particle diffusivity $D_{n,neo}$ instead of the electron neoclassical particle diffusivity. This approximated description has been revised later, for the more extended validation of the model which is presented in the chapter 6. However, we found that, for the experimental cases considered in this chapter, this difference has an almost negligible impact on the final results, since the two different combinations of these parameters ($c_{D/\chi}$ and $D_{n,neo}$) result in similar values of the particle diffusion coefficient in the pedestal region $D_{n,ped}$. Finally, this version of the modeling workflow was not yet adopting the pedestal width solver presented in section 4.3. A wide and fine scan in pedestal width was executed by running ~ 30 ASTRA simulations in parallel to accurately resolve the pedestal pressure in a single iteration. Such large number of simulations was still acceptable for the limited number of experimental cases considered in this first application.

5.2 Experimental results considered for the first application of the model

For this first test of the modeling framework we selected 10 different stationary phases from a total of 4 different AUG discharges, in order to have a reasonably wide range of parameter variations. Table 5.1 gives an overview of the main plasma parameters for the discharges taken into consideration. In this database the magnetic field is constant $B_t = -2.5$ T. We have selected a variation in plasma current $I_p = 0.6 - 1$ MA, heating power $P_{heat} = 4.5 - 13$ MW, and fueling rate $\Gamma_D = 0.15 - 2 \times 10^{22}$ e/s, resulting in a variation of the line averaged density $\bar{n}_e = 4.8 - 7.7 \times 10^{19} \text{m}^{-3}$. All these experimental cases have similar plasma shape, with a relatively low plasma triangularity, typical of AUG. In these discharges on-axis ECRH was regularly applied to avoid tungsten accumulation [143]. The values for the effective charge Z_{eff} are calculated using the Integrated Data Analysis (IDA) [123]. This selection allows us to test the model on the variation of parameters which are included in the IPB98(y,2) scaling law (heating power, and plasma current), with in addition the possibility of investigating whether the model can capture the effect of fueling on confinement in direct comparison with

shot	time [s]	B_t [T]	I_p [A]	P_{NBI} [MW]	P_{ECRH} [MW]	q_{95}	\bar{n}_e [$10^{19}/\text{m}^3$]	Γ_D [10^{22}e/s]	Z_{eff}	color
34153	2.0	2.5	0.6	10	1.77	7.1	4.8	0.46	1.80	■
33173	2.7	2.5	1	10	2.00	4.0	6.3	0.46	1.45	■
33173	3.7	2.5	1	10	2.00	4.0	7.0	1.00	1.35	■
33173	4.7	2.5	1	10	2.00	4.0	7.6	1.88	1.30	■
32201	2.9	2.5	1	5	1.35	4.0	7.3	0.96	1.15	■
32201	3.7	2.5	1	5	1.35	4.0	7.7	1.90	1.15	■
32201	4.9	2.5	1	7.5	1.35	4.0	7.7	1.90	1.15	■
32201	5.7	2.5	1	7.5	1.35	4.0	7.3	0.96	1.15	■
33616	5.2	2.5	0.8	5	1.16	5.2	6.1	0.35	1.12	■
33616	7.2	2.5	0.8	2.5	1.63	5.2	6.1	0.15	1.12	■

Table 5.1 – Summary of the experimental cases considered. The columns contain the shot number, the central time of the considered time-window, the toroidal magnetic field, the plasma current, the NBI power, the edge safety factor, the line averaged density, the deuterium fueling rate, the effective charge, and the color code used for identification in the figures. The first two lines correspond to the two cases representing a scan in plasma current. Lines 2 to 4 represent a fueling scan. Lines 3, 5, and 8 represent a power scan at constant fueling, as also lines 4, 6, and 7 but at a higher fueling level. Lines 9 and 10 represent another power scan, at lower plasma current and with fixed line averaged density instead of fixed fueling rate.

the dependence on density contained by the scaling law. We decided to include a fueling rate scan, instead of a scan directly on the line averaged density, since the model requires the fueling rate as input, while the plasma density is given as output. The main confinement time dependencies of the IPB98(y,2) scaling law (\bar{n}_e , P_{heat} , and I_p) translate therefore in the corresponding inputs of the model Γ_D , P_{heat} , and I_p , for which dedicated experimental scans have been analyzed in this chapter.

5.3 Results from the first application of the model

Figure 5.1 shows a comparison of the measured thermal energy with the prediction of the model (colored squares), and IPB98(y,2) (gray diamonds). The experimental thermal stored energies have been calculated as the average between the values obtained using different techniques. These are: the integral of the experimental kinetic profiles obtained in the stationary phase before an ELM crash, and $W_{MHD} - W_{\text{fast}}$, where W_{MHD} is the plasma energy obtained from the equilibrium reconstruction and W_{fast} is the energy of the fast ions. The error-bars represent the maximum and minimum values obtained using the different techniques, and include the uncertainty on the calculation of the fast ions energy, and the one given by the ELMs filtering.

5.3 Results from the first application of the model

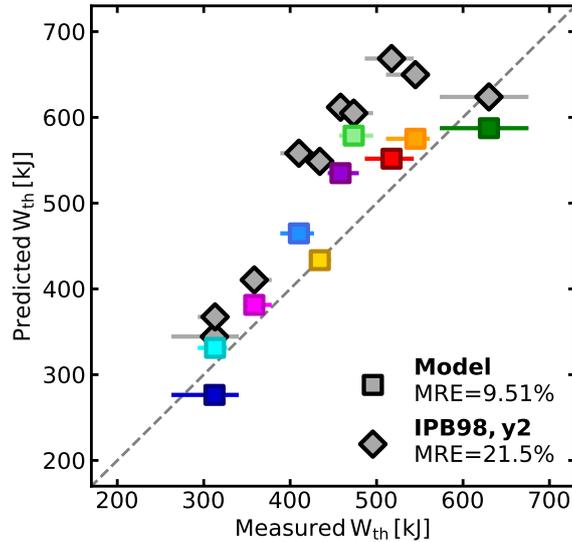


Figure 5.1 – Comparison of the measured thermal energy with the prediction of the model (colored squares), and IPB98(y,2) (gray diamonds). The different colors of the squares refer to the different entries in table 5.1.

In the experimental cases considered in this work the time averaged plasma energy content calculated over multiple ELMs cycles differs from that just before the ELMs crash by less than 2%. This difference is negligible with respect to the error-bars of the measurements and with respect to the differences among the various predictions. It is therefore acceptable to compare the time averaged thermal energy predicted by the IPB98(y,2) with the thermal energy just before the ELM onset predicted by the model and calculated from experimental data.

The core and pedestal experimental thermal energies are calculated as integrals of the pressure profile. Specifically, the pedestal stored energy $W_{th,ped}$ is the energy in the entire plasma volume, with pressure constantly equal to the pedestal top pressure from the pedestal top inward. The core stored energy $W_{th,core}$ is the total stored energy minus the pedestal energy $W_{th,core} = W_{th,tot} - W_{th,ped}$. The pressure profile is constructed by fitting the experimental measurements of the electron and ion temperatures, and of the electron density. The fits are obtained using the AUGPED tool, as described in section 2.3.3, which combines together the data acquired from several diagnostics, presented in section 2.2. In particular we used the two Thomson scattering systems (one for the core and one for the edge of the plasma) and the electron cyclotron emission (ECE) system for the electron temperature, the two Thomson scattering systems, the lithium beam emission spectroscopy (LiBES) diagnostic, and the deuterium-cyanide-nitrogen (DCN) laser interferometer for the electron density, and the charge exchange recombination spectroscopy (CXRS) systems for the ion temperature. The edge Thomson scattering data is used to fit

5 First model validation on main confinement time dependencies, current, power, and density

both electron temperature and density, together with the ECE and lithium beam data, so the profiles in every time window are automatically aligned to each other, as described in section 2.3.3. The electron temperature and density are shifted together such that the separatrix electron temperature is ~ 100 eV, as typical of AUG [79]. The profiles are fitted using a modified hyperbolic tangent for the temperatures, and the 2-line fit [121] for the density. We found the 2-line fitting tool to be more robust for evaluating the pedestal top density, while the modified hyperbolic tangent can sometimes underestimate it due to the usually large scatter of the experimental data in this region of the plasma.

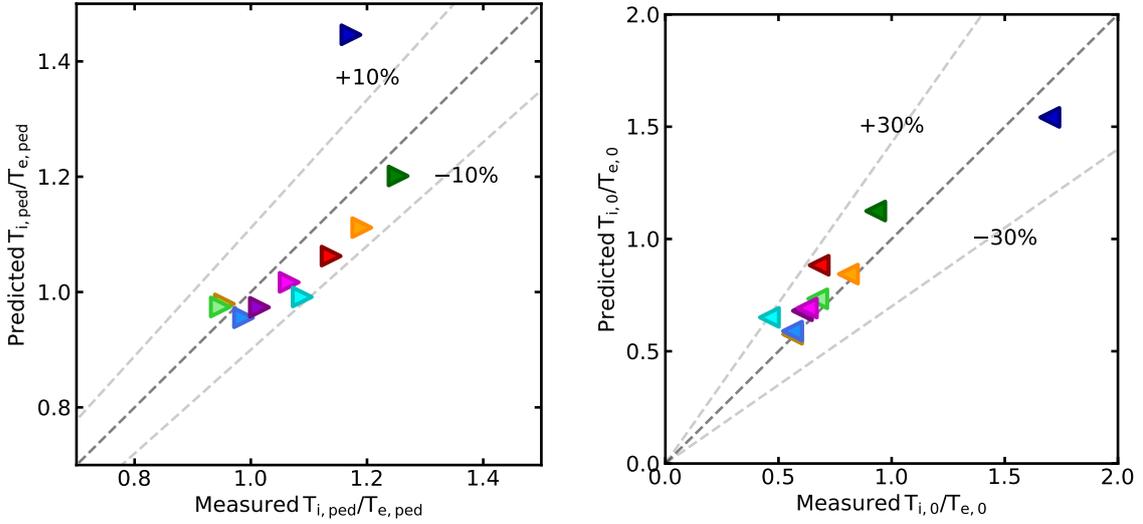


Figure 5.2 – Comparison between the predicted and measured values of T_i/T_e at the pedestal top (left) and at the center of the plasma, at $\rho_{tor} = 0.1$ (right). The different colors of the symbols refer to the different entries in table 5.1.

The mean relative error for the model $MRE = 9.51\%$ suggests that the prediction is accurate in reproducing the change in energy confinement caused by the different parameters of plasma operation, and is more accurate with respect to the IPB98(y,2) scaling law $MRE = 21.5\%$. We underline that no boundary condition is taken from the measurements of the kinetic profiles in the ASTRA simulations, thereby to large extent we can consider that the two approaches use a similar set of input parameters, with the exception of Z_{eff} , which is required by our model, but does not play an important role and can also be easily guessed through simple scalings. Some of the engineering parameters (heating power and plasma current) are well correlated to plasma confinement, and therefore a statistical regression (i.e. a scaling law) can robustly describe these dependencies. However, this kind of approach is limited by the fact that some other engineering parameters (e.g. the fueling rate) do not exhibit a direct correlation with confinement, and it is therefore very difficult to

5.3 Results from the first application of the model

include the effect of such hidden parameters into a multivariate regression. This implies that the predictions of scaling laws become less reliable when there is a strong variation in this kind of parameters, as in this case for the IPB98(y,2) where the main reason for the large MRE is the relatively large values of the fueling rate. Our model instead captures the dependence of confinement on the engineering parameters by giving a description of the physics that regulates these effects, by combining theoretical models and empirical elements. This allows us to capture the dependencies on operational parameters beyond the capabilities of scaling laws, as long as the description of their behaviors is included in the model. As a result the model is more accurate than the IPB98(y,2) for these cases, and more in general we can expect that it will also be more precise for a larger number of cases if the theoretical models and the empirical elements adopted are reliable and general enough to cover the new regions of the parameters space in which they are applied.

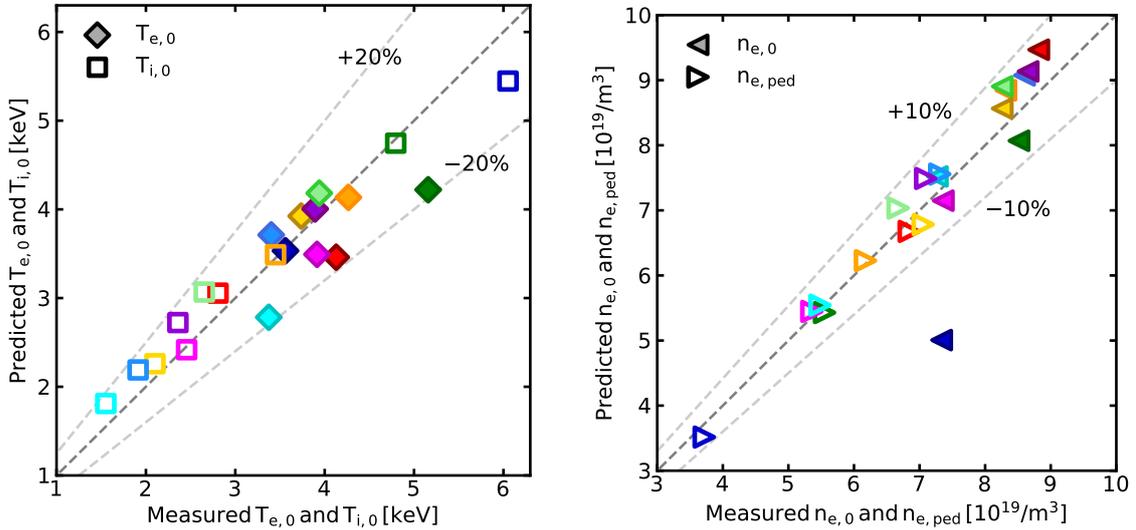


Figure 5.3 – Comparison between the predicted and measured values of T_i (empty squares) and T_e (full diamonds) at the center of the plasma, at $\rho_{tor} = 0.1$ (left), and (right) of n_e at the pedestal top (empty triangles) and n_e at the center of the plasma (full triangles). The different colors of the symbols refer to the different entries in table 5.1.

Figure 5.2 shows a comparison between the predicted and measured values of T_i/T_e at the pedestal top (left) and at the center of the plasma, at $\rho_{tor} = 0.1$ (right). This radial location has been chosen instead of $\rho_{tor} = 0$ since at the magnetic axis some of the experimental measurements are missing and fitted profiles result from extrapolations. We recall that the ion temperature at the separatrix is assumed to be the double of the separatrix electron temperature $T_{i,sep} = 2T_{e,sep}$, and that the pedestal ion heat diffusivity is assumed to be equal to that of the electrons summed with the ion neoclassical diffusivity $\chi_{i,ped} = \chi_{e,ped} + \chi_{i,neo}$. The model can

5 First model validation on main confinement time dependencies, current, power, and density

well reproduce the values of T_i/T_e at the pedestal top. This is an important result, and is an improvement over the EPED model, which assumes $T_{e,ped} = T_{i,ped}$. As described in 5.3.4, $T_{e,ped}$ is underestimated for the case at $I_p = 0.6$ MA (blue), and therefore it exhibits a larger error respect to the other cases. Also the values of T_i/T_e at the center of the plasma are well reproduced by the model.

Figure 5.3 shows a comparison between the predicted and measured values of T_i (empty squares) and T_e (full diamonds) at the center of the plasma, at $\rho_{tor} = 0.1$ (left), and (right) of n_e at the pedestal top (empty triangles) and n_e at the center of the plasma (full triangles). An important aspect is that the model can correctly predict the pedestal top electron density. This is another improvement over the EPED model, which lacks the capability of predicting the pedestal top electron density, as this must be given as input.

5.3.1 Fuelling scan

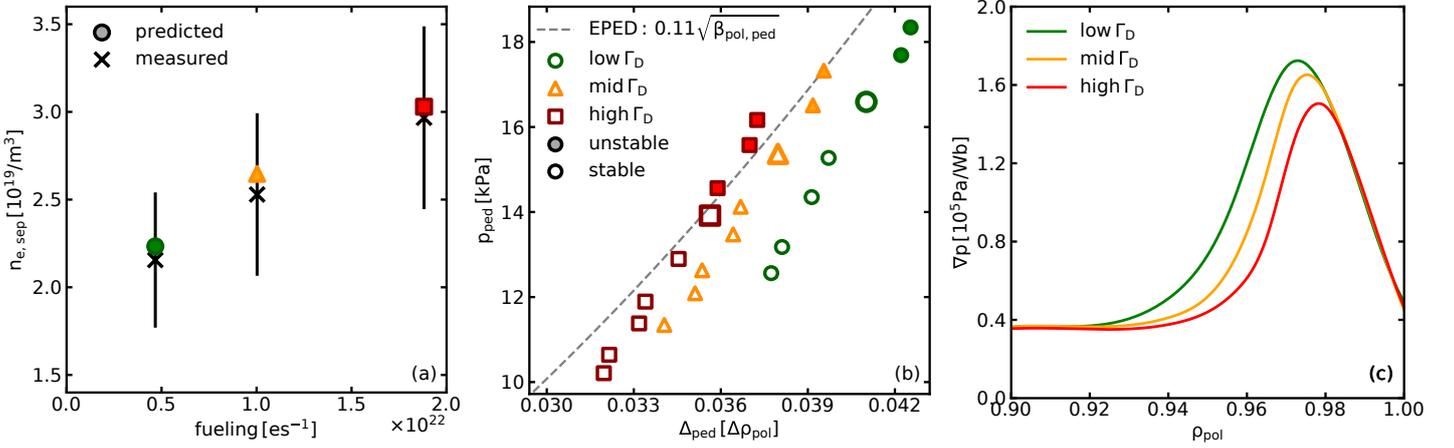


Figure 5.4 – a) Predicted (filled symbols) and measured (crosses) separatrix electron density as a function of the fueling rate. b) ASTRA pedestal width scan for the 3 fueling rate levels. The empty symbols correspond to PB stable pedestal conditions as predicted by the MISHKA MHD stability calculation, while the filled symbols correspond to unstable conditions (i.e. ELM onset). The dashed line represents the solution that would be provided by the EPED transport constraint, assuming a fixed value, typical of AUG, of the proportionality term between $\Delta\psi_N$ and $\sqrt{\beta_{p,ped}}$. c) Pressure gradients profiles corresponding to the highest stable pedestal pressure.

Among these cases, we focus on the stationary phases of the AUG discharge #33173, a gas puff scan at $B_t = -2.5$ T, $I_p = 1$ MA, $P_{heat} = 13$ MW. We selected an experimental case with a fueling rate scan, instead of a scan directly on the line averaged density, since the plasma density is an output of the integrated model. The

5.3 Results from the first application of the model

fueling rate is an input of the model, as it is an external actuator of a tokamak, which allows the control of the line averaged density of the plasma. The main confinement time dependencies of the scaling laws analyzed in this chapter \bar{n}_e , P_{heat} , and I_p translate therefore in the corresponding inputs of the model Γ_D , P_{heat} , and I_p . A scan in the fueling rate is particularly interesting because it features the typical confinement degradation with increasing gas puff, observed in AUG, JET-ILW and TCV [63–65]. This effect is clearly not captured by the IPB98(y,2) scaling law, which predicts a clear increase of confinement time with increasing density at the rate $\bar{n}_e^{0.41}$. The reduction in pedestal and global confinement has been related to an outward shift of the density profile, which appears together with an increased value of the separatrix density [63]. The negative impact of an increase of the separatrix density was already realized in early confinement studies at AUG [144]. Figure 5.4 (a) shows that the predicted separatrix density is in excellent agreement with the measurements, evaluated with the IDA technique, and the effect of fueling is well captured. In AUG experiments it has been observed that the separatrix density is strongly related to the divertor neutral pressure [127], which increases with increasing fueling rate. The SOL model we included in ASTRA allows us to describe how an increase in the fueling rate causes an increase in the divertor neutral pressure (eq. 4.1) and ultimately how an increase in the divertor neutral pressure causes an increase in the separatrix density (eq. 3.32, eq. 8 from [9]). Figure 5.4 (b) shows the scans in pedestal width, where the filled symbols correspond to PBM unstable conditions, while the open ones represent stable conditions. The larger open symbols identify the highest stable pedestal pressure, which correspond to the final result of the model for the pedestal prediction. As one can see the predicted pedestal pressure decreases with increasing fueling rate (Γ_D). One can also see that the same pedestal pressure among the 3 different cases (low, medium, and high fueling) corresponds to different values of pedestal widths, and therefore the same pedestal width among the 3 different cases corresponds to different values of pedestal pressure. This is because, in the ASTRA prediction of the kinetic profiles, when the fueling rate is increased, the separatrix density and then the whole pedestal density profile increase. For the same value of the pedestal width, the electron temperature at the pedestal top is similar among the 3 different cases due to the constraint $\langle \nabla T_e \rangle / T_{e,ped} = -0.5 [\text{cm}^{-1}]$, while the pedestal top density is higher with higher fueling. Therefore, for the same value of the pedestal width, the pedestal top pressure is higher with higher fueling, or, for the same value of the pedestal pressure, the pedestal width is smaller with higher fueling. Since the peak of the pressure gradient is located approximately in the middle of the pedestal width, this moves outwards with higher fueling. Because the ballooning stability is sensitive to the location of this peak (the closer to the separatrix the more it is unstable), the higher fueling case will be limited to a lower value of the pressure gradient, because of the lower ballooning stability limit. This is illustrated in figure 5.4 (c), which shows the pressure gradient profiles of the highest stable pedestals for the 3 different cases.

As depicted by the gray dashed line in figure 5.4 (b), with the transport assumption of the EPED1 [7] model, assuming a fixed value (0.11, typical of AUG) of the proportionality term between $\Delta\psi_N$ and $\sqrt{\beta_{p,ped}}$, the three cases would have the same pedestal pressure at the same pedestal width, being all aligned on the same line. This would mean that the peak of the pressure gradients would be located at a similar position, obtaining a similar ballooning stability limit. The change of the value of the pedestal top density alone would not cause a large change in the predicted pedestal pressure. The EPED model would therefore predict a similar value of the pedestal pressure for the 3 different fueling levels. One should note that this figure does not provide any information on what would be the pedestal pressure predicted by EPED for these cases, it only illustrates the dependence of the pedestal pressure on the width for the two different transport constraints ($\Delta\psi_N = 0.11\sqrt{\beta_{p,ped}}$ and the one resulting from $\langle \nabla T_e \rangle / T_{e,ped} = -0.5 [\text{cm}^{-1}]$).

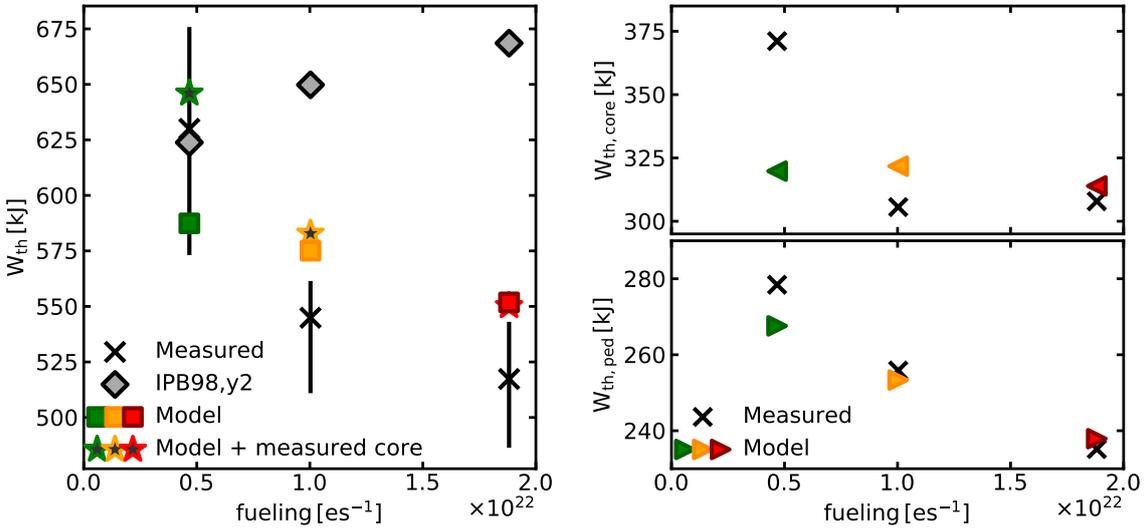


Figure 5.5 – Thermal energy predicted by the model (colored squares), by the IPB98(y,2) (gray diamonds), and measured (black crosses) as a function of fueling rate (left). The colored stars with black filling show the thermal energies obtained by combining the predicted pedestal profiles with the experimental core profiles. Experimental and predicted thermal energy separated in the pedestal and core components (right).

Figure 5.5 shows the thermal energy predicted by the model (colored squares), compared to the measurements (black crosses) for the three different cases. We also show the experimental and predicted thermal energy separated in the pedestal and core components, from which we can see that for the lowest fueling case (in green) there is a large disagreement between the predicted and the measured core thermal energy. This is because for this case TGLF overestimates the electron heat transport, as depicted in figure 5.6 where it can be seen that the predicted electron temperature (solid line) is lower than the experimental measurements (dots). The

5.3 Results from the first application of the model

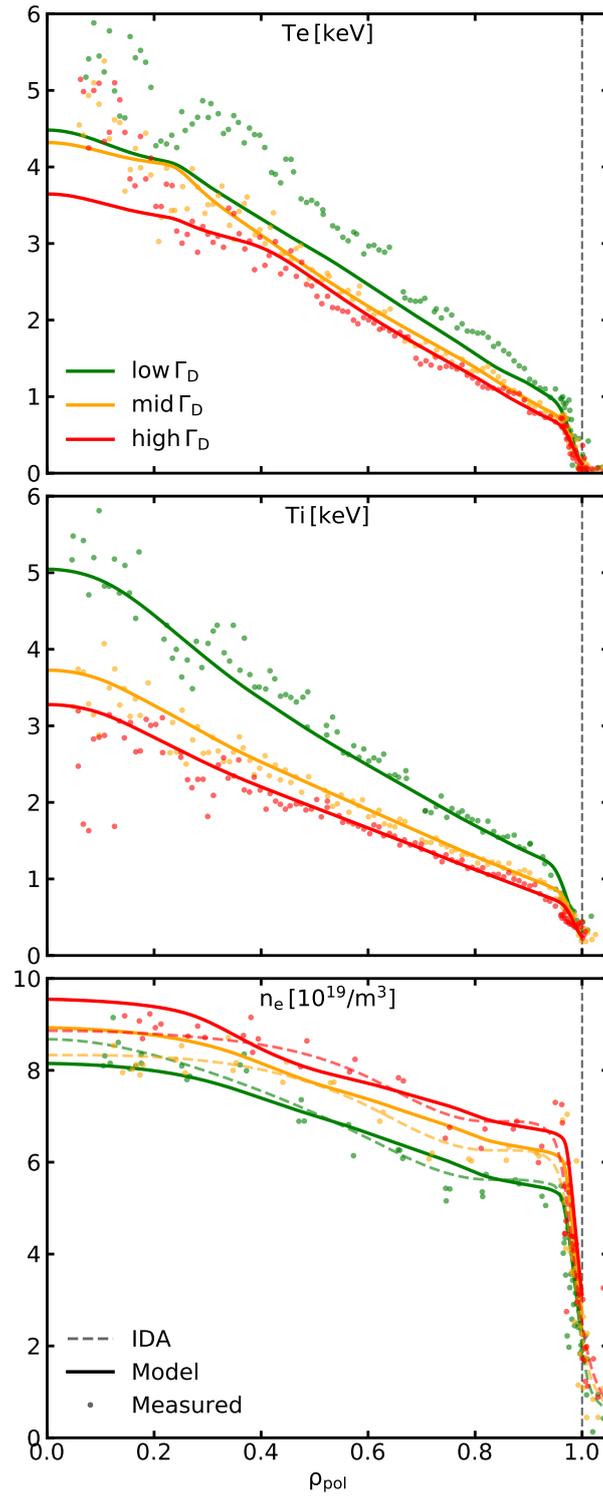


Figure 5.6 – Experimental measurements (dots), and predicted profiles (lines) of electron and ion temperature, and electron density for the different fueling rates. The dashed lines show the electron density profile obtained with the Integrated Data Analysis (IDA).

colored stars with black filling show the thermal energies obtained by combining the predicted pedestal profiles with the experimental core profiles, which are in good agreement with the measurements. This highlights the accurate prediction of the pedestal. The IPB98(y,2) scaling law (gray diamonds) fails to capture this effect, and in contrast to the experimental trend, predicts an increasing stored energy with increasing fueling, as a consequence of the positive dependence of the confinement time on the line averaged density in IPB98(y,2).

5.3.2 Power scan at high fueling

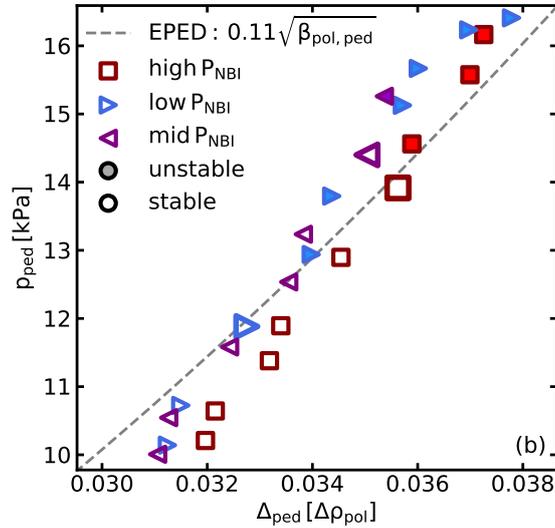


Figure 5.7 – ASTRA pedestal width scan for the 3 time windows corresponding to a heating power scan. The empty symbols correspond to PB stable pedestal conditions as predicted by the MISHKA MHD stability calculation, while the filled symbols correspond to unstable conditions (i.e. ELM onset). The dashed line represents the solution that would be provided by the EPED transport constraint, assuming a fixed value, typical of AUG, of the proportionality term between Δ_{ψ_N} and $\sqrt{\beta_{p,ped}}$.

Combining different stationary phases from discharges #33173 and #32201 we obtain two power scans at two different fueling levels. Figure 5.7 shows the pedestal width scans for the three different levels of NBI power at the highest fueling rate (#33173 at 4.7s, #32201 at 3.7s and at 4.9s). As one can see the curves corresponding to the three different power levels do not exhibit a large offset like in the fueling scan case (i.e. the three cases have dependencies which are aligned), since the fueling rate is constant and therefore there is no evident shift of the density profile.

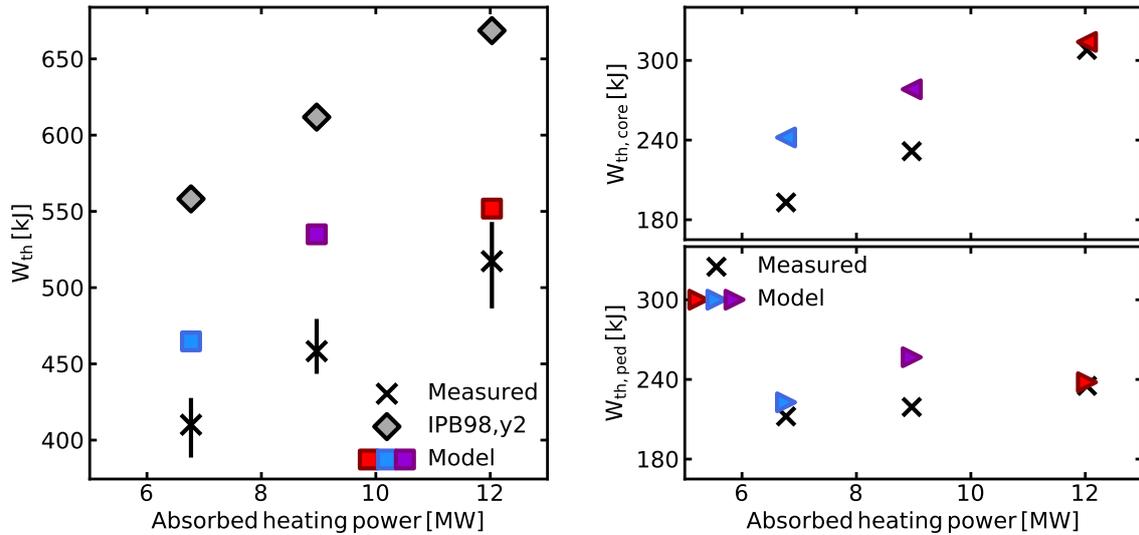


Figure 5.8 – Thermal energy predicted by the model (squares), by the IPB98(y,2) (diamonds), and measured (black crosses) as a function of the heating power (left). Experimental and predicted thermal energy separated in the pedestal and core components (right).

Figure 5.8 shows that the predicted pedestal pressure is in good agreement with the measurements, except for the case corresponding to the medium power level, for which the pedestal pressure is overpredicted. The core pressure is overpredicted by TGLF for the two cases with the lowest power levels. Overall, the dependence of heating power on the total thermal energy is well captured, and the prediction of the model is more accurate with respect to the one of the IPB98(y,2), although the trend is better predicted by the scaling law. Interestingly the different levels of heating power have a much stronger effect on the core stored energy than on the pedestal. The results are similar also for the other power scan at lower fueling rate. Figure 5.8 shows a good agreement for the individual core and pedestal contributions to the stored energy at the highest heating power (right), while a small difference can be noticed in the total thermal stored energy (left). This is because the core and pedestal components are calculated using the fits of the experimental T_e , n_e , and T_i measurements, while the total thermal energy is calculated as the mean of two values: the fitted profiles and the stored energy from the equilibrium reconstruction. The error-bar represents the difference between these two values, and in this case the stored energy obtained from the fits corresponds to the top of the error-bar.

The kinetic profiles are shown in figure 5.9, where it can be seen that the predicted density profiles match the experimental ones, reproducing well the peaking. The electron and ion temperatures are slightly overpredicted for the lower heating power cases, with their gradients starting to deviate from the experimental ones at around $\rho_{pol} \sim 0.8$, the transport short-fall region of the previous TGLF version. A large electron heat flux is predicted by TGLF at the highest heating power in the region

5 First model validation on main confinement time dependencies, current, power, and density

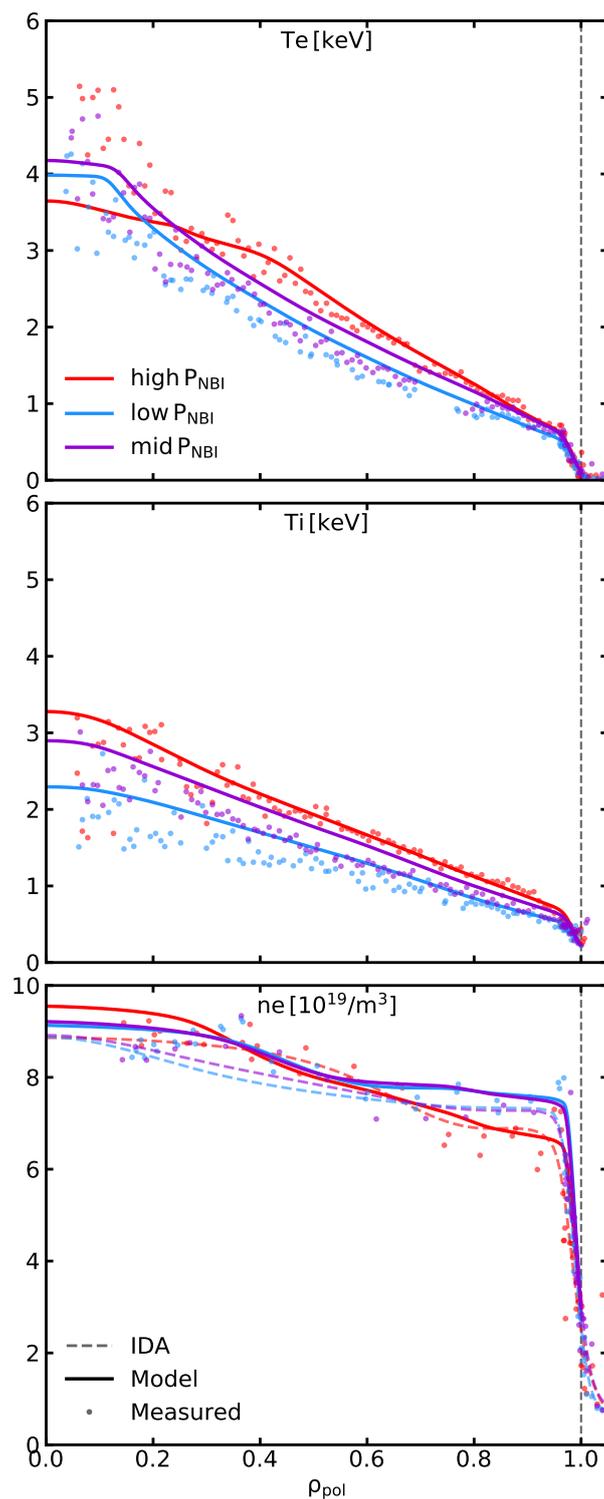


Figure 5.9 – Experimental measurements (dots), and predicted profiles (lines) of electron and ion temperature, and electron density for the different levels of heating power. The dashed lines show the electron density profile obtained with the Integrated Data Analysis (IDA).

within $\rho_{pol} \sim 0.4$, causing a slight underprediction of the central electron temperature.

5.3.3 Power scan at fixed line averaged density

Another heating power scan is provided by the two stationary phases of the discharge #33616. In this case we scan the heating power while keeping all the other parameters of the IPB98(y,2) scaling law fixed, in facts in this discharge the line averaged density is constant, achieved using gas puff as feedback. Another difference with respect to the previously discussed cases is in the plasma current $I_p = 0.8$ MA. The two different time windows analyzed have different heating power levels, the first with ~ 6.5 MW (5 MW NBI + 1.16 MW ECRH), and the second with ~ 4.5 MW (2.5 MW NBI + 1.63 MW ECRH). This discharge has a relatively low ELM frequency and very good quality measurements, which allows us to perform an accurate comparison between the predicted and the measured kinetic profiles in the pedestal.

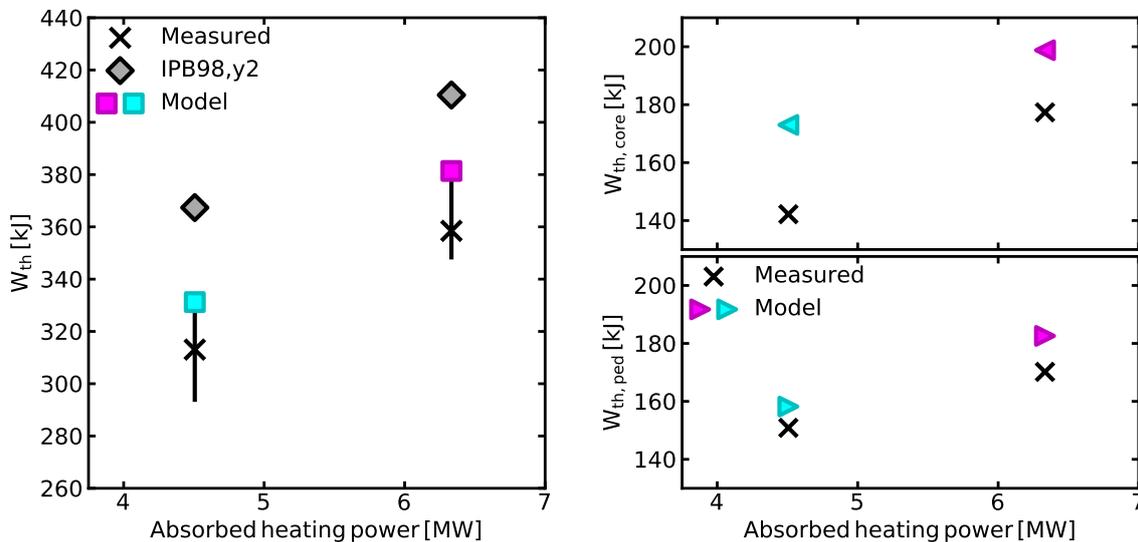


Figure 5.10 – Thermal energy predicted by the model (squares), by the IPB98(y,2) (diamonds), and measured (black crosses) as a function of the heating power (also the fueling rate is slightly changed, while the line averaged density is constant) (left). Experimental and predicted thermal energy separated in the pedestal and core components (right).

The thermal energy predicted for these cases is shown in figure 5.10. The prediction of the model is in very good agreement with the measurements, and surprisingly is more accurate with respect to the IPB98(y,2), since the scaling law is usually very robust for such low levels of fueling (in this case required to obtain the requested line averaged density). The mismatch between the predictions and the measurements is mostly associated to the core, again due to underestimated heat transport by TGLF in the region around $\rho_{pol} \sim 0.8$, as it can be noticed by looking at the temperature

profiles in figure 5.11, while the pedestal is accurately predicted. The change in stored energy with different heating powers is well captured.

An interesting aspect highlighted by this case is the role of particle transport and sources in determining the pedestal density profile. Since the core density peaking is practically identical in the two different time windows, the constant line averaged density results in a constant density at the pedestal top. The required fueling rate in the time window with the lowest heating power level is extremely low $\Gamma_D \sim 0.15[10^{22}e/s]$, so most of the particle source is given by recycling. In the time window with higher heating power the fueling rate is larger by more than 100% to satisfy the requirements on the density, meaning that the pedestal particle transport has increased. The separatrix density has also increased due to the higher divertor neutral pressure (caused by higher fueling and NBI power), so the decay of the neutral density in the SOL is stronger, but we found that this effect is not strong enough to explain alone the higher fueling requirement: with the same value of pedestal particle diffusion coefficient for the 2 different cases, the change in the source of neutrals is not large enough to reproduce the change in the pedestal density gradient.

Figure 5.12 shows how the pedestal electron heat diffusivity $\chi_{e,ped}$ increases with increased heating power, causing an increase in the particle diffusion coefficient (we recall that $D_{n,ped} = c_{D/\chi}\chi_{e,ped} + D_{n,neo}$), and therefore causing a reduction in the pedestal density gradient. The relative increase of total heating power produced by an increase of the NBI heating is significantly larger than the corresponding relative increase of the total particle flux in the pedestal, which is dominated by the neutrals coming from the wall.

The elements included in the model, that describe all these effects, especially the pedestal particle transport that we find to increase with increasing heating power, can predict with excellent agreement the pedestal density profile. In particular we find that the pedestal density gradient decreases with increasing heating power, due to higher pedestal transport, and this is also observed from the measurements and described by the model for the power scan case at fixed fueling rate, as can be seen in figure 5.13.

Figure 5.14 shows the ratio between the electron density at the pedestal top and at the separatrix $n_{e,top}/n_{e,sep}$, which is a proxy for the pedestal logarithmic density gradient, for the three power scans at the different fueling levels (color bar). As one can see, the prediction of the model (diamonds) reproduces the trend of the measurements (crosses), and most importantly one can see that with constant fueling rate the increasing heating power causes a reduction in the pedestal logarithmic density gradient. We associate this to an increase of the pedestal particle transport, caused by the increased heating power. This is also in line with Ref. [33, 145, 146], where it is observed that $n_{e,top}$ has a negative dependence on NBI power, and is a step forward with respect to the work on the integrated model in Ref. [54] where it is reported that a limitation of the neutral penetration model used to predict the pedestal density is the fact that it could not capture the power dependence on the

5.3 Results from the first application of the model

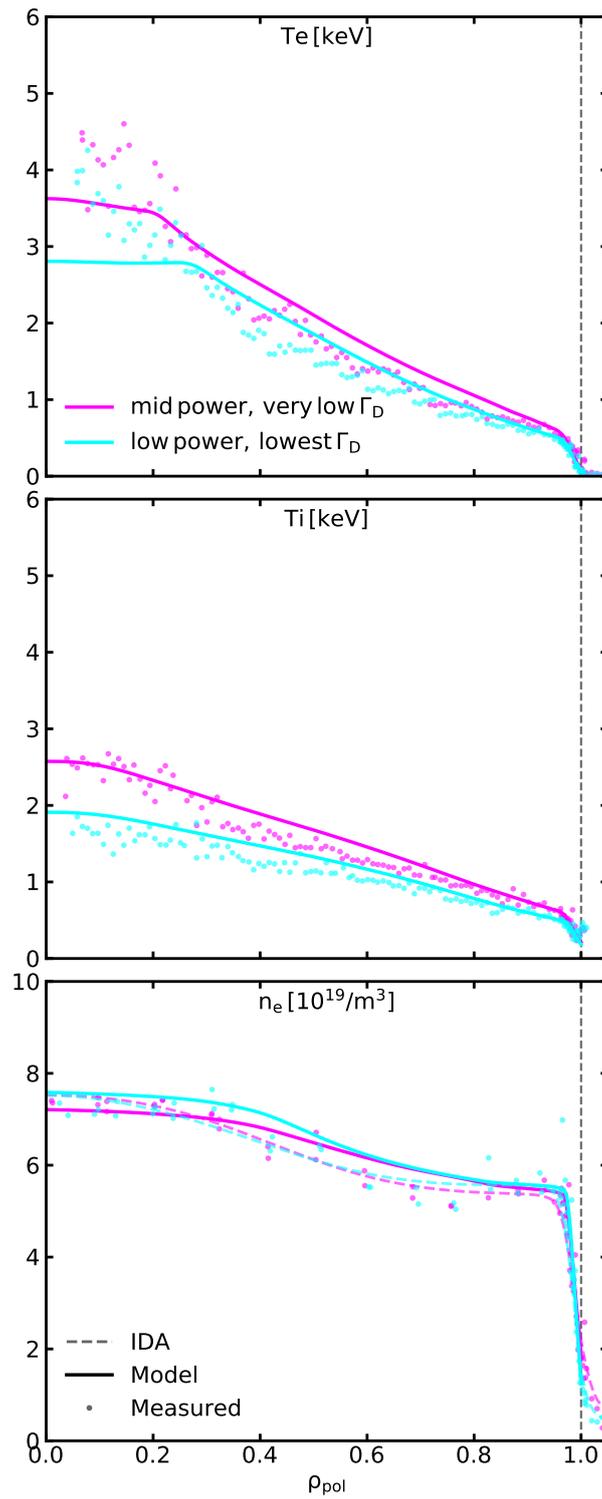


Figure 5.11 – Experimental measurements (dots), and predicted profiles (lines) of electron and ion temperature, and electron density for the different levels of heating power and fueling rate. The dashed lines show the electron density profile obtained with the Integrated Data Analysis (IDA).

5 First model validation on main confinement time dependencies, current, power, and density

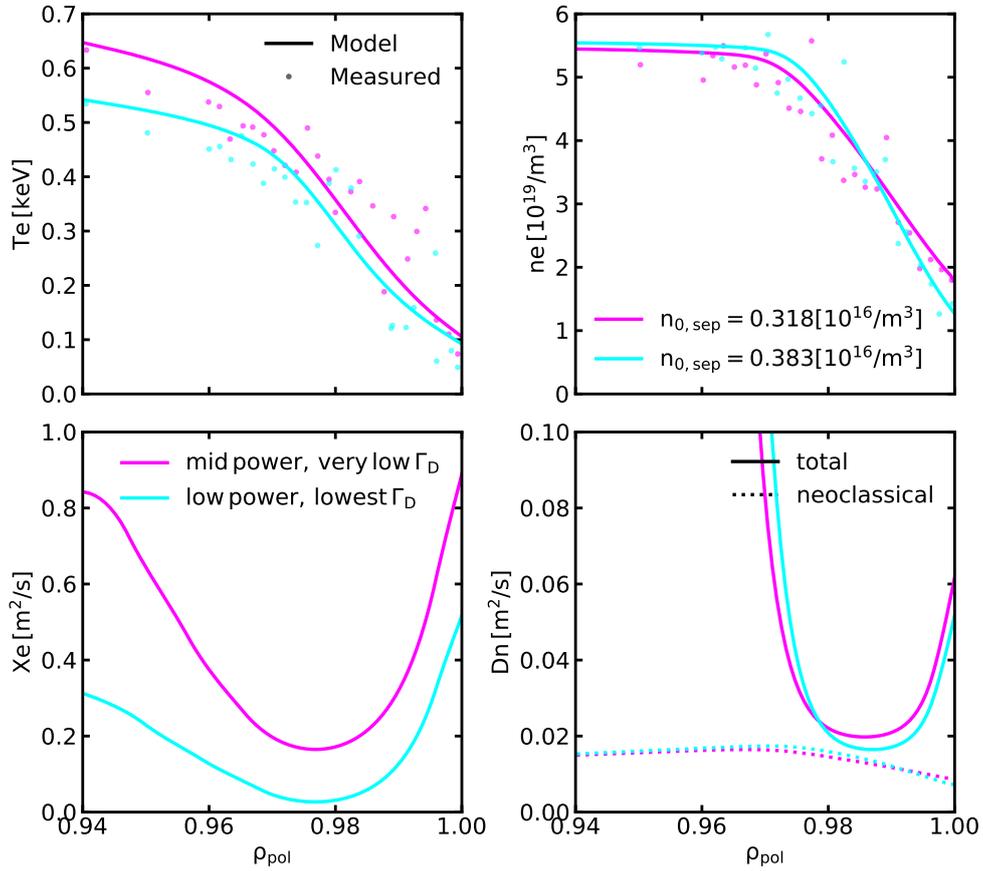


Figure 5.12 – Predicted profiles (solid lines) of the pedestal electron heat diffusivity (lower left), and particle diffusivity (lower right) with its neoclassical component (dashed) for the different levels of heating power and fueling rate, and resulting electron temperature (upper left) and density (upper right) profiles. The measurements are represented by the dots. The label in the upper right figure shows the values of the neutral density at the separatrix for the two cases.

5.3 Results from the first application of the model

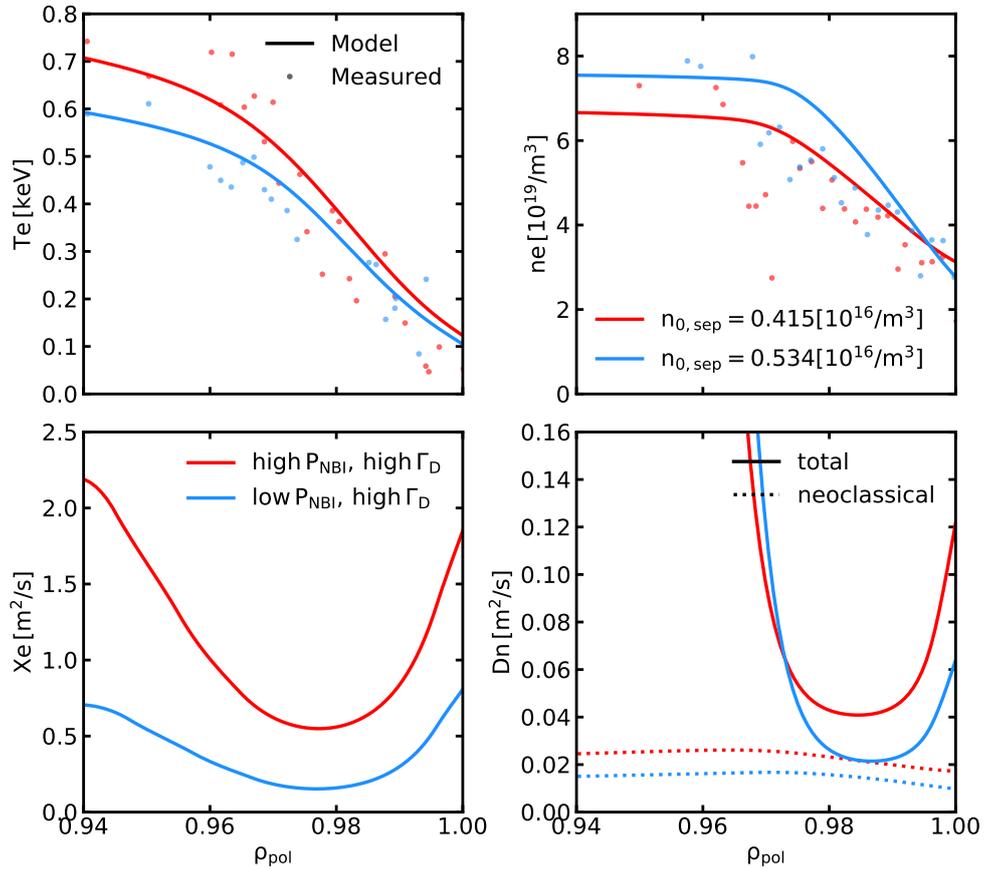


Figure 5.13 – Predicted profiles (solid lines) of the pedestal electron heat diffusivity (lower left), and particle diffusivity (lower right) with its neoclassical component (dashed) for the different levels of heating power, and resulting electron temperature (upper left) and density (upper right) profiles. The measurements are represented by the dots. The label in the upper right figure shows the values of the neutral density at the separatrix for the two cases.

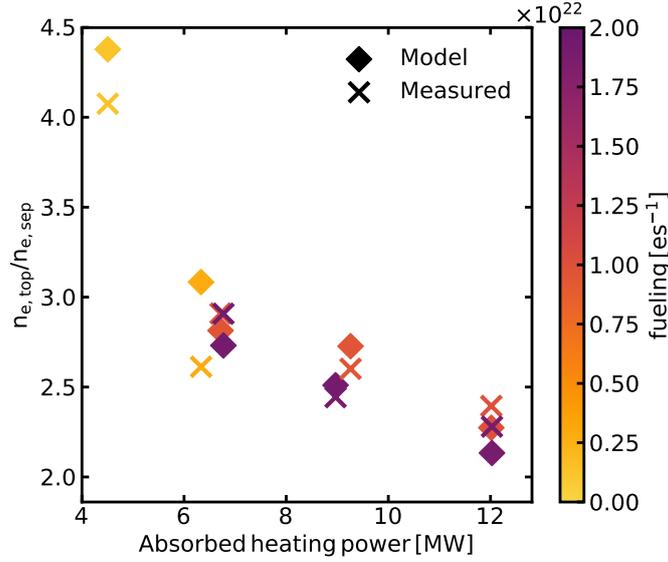


Figure 5.14 – Dependence of the ratio between the pedestal top density and the separatrix density on the heating power, for different levels of fueling.

pedestal density due to missing transport physics.

5.3.4 Current scan

Combining the discharge #34153 with the stationary phase at lowest fueling rate from discharge #33173 we obtain a scan in plasma current $I_p = 0.6 - 1$ MA keeping constant all the remaining parameters, with constant low fueling rate instead of constant line averaged density. The density changes from $\bar{n}_e = 4.8 \times 10^{19} \text{m}^{-3}$ to $\bar{n}_e = 6.3 \times 10^{19} \text{m}^{-3}$ by increasing the plasma current.

In figure 5.15 we can see that the change in the thermal energy caused by the different values of I_p is well captured by the model, and the accuracy of its prediction is comparable to that of the IPB98(y,2). The case at $I_p = 1$ MA has been already discussed in the fueling scan section. The predicted pedestal for the case at $I_p = 0.6$ MA has a slightly lower top pressure with respect to the measurements, probably due to the fact that TGLF predicts a very large electron heat flux at the pedestal top ($\rho_{tor} \sim 0.78$), affecting also the electron heat transport coefficients in the inner part of the pedestal, and resulting in a lower pedestal top electron temperature, as can be seen in figure 5.16. It is also interesting to notice that the increase of the density with I_p is well captured. The model can reproduce this experimental feature because the value of $\chi_{e,ped}$, resulting from imposing $\langle \nabla T_e \rangle / T_{e,ped} = -0.5 [\text{cm}^{-1}]$, decreases with increasing I_p , causing a reduction in $D_{n,ped}$, and therefore causing an increase in the pedestal density gradient. The increase in pedestal pressure, produced by the increase in I_p , is related to a change in the PBM stability, which is described by the MISHKA MHD code, and is therefore well captured by the model.

5.3 Results from the first application of the model

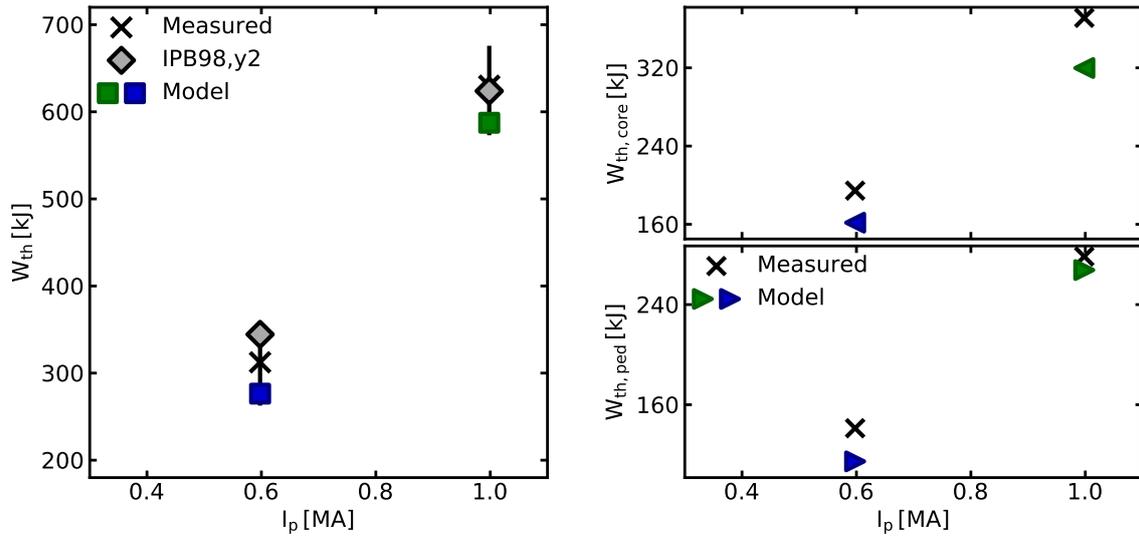


Figure 5.15 – Thermal energy predicted by the model (squares), by the IPB98(y,2) (diamonds), and measured (black crosses) as a function of the plasma current (left). Experimental and predicted thermal energy separated in the pedestal and core components (right).

Overall, the TGLF prediction describes well the core kinetic profiles for this case, although in the inner part of the plasma the density gradient is underestimated.

Another scan in plasma current is presented in section 6.4.4, where instead of keeping fixed the fueling rate, two discharges with a similar line averaged density are selected. This allows to compare how the effect of the plasma current is reproduced by the model and by the IPB98(y,2), where all its remaining input parameters are kept constant.

5 First model validation on main confinement time dependencies, current, power, and density

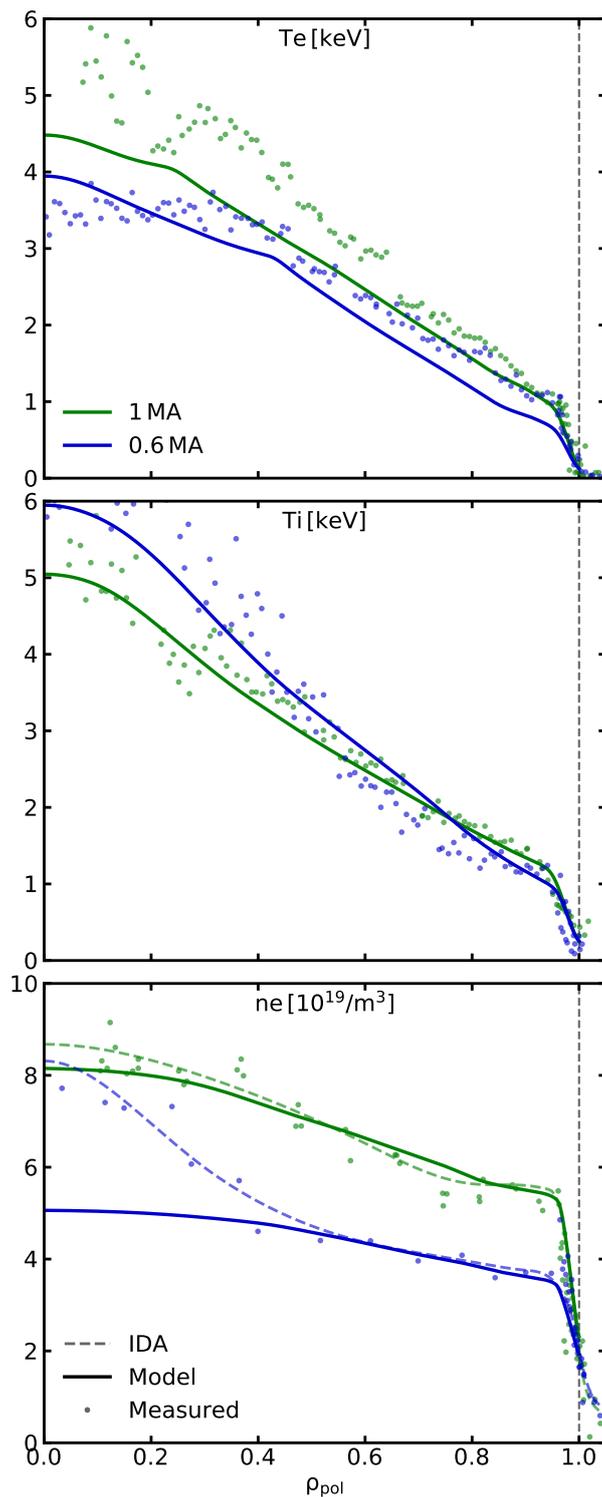


Figure 5.16 – Experimental measurements (dots), and predicted profiles (lines) of electron and ion temperature, and electron density for the different levels of the plasma current. The dashed lines show the electron density profile obtained with the Integrated Data Analysis (IDA).

6 Extensive validation of the model

Summary

6.1	Introduction	117
6.2	Experimental results considered for the extended validation of the model	118
6.3	Results from model application	119
6.3.1	Comparison with recent scaling laws	123
6.3.2	Accuracy of kinetic profiles prediction	125
6.4	Analysis of specific dependencies	128
6.4.1	Triangularity scan	128
6.4.2	Magnetic field scan	130
6.4.3	NBI voltage scan	135
6.4.4	Current scan at similar line averaged density	140

6.1 Introduction

The first test of the integrated model established its reliability to capture some fundamental dependencies of plasma confinement, specifically, that on the current, heating power, and fueling rate, and therefore on the density. The positive outcome of this first validation suggested that no major ingredient of the model required a significant revision. Therefore, it has been possible to concentrate on a small refinement of the physics description included into the model, and an improvement of the modeling workflow execution in order to automatically run it over a large experimental database in an efficient manner. The version of the model used for this application is the one presented in chapter 4. The main differences with respect to the version used in the first test, presented in chapter 5, consist in the modeling of the toroidal rotation, the more recent version of TGLF, the estimate of the radiated power, and the adoption of the automatic pedestal width solver. Another difference consists in the pedestal particle diffusivity $D_{n,ped} = c_{D/\chi}\chi_{e,ped} + D_{n,neo}$, which is now calculated with the electron neoclassical particle diffusivity $D_{n,neo}$ instead of the ion neoclassical particle diffusivity (which is usually larger in the presence of impurities), and with a different value of the coefficient $c_{D/\chi} = 0.06$ (instead of $c_{D/\chi} = 0.03$). This difference has an almost negligible impact on the final results, but gives a more precise and rigorous description of the electron particle transport in the pedestal region.

The extended validation of the model includes experimental scans of other important engineering parameters that are possible to change on a single device, such as the magnetic field and the plasma triangularity. We also explore the validity of the model on the small ELMs and ITER baseline scenarios as developed at AUG. It is important to understand whether the model can reproduce the experimental behavior of these operational parameters, since they are relevant for future fusion reactors. The application of the integrated model on a large experimental database provides a more complete test of this approach, where the interplay of many different variations in the operational parameters produce effects on confinement which are more subtle than those which are produced by main dependencies included in scaling laws (and therefore harder to reproduce by the model). Therefore, this application allows us to better address the reliability of this approach in correctly describing the coupling between the different plasma regions and their role on defining plasma confinement.

6.2 Experimental results considered for the extended validation of the model

The validation of the modeling workflow has been extended to a database of 50 AUG experimental cases, including the 10 cases from the first test of the model already presented in section 5.2, which have been recomputed with the most complete model, as described in chapter 4, plus 40 new ones, which include: a triangularity scan, a magnetic field scan, a plasma current scan at similar line averaged density, a NBI voltage scan (obtaining the same total heating power but with different particle source), scans in the heating systems (on and off axis heating, ratio of ion to electron heating), ITER baseline scenarios, and small ELMs scenarios. In comparison with the first application, presented in chapter 5, the extended database allows us to test the model on the variation of the magnetic field, which is another important parameter included in the IPB98(y,2) scaling law which is possible to test on a single device such as AUG. The entries in the database have been chosen in order to obtain the largest possible variation in the main engineering parameters, and in order to include some particularly relevant cases. This results in a variation across the database in plasma current $I_p = 0.6 - 1.2$ MA, magnetic field $B_t = 1.5 - 2.85$ T, safety factor $q_{95} = 3 - 8$, heating power $P_{heat} = 2 - 14$ MW, triangularity $\delta = 0.19 - 0.42$, fueling rate $\Gamma_D = 0 - 8 \times 10^{22}$ e/s.

We selected a triangularity scan to address the robustness of the MHD stability calculation, since the change in pedestal pressure with different plasma shapes is caused by a change in the peeling-ballooning stability boundary. These effects have been shown to be captured by linear ideal MHD stability codes [113, 147–149], like MISHKA, so our model should be able to capture this effect. Another important test is provided by the scan in the NBI voltage, which causes a change in plasma parameters in every plasma region: it changes the core particle source

provided by the NBI, causing a change in particle flux crossing the separatrix which affects the amount of recycled neutrals in the SOL, ultimately driving a change in pedestal pressure. This NBI voltage scan provides a stringent test on the consistency among the different components of the integrated model, addressing in particular the reliability of the transport assumptions adopted to describe the pedestal, and their consistency with the MHD stability.

The values for the effective charge Z_{eff} were taken from the Integrated Data Analysis (IDA) [123] when available (if previously calculated), however for most of the cases this was not available so for simplicity we assumed a fixed effective charge equal to $Z_{\text{eff}} = 1.2$ (typical AUG value for H-mode plasmas without seeding of impurities, in the intermediate to high density range). The result of the model is anyway very little sensitive to the effective charge in this range of values relatively close to $Z_{\text{eff}} = 1$.

6.3 Results from model application

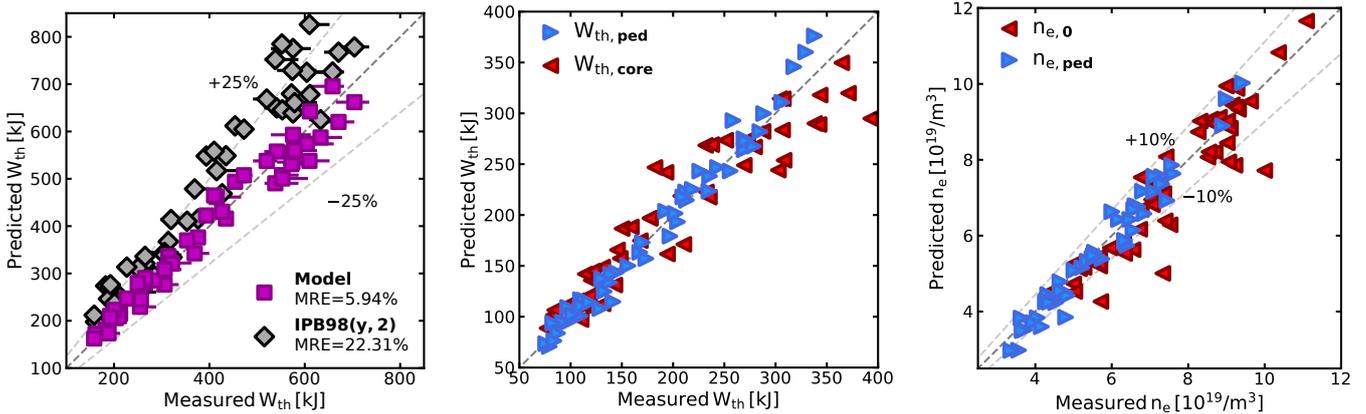


Figure 6.1 – (left) Comparison of the measured thermal energy with the prediction of the model (purple squares), and IPB98(y,2) (gray diamonds). (middle) Comparison between predicted and measured thermal energy separated in the pedestal (blue) and core (red) components. (right) Comparison between the predicted and measured values of n_e at the pedestal top (blue) and n_e at the center of the plasma (red).

Figure 6.1 (a) shows a comparison of the measured thermal energy with the prediction of the model (purple squares), and IPB98(y,2) (gray diamonds). The experimental thermal stored energies have been calculated with the same procedure as described in section 5.3. The mean relative error for the model $MRE = 5.94\%$ suggests that the prediction is accurate in reproducing the change in energy confinement caused by the different parameters of plasma operation, and is considerably

6 Extensive validation of the model

more accurate with respect to the IPB98(y,2) scaling law $MRE = 22.31\%$, which tends to overestimate the thermal energy. We underline that no boundary condition is taken from the measurements of the kinetic profiles in the ASTRA simulations. The model and the scaling law use similar input parameters, with the exception of the density, which is required by the IPB98(y,2), while it is predicted by the model, using the fueling rate as additional information. However, the integrated model makes use of empirical elements, in particular for the description of the pedestal and SOL regions, that could be AUG specific, and that the scaling law can not benefit of.

Figure 6.1 (b) shows a comparison between the predicted and measured values of the thermal energy separated in the pedestal and core components. It is visible that the prediction of the pedestal pressure is very accurate and robust, while the core thermal energy exhibits more scatter. This means that the core energy is the term responsible for the largest portion of the error on the total thermal energy, somewhat reversing the common view that core transport is better predicted than the pedestal pressure. The core thermal energy tends to be overestimated at low energies, and underestimated at high energies. This could be due to an inaccurate stiffness of TGLF, or due to the fact that the high energy points, in the upper right part of the figure (red symbols), correspond to high NBI heating power levels, which then can cause a strong fast ions stabilization of the turbulent transport. The fast ion stabilization can take place through a nonlinear effect [150] that is not captured by TGLF, and has a much stronger effect than the simple dilution. Since our model does not include this effect, it can underestimate confinement for cases with relatively large NBI power.

Figure 6.1 (c) shows a comparison between the predicted and measured values of n_e at the pedestal top (blue triangles) and n_e at the center of the plasma (red triangles), at $\rho_{tor} = 0.1$. We chose this radial location instead of $\rho_{tor} = 0$ since at the magnetic axis some of the experimental measurements are missing and fitted profiles result from extrapolations. The stabilization of turbulence by the fast ions allows the core gradients to reach higher values, and this is usually true also for the electron density. This, together with a possible inaccurate stiffness, could also be a reason why for some cases the central density is underpredicted. An important aspect is that the model can correctly predict the pedestal top electron density. This is an improvement over the EPED model, which lacks the capability of predicting the pedestal top electron density, as this must be given as input.

Figure 6.2 shows again a comparison of the measured thermal energy with the prediction of the model (squares), and IPB98(y,2) (crosses), but with color-maps which show the change in the main plasma parameters across the data set. It is clearly visible that the plasma current is the plasma parameter most strongly correlating with the thermal energy. This is because energy confinement has a strong dependence on this parameter (it scales almost linearly with I_p). The effect of plasma current is well captured by the model and the scaling law. As one can see the points for which the IPB98(y,2) is less accurate correspond to high fueling

6.3 Results from model application

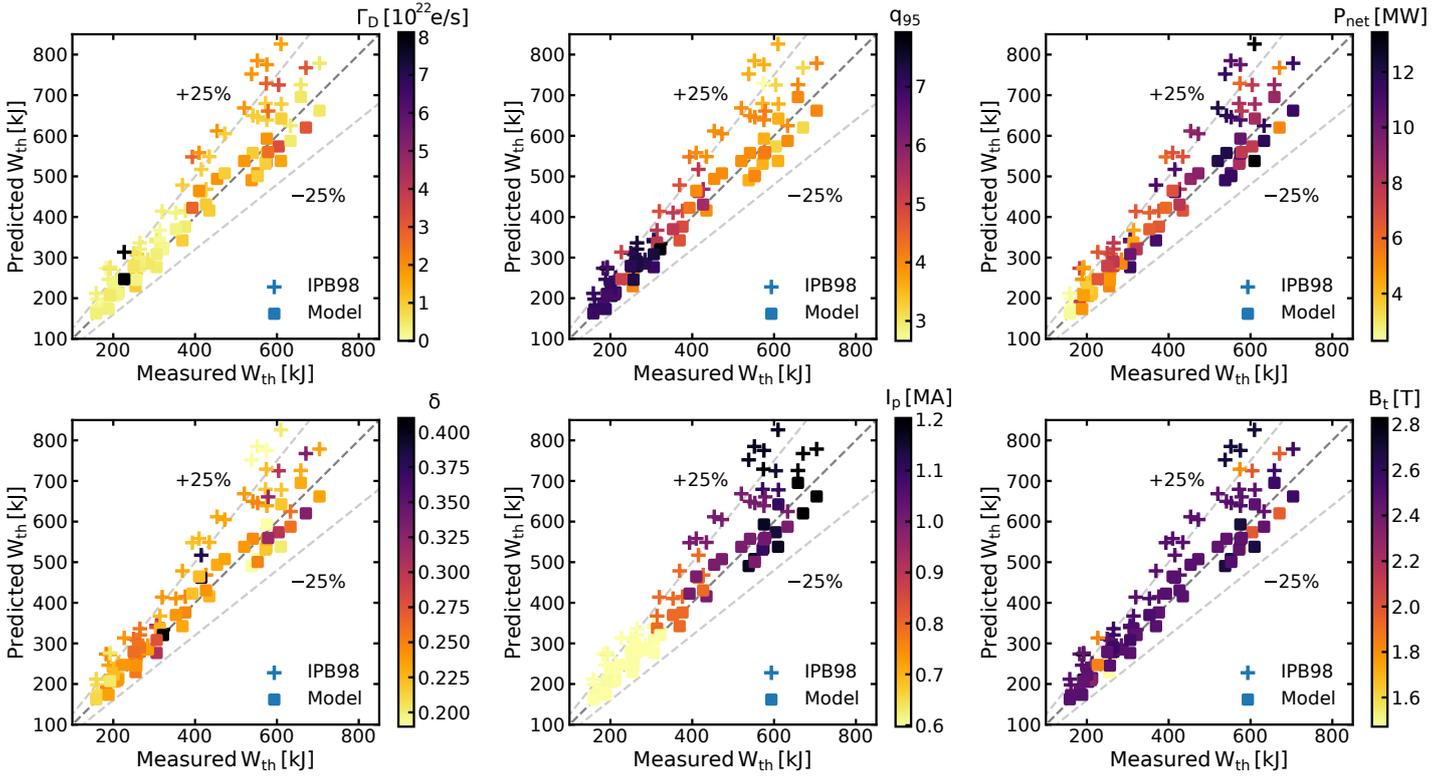


Figure 6.2 – Comparison of the measured thermal energy with the prediction of the model (squares), and IPB98(y,2) (crosses), colored as a function of different plasma parameters.

rate (Γ_D) levels, which can cause strong confinement degradation, and this effect is not captured by the scaling law. Our model is instead capable of capturing this dependence, as described in section 5.3.1. We observed that in our simulations a different fueling rate causes the peeling-ballooning stability boundary to be crossed at different locations (different toroidal mode numbers). The toroidal mode number (n) of the most unstable modes calculated by MISHKA, for the pedestals predicted by the model, becomes larger at higher fueling levels. The transition from PBM stable to unstable conditions is located at high toroidal mode numbers ($n \geq 20$) for high fueling cases ($\Gamma_D \geq 2 \times 10^{22} \text{e/s}$), therefore at the ballooning-dominated (low current and high pressure gradient) part of the stability diagram. The pedestals sitting in this region are limited to a lower pressure, since they are closer to the ballooning limit. At low fueling rate instead the stability boundary is crossed at the 'nose' of the diagram (corresponding to lower toroidal mode numbers), which is a more optimal region, where higher pressures are allowed. This is an indication that the model is correctly capturing the effect of fueling on confinement, which usually causes a reduction in pedestal pressure, and that the transport description is consistent with the MHD stability calculation, well reproducing the physics of this dependence.

6 Extensive validation of the model

It is also visible that most of the points in the database have a value of the magnetic field $B_t = -2.5$ T. This is because the AUG ECRH system is optimized for central heating with such magnetic field value, which is therefore the one used for most of the experiments. It is therefore difficult to obtain a scan in B_t , since this requires different settings of the ECRH system in order to achieve similar profiles of the power deposition at the two different B_t values. Nevertheless, we found and included into the database two similar discharges constituting a scan in B_t , where no ECRH power was used, without being affected by tungsten accumulation problems thanks to the low value of the plasma current.

The prediction of the model is also accurate for the ITER baseline scenarios, meaning that the model is robust also when applied on ITER relevant range of parameters ($q_{95} = 3$). The model has shown to be accurate also when tested on the two small ELMs cases considered, showing that indeed (at least for these cases) a linear ideal MHD stability code like MISHKA is capable of reproducing the correct pedestal pressure for the small ELMs. In our selection we chose a case with a high H_{98} -factor ($H_{98} = \tau_{th}^{exp} / \tau_{th}^{IPB98(y,2)} = 1.05$), with relatively low fueling ($\Gamma_D \sim 0.5 \times 10^{22}$ e/s) and high triangularity ($\delta = 0.4$), and a case with low H_{98} -factor ($H_{98} = 0.8$), with very high fueling ($\Gamma_D \sim 8 \times 10^{22}$ e/s) and low triangularity ($\delta = 0.24$). The model proved to be capable of capturing the effects of these different operating parameters on pedestal (and global) confinement also for the small ELMs. This can be interpreted as a sign that the plasmas in the small ELMs regime considered in this work are not far from the PBM boundary.

Another important experimental case included in this analysis is the stationary phase at 1.9s of the discharge #35681, with $B_t = -2.5$ T, $I_p = 0.6$ MA, $P = 7.5$ MW, $\delta = 0.24$, $\Gamma_D = 0.14 \times 10^{22}$ e/s. This experiment aimed at studying the effect of ELMs on the fast-ion densities at the plasma edge using a new edge FIDA spectrometer installed at AUG [151]. From a modeling perspective it is particularly interesting for two reasons: first, in the experiment tangential NBI sources were used, obtaining a strongly off-axis power deposition, and second, the edge FIDA spectrometer is capable of measuring the intensity of the edge D-alpha line simultaneously with the FIDA radiation, which allows the determination of the background neutrals density. The first point provides a test of the model when using off-axis heating, which can have an impact on core confinement. The second point allows us to compare the model prediction of the neutrals density with the one inferred from the experiment. The discharge has been performed with a large amount of ECRH power ($P_{ECRH} = 2.5$ MW), and strongly off-axis NBI heating ($P_{NBI} = 5$ MW), at relatively low electron density ($\bar{n}_e = 4 \times 10^{19}$ /m³). This results in a high electron to ion temperature ratio ($T_e/T_i \sim 2$) at the center of the plasma, which has a strong impact on core turbulent transport, destabilizing ITG modes [152–155]. As a result, this causes a decrease in core confinement. The IPB98(y,2) scaling law has been created including cases with on-axis heating only without ECRH, and does not include this physics, therefore it does not reproduce such effects on confinement. The relative error is very large for this case $RE_{W_{th,IPB98(y,2)}} \sim 50\%$. Our model

instead can reproduce this effect, as this physics is captured by TGLF, proving to be very accurate also for this case $RE_{W_{th,model}} < 5\%$.

The experimental neutral density has been obtained combining the calculation of the KN1D code [156] and the FIDA measurements, as described in Ref. [151]. This sophisticated procedure yields to an accurate estimate of the density of the neutrals at the separatrix $n_{0,sep,exp} \sim 3.0 \times 10^{15}/\text{m}^3$. The model predicts a value of $n_{0,sep,model} \sim 2.2 \times 10^{15}/\text{m}^3$. Given the simplicity of the model describing the neutrals in the SOL, this result is quite encouraging. This case has a very low fueling rate, meaning that recycling is probably the major component contributing to the neutrals density at the separatrix. By this way we are directly testing the recycled neutrals term included in our model, without the need of disentangling the contributions of two different components (the one coming from recycling and that coming from the fueling valves) on the neutrals density. Even though $n_{0,sep}$ is slightly underpredicted by the model, the relative error on the pedestal top density prediction is absolutely acceptable $RE_{n_{e,top,model}} \sim 10\%$. Overall, these results are providing further confidence on both the core transport modeling and the description of the neutrals in the SOL, although the latter is approximated with quite simple assumptions.

6.3.1 Comparison with recent scaling laws

During the final phase of the development of this PhD thesis, a new scaling law for the prediction of ITER plasma performance has been created, the ITPA20-IL (ITER-like), which is presented in a publication to be soon submitted [157].

$$\tau_{th}^{ITPA20-IL} = 0.067 \times I_p^{1.29} B_T^{-0.13} P^{-0.644} n_e^{0.15} M^{0.30} R^{1.19} (1 + \delta)^{0.56} \kappa_a^{0.67} \quad (6.1)$$

The new ITPA20-IL scaling law has been obtained from the ITER-like subset of the updated ITPA global H-mode confinement database, including plasma triangularity as variable, and ignoring the dependence on the aspect ratio. The updated ITPA H-mode global confinement database contains new data with metallic wall from JET-ILW and ASDEX Upgrade W (tungsten) wall and an increased number of observations which better envelope the ITER operational conditions. An important difference between the IPB98(y,2) and the ITPA20-IL is the strongly reduced dependence on the line averaged density. The new ITPA20-IL scaling law predicts an energy confinement time of 2.79s for the standard inductive $Q = 10$ ELMy H-mode scenario in ITER. The lower dependence on the machine size R might play an important role in the lower prediction with respect to the IPB98(y,2).

Figure 6.3 shows a comparison between the measured thermal energy with the prediction of the model (purple squares), IPB98(y,2) (gray diamonds), and ITPA20-IL (orange circles) scaling laws. The new ITPA20-IL scaling law is more accurate than the IPB98(y,2) on the selection of AUG experimental cases considered in this work, reducing the mean relative error from $MRE_{IPB98(y,2)} = 22.31\%$ to $MRE_{ITPA20-IL} = 14.45\%$. In particular, it can be seen that the ITPA20-IL is very accurate at lower

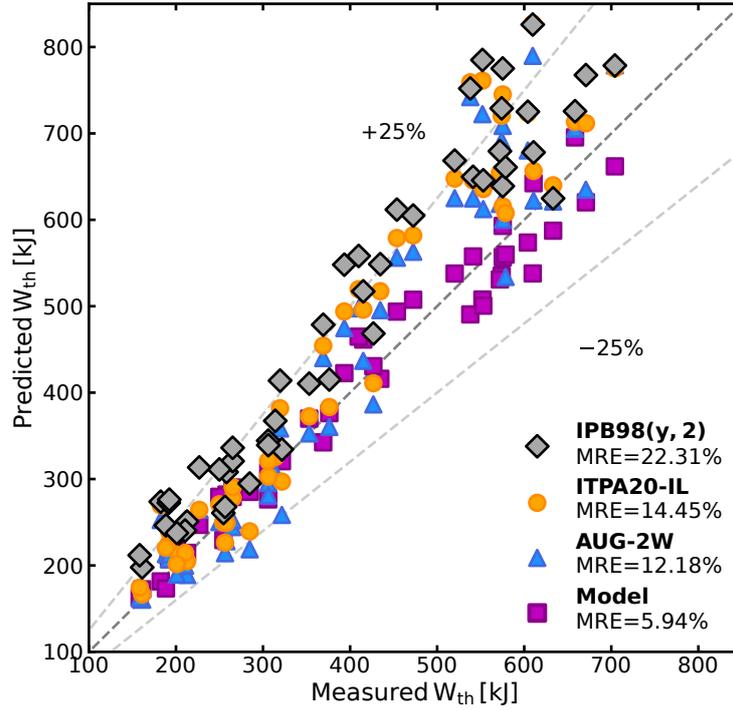


Figure 6.3 – Comparison of the measured thermal energy with the prediction of the model (purple squares), IPB98(y,2) (gray diamonds), ITPA20-IL (orange circles), and AUG-2W (blue triangles) scaling laws.

energies, while at higher energies its error tends to be larger. A more detailed analysis hints that the error becomes larger with larger values of the fueling rate, as shown by figure 6.4 (left). This is consistent with the observations from figure 6.2, but this feature is even more evident for the new scaling law since the ITPA20-IL is more accurate than the IPB98(y,2) at low fueling rate, while the error of the two scalings is comparably large at high fueling rate. This could be interpreted as a limitation of the ITPA20-IL in capturing the confinement degradation caused by an increase in the fueling rate, which can not be directly described as a dependence on the plasma density, figure 6.4 (right).

Figure 6.3 also shows a comparison with the prediction of the AUG-2W scaling law (soon to be published [158]), which is obtained performing a regression on the W wall subset of the ASDEX Upgrade confinement database.

$$\tau_{th}^{AUG-2W} = 0.323 \times I_p^{1.412} B_T^{-0.344} P^{-0.609} \quad (6.2)$$

The AUG-2W scaling law gives very similar results to the ITPA20-IL, with the tendency to predict lower values of the thermal energy, and therefore resulting in a lower mean relative error $MRE_{AUG-2W} = 12.18\%$. The AUG-5C+W is another AUG only scaling law, containing also data from AUG operation with C (carbon) wall,

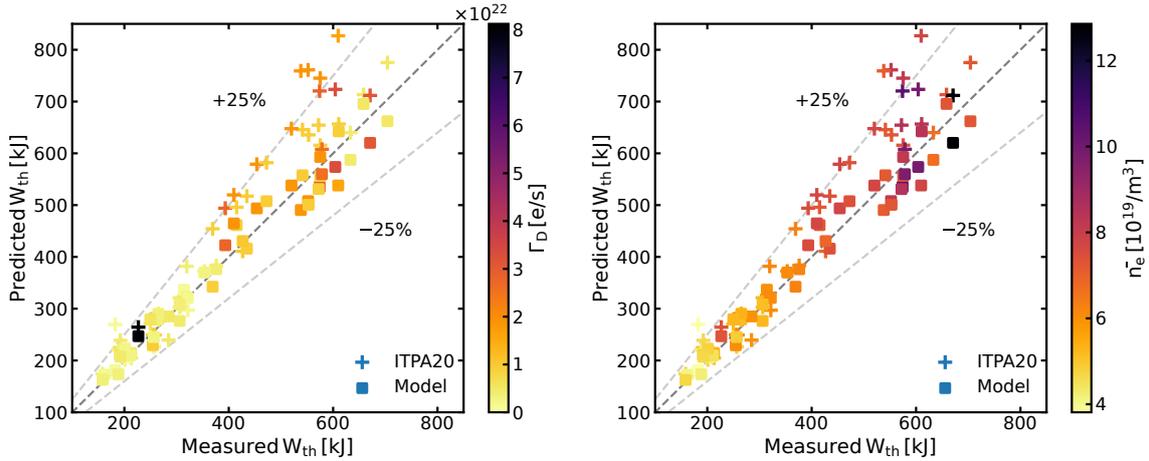


Figure 6.4 – Comparison of the measured thermal energy with the prediction of the model (squares), and ITPA20-IL (crosses), colored as a function of fueling rate (left) and line averaged density (right).

and using as variables also the plasma density and triangularity. The predictions of the AUG-5C+W are very similar to the ITPA20-IL ($MRE_{AUG-5C+W} = 14.38\%$), and thereby it has not been included in the figure. Remarkably, the model, which is capable of capturing the effect on confinement caused by different fueling rate levels, results more accurate than all of the scaling laws considered. The approach presented in this thesis describes plasma confinement on the vast parameters variations considered with more accuracy than a regression on AUG data, meaning that indeed an integrated model has the capability to capture hidden dependencies beyond the possibilities of scaling laws.

6.3.2 Accuracy of kinetic profiles prediction

Since a comparison of integral quantities, such as the stored energy, and local plasma quantities, such as the pedestal top density, does not give information on the quality of the prediction of the plasma profiles, two figures of merit are also adopted to describe how well the predicted profiles reproduce the fits of the experimental measurements. The two figures of merit are the root mean square relative error (RMSRE) and the mean relative error (MRE). The RMSRE is calculated as

$$RMSRE = \sqrt{\frac{1}{n} \sum_i^n \left(\frac{y_{i,pred} - y_{i,exp}}{y_{i,exp}} \right)^2}, \quad (6.3)$$

where the index i represents a given radial location, and n is the total number of radial points. The error is calculated between the plasma quantities predicted by the model $y_{i,pred}$ and estimated by the fits of the experimental measurements $y_{i,exp}$.

6 Extensive validation of the model

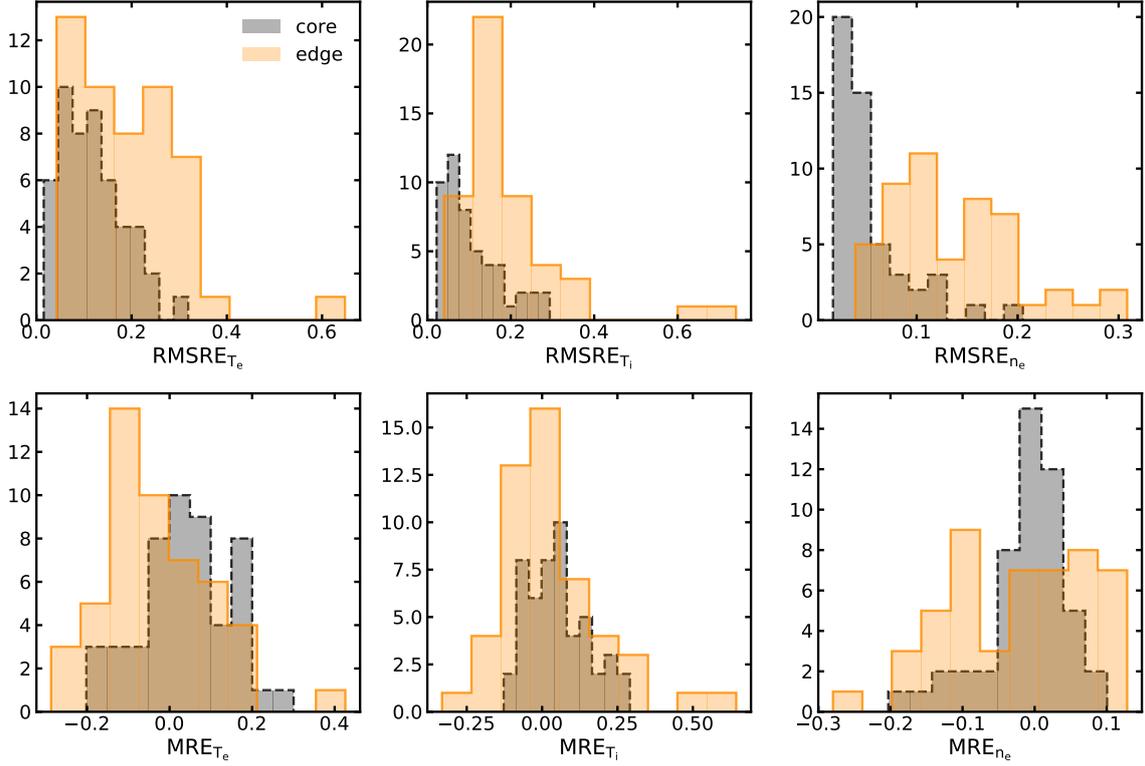


Figure 6.5 – Histograms of number of simulations as a function of the corresponding root mean square relative error (top) and mean relative error (bottom) of the predicted T_e (left), T_i (middle), and n_e (right) profiles with respect to the fits of the experimental measurements in the core (black) and edge (orange) regions of the plasma.

The MRE is calculated as

$$MRE = \frac{1}{n} \sum_i^n \left(\frac{y_{i,pred} - y_{i,exp}}{y_{i,exp}} \right). \quad (6.4)$$

Figure 6.5 shows histograms of the RMSRE (top) and MRE (bottom) calculated for the T_e (left), T_i (middle), and n_e (right) profiles corresponding to the 50 different experimental cases considered. The errors are calculated for the core (black) $0.2 < \rho_{tor} < 0.85$, which is the TGLF computational domain, avoiding the sawteeth region, and the edge (orange) $0.85 < \rho_{tor} < 1$ regions of the plasma. The core profiles of T_e , T_i , and n_e exhibit similar low values of the RMSRE, which indicates the good quality of the prediction, especially for n_e . The edge profiles exhibit a higher value of the RMSRE. The large scatter of the experimental measurements and the steep gradients typical of the pedestal region cause difficulties in obtaining fits with a high level of accuracy. In particular, the evaluation of the pedestal width contains very large uncertainties. Therefore, the fits of the experimental measurements and the profiles predicted by the model can be radially misaligned to each other,

and because of the steep gradients, this can result in large relative errors. This is the reason why the RMSRE is larger in the edge than in the core of the plasma, which does not necessarily mean that the predicted pedestal profiles are in bad agreement with the experimental measurements. The experimental pedestal top plasma quantities are instead very robustly estimated by the fits, due to the very low gradients typical of this region. This allows an accurate and reliable comparison between the predicted and measured pedestal top values. When analyzing the accuracy of the pedestal prediction it is therefore more important and reliable to compare the pedestal top quantities (T_e , T_i , and n_e), which are very accurately reproduced by the model, rather than the RMSRE between the predicted profiles and the fits of experimental measurements. Also, the pedestal thermal energy is very little sensitive to the pedestal width, while it is mainly determined by the pedestal top pressure. The MRE gives information if the model tends to overestimate ($MRE > 0$) or underestimate ($MRE < 0$) the plasma profiles. It can be noticed that all edge quantities are quite well centered around $MRE = 0$. For the core T_i and T_e profiles, the majority of cases exhibit a $MRE > 0$, which suggest that TGLF tends to overestimate the core temperatures profiles, especially T_i . The core density profile instead, tends to be slightly underestimated, as already deduced from figure 6.1 (c), partly compensating the overprediction of the temperature profiles, and producing therefore a mean relative error on the core thermal energy which is quite well centered around zero.

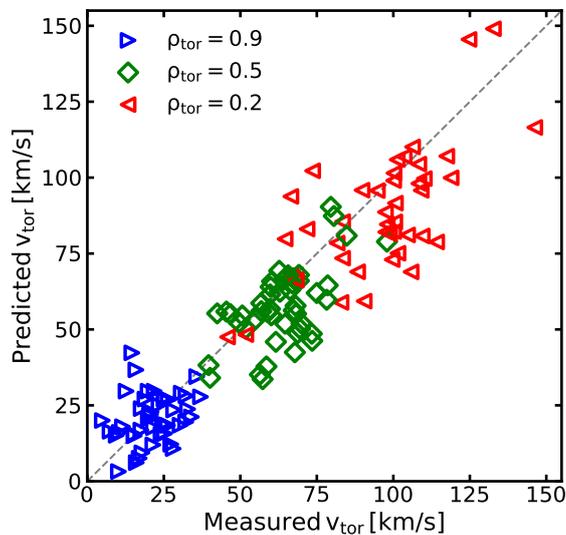


Figure 6.6 – Comparison between predicted and measured toroidal rotation at three different radial location: pedestal top (blue), mid-radius (green), and center of the plasma (red).

The quality of the toroidal rotation prediction is illustrated in figure 6.6, which shows a comparison between the measured and predicted rotation values at three

different radial locations: pedestal top (blue), mid-radius (green), and center of the plasma (red). The prediction of v_{tor} exhibits a larger scatter with respect to the other quantities previously analyzed, maintaining nevertheless a reasonable mean relative error. The scatter does not increase significantly towards the center of the plasma, meaning that the estimate of core momentum transport is quite accurate and robust. Instead, the formula that calculates the pedestal top rotation (from Ref. [8]) seems to not accurately capture all the effects caused by the different operational parameters. The prediction of the toroidal rotation profile has the only purpose of calculating the radial electric field in the core, without using any experimental information from profile measurements. This is needed to calculate the $\mathbf{E} \times \mathbf{B}$, which is an input parameter required by TGLF, and can have an impact on the final prediction of the kinetic profiles. However, since TGLF is little sensitive to the $\mathbf{E} \times \mathbf{B}$ in the parameter domain of these experiments, it is not important that the prediction of the toroidal rotation is very accurate. Therefore we can accept a relatively large error on the predicted toroidal rotation.

6.4 Analysis of specific dependencies

The following subsections describe in greater details the effects of changes in plasma triangularity, magnetic field, NBI voltage, and plasma current with similar line averaged density.

6.4.1 Triangularity scan

Among the cases included in the database, we focus on the two stationary phases of the AUG discharges #33195 and #33194, respectively at 4.2s and 5.1s, constituting a triangularity scan ($\delta = 0.22 - 0.39$) at $B_t = -2.5$ T, $I_p = 0.8$ MA, $P_{heat} = 11.4$ MW, $\Gamma_D \sim 0.9 \times 10^{22}$ e/s. An increase in plasma triangularity usually causes an increase in confinement which stems from the pedestal, due to a stabilization of the MHD modes. In particular, the higher triangularity alters the shape of the peeling-ballooning boundary, allowing the pedestal to reach a higher pressure gradient and current density.

In our model the transport in the pedestal is not affected by triangularity, as it does not have any impact on the pedestal transport coefficients (apart from neoclassical transport which has a very small contribution). Therefore, without considering the MHD stability calculation yet, when comparing the ASTRA simulations results obtained at different triangularity for the same value of the pedestal width, we get the same pedestal pressure (also the TGLF results show a weak dependence on triangularity). This means that the relation between the pedestal width and the pedestal pressure does not change when changing triangularity. The change in confinement has then to be captured by the MHD stability calculation.

Figure 6.7 shows the spectra of the ideal growth rates calculated by MISHKA for a set of toroidal mode numbers ($1 \leq n \leq 40$), corresponding to low (purple circles)

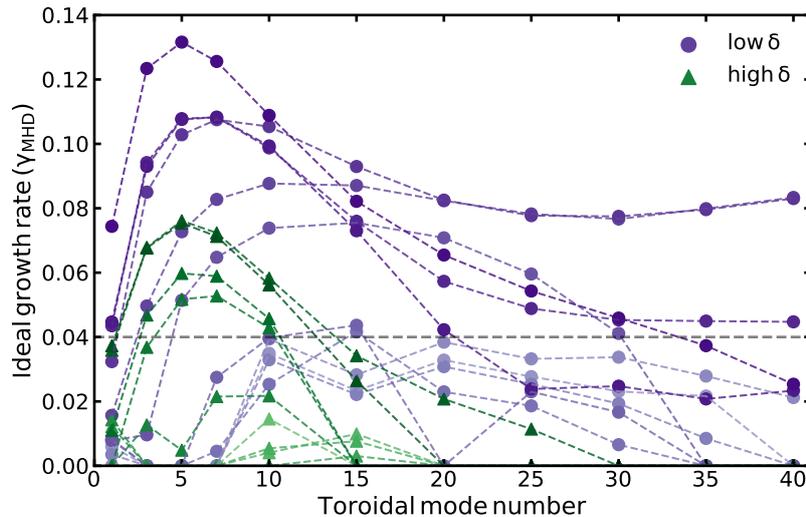


Figure 6.7 – Spectra of the ideal growth rates of the pedestal MHD instabilities calculated by MISHKA for a set of toroidal mode numbers, corresponding to low (purple circles) and high (green triangles) plasma triangularity. The increasing darkness corresponds to increasing value of pedestal width.

and high (green triangles) plasma triangularity. The different curves correspond to different values of the pedestal width, with the increasing darkness corresponding to increasing value of pedestal width. The pedestal pressure and its gradient increase with the pedestal width, as explained in section 4.2.2, thereby also the growth rates increase. We selected the same range of pedestal widths values for this scan, in order to perform a better comparison. So for example the darkest green line and the darkest purple line correspond to the same value of the pedestal width. As one can see the growth rates are strongly reduced at higher triangularity, especially for the higher toroidal mode numbers, which correspond to ballooning modes. This results in a higher value of the highest stable pedestal width at higher triangularity, and therefore a higher pedestal pressure. Corresponding to the highest stable pedestal width, the toroidal mode number of the most unstable mode is higher at low triangularity ($n = 15$) than at high triangularity ($n = 7$), meaning that the pedestal is closer to the ballooning limit at low triangularity.

Figure 6.8 (right) shows that the predicted pedestal pressure is in good agreement with the measurements both at high and low triangularity, while the core thermal energy is overpredicted. As a result the change in total thermal energy predicted by the model is slightly overestimated, as it can be seen in figure 6.8 (left). The reason for this can be attributed to an underestimate of turbulent transport by TGLF for the case at high triangularity. The IPB98(y,2) captures the change in confinement due to the positive dependence on the density, which increases with triangularity.

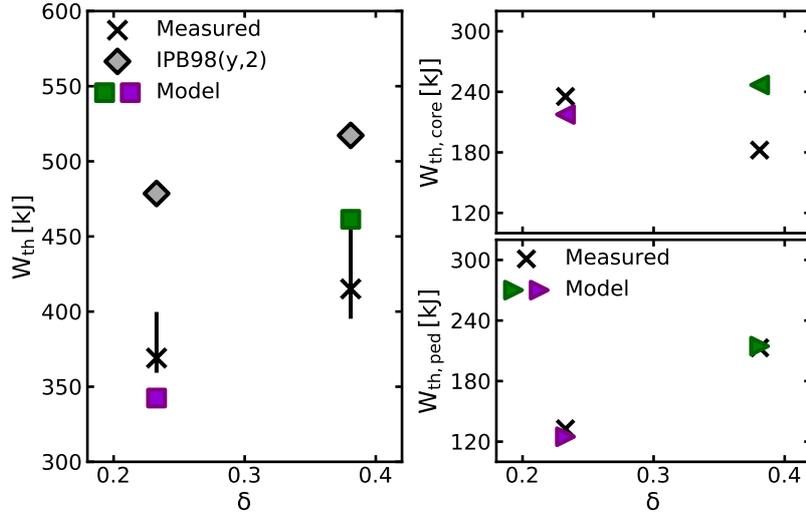


Figure 6.8 – Thermal energy predicted by the model (colored squares), by the IPB98(y,2) (gray diamonds), and measured (black crosses) as a function of triangularity (left). Experimental and predicted thermal energy separated in the pedestal and core components (right).

Figure 6.9 shows a comparison between experimental measurements (dots) and predicted profiles (lines) of electron and ion temperature and electron density at high (green) and low (purple) triangularity. As one can see the values at the pedestal top are well reproduced, capturing the increase of both temperature and density with triangularity. The core gradients are very well reproduced at low triangularity (with the exception of T_i inside $\rho_{pol} < 0.4$, possibly due to missing fast ions stabilization mechanisms), while at high triangularity the core gradients are overestimated by TGLF, especially for the electron and ion temperature. As a result TGLF does not predict a change in core profiles gradients as strong as the one observed from the measurements.

Overall, the model well captures the change in confinement with triangularity, especially for pedestal confinement.

6.4.2 Magnetic field scan

A scan in the toroidal magnetic field is provided by the two stationary phases of the discharges #31555 and #34955. In these two similar discharges with $I_p = 0.6$ MA, $P_{heat} = 5$ MW, $\delta = 0.22$, the magnetic field is varied between $B_t = 1.5 - 2.8$ T. The fueling rate is slightly different, being higher at lower magnetic field $\Gamma_{D,1.5[T]} \sim 0.97 \times 10^{22}$ e/s, $\Gamma_{D,2.8[T]} \sim 0.70 \times 10^{22}$ e/s. A scan in the magnetic field is another variation included in the IPB98(y,2) that is possible to test on AUG. The two stationary time windows selected represent the most similar pair of AUG discharges

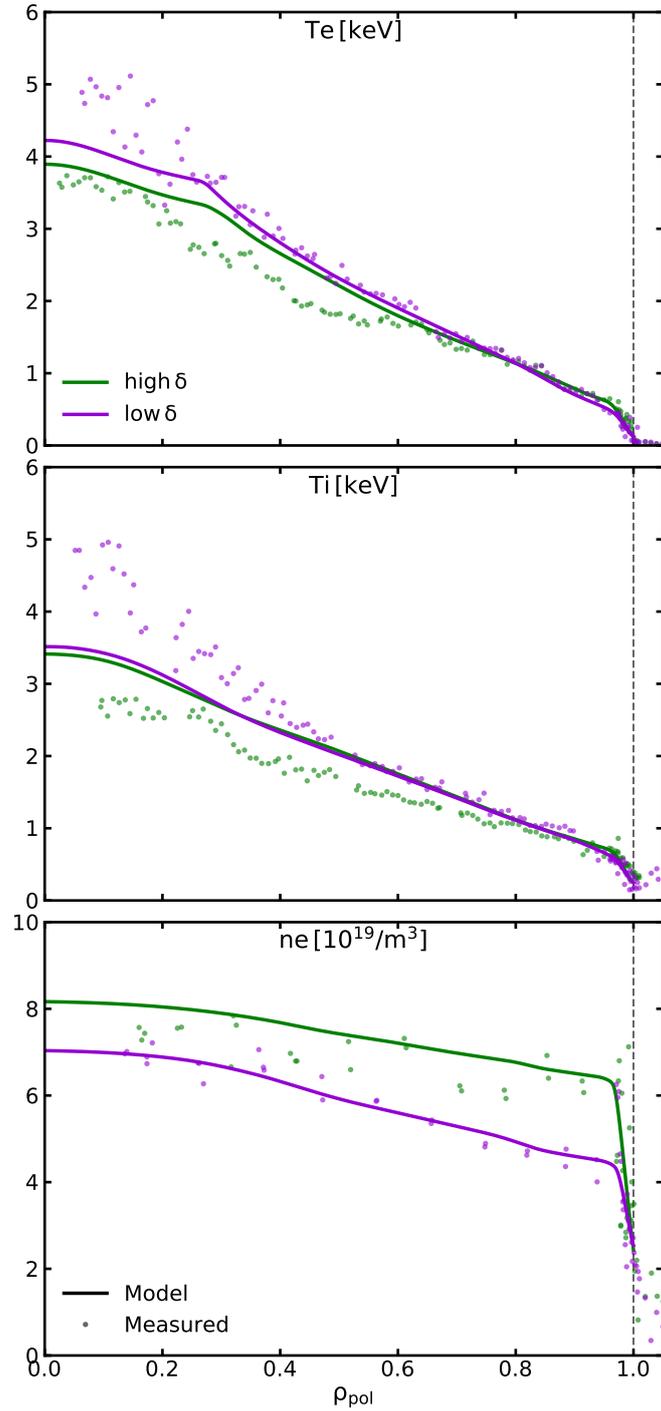


Figure 6.9 – Experimental measurements (dots), and predicted profiles (lines) of electron and ion temperature, and electron density for the different triangularity values.

6 Extensive validation of the model

with the largest variation in B_t we found. At these values of the magnetic field, it is difficult to get a similar radial distribution of the ECRH power, so we selected two cases without ECRH power, therefore with NBI heating only.

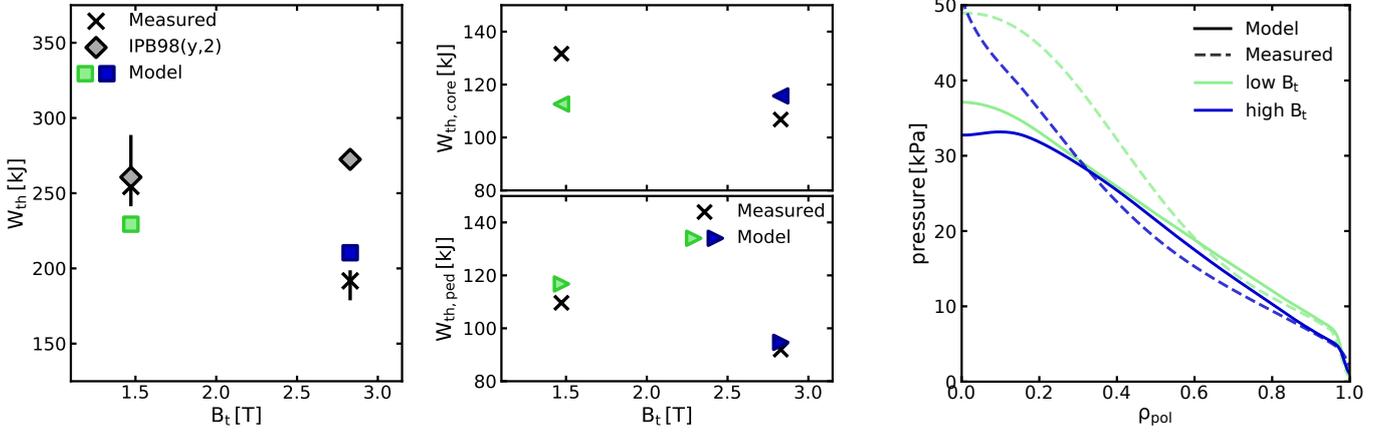


Figure 6.10 – Thermal energy predicted by the model (colored squares), by the IPB98(y,2) (gray diamonds), and measured (black crosses) as a function of the magnetic field (left). Experimental and predicted thermal energy separated in the pedestal and core components (middle). Measured (dashed) and predicted (solid) pressure profiles for the different magnetic field values (right).

The measured thermal energy, showed in figure 6.10 (left), exhibits a negative dependence on the magnetic field, that is not captured by the IPB98(y,2) scaling law, which instead predicts a slightly higher energy with increasing magnetic field. The IPB98(y,2) has a positive exponent of B_t , although very small. The model predicts the correct trend, but does not predict a change in thermal energy as strong as observed experimentally. This is because the model, while it correctly captures the change in pedestal thermal energy (higher at lower B_t), predicts the same or even decreasing core thermal energy when going to lower magnetic field values, as it can be seen in figure 6.10 (middle), while the measured core energy is higher at lower B_t values. Figure 6.10 (right) shows the predicted (solid) and measured (dashed) pressure profiles for the different magnetic field values, where it can be seen that, while the pedestal pressure is accurately matched, the core gradients are underpredicted at low magnetic field (green lines). In particular, the prediction starts to deviate significantly from the measurements at $\rho_{pol} \sim 0.6$. The reason why TGLF fails in capturing this change in core confinement is most likely associated to the effect of β on turbulent transport. Since β has a quadratic dependence on B_t , by reducing the magnetic field by almost a factor of 2, β increases by a factor of ~ 4 . In addition to this effect, the pressure decreases with increasing field, leading to an even stronger increase in β by reducing the magnetic field ($\beta_{1.5[T]} = 2.1\% \sim 5 \times \beta_{2.8[T]} = 0.42\%$).

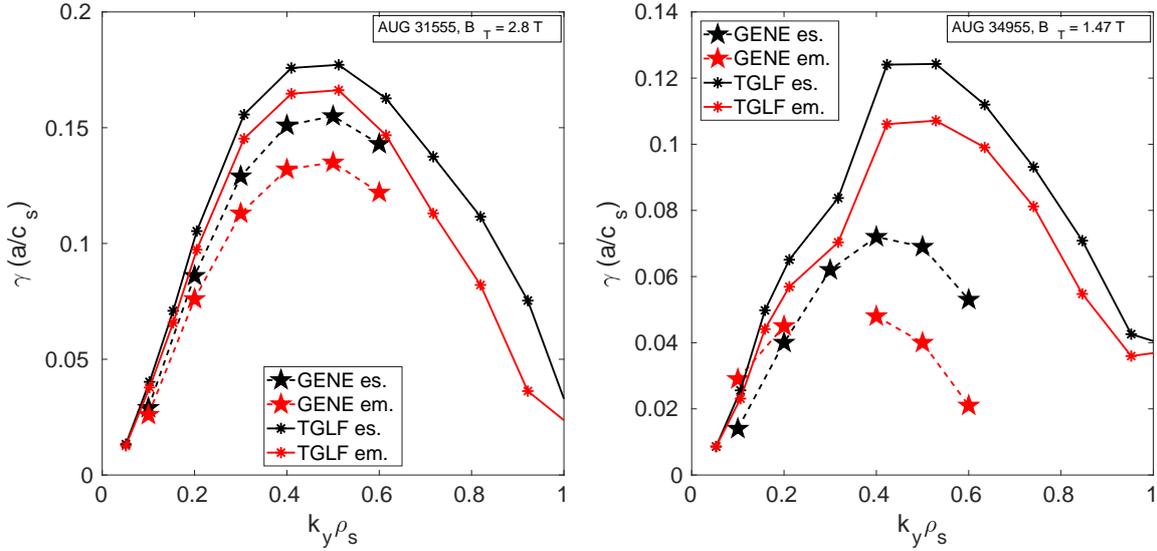


Figure 6.11 – Spectra of the dominant microinstability (ITG modes) at mid-radius ($\rho_{tor} = 0.5$) computed by linear GENE (dashed) and TGLF (solid) for the high (left) and low (right) magnetic field cases. Electromagnetic simulations are in red, while electrostatic ones are in black.

In non-linear gyrokinetic simulations turbulent transport is strongly reduced by an increase in β , but in linear simulations this effect is weaker [159, 160]. A comparison between linear gyrokinetic simulations, performed with the GENE code [161, 162], and TGLF at mid radius ($\rho_{pol} \sim 0.6$), illustrated in figure 6.11 shows that TGLF underestimates the effect of β even against linear GENE. While the spectra of TGLF and GENE exhibit similar growth rates at high B_t , a large difference between the growth rates predicted by the two models is noticeable at low field. In particular, by increasing β , GENE (linear) predicts a reduction of the maximum growth rates by almost a factor 3 ($\gamma_{1.5[T]} \sim 0.37 \times \gamma_{2.8[T]}$), while TGLF predicts a change in the maximum growth rate by only a factor $\sim 1/3$ ($\gamma_{1.5[T]} \sim 0.66 \times \gamma_{2.8[T]}$). The instabilities which are found by both codes at these wave numbers ($k_y \rho_s$) are ion temperature gradient (ITG) modes. As already mentioned, the non linear effect of β on the growth rates (in particular for ITGs) is stronger than the linear one, and since in TGLF this effect is even weaker than respect to linear GENE, we can conclude that with our model we strongly underestimate the turbulence stabilization with beta, and therefore the change in core confinement with B_t is underestimated.

Another element in support of this hypothesis is represented by figure 6.12, which shows the measured and predicted electron and ion temperatures and the electron density at the different magnetic field values. As one can see, the larger disagreement between the model prediction and the measurements is in the ion temperature for the low field case. Also the predicted core density profile is flatter than the measured one. Turbulent transport driven by ITG modes usually affects both temperature and

6 Extensive validation of the model

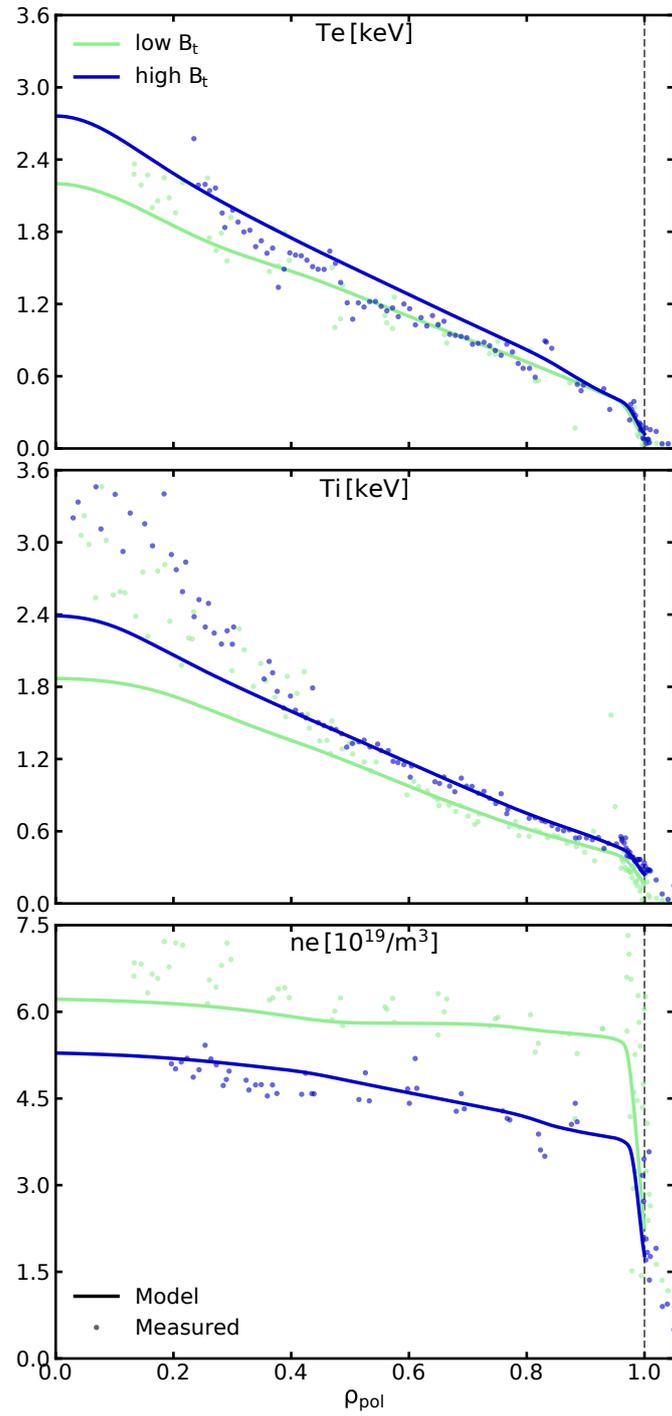


Figure 6.12 – Experimental measurements (dots), and predicted profiles (lines) of electron and ion temperature, and electron density for the different magnetic field values.

density profiles, limiting their gradients. The core density profile is not very sensitive to the particle source, and it is rather determined by turbulent transport [44]. This considerations suggest that TGLF is underpredicting the ITG stabilization caused by the increase in β .

Overall the model has shown to capture the effect of the magnetic field on confinement more accurately than the IPB98(y,2) scaling law. The pedestal prediction has proven to be robust also with respect to a variation in B_t , while the accuracy of the core thermal energy prediction is affected by a too weak stabilization of ITG modes by β in TGLF, which is responsible for a larger error on the total thermal energy evaluation at low field.

6.4.3 NBI voltage scan

In our database we also included the stationary phases at 2.8s of the discharges #35288 and #35289. In these two similar discharges with $B_t = -2.5$ T, $I_p = 0.8$ MA, $P_{heat} = 7.25$ MW, $\Gamma_D \sim 0.4 \times 10^{22}$ e/s, $\delta = 0.22$, the NBI power is the same $P_{NBI} = 5$ MW, but obtained with different NBI voltage ($V_{NBI} = 42 - 92$ kV) [163].

In these experiments the density remains almost the same, while one would have expected a change caused by operating the NBI heating system at different voltage, due to the resulting different particle source (as explained later in this section). We were then interested to see if the model can reproduce the experimental observation. These experimental cases provide an essential test of the model in validating the consistency between transport and pedestal stability and the connection between heat and particle transport. The prediction of the model can result accurate only if the change in the temperature and density profiles (and therefore also in confinement) caused by the different NBI voltage levels is well reproduced. We can test if the model contains the corrects elements to achieve this. For this reason these cases have been chosen for a detailed analysis in this work. Another important point that motivated this analysis is that the IPB98(y,2) scaling law fails in reproducing the change in confinement observed experimentally, caused by the different voltage levels. It is therefore interesting to see if our model performs better than the scaling law by capturing these effects.

When operating at lower voltage the power provided by each beam is lower, so to deliver the same power, at $V_{NBI} = 42$ kV 8 beams are needed, while only 3 beams are needed at $V_{NBI} = 92$ kV. Even though the power delivered by each beam changes with voltage, the amount of particles injected by each beam into the plasma remains unchanged. This means that for the lower NBI voltage case, in which more beams are used to achieve the same heating power, the particle source is much larger (by a factor ~ 2). Therefore, one could expect that at lower voltage the density is higher, due to the higher particle source. Instead, as shown by the experimental data in figure 6.13 (c), the density is similar for the two cases. This is because going from high to low voltage, the experimentally measured pedestal pressure has decreased by $\sim 25\%$, due to the higher particle source, which causes an outward shift of the density profile. The electron temperature is lower at lower

6 Extensive validation of the model

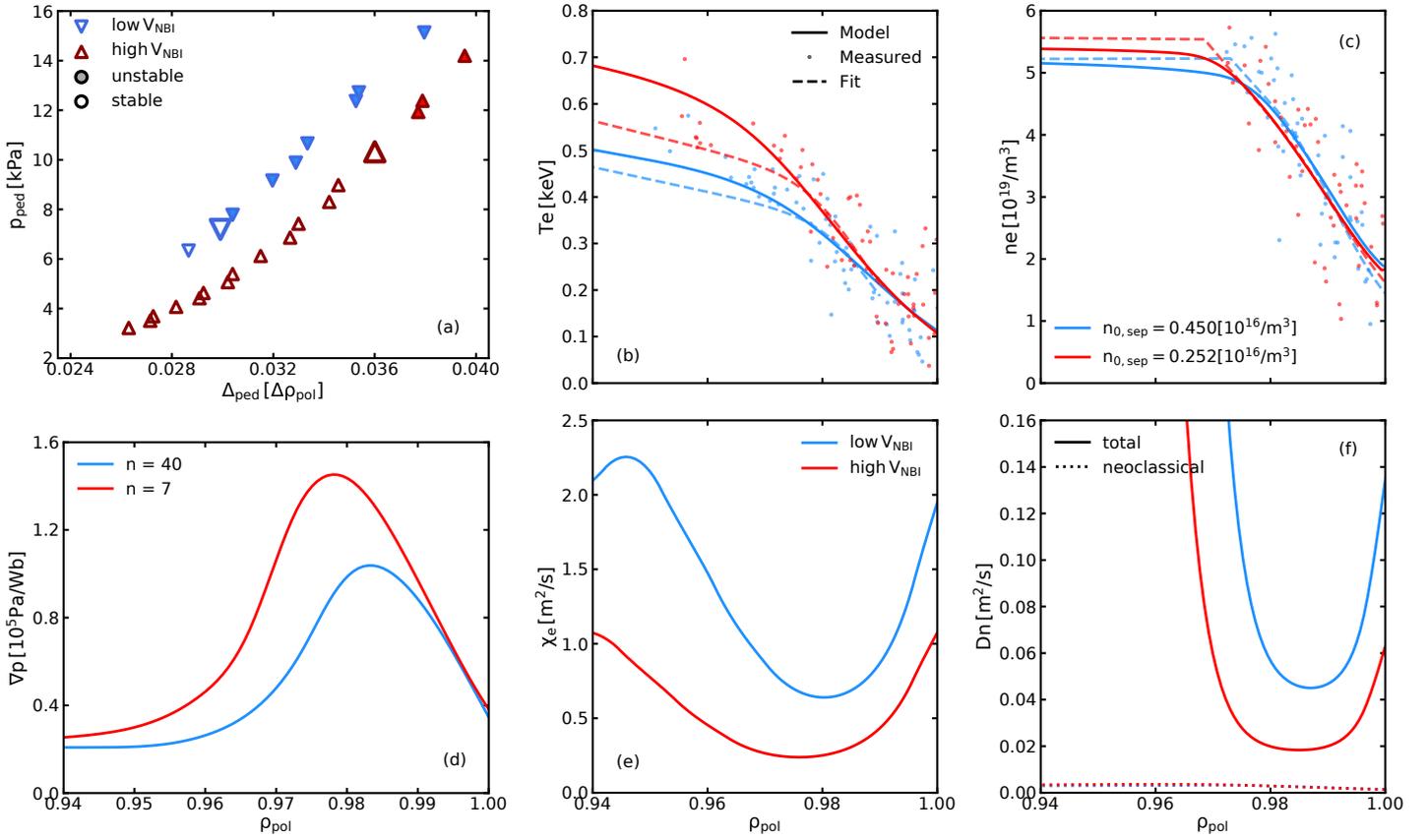


Figure 6.13 – (a) ASTRA pedestal width scan for the 2 NBI voltage levels. The empty symbols correspond to PB stable pedestal conditions as predicted by the MISHKA MHD stability calculation, while the filled symbols correspond to unstable conditions (i.e. ELM onset). The largest open symbols identify the highest stable pedestal pressure, corresponding to the final result of the model. (d) Pressure gradient profiles corresponding to the highest stable pedestal pressure for the different values of the NBI voltage. The corresponding most unstable toroidal mode number (n) is also shown in the legend. Predicted profiles (solid lines) of the pedestal electron heat diffusivity (e), and particle diffusivity (f) with its neoclassical component (dashed) for the different levels of NBI voltage, and resulting electron temperature (b) and density (c) profiles. The measurements are represented by the dots, and their fits by the dashed lines. The label in the upper right figure shows the values of the neutral density at the separatrix for the two cases.

voltage, figure 6.13 (b). The mechanism of the reduction in pedestal confinement is similar to that coming from an increase in the fueling rate, described in section 5.3.1. The higher particle source from the NBI causes an increase in the particle flux leaving the plasma, leading to a higher neutrals density via recycling. This causes a steepening of the density profile in the pedestal region, as observed from experimental measurements, and reproduced by the model.

Figure 6.13 (a) shows the scans in pedestal width, where the filled symbols correspond to PBM unstable conditions, while the open ones represent stable conditions. The largest open symbols identify the highest stable pedestal pressure, which correspond to the final result of the model for the pedestal prediction. As one can see the predicted pedestal pressure is lower at lower NBI voltage. One can also see that the same pedestal pressure among the 2 different cases (low and high V_{NBI}) corresponds to different values of pedestal widths, and therefore the same pedestal width among the 2 different cases corresponds to different values of pedestal pressure. This is because, in the ASTRA prediction of the kinetic profiles, the higher particle source from the NBI (at lower voltage) causes an increase in the particle flux leaving the plasma, leading to a higher neutrals density via recycling which causes a steepening (and therefore an increase) of the density profile. For the same value of the pedestal width, the electron temperature at the pedestal top is similar among the 2 different cases due to the constraint $\langle \nabla T_e \rangle / T_{e,top} = -0.5 [\text{cm}^{-1}]$, while the pedestal top density is higher with lower voltage (due to the higher particle source). Therefore, for the same value of the pedestal width, the pedestal top pressure is higher with lower voltage, or, for the same value of the pedestal pressure, the pedestal width is smaller with lower voltage. Since the peak of the pressure gradient is located approximately in the middle of the pedestal width, this moves outwards with lower voltage. Because the ballooning stability is sensitive to the location of this peak (the closer to the separatrix the more it is unstable), the lower voltage case will be limited to a lower value of the pressure gradient, because of the lower ballooning stability limit. This is illustrated in figure 6.13 (d), which shows the pressure gradient profiles of the highest stable pedestals for the 2 different cases. The legend of the figure also indicates the toroidal mode number (n) of the most unstable mode, which is higher at lower voltage ($n = 40$), meaning that it is more ballooning unstable.

In the pedestal width scan the pedestal pressure increases more than linearly with the width, in fact also the pressure gradient increases with the width. This comes from the imposition of the constraint $\langle \nabla T_e \rangle / T_{e,top} = -0.5 [\text{cm}^{-1}]$, which causes the pedestal electron heat diffusivity $\chi_{e,ped}$ to decrease in value with increasing pedestal width, as already explained in section 4.2.2. Because of this, and because the highest stable pedestal width is lower at lower voltage, the value of the electron heat diffusivity $\chi_{e,ped}$ is larger at lower voltage, and so is the particle diffusivity (since $D_{n,ped} \propto \chi_{e,ped}$), as it can be seen in figure 6.13 (e,f). The particle diffusivity becomes larger by a factor ~ 2 at lower voltage, compensating for the almost double source of neutrals (the value of the separatrix neutral density is shown in the legend

of figure 6.13 (c)), and resulting in a similar pedestal top density.

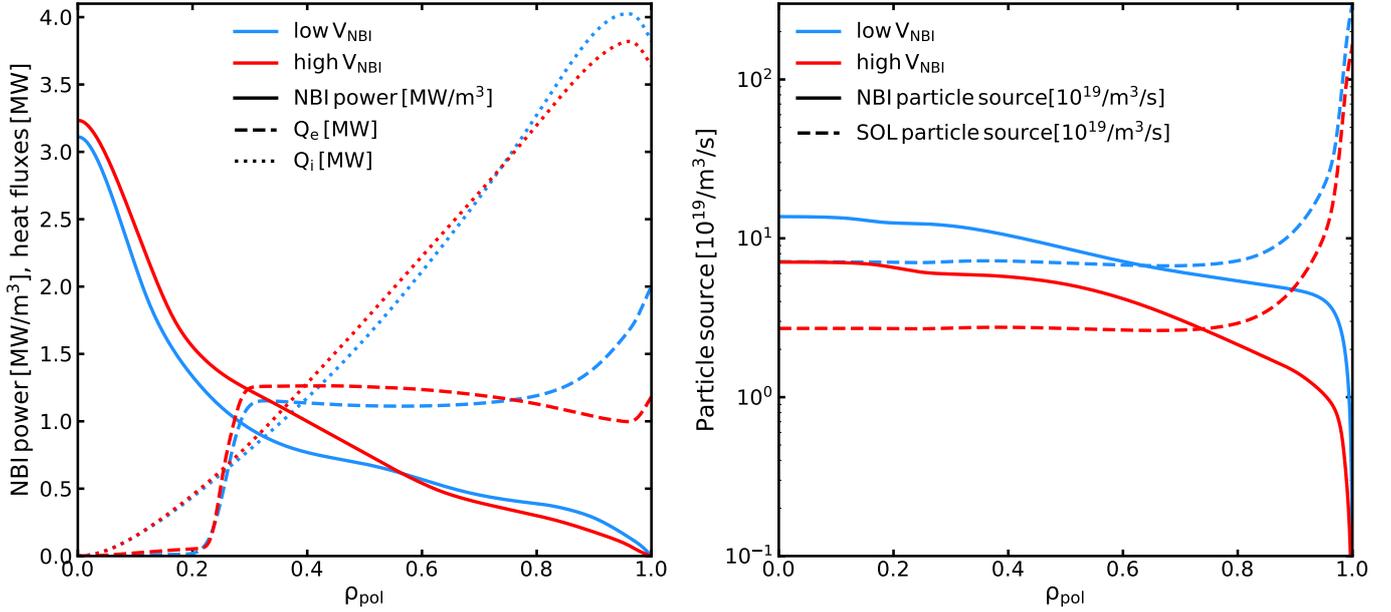


Figure 6.14 – Radial profiles of the NBI power deposition (solid), and of the ion (dashed) and electron (dotted) heat fluxes for the two different NBI voltage levels (left). Radial profiles of the particle source provided by the NBI (solid), and by the SOL neutrals (dashed), produced mainly by recycling, for the two different NBI voltage levels (right).

Another effect that might play a role, although its importance has not been studied, is the different power deposition of the NBI with different voltage. The beams are absorbed more in the edge of the plasma at lower voltage, as it can be seen in figure 6.14 (left, solid lines). This effect is consistently included in the simulations. The profiles in the figure are calculated with the ASTRA NBI module, but we have not studied this effect directly by replacing the power density profiles from one case to the other. Figure 6.14 (left) also shows the electron (dotted) and ion (dashed) heat fluxes. The different beam deposition can also contribute to the difference in the electron heat flux and diffusivity in the pedestal region at the different NBI voltage levels (higher at lower voltage). Figure 6.14 (right) shows the radial profiles of the particle source provided by the NBI (solid) and by the SOL neutrals (dashed), produced mainly by recycling, for the two different NBI voltage levels. The NBI particle source changes significantly with the different voltage levels (by a factor ~ 2). As a consequence, also the source provided by the SOL recycled neutrals changes (also by a factor ~ 2). It can be noticed that the differences in the particle source profiles, produced by the different NBI voltage levels, are significantly larger than the differences in the heating power densities (note the logarithmic scale). However, in the pedestal region these differences (in the particle source and in the power density) are comparable. Therefore, it is not possible to draw a conclusion on which of the two is the dominant mechanism affecting the pedestal profiles.

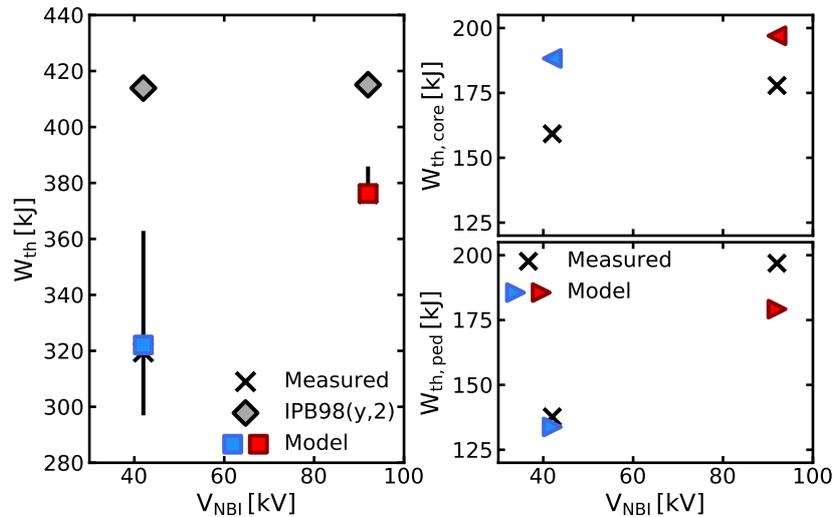


Figure 6.15 – Thermal energy predicted by the model (colored squares), by the IPB98(y,2) (gray diamonds), and measured (black crosses) as a function of the NBI voltage (left). Experimental and predicted thermal energy separated in the pedestal and core components (right).

Figure 6.15 shows that the predicted pedestal energy matches the measurements, and the model well captures the change in pedestal confinement with the different NBI voltage levels. The change in core energy, and then in total thermal energy as well, is also well captured. The prediction of the IPB98(y,2) does not change with the different NBI voltage levels, since all its input parameters (including the line averaged density) do not change, strongly overestimating the plasma energy at low voltage.

This case provides a demonstration of how important it is to take into account core, pedestal, and SOL effects self-consistently. The combined estimation of core particle transport and sources with the different NBI voltages affects the SOL neutrals source via recycling, which (the source) impacts the pedestal MHD stability. This allows us to capture the change in confinement caused by the different NBI voltage, highlighting the advantages of our model over the IPB98(y,2) scaling law. This analysis is also a very stringent test for the assumption on the pedestal transport, and on the description of the neutrals in the SOL, which can only result accurate with a correct representation of the underlying physics. It would also not be possible to obtain such results without assuming that the pedestal particle diffusivity is proportional to the pedestal electron heat diffusivity ($D_{n,ped} \propto \chi_{e,ped}$). This suggests that our assumptions on pedestal transport and its consistency with the pedestal stability give a correct representation of these phenomena, at least in the modeling of this type of results for this experimental conditions.

6.4.4 Current scan at similar line averaged density

The large database considered for the extended validation of the model allowed us to also analyze a scan in plasma current at similar line averaged density, instead of fixed fueling rate as in the case presented in section 5.3.4. The scan is represented by stationary phases of the discharges #33195 and #30668 corresponding to a change in plasma current from $I_p = 0.8$ MA to $I_p = 1.2$ MA, respectively. The two discharges have similar parameters $B_t = -2.5$ T, $P_{heat} = 12$ MW, $\delta = 0.3$, and similar line averaged density, being higher at higher current $\bar{n}_{e,0.8[MA]} = 5.5 \times 10^{19}/\text{m}^3$, $\bar{n}_{e,1.2[MA]} = 6.6 \times 10^{19}/\text{m}^3$. The corresponding Greenwald fractions $f_G = \bar{n}_e/n_G$, where $n_G = I_p/(\pi a^2)$, are $f_{G,0.8[MA]} = 0.57$ and $f_{G,1.2[MA]} = 0.45$, respectively. As already discussed in section 5.3.4, an increase in plasma current at fixed fueling rate produces an increase in the pedestal top density, due to the extended PBM stability. Therefore, to achieve a similar density, a higher fueling rate is required at lower current $\Gamma_{D,0.8[MA]} = 0.95 \times 10^{22}\text{e/s}$, $\Gamma_{D,1.2[MA]} = 0.51 \times 10^{22}\text{e/s}$.

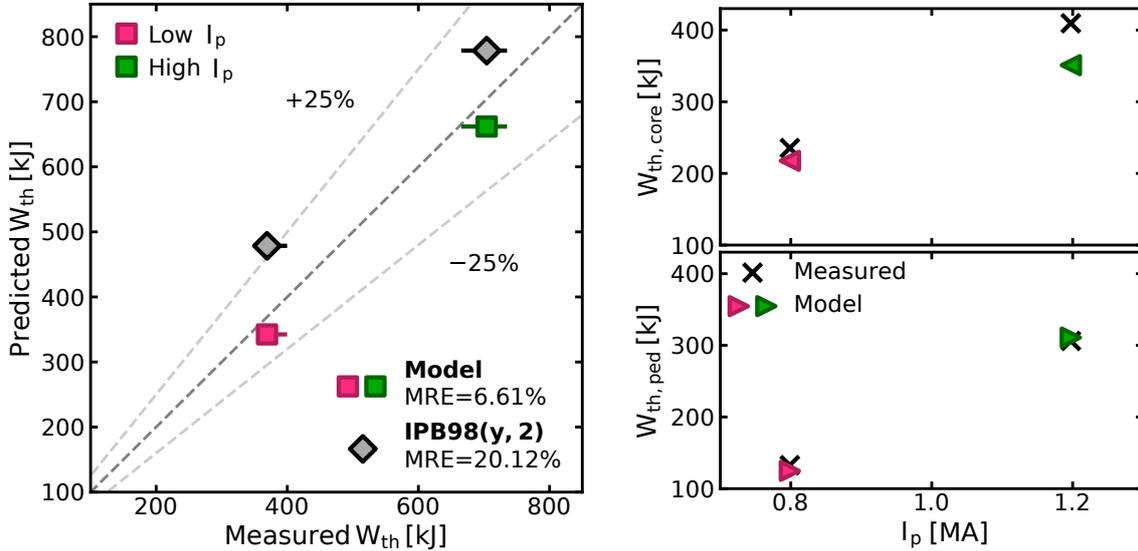


Figure 6.16 – Comparison of the measured thermal energy with the prediction of the model (colored squares), and IPB98(y,2) (gray diamonds) for different values of the plasma current at similar line averaged density (left). Experimental (black crosses) and predicted (colored triangles) thermal energy as a function of the plasma current separated in the pedestal and core components (right).

This scan allows a better comparison between the model and the scaling law on the accuracy in capturing the effect of the plasma current, while keeping all the other parameters of the IPB98(y,2) fixed, or within a small variation as for the density. However, as discussed in section 5.3.1 and 6.3, a change in fueling rate such as the one in these discharges is sufficient to produce a strong decrease in pedestal confinement. As a consequence, the decrease in global confinement going to lower

plasma current is stronger than that predicted by the IPB98(y,2), which strongly overestimates the thermal energy at low I_p (and high Γ_D) $H_{98} = 0.7$, as it can be seen in figure 6.16. The model instead, is capable of capturing the combined effect of the fueling rate and the plasma current on the pedestal pressure and on core confinement, leading to a prediction of the plasma stored energy with a significantly lower mean relative error $MRE = 6.61\%$ than the IPB98(y,2) scaling law $MRE = 20.12\%$. The change in pedestal top density is also well reproduced by the model.

7 Conclusion

In order to produce electricity via controlled thermonuclear fusion, reactors must be built with sufficiently high performance. This constitutes a difficult scientific and technological challenge, which requires an economically sustainable solution. The design of a future fusion reactor has to be optimized in order to contain the investment cost, and therefore it has to rely on an accurate and robust prediction of at least the plasma energy confinement time, but possibly also of the radial profiles of densities and temperatures.

The main parameters in the design of the ITER tokamak are largely based on scaling laws from regressions on multi-device experimental data-sets, which allow the prediction of the energy confinement time. However, while this approach can potentially capture the dependencies of confinement on the principal engineering parameters, it contains large uncertainties in the extrapolation to reactor conditions, which are largely outside of the multi-dimensional domain of data over which the statistical analysis is performed.

A different and complementary way of estimating the energy confinement time, is by predicting the plasma kinetic profiles by means of one dimensional (1D) approaches which combine different modules describing plasma transport and sources at various levels of integration, and various levels of realism. Such integrated models can capture physics phenomena, which can have a strong impact on confinement, beyond the possibilities of scaling laws, and have therefore the potential to more accurately describe the plasma performance. However, this approach usually requires to include empirical elements (e.g. for the definition of the boundary conditions) or to make assumptions which can be specific to an existing device, and thereby which can limit their reliability and predictive capabilities when applied to other present and future devices.

Within this framework, during this PhD thesis a new integrated modeling workflow has been developed that for the first time describes the entire confined plasma domain in H-mode conditions, including the pedestal, up to the last closed flux surface. This allows an accurate prediction of plasma confinement and of the radial kinetic profiles only using global parameters as inputs, the same that are also used for planning a tokamak plasma discharge, without the need of any experimental information from profile measurements. This was achieved by including into the ASTRA transport code a new pedestal transport model in combination with a state-of-the-art core turbulent transport model, which allow for a simultaneous evolution of the core and pedestal kinetic profiles, and a simple but sufficiently realistic analytical model for

the open field line scrape-off layer (SOL) region, which self-consistently calculates the boundary conditions.

The workflow combines theory-based components (like the quasilinear TGLF [1] model for core turbulent transport, the NCLASS [2] model for neoclassical transport, the MHD code MISHKA [3] for the pedestal stability and the two-point model for the SOL [4, 5]) with empirical elements, in particular for the description of the transport in the pedestal region and for the connection between divertor and SOL parameters.

The pedestal transport model is based on the experimental observation showing that the ratio of the average gradient of the electron temperature in the pedestal region to the pedestal top temperature $\langle \nabla T_e \rangle / T_{e,ped}$ is approximately constant and equal to $-0.5 [\text{cm}^{-1}]$ in a multi-device analysis [6]. This observation gives a new transport constraint for the pedestal evolution in the inter-ELM recovery phase, which is different from the usual technique adopted by the EPED model [7] ($\Delta\psi_N \propto \sqrt{\beta_{p,ped}}$). The inclusion of this constraint into the ASTRA transport code allows us, for a given pedestal width, to find the electron heat conductivity ($\chi_{e,ped}$) that fulfills the condition $\langle \nabla T_e \rangle / T_{e,ped} \approx \text{const} = -0.5 [\text{cm}^{-1}]$. We assume that the ion heat conductivity and the particle diffusivity are proportional to the value of $\chi_{e,ped}$ which is consistently determined in the ASTRA simulation.

The ASTRA simulations combine the pedestal transport coefficients, obtained through this technique, with the transport coefficients calculated with the TGLF and NCLASS models to give a complete description of transport over the whole radial profile. This allows the simulation of the kinetic profiles, namely the electron and ion temperature and density (T_e, T_i, n_e, n_i), and the current density (j) profiles from the magnetic axis to the separatrix.

The modeling of the toroidal rotation is also included in the ASTRA simulations. An analytical formula for the residual toroidal stress at the edge [8] calculates the toroidal rotation at the pedestal top, and the core rotation profile is obtained assuming a Prandtl number $P_r = 1$, which means that we assume a momentum diffusivity equal to the ion heat diffusivity. The torque provided by the NBI is calculated by the ASTRA NBI module. By doing this we calculate all the components of the radial electric field core profile, which is used by TGLF to calculate the effect of the $\mathbf{E} \times \mathbf{B}$ shear on turbulent transport, without the need of using any experimental information from profile measurements.

The core turbulent transport coefficients are given by the TGLF quasilinear model, which is interfaced with the pedestal transport model using a radial buffer in the transition between the TGLF boundary and the pedestal top ($0.85 < \rho_{tor} < \rho_{ped}^{top}$) where we include an additional contribution to the heat and particle transport coefficients ($\chi_{e,tr}, \chi_{i,tr}, D_{n,tr}$) in order to obtain smooth gradients of the kinetic profiles. These additional values are composed of two terms, one which is constant and one which is proportional to the pedestal electron heat diffusivity, that is $\chi_{tr} = c_1 + c_2 \chi_{ped}$, where c_1 and c_2 are constant coefficients, and are different for

7 Conclusion

electrons and ions. This approach was necessary as TGLF would otherwise (at least in the analyzed cases) under-predict the particle and ion heat fluxes in the region just inside the pedestal top, resulting in an over prediction of the density and ion temperature peaking. Also, the small gradients of the kinetic profiles and the large fluxes typical of this region make it difficult for TGLF to converge to stationary conditions. This is because small changes in the kinetic profiles, during the different iterations of the ASTRA transport code, can cause large differences in the fluxes predicted by TGLF. This is particularly severe in the region just inside the pedestal top, causing large fluctuations from very small to very large fluxes, hampering the convergence to stationary conditions of the kinetic profiles with practical time steps. The adoption of prescribed diffusion coefficients in this transition region ($\chi_{e,tr}$, $\chi_{i,tr}$, $D_{n,tr}$) strongly facilitates the convergence of the ASTRA simulations, making them more stable and robust.

The SOL model consists of a set of analytical formulas, obtained through an extension of the two point model [9], which calculate $n_{e,sep}$, $T_{e,sep}$, $T_{i,sep}$, and the source of neutrals at the separatrix, and has proven to robustly describe the effect of the fueling rate on $n_{e,sep}$ for the AUG cases considered. An important input parameter to the formula evaluating $n_{e,sep}$ is the divertor neutral pressure p_0 . To estimate this quantity, a scaling has been derived using AUG experimental data. We have shown that a self-consistent treatment of the boundary conditions is a key element of this approach, and is necessary to capture the dependence of the pedestal pressure on the separatrix density, and therefore on the fueling rate, increasing the detail of the physics describing pedestal and global confinement.

In the modeling workflow, many ASTRA simulations are launched in parallel, each with a different value of the pedestal width, where the kinetic profiles are evolved until stationary conditions are reached. As a result of the imposition of the condition $\langle \nabla T_e \rangle / T_{e,ped} \approx const = -0.5 [\text{cm}^{-1}]$, by increasing the pedestal width the pedestal top temperature increases, and therefore also the total pressure. Therefore, a fine scan in pedestal width allows us to obtain a fine scan in pedestal top pressure. The MISHKA code [3] is then used to calculate the peeling-ballooning mode (PBM) stability of the pedestals corresponding to the different values of the pedestal width. The final pressure profile, providing the result of the modeling workflow, is the one with the highest stable pedestal pressure, corresponding to pre-ELM conditions.

The model has been extensively validated, testing it on a database of 50 experimental cases covering the strongest possible AUG operational parameter variations. The prediction of the model is compared with experimental measurements and with the scaling law of the ITER physics basis IPB98(y,2), regularly applied over the last two decades to qualify confinement in present experiments. Comparisons are also performed with the most recently derived scaling law ITPA20-IL from the international

multi-device tokamak confinement database specific for ITER like plasmas, and with AUG specific regressions, made on the AUG confinement database only. It has been shown that the prediction of the model is very accurate and robust across the database, with a significantly lower mean relative error with respect to each of the scaling laws considered. This shows that indeed a sophisticated model which contains a description of the physics regulating plasma confinement can capture important dependencies beyond the possibilities of a log-linear regression of experimental data. In particular we have noticed that, for the AUG experimental cases considered, both the IPB98(y,2) and the ITPA20-IL scaling laws tend to be less accurate at higher values of the fueling rate (Γ_D), as they do not capture the confinement degradation caused by this parameter. The fact that the model is instead capable of capturing the effect of fueling correctly is a very important aspect for the study of the scenarios for ITER and future fusion reactors. Power exhaust sets constraints on the possible variation of the fueling rate, therefore it is important to take into account the effect that the operating conditions have on the fusion performance, by including it in the simulations.

Overall, the analysis carried out in this work shows that the model can accurately reproduce the change in confinement caused by a change in plasma current, heating power, fueling rate, triangularity, and magnetic field. Some important experimental cases have been included in the data set, which has been considered in this thesis to provide specific stringent tests for the model. In particular, the model has proven to reliably capture the effect of different heating mix (e.g. correctly predicting the effect on confinement caused by a change in T_e/T_i), and of different NBI voltage (i.e. the effect of a change in the core particle source). This modeling framework has proven to also correctly describe plasma confinement for two particular operating regimes, such as the ITER baseline scenarios, and the small ELMs scenario. This shows that plasmas in the small ELMs regime are not far from the peeling-ballooning limit provided by linear MHD stability codes, such as MISHKA, allowing accurate predictions also in this plasma regime, at least for the cases taken into account.

The new pedestal transport model we presented can robustly capture the effect of the different plasma parameters on the pedestal pressure. It also brings important advantages, as it can accurately predict the pedestal top density with no need of experimental information, as opposed to the widely applied EPED model where this must be given as input, increasing the predictive capabilities of previous integrated models. It also brings for the first time (to our knowledge) the capabilities of modeling separately the electron temperature and the ion temperature profiles in the pedestal region. Even though this is obtained with quite rough assumptions, i.e. considering that the pedestal ion heat diffusivity is equal to that of the electrons summed with the ion neoclassical diffusivity $\chi_{i,ped} = \chi_{e,ped} + \chi_{i,neo}$, it allows the determination of the pedestal top ion and electron temperature separately (without assuming $T_{e,ped} = T_{i,ped}$).

The capability of simulating the kinetic profiles of the confined plasma increases the

7 Conclusion

accuracy and the reliability in the prediction of energy confinement with respect to 0D scaling laws, as a 1D model can include the description of the physics phenomena which are strongly dependent on the gradients of the kinetic quantities, both in the core and in the pedestal regions. In particular we have shown that the density profile affects the shapes of the pressure gradients, which has a strong impact on the pedestal stability. Also, the prediction of 1D profiles is important for a reactor, since the shape of the kinetic profiles can influence the design and the prediction of the operation of a reactor [164], and therefore this is a great advantage that the integrated model provides over 0D approaches. In a reactor the fusion power is proportional to the central density squared and to the central temperature to the power of a value between 1 and 2. Thereby, already from this consideration, it is possible to deduce that profile effects can become important in determining the fusion power in a reactor. Instead, the simple prediction of the total stored energy by means of 0D approaches does not allow the estimation of the central temperature and density with high accuracy. Comparing the quality of the prediction on the pedestal and core thermal energy components, we found that the larger error is associated to the core. This could be surprising, as core transport is considered to be better understood and reproduced than pedestal confinement. This does not mean that the description of core transport is performing worse than expected (the error of the predicted core energy is small), but rather that the new pedestal modeling included in this work is robust and accurate. The successful application of the empirical pedestal model could therefore give guidelines in the understanding of the actual physical properties of transport in the pedestal. We have seen that TGLF tends to overestimate transport for cases with a relatively large fast ions density (at high NBI power), for which the turbulence stabilization can be important (but is not reproduced by TGLF), and for cases at high β . We have noticed that TGLF can underestimate the reduction of the ITGs growth rates when increasing β compared to linear gyrokinetic simulations, and it also does not include the nonlinear effect, which is usually considerably larger.

The identification and the discussion of the analogies and the differences between the present integrated model and the traditional 0D scaling laws, like the IPB98(y,2), reveal interesting aspects. The integrated model and the IPB98(y,2) scaling law make use of the same input parameters, with the exception of the line averaged density which is required by the IPB98(y,2). The model is instead capable of predicting the plasma density profile, but contains supplementary information and other elements in order to calculate it. Additional inputs are the effective charge Z_{eff} , the fueling rate, and the engineering parameters of the heating systems (e.g. power, angles, voltage of the beams, frequency of the gyrotrons, etc.). Another important aspect is that the model relies on empirical elements (in particular for the description of the pedestal and SOL) and a set of coefficients which increase the accuracy of its prediction, that the scaling law can not benefit of.

Parts of such components of the integrated modeling workflow, however, could be specific and applicable only to AUG, while scaling laws can readily be used for many different machines. In particular the pedestal transport model is based on experimental observations that we expect to be applicable to other devices since it relies on a multi-machine analysis which has identified a common parameter. However, because such common parameter is dimensional, the validity of this assumption needs to be tested for machines with a different size than AUG. An interesting consideration is that the application of the pedestal model to smaller machines could be limited by the locality of the description of pedestal transport, which in contrast becomes increasingly applicable towards a reactor, since the relative gyro-radius $\rho_* = \rho_s/a$ becomes smaller at increasing size a of the device. Of course this modeling of the pedestal can be easily and readily replaced by a theory-based model in case this becomes available.

The main aspects which produce a strong machine dependency are the geometry of the divertor and its baffles, the location of the gas valves, and the materials of the walls and the plasma facing components, which would probably make the estimation of the divertor neutral pressure not valid for different machines or divertors. A new scaling should be then derived for the tokamak of interest, using either experimental measurements if available, and/or synthetic data from simulations, particularly for non existing devices. Codes for the simulation of the SOL profiles are capable of predicting the divertor neutral pressure, therefore it would be interesting to study if a small database of such simulations would be sufficient to obtain a scaling for divertor neutral pressure p_0 , based on synthetic data rather than experimental measurements. If this approach results successful, leading to a similar accuracy of the prediction for AUG cases, the validation of the integrated model could be extended to other tokamaks. Testing the model on a larger device, such as JET, and on a smaller one, e.g. TCV, would allow us to obtain also a scan in the size of the device, which, if successful, would increase the confidence in the prediction for ITER, for which a large database of SOL simulations is already available, and therefore a dependence of p_0 on the main engineering parameters could be extracted.

In conclusion, this thesis clearly demonstrates that it is possible to combine together many different components for the description of plasma confinement into an integrated modeling workflow, which produces very realistic results. For the first time it has been proved that a 1D modeling approach can reproduce experimental results over the largest parameter variations allowed by a single device, with a higher accuracy than any statistical regression, even those performed on the device itself only. The approach of integrated models, like the one presented in this work, has therefore the potential to improve the prediction of the fusion performance in future tokamak reactors.

Moreover, even if some elements in the modeling are not completely based on theory, the integration of the different modules can provide important insights to better understand interdependencies, particularly between different plasma regions,

7 Conclusion

which are not possible to explore otherwise. Thereby, in addition to the increased predictive capabilities, which are promising also for applications to other devices, this approach has proven very helpful in the identification of hidden dependencies, specifically those resulting from effects that connect the different plasma regions (from SOL to core) which cannot be identified in 0D statistical studies nor in physics studies focusing on specific plasma regions.

Bibliography

- [1] G M Staebler, J E Kinsey, and R E Waltz. “A theory-based transport model with comprehensive physics”. In: *Phys. Plasmas* 14 (2007), p. 055909 (cit. on pp. 12, 41, 60, 75, 143).
- [2] W.A. Houlberg, K.C. Shaing, S.P. Hirshman, et al. “Bootstrap current and neoclassical transport in tokamaks of arbitrary collisionality and aspect ratio”. In: *Phys. Plasmas* 4 (1997), p. 3230 (cit. on pp. 12, 57, 75, 143).
- [3] A.B. Mihailovskii. “Optimization of computational MHD normal-mode analysis for tokamaks”. In: *Plasma Phys. Rep.* 23.10 (1997), p. 844 (cit. on pp. 13, 66, 91, 143, 144).
- [4] Stangeby. *The Plasma Boundary of Magnetic Fusion Devices*. Ed. by IOP. IOP Publishing Ltd., 2000 (cit. on pp. 13, 55, 68, 143).
- [5] P C Stangeby. “Basic physical processes and reduced models for plasma detachment”. In: *Plasma Physics and Controlled Fusion* 60.4 (2018), p. 044022. DOI: [10.1088/1361-6587/aaacf6](https://doi.org/10.1088/1361-6587/aaacf6) (cit. on pp. 13, 35, 55, 68, 143).
- [6] PA Schneider, E Wolfrum, RJ Groebner, et al. “Analysis of temperature and density pedestal gradients in AUG, DIII-D and JET”. In: *Nuclear Fusion* 53.7 (2013), p. 073039 (cit. on pp. 13, 73, 74, 143).
- [7] P.B. Snyder, R.J. Groebner, A.W. Leonard, et al. “Development and validation of a predictive model for the pedestal height”. In: *Phys. Plasmas* 16 (2009), p. 056118 (cit. on pp. 13, 42, 54, 62, 83, 104, 143).
- [8] T. Stoltzfus-Dueck. “Transport-Driven Toroidal Rotation in the Tokamak Edge”. In: *Phys. Rev. Lett.* 108 (6 2012), p. 065002. DOI: [10.1103/PhysRevLett.108.065002](https://doi.org/10.1103/PhysRevLett.108.065002). URL: <https://link.aps.org/doi/10.1103/PhysRevLett.108.065002> (cit. on pp. 13, 87, 94, 128, 143).
- [9] A Kallenbach, M Bernert, R Dux, et al. “Neutral pressure and separatrix density related models for seed impurity divertor radiation in ASDEX Upgrade”. In: *Nuclear Materials and Energy* 18 (2019), pp. 166–174 (cit. on pp. 14, 68, 76, 94, 103, 144).
- [10] Enzo De Sanctis, Stefano Monti, and Marco Ripani. “The Building Blocks of Matter”. In: *Energy from Nuclear Fission: An Introduction*. Cham: Springer International Publishing, 2016, pp. 3–38. ISBN: 978-3-319-30651-3. DOI: [10.1007/978-3-319-30651-3_1](https://doi.org/10.1007/978-3-319-30651-3_1). URL: https://doi.org/10.1007/978-3-319-30651-3_1 (cit. on p. 27).

Bibliography

- [11] J.P. Freidberg. *Plasma physics and fusion energy*. Cambridge University Press, 2007. ISBN: 0521851076 (cit. on pp. 29, 30).
- [12] M. Zucchetti, L.A. El-Guebaly, R.A. Forrest, et al. “The feasibility of recycling and clearance of active materials from fusion power plants”. In: *Journal of Nuclear Materials* 367-370 (2007). Proceedings of the Twelfth International Conference on Fusion Reactor Materials (ICFRM-12), pp. 1355–1360. ISSN: 0022-3115. DOI: <https://doi.org/10.1016/j.jnucmat.2007.03.248>. URL: <http://www.sciencedirect.com/science/article/pii/S0022311507006058> (cit. on p. 30).
- [13] J. Wesson and DJ Campbell. *Tokamaks*. Oxford University Press, USA, 2004 (cit. on pp. 31, 35).
- [14] V.S. Mukhovatov and V.D. Shafranov. “Plasma equilibrium in a Tokamak”. In: *Nuclear Fusion* 11.6 (1971), pp. 605–633. DOI: [10.1088/0029-5515/11/6/005](https://doi.org/10.1088/0029-5515/11/6/005). URL: <https://doi.org/10.1088/0029-5515/11/6/005> (cit. on p. 31).
- [15] J.P. Gunn, S. Carpentier-Chouchana, F. Escourbiac, et al. “Surface heat loads on the ITER divertor vertical targets”. In: *Nuclear Fusion* 57.4 (2017), p. 046025. DOI: [10.1088/1741-4326/aa5e2a](https://doi.org/10.1088/1741-4326/aa5e2a). URL: <https://doi.org/10.1088/1741-4326/aa5e2a> (cit. on p. 35).
- [16] M. Shimada, M. Nagami, K. Ioki, et al. “Helium Ash Exhaust with Single-Null Poloidal Divertor in Doublet III”. In: *Phys. Rev. Lett.* 47 (11 1981), pp. 796–799. DOI: [10.1103/PhysRevLett.47.796](https://doi.org/10.1103/PhysRevLett.47.796). URL: <https://link.aps.org/doi/10.1103/PhysRevLett.47.796> (cit. on p. 35).
- [17] F. Wagner, G. Becker, K. Behringer, et al. “Regime of Improved Confinement and High Beta in Neutral-Beam-Heated Divertor Discharges of the ASDEX Tokamak”. In: *Phys. Rev. Lett.* 49 (19 1982), pp. 1408–1412. DOI: [10.1103/PhysRevLett.49.1408](https://doi.org/10.1103/PhysRevLett.49.1408). URL: <https://link.aps.org/doi/10.1103/PhysRevLett.49.1408> (cit. on p. 36).
- [18] Y R Martin, T Takizuka, and the ITPA CDBM H-mode Threshold Data Group. “Power requirement for accessing the H-mode in ITER”. In: *Journal of Physics: Conference Series* 123 (2008), p. 012033. DOI: [10.1088/1742-6596/123/1/012033](https://doi.org/10.1088/1742-6596/123/1/012033). URL: <https://doi.org/10.1088/1742-6596/123/1/012033> (cit. on p. 36).
- [19] F. Ryter, T. Pütterich, M. Reich, et al. “H-mode threshold and confinement in helium and deuterium in ASDEX Upgrade”. In: *Nuclear Fusion* 49.6 (2009), p. 062003. DOI: [10.1088/0029-5515/49/6/062003](https://doi.org/10.1088/0029-5515/49/6/062003). URL: <https://doi.org/10.1088/0029-5515/49/6/062003> (cit. on p. 36).
- [20] Marco Cavedon. *The role of the radial electric field in the development of the edge transport barrier in the ASDEX Upgrade tokamak*. 2016 (cit. on p. 36).

- [21] H. Biglari, P. H. Diamond, and P. W. Terry. “Influence of sheared poloidal rotation on edge turbulence”. In: *Physics of Fluids B: Plasma Physics* 2.1 (1990), pp. 1–4. DOI: [10.1063/1.859529](https://doi.org/10.1063/1.859529). eprint: <https://doi.org/10.1063/1.859529>. URL: <https://doi.org/10.1063/1.859529> (cit. on p. 36).
- [22] E Viezzer, T Pütterich, R M McDermott, et al. “Parameter dependence of the radial electric field in the edge pedestal of hydrogen, deuterium and helium plasmas”. In: *Plasma Physics and Controlled Fusion* 56.7 (2014), p. 075018. DOI: [10.1088/0741-3335/56/7/075018](https://doi.org/10.1088/0741-3335/56/7/075018). URL: <https://doi.org/10.1088/0741-3335/56/7/075018> (cit. on p. 36).
- [23] H Zohm. “Edge localized modes (ELMs)”. In: *Plasma Physics and Controlled Fusion* 38.2 (1996), p. 105 (cit. on p. 37).
- [24] A Loarte, G Saibene, R Sartori, et al. “Transient heat loads in current fusion experiments, extrapolation to ITER and consequences for its operation”. In: *Physica Scripta* T128 (2007), pp. 222–228. DOI: [10.1088/0031-8949/2007/t128/043](https://doi.org/10.1088/0031-8949/2007/t128/043). URL: <https://doi.org/10.1088/0031-8949/2007/t128/043> (cit. on p. 37).
- [25] G. Taylor, J. D. Strachan, R. V. Budny, et al. “Fusion Heating in a Deuterium-Tritium Tokamak Plasma”. In: *Phys. Rev. Lett.* 76 (15 1996), pp. 2722–2725. DOI: [10.1103/PhysRevLett.76.2722](https://link.aps.org/doi/10.1103/PhysRevLett.76.2722). URL: <https://link.aps.org/doi/10.1103/PhysRevLett.76.2722> (cit. on p. 38).
- [26] P. R. Thomas, P. Andrew, B. Balet, et al. “Observation of Alpha Heating in JET DT Plasmas”. In: *Phys. Rev. Lett.* 80 (25 1998), pp. 5548–5551. DOI: [10.1103/PhysRevLett.80.5548](https://link.aps.org/doi/10.1103/PhysRevLett.80.5548). URL: <https://link.aps.org/doi/10.1103/PhysRevLett.80.5548> (cit. on p. 38).
- [27] R.V. Budny and. “Alpha heating, isotopic mass, and fast ion effects in deuterium–tritium experiments”. In: *Nuclear Fusion* 58.9 (2018), p. 096011. DOI: [10.1088/1741-4326/aaca04](https://doi.org/10.1088/1741-4326/aaca04). URL: <https://doi.org/10.1088/1741-4326/aaca04> (cit. on p. 38).
- [28] M Keilhacker, A Gibson, C Gormezano, et al. “High fusion performance from deuterium-tritium plasmas in JET”. In: *Nuclear Fusion* 39.2 (1999), pp. 209–234. DOI: [10.1088/0029-5515/39/2/306](https://doi.org/10.1088/0029-5515/39/2/306). URL: <https://doi.org/10.1088/0029-5515/39/2/306> (cit. on p. 39).
- [29] ITER Physics Basis Editors. In: *Nucl. Fusion* 39 (1999), p. 2175 (cit. on pp. 40, 96).
- [30] M Shimada, DJ Campbell, M Wakatani, et al. *Physics basis of ITER-FEAT*. Tech. rep. ITER Joint Central Team, 2001 (cit. on p. 40).
- [31] E.J. Doyle (Chair Transport Physics), W.A. Houlberg (Chair Confinement Da Modelling), Y. Kamada (Chair Pedestal, et al. “Chapter 2: Plasma confinement and transport”. In: *Nuclear Fusion* 47.6 (2007), S18–S127. DOI: [10.1088/0029-5515/47/6/s02](https://doi.org/10.1088/0029-5515/47/6/s02). URL: <https://doi.org/10.1088/0029-5515/47/6/s02> (cit. on p. 40).

- [32] T C Luce, C C Petty, and J G Cordey. “Application of dimensionless parameter scaling techniques to the design and interpretation of magnetic fusion experiments”. In: *Plasma Physics and Controlled Fusion* 50.4 (2008), p. 043001. DOI: [10.1088/0741-3335/50/4/043001](https://doi.org/10.1088/0741-3335/50/4/043001). URL: <https://doi.org/10.1088%2F0741-3335%2F50%2F4%2F043001> (cit. on p. 41).
- [33] C.D. Challis, J. Garcia, M. Beurskens, et al. “Improved confinement in JET high beta plasmas with an ITER-like wall”. In: *Nuclear Fusion* 55.5 (2015), p. 053031. DOI: [10.1088/0029-5515/55/5/053031](https://doi.org/10.1088/0029-5515/55/5/053031). URL: <https://doi.org/10.1088%2F0029-5515%2F55%2F5%2F053031> (cit. on pp. 41, 110).
- [34] J Garcia and D Cambon and. “On the universality of power laws for tokamak plasma predictions”. In: *Plasma Physics and Controlled Fusion* 60.2 (2018), p. 025028. DOI: [10.1088/1361-6587/aa9878](https://doi.org/10.1088/1361-6587/aa9878). URL: <https://doi.org/10.1088%2F1361-6587%2Faa9878> (cit. on p. 41).
- [35] J.E. Kinsey, G.M. Staebler, and R.E. Waltz. “The first transport code simulations using the trapped gyro-Landau-fluid model”. In: *Phys. Plasmas* 15 (2008), p. 055908 (cit. on p. 41).
- [36] J. Candy, C. Holland, R.E. Waltz, et al. “Tokamak profile prediction using direct gyrokinetic and neoclassical simulation”. In: *Phys. Plasmas* 16 (2009), p. 060704 (cit. on p. 41).
- [37] J.E. Kinsey, G.M. Staebler, J. Candy, et al. “ITER predictions using the GYRO verified and experimentally validated trapped gyro-Landau fluid transport model”. In: *Nucl. Fusion* 51 (2011), p. 083001 (cit. on p. 41).
- [38] M. Murakami, J.M. Park, G. Giruzzi, et al. “Integrated modelling of steady-state scenarios and heating and current drive mixes for ITER”. In: *Nucl. Fusion* 51.10 (2011), p. 103006. URL: <http://stacks.iop.org/0029-5515/51/i=10/a=103006> (cit. on p. 41).
- [39] L. Garzotti, P. Belo, G. Corrigan, et al. “Simulations of density profiles, pellet fuelling and density control in ITER”. In: *Nuclear Fusion* 52.1 (2011), p. 013002. DOI: [10.1088/0029-5515/52/1/013002](https://doi.org/10.1088/0029-5515/52/1/013002). URL: <https://doi.org/10.1088%2F0029-5515%2F52%2F1%2F013002> (cit. on p. 41).
- [40] G.L. Falchetto and et al. “The European Integrated Tokamak Modelling (ITM) effort: achievements and first physics results”. In: *Nucl. Fusion* 54 (2014), p. 043018 (cit. on p. 41).
- [41] M Romanelli, G Corrigan, V Parail, et al. “JINTRAC: A system of codes for integrated simulation of tokamak scenarios”. In: *Plasma Fusion Res* (2014) (cit. on p. 41).
- [42] S. Breton, F.J. Casson, C. Bourdelle, et al. “First principle integrated modeling of multi-channel transport including Tungsten in JET”. In: *Nuclear Fusion* 58.9 (2018), p. 096003. DOI: [10.1088/1741-4326/aac780](https://doi.org/10.1088/1741-4326/aac780). URL: <https://doi.org/10.1088%2F1741-4326%2Faac780> (cit. on p. 41).

- [43] O. Linder, J. Citrin, G.M.D. Hogeweij, et al. “Flux-driven integrated modelling of main ion pressure and trace tungsten transport in ASDEX Upgrade”. In: *Nuclear Fusion* 59.1 (2018), p. 016003. DOI: [10.1088/1741-4326/aae875](https://doi.org/10.1088/1741-4326/aae875). URL: <https://doi.org/10.1088/1741-4326/aae875> (cit. on p. 41).
- [44] E. Fable, C. Angioni, V. Bobkov, et al. “The role of the source versus the collisionality in predicting a reactor density profile as observed on ASDEX Upgrade discharges”. In: *Nuclear Fusion* 59.7 (2019), p. 076042. DOI: [10.1088/1741-4326/ab1f28](https://doi.org/10.1088/1741-4326/ab1f28). URL: <https://doi.org/10.1088/1741-4326/ab1f28> (cit. on pp. 41, 78, 135).
- [45] Glenn Bateman, Thawatchai Onjun, and Arnold H Kritz. “Integrated predictive modelling simulations of burning plasma experiment designs”. In: *Plasma Physics and Controlled Fusion* 45.11 (2003), p. 1939. URL: <http://stacks.iop.org/0741-3335/45/i=11/a=001> (cit. on p. 41).
- [46] R.V. Budny, R. Andre, G. Bateman, et al. “Predictions of H-mode performance in ITER”. In: *Nucl. Fusion* 48 (2008), p. 075005 (cit. on p. 41).
- [47] R.V. Budny. “Comparisons of predicted plasma performance in ITER H-mode plasmas with various mixes of external heating”. In: *Nucl. Fusion* 49.8 (2009), p. 085008. URL: <http://stacks.iop.org/0029-5515/49/i=8/a=085008> (cit. on p. 41).
- [48] A.H. Kritz, T. Rafiq, C. Kessel, et al. “Integrated modelling for prediction of optimized ITER performance”. In: *Nucl. Fusion* 51.12 (2011), p. 123009 (cit. on p. 41).
- [49] T. Rafiq, A. H. Kritz, C. E. Kessel, et al. “Fusion power production in ITER baseline H-mode scenarios”. In: *Phys. Plasmas* 22.4, 042511 (2015) (cit. on p. 41).
- [50] M Murakami, JM Park, DB Batchelor, et al. “Exploration of ITER Steady-State Scenarios Using FASTRAN/IPS Integrated Transport Modeling”. In: *APS Meeting Abstracts*. Vol. 1. 2013, 8021P (cit. on p. 41).
- [51] FM Poli, CE Kessel, PT Bonoli, et al. “External heating and current drive source requirements towards steady-state operation in ITER”. In: *Nucl. Fusion* 54.7 (2014), p. 073007 (cit. on p. 41).
- [52] O. Meneghini, P. B. Snyder, S. P. Smith, et al. “Integrated fusion simulation with self-consistent core-pedestal coupling”. In: *Physics of Plasmas* 23.4, 042507 (2016). DOI: <http://dx.doi.org/10.1063/1.4947204>. URL: <http://scitation.aip.org/content/aip/journal/pop/23/4/10.1063/1.4947204> (cit. on pp. 41, 42).
- [53] O. Meneghini, S.P. Smith, P.B. Snyder, et al. “Self-consistent core-pedestal transport simulations with neural network accelerated models”. In: *Nuclear Fusion* 57.8 (2017), p. 086034. DOI: [10.1088/1741-4326/aa7776](https://doi.org/10.1088/1741-4326/aa7776). URL: <https://doi.org/10.1088/1741-4326/aa7776> (cit. on pp. 41, 42).

- [54] S Saarelma, C D Challis, L Garzotti, et al. “Integrated modelling of H-mode pedestal and confinement in JET-ILW”. In: *Plasma Physics and Controlled Fusion* 60.1 (2017), p. 014042. DOI: [10.1088/1361-6587/aa8d45](https://doi.org/10.1088/1361-6587/aa8d45). URL: <https://doi.org/10.1088/1361-6587/aa8d45> (cit. on pp. 41, 42, 110).
- [55] G.M. Staebler, N.T. Howard, J. Candy, et al. “A model of the saturation of coupled electron and ion scale gyrokinetic turbulence”. In: *Nuclear Fusion* 57.6 (2017), p. 066046 (cit. on pp. 41, 86).
- [56] C. Bourdelle, X. Garbet, F. Imbeaux, et al. “A new gyrokinetic quasilinear transport model applied to particle transport in tokamak plasmas”. In: *Physics of Plasmas* 14.11, 112501 (2007). DOI: <http://dx.doi.org/10.1063/1.2800869> (cit. on pp. 41, 60).
- [57] J Citrin, C Bourdelle, F J Casson, et al. “Tractable flux-driven temperature, density, and rotation profile evolution with the quasilinear gyrokinetic transport model QuaLiKiz”. In: *Plasma Physics and Controlled Fusion* 59.12 (2017), p. 124005. DOI: [10.1088/1361-6587/aa8aeb](https://doi.org/10.1088/1361-6587/aa8aeb). URL: <https://doi.org/10.1088/1361-6587/aa8aeb> (cit. on p. 41).
- [58] *Summary of the ITER Final Design Report*. ITER EDA Documentation Series 22. Vienna: INTERNATIONAL ATOMIC ENERGY AGENCY, 2001. URL: <https://www.iaea.org/publications/6442/summary-of-the-iter-final-design-report> (cit. on p. 41).
- [59] A.R. Polevoi, A. Loarte, N. Hayashi, et al. “Assessment of operational space for long-pulse scenarios in ITER”. In: *Nuclear Fusion* 55.6 (2015), p. 063019. DOI: [10.1088/0029-5515/55/6/063019](https://doi.org/10.1088/0029-5515/55/6/063019). URL: <https://doi.org/10.1088/0029-5515/55/6/063019> (cit. on p. 42).
- [60] G.W. Pacher, H.D. Pacher, A.S. Kukushkin, et al. “Core plasma operation consistent with SOL parameters in ITER”. In: *Nucl. Fusion* 43.3 (2003), p. 188. URL: <http://stacks.iop.org/0029-5515/43/i=3/a=304> (cit. on p. 42).
- [61] G W Pacher, H D Pacher, G Janeschitz, et al. “Operating window of ITER from consistent core–pedestal–SOL modelling with modified MMM transport and carbon”. In: *Plasma Physics and Controlled Fusion* 46.5A (2004), A257–A264. DOI: [10.1088/0741-3335/46/5a/028](https://doi.org/10.1088/0741-3335/46/5a/028). URL: <https://doi.org/10.1088/0741-3335/46/5a/028> (cit. on p. 42).
- [62] R. Zagórski, I. Voitsekhovitch, I. Ivanova-Stanik, et al. “Integrated core–SOL–divertor modelling for ITER including impurity: effect of tungsten on fusion performance in H-mode and hybrid scenario”. In: *Nuclear Fusion* 55.5 (2015), p. 053032. DOI: [10.1088/0029-5515/55/5/053032](https://doi.org/10.1088/0029-5515/55/5/053032). URL: <https://doi.org/10.1088/0029-5515/55/5/053032> (cit. on p. 42).

- [63] M G Dunne, S Potzel, F Reimold, et al. “The role of the density profile in the ASDEX-Upgrade pedestal structure”. In: *Plasma Physics and Controlled Fusion* 59.1 (2016), p. 014017. DOI: [10.1088/0741-3335/59/1/014017](https://doi.org/10.1088/0741-3335/59/1/014017) (cit. on pp. 43, 103).
- [64] E. Stefanikova, L. Frassinetti, S. Saarelma, et al. “Effect of the relative shift between the electron density and temperature pedestal position on the pedestal stability in JET-ILW and comparison with JET-C”. In: *Nuclear Fusion* 58.5 (2018), p. 056010. DOI: [10.1088/1741-4326/aab216](https://doi.org/10.1088/1741-4326/aab216). URL: <https://doi.org/10.1088/1741-4326/aab216> (cit. on pp. 43, 103).
- [65] L. Frassinetti, M.G. Dunne, U. Sheikh, et al. “Role of the pedestal position on the pedestal performance in AUG, JET-ILW and TCV and implications for ITER”. In: *Nuclear Fusion* 59.7 (2019), p. 076038. DOI: [10.1088/1741-4326/ab1eb9](https://doi.org/10.1088/1741-4326/ab1eb9). URL: <https://doi.org/10.1088/1741-4326/ab1eb9> (cit. on pp. 43, 64, 103).
- [66] U. Stroth for the ASDEX Upgrade Team and the EUROfusion MST1 Team. “Overview of ASDEX Upgrade results”. In: *Nuclear Fusion* 53.10 (2013), p. 104003. DOI: [10.1088/0029-5515/53/10/104003](https://doi.org/10.1088/0029-5515/53/10/104003). URL: <https://doi.org/10.1088/0029-5515/53/10/104003> (cit. on p. 45).
- [67] H. Zohm and the ASDEX Upgrade team. “Recent ASDEX Upgrade research in support of ITER and DEMO”. In: *Nuclear Fusion* 55.10 (2015), p. 104010. DOI: [10.1088/0029-5515/55/10/104010](https://doi.org/10.1088/0029-5515/55/10/104010). URL: <https://doi.org/10.1088/0029-5515/55/10/104010> (cit. on p. 45).
- [68] A Kallenbach for the ASDEX Upgrade Team and the EUROfusion MST1 Team. “Overview of ASDEX Upgrade results”. In: *Nuclear Fusion* 57.10 (2017), p. 102015. DOI: [10.1088/1741-4326/aa64f6](https://doi.org/10.1088/1741-4326/aa64f6). URL: <https://doi.org/10.1088/1741-4326/aa64f6> (cit. on p. 45).
- [69] Patrick J McCarthy, Peter Martin, and Wolfgang Schneider. *The CLISTE interpretive equilibrium code*. Tech. rep. 1999 (cit. on p. 46).
- [70] Ian Hutchinson. *Principles of Plasma Diagnostics (second edition)*. Ed. by Cambridge University press. Cambridge University press, 2001 (cit. on p. 46).
- [71] B. Kurzan and H. D. Murmann. “Edge and core Thomson scattering systems and their calibration on the ASDEX Upgrade tokamak”. In: *Review of Scientific Instruments* 82.10 (2011), p. 103501. DOI: [10.1063/1.3643771](https://doi.org/10.1063/1.3643771). eprint: <https://doi.org/10.1063/1.3643771>. URL: <https://doi.org/10.1063/1.3643771> (cit. on p. 47).
- [72] S K Rathgeber, L Barrera, T Eich, et al. “Estimation of edge electron temperature profiles via forward modelling of the electron cyclotron radiation transport at ASDEX Upgrade”. In: *Plasma Physics and Controlled Fusion* 55.2 (2012), p. 025004. DOI: [10.1088/0741-3335/55/2/025004](https://doi.org/10.1088/0741-3335/55/2/025004). URL: <https://doi.org/10.1088/0741-3335/55/2/025004> (cit. on p. 48).

- [73] S S Denk, R Fischer, H M Smith, et al. “Analysis of electron cyclotron emission with extended electron cyclotron forward modeling”. In: *Plasma Physics and Controlled Fusion* 60.10 (2018), p. 105010. DOI: [10.1088/1361-6587/aadb2f](https://doi.org/10.1088/1361-6587/aadb2f). URL: <https://doi.org/10.1088/1361-6587/aadb2f> (cit. on p. 48).
- [74] H. Weisen, E. Delabie, J. Flanagan, et al. “Analysis of the inter-species power balance in JET plasmas”. In: *Nuclear Fusion* 60.3 (2020), p. 036004. DOI: [10.1088/1741-4326/ab6307](https://doi.org/10.1088/1741-4326/ab6307). URL: <https://doi.org/10.1088/1741-4326/ab6307> (cit. on p. 49).
- [75] E. Viezzer, T. Pütterich, R. Dux, et al. “High-resolution charge exchange measurements at ASDEX Upgrade”. In: *Review of Scientific Instruments* 83.10 (2012), p. 103501. DOI: [10.1063/1.4755810](https://doi.org/10.1063/1.4755810). eprint: <https://doi.org/10.1063/1.4755810>. URL: <https://doi.org/10.1063/1.4755810> (cit. on p. 49).
- [76] R. Fischer, C. J. Fuchs, B. Kurzan, et al. “Integrated Data Analysis of Profile Diagnostics at ASDEX Upgrade”. In: *Fusion Science and Technology* 58.2 (2010), pp. 675–684. DOI: [10.13182/FST10-110](https://doi.org/10.13182/FST10-110) (cit. on p. 49).
- [77] A. Ho, J. Citrin, F. Auriemma, et al. “Application of Gaussian process regression to plasma turbulent transport model validation via integrated modelling”. In: *Nuclear Fusion* 59.5 (2019), p. 056007. DOI: [10.1088/1741-4326/ab065a](https://doi.org/10.1088/1741-4326/ab065a). URL: <https://doi.org/10.1088/1741-4326/ab065a> (cit. on p. 50).
- [78] Judith Illerhaus, Rainer Fischer, G. Birkenmeier, et al. “Estimation, Validation and Uncertainty of the Position of the Separatrix Contour at ASDEX Upgrade”. In: 2017 (cit. on p. 50).
- [79] J Neuhauser, D Coster, H U Fahrbach, et al. “Transport into and across the scrape-off layer in the ASDEX Upgrade divertor tokamak”. In: *Plasma Physics and Controlled Fusion* 44.6 (2002), pp. 855–869. DOI: [10.1088/0741-3335/44/6/316](https://doi.org/10.1088/0741-3335/44/6/316). URL: <https://doi.org/10.1088/0741-3335/44/6/316> (cit. on pp. 51, 100).
- [80] W Horton. “Drift waves and transport”. In: *Reviews of Modern Physics* 71.3 (1999), p. 735 (cit. on p. 54).
- [81] Bruce D. Scott. “Drift wave versus interchange turbulence in tokamak geometry: Linear versus nonlinear mode structure”. In: *Physics of Plasmas* 12.6 (2005), p. 062314. DOI: [10.1063/1.1917866](https://doi.org/10.1063/1.1917866). eprint: <https://doi.org/10.1063/1.1917866>. URL: <https://doi.org/10.1063/1.1917866> (cit. on p. 54).
- [82] Bruce D Scott. “Tokamak edge turbulence: background theory and computation”. In: *Plasma Physics and Controlled Fusion* 49.7 (2007), S25–S41. DOI: [10.1088/0741-3335/49/7/s02](https://doi.org/10.1088/0741-3335/49/7/s02). URL: <https://doi.org/10.1088/0741-3335/49/7/s02> (cit. on pp. 54, 62).

- [83] B.D. Scott, A. Kendl, and T. Ribeiro. “Nonlinear Dynamics in the Tokamak Edge”. In: *Contributions to Plasma Physics* 50.3-5 (2010), pp. 228–241. DOI: [10.1002/ctpp.201010039](https://doi.org/10.1002/ctpp.201010039). eprint: <https://onlinelibrary.wiley.com/doi/pdf/10.1002/ctpp.201010039>. URL: <https://onlinelibrary.wiley.com/doi/abs/10.1002/ctpp.201010039> (cit. on p. 54).
- [84] N. Bonanomi, C. Angioni, P.C. Crandall, et al. “Effect of the isotope mass on the turbulent transport at the edge of L-mode plasmas in ASDEX Upgrade and JET-ILW”. In: *Nuclear Fusion* 59.12 (2019), p. 126025. DOI: [10.1088/1741-4326/ab3ecc](https://doi.org/10.1088/1741-4326/ab3ecc). URL: <https://doi.org/10.1088/1741-4326/ab3ecc> (cit. on p. 54).
- [85] AA Galeev and RZ Sagdeev. “Transport phenomena in a collisionless plasma in a toroidal magnetic system”. In: *Sov. Phys. JETP* 26.1 (1968), pp. 233–240 (cit. on p. 57).
- [86] RJ Bickerton, JW Connor, and JB Taylor. “Diffusion driven plasma currents and bootstrap tokamak”. In: *Nature Physical Science* 229.4 (1971), pp. 110–112 (cit. on p. 57).
- [87] AG Peeters. “The bootstrap current and its consequences”. In: *Plasma Physics and Controlled Fusion* 42.12B (2000), B231 (cit. on p. 57).
- [88] Olivier Sauter, Clemente Angioni, and YR Lin-Liu. “Neoclassical conductivity and bootstrap current formulas for general axisymmetric equilibria and arbitrary collisionality regime”. In: *Phys. Plasmas* 6.7 (1999), pp. 2834–2839 (cit. on p. 57).
- [89] O. Sauter, C. Angioni, and Y.R. Lin-Liu. “Neoclassical conductivity and bootstrap current formulas for general axisymmetric equilibria and arbitrary collisionality regime”. In: *Phys. Plasmas* 6 (1999), p. 2834 (cit. on pp. 57, 58).
- [90] O. Sauter, C. Angioni, and Y.R. Lin-Liu. “Erratum: "Neoclassical conductivity and bootstrap current formulas for general axisymmetric equilibria and arbitrary collisionality regime" [Phys. Plasmas 6, 2834 (1999)]”. In: *Phys. Plasmas* 9 (2002), p. 5140 (cit. on pp. 57, 58).
- [91] D. R. Smith, R. J. Fonck, G. R. McKee, et al. “Characterization and parametric dependencies of low wavenumber pedestal turbulence in the National Spherical Torus Experiment”. In: *Physics of Plasmas* 20.5 (2013), p. 055903. DOI: [10.1063/1.4803913](https://doi.org/10.1063/1.4803913). eprint: <https://doi.org/10.1063/1.4803913>. URL: <https://doi.org/10.1063/1.4803913> (cit. on p. 62).
- [92] P Manz, J E Boom, E Wolfrum, et al. “Velocimetry analysis of type-I edge localized mode precursors in ASDEX Upgrade”. In: *Plasma Physics and Controlled Fusion* 56.3 (2014), p. 035010. DOI: [10.1088/0741-3335/56/3/035010](https://doi.org/10.1088/0741-3335/56/3/035010). URL: <https://doi.org/10.1088/0741-3335/56/3/035010> (cit. on p. 62).

Bibliography

- [93] Z. Yan, G.R. McKee, R.J. Groebner, et al. “Pedestal density fluctuation dynamics during the inter-ELM cycle in DIII-D”. In: *Phys. Plasmas* 18 (2011), p. 056117 (cit. on p. 62).
- [94] Z. Yan, G.R. McKee, R.J. Groebner, et al. “High-Frequency Coherent Edge Fluctuations in a High-Pedestal-Pressure Quiescent H-mode Plasma”. In: *Phys. Rev. Lett.* 107 (2011), p. 055004 (cit. on p. 62).
- [95] A. Diallo, J. W. Hughes, M. Greenwald, et al. “Observation of Edge Instability Limiting the Pedestal Growth in Tokamak Plasmas”. In: *Phys. Rev. Lett.* 112 (11 2014), p. 115001. DOI: [10.1103/PhysRevLett.112.115001](https://doi.org/10.1103/PhysRevLett.112.115001). URL: <https://link.aps.org/doi/10.1103/PhysRevLett.112.115001> (cit. on p. 62).
- [96] D. Dickinson, C.M. Roach, S. Saarelma, et al. “Kinetic Instabilities that Limit beta in the Edge of a Tokamak Plasma: A Picture of an H-Mode Pedestal”. In: *Phys. Rev. Lett.* 108 (2012), p. 135002 (cit. on p. 62).
- [97] D Dickinson, C M Roach, S Saarelma, et al. “Microtearing modes at the top of the pedestal”. In: *Plasma Physics and Controlled Fusion* 55.7 (2013), p. 074006. DOI: [10.1088/0741-3335/55/7/074006](https://doi.org/10.1088/0741-3335/55/7/074006). URL: <https://doi.org/10.1088/0741-3335/55/7/074006> (cit. on p. 62).
- [98] S. Saarelma, M.N.A. Beurskens, D. Dickinson, et al. “MHD and gyro-kinetic stability of JET pedestals”. In: *Nuclear Fusion* 53.12 (2013), p. 123012. DOI: [10.1088/0029-5515/53/12/123012](https://doi.org/10.1088/0029-5515/53/12/123012). URL: <https://doi.org/10.1088/0029-5515/53/12/123012> (cit. on p. 62).
- [99] J.M. Canik, W. Guttenfelder, R. Maingi, et al. “Edge microstability of NSTX plasmas without and with lithium-coated plasma-facing components”. In: *Nuclear Fusion* 53.11 (2013), p. 113016. DOI: [10.1088/0029-5515/53/11/113016](https://doi.org/10.1088/0029-5515/53/11/113016). URL: <https://doi.org/10.1088/0029-5515/53/11/113016> (cit. on p. 62).
- [100] D.R. Hatch, D. Told, F. Jenko, et al. “Gyrokinetic study of ASDEX Upgrade inter-ELM pedestal profile evolution”. In: *Nuclear Fusion* 55.6 (2015), p. 063028. DOI: [10.1088/0029-5515/55/6/063028](https://doi.org/10.1088/0029-5515/55/6/063028). URL: <https://doi.org/10.1088/0029-5515/55/6/063028> (cit. on pp. 62, 85).
- [101] D. P. Fulton, Z. Lin, I. Holod, et al. “Microturbulence in DIII-D tokamak pedestal. I. Electrostatic instabilities”. In: *Physics of Plasmas* 21.4 (2014), p. 042110. DOI: [10.1063/1.4871387](https://doi.org/10.1063/1.4871387). eprint: <https://doi.org/10.1063/1.4871387>. URL: <https://doi.org/10.1063/1.4871387> (cit. on p. 62).
- [102] D. Told, F. Jenko, P. Xanthopoulos, et al. “Gyrokinetic microinstabilities in ASDEX Upgrade edge plasmas”. In: *Physics of Plasmas* 15.10 (2008), p. 102306. DOI: [10.1063/1.3000132](https://doi.org/10.1063/1.3000132). eprint: <https://doi.org/10.1063/1.3000132>. URL: <https://doi.org/10.1063/1.3000132> (cit. on p. 62).

- [103] F. Jenko, D. Told, P. Xanthopoulos, et al. “Gyrokinetic turbulence under near-separatrix or nonaxisymmetric conditions”. In: *Physics of Plasmas* 16.5 (2009), p. 055901. DOI: [10.1063/1.3089603](https://doi.org/10.1063/1.3089603). eprint: <https://doi.org/10.1063/1.3089603>. URL: <https://doi.org/10.1063/1.3089603> (cit. on p. 62).
- [104] Weigang Wan, Scott E. Parker, Yang Chen, et al. “Global Gyrokinetic Simulation of Tokamak Edge Pedestal Instabilities”. In: *Phys. Rev. Lett.* 109 (2012), p. 185004 (cit. on p. 62).
- [105] D.R. Hatch, M. Kotschenreuther, S. Mahajan, et al. “Microtearing turbulence limiting the JET-ILW pedestal”. In: *Nuclear Fusion* 56.10 (2016), p. 104003 (cit. on pp. 62, 84).
- [106] D.R. Hatch, M. Kotschenreuther, S. Mahajan, et al. “A gyrokinetic perspective on the JET-ILW pedestal”. In: *Nuclear Fusion* 57.3 (2017), p. 036020. DOI: [10.1088/1741-4326/aa51e1](https://doi.org/10.1088/1741-4326/aa51e1). URL: <https://doi.org/10.1088/1741-4326/aa51e1> (cit. on pp. 62, 84).
- [107] P.B. Snyder, N. Aiba, M. Beurskens, et al. “Pedestal stability comparison and ITER pedestal prediction”. In: *Nucl. Fusion* 49 (2009), p. 085035 (cit. on p. 63).
- [108] H. R. Wilson, J. W. Connor, A. R. Field, et al. “Ideal magnetohydrodynamic stability of the tokamak high-confinement-mode edge region”. In: *Physics of Plasmas* 6.5 (1999), pp. 1925–1934. DOI: [10.1063/1.873492](https://doi.org/10.1063/1.873492). eprint: <https://doi.org/10.1063/1.873492>. URL: <https://doi.org/10.1063/1.873492> (cit. on p. 63).
- [109] H.R. Wilson, P.B. Snyder, and G.T.A. Huysmans. “Numerical studies of edge localized instabilities in tokamaks”. In: *Phys. Plasmas* 9 (2002), p. 1277 (cit. on p. 63).
- [110] P.B. Snyder, H.R. Wilson, J.R. Ferron, et al. “Edge localized modes and the pedestal: A model based on coupled peeling-ballooning modes”. In: *Phys. Plasmas* 9 (2002), p. 2037 (cit. on pp. 63, 64).
- [111] P.B. Snyder, K.H. Burrell, H.R. Wilson, et al. “Stability and dynamics of the edge pedestal in the low collisionality regime: physics mechanisms for steady-state ELM-free operation”. In: *Nucl. Fusion* 47 (2007), p. 961 (cit. on p. 63).
- [112] P.B. Snyder, R.J. Groebner, J.W. Hughes, et al. “A first-principles predictive model of the pedestal height and width: development, testing and ITER optimization with the EPED model”. In: *Nucl. Fusion* 51 (2011), p. 103016 (cit. on p. 63).
- [113] P.B. Snyder, H.R. Wilson, J.R. Ferron, et al. “ELMs and constraints on the H-mode pedestal: peeling-ballooning stability calculation and comparison with experiment”. In: *Nucl. Fusion* 44 (2004), p. 320 (cit. on pp. 64, 118).

Bibliography

- [114] Hannes Alfvén. “Existence of electromagnetic-hydrodynamic waves”. In: *Nature* 150.3805 (1942), pp. 405–406 (cit. on p. 65).
- [115] S.I. Braginskii. “Review of Plasma Physics”. In: ed. by M.A. Leontovich. Vol. 1. New York: Consultants Bureau, 1965, p. 214 (cit. on p. 68).
- [116] R J Goldston, M L Reinke, and J A Schwartz. “A new scaling for divertor detachment”. In: *Plasma Physics and Controlled Fusion* 59.5 (2017), p. 055015. DOI: [10.1088/1361-6587/aa5e6e](https://doi.org/10.1088/1361-6587/aa5e6e). URL: <https://doi.org/10.1088/2F1361-6587%2Faa5e6e> (cit. on pp. 68, 76).
- [117] G V Pereverzev and P N Yushmanov. “ASTRA-an automatic system for transport analysis in a tokamak”. In: *IPP-report* (1991) (cit. on pp. 69, 70).
- [118] E Fable, C Angioni, F J Casson, et al. “Novel free-boundary equilibrium and transport solver with theory-based models and its validation against ASDEX Upgrade current ramp scenarios”. In: *Plasma Phys. Control. Fusion* 55.12 (2013), p. 124028. DOI: [10.1088/0741-3335/55/12/124028](https://doi.org/10.1088/0741-3335/55/12/124028). URL: <https://doi.org/10.1088/2F0741-3335%2F55%2F12%2F124028> (cit. on pp. 69, 88).
- [119] E Poli, AG Peeters, and GV Pereverzev. “TORBEAM, a beam tracing code for electron-cyclotron waves in tokamak plasmas”. In: *Computer physics communications* 136.1 (2001), pp. 90–104 (cit. on pp. 70, 75).
- [120] AA Ivanov et al. “New adaptive grid plasma evolution code SPIDER”. In: *32nd EPS Conf. on Plasma Physics* 29C (2005). URL: <http://tinyurl.sfx.mpg.de/v4z0> (cit. on pp. 70, 75).
- [121] PA Schneider, E Wolfrum, RJ Groebner, et al. “Differences in the H-mode pedestal width of temperature and density”. In: *Plasma Physics and Controlled Fusion* 54.10 (2012), p. 105009 (cit. on pp. 74, 100).
- [122] Alexei Polevoi, Hiroshi Shirai, and Tomonori Takizuka. *Benchmarking of the NBI block in ASTRA code versus the OFMC calculations*. Tech. rep. Japan Atomic Energy Research Inst., 1997 (cit. on p. 75).
- [123] R Fischer. “Effective ion charge Z_{eff} from integrated analysis of multiple diagnostics at ASDEX Upgrade”. In: *37th EPS Conf. on Plasma Physics* 34A (2010). URL: <http://tinyurl.sfx.mpg.de/v7oe> (cit. on pp. 75, 97, 119).
- [124] M Siccino, E Fable, K Lackner, et al. “A 0D stationary model for the evaluation of the degree of detachment on the divertor plates”. In: *Plasma Physics and Controlled Fusion* 58.12 (2016), p. 125011. DOI: [10.1088/0741-3335/58/12/125011](https://doi.org/10.1088/0741-3335/58/12/125011). URL: <https://doi.org/10.1088/2F0741-3335%2F58%2F12%2F125011> (cit. on p. 76).
- [125] A.W. Leonard, M.A. Mahdavi, C.J. Lasnier, et al. “Scaling radiative divertor solutions to high power in DIII-D”. In: *Nuclear Fusion* 52.6 (2012), p. 063015. DOI: [10.1088/0029-5515/52/6/063015](https://doi.org/10.1088/0029-5515/52/6/063015). URL: <https://doi.org/10.1088/2F0029-5515%2F52%2F6%2F063015> (cit. on p. 76).

- [126] D. Brida, T. Lunt, M. Wischmeier, et al. “Heat flux pattern in detached L-modes and ELM mitigated H-modes with rotating magnetic perturbations in ASDEX Upgrade”. In: *Nuclear Fusion* 57.11 (2017), p. 116006. DOI: [10.1088/1741-4326/aa78b9](https://doi.org/10.1088/1741-4326/aa78b9). URL: <https://doi.org/10.1088/1741-4326/aa78b9> (cit. on p. 76).
- [127] A Kallenbach, H J Sun, T Eich, et al. “Parameter dependences of the separatrix density in nitrogen seeded ASDEX Upgrade H-mode discharges”. In: *Plasma Physics and Controlled Fusion* 60.4 (2018), p. 045006. DOI: [10.1088/1361-6587/aaab21](https://doi.org/10.1088/1361-6587/aaab21) (cit. on pp. 76, 77, 79, 103).
- [128] A. Herrmann, H. Greuner, N. Jaksic, et al. “Solid tungsten Divertor-III for ASDEX Upgrade and contributions to ITER”. In: *Nuclear Fusion* 55.6 (2015), p. 063015. DOI: [10.1088/0029-5515/55/6/063015](https://doi.org/10.1088/0029-5515/55/6/063015). URL: <https://doi.org/10.1088/0029-5515/55/6/063015> (cit. on p. 76).
- [129] S. Potzel, M. Wischmeier, M. Bernert, et al. “A new experimental classification of divertor detachment in ASDEX Upgrade”. In: *Nuclear Fusion* 54.1 (2013), p. 013001. DOI: [10.1088/0029-5515/54/1/013001](https://doi.org/10.1088/0029-5515/54/1/013001). URL: <https://doi.org/10.1088/0029-5515/54/1/013001> (cit. on p. 77).
- [130] S. Potzel, M. Wischmeier, M. Bernert, et al. “Formation of the high density front in the inner far SOL at ASDEX Upgrade and JET”. In: *Journal of Nuclear Materials* 463 (2015), pp. 541–545. DOI: <https://doi.org/10.1016/j.jnucmat.2014.12.008>. URL: <http://www.sciencedirect.com/science/article/pii/S0022311514009490> (cit. on pp. 77, 78).
- [131] C. Angioni, A. G. Peeters, G. V. Pereverzev, et al. “Density Peaking, Anomalous Pinch, and Collisionality in Tokamak Plasmas”. In: *Phys. Rev. Lett.* 90 (20 2003), p. 205003. DOI: [10.1103/PhysRevLett.90.205003](https://doi.org/10.1103/PhysRevLett.90.205003). URL: <https://link.aps.org/doi/10.1103/PhysRevLett.90.205003> (cit. on p. 78).
- [132] C. Angioni, R.M. McDermott, E. Fable, et al. “Gyrokinetic modelling of electron and boron density profiles of H-mode plasmas in ASDEX Upgrade”. In: *Nuclear Fusion* 51.2 (2011), p. 023006. DOI: [10.1088/0029-5515/51/2/023006](https://doi.org/10.1088/0029-5515/51/2/023006). URL: <https://doi.org/10.1088/0029-5515/51/2/023006> (cit. on p. 78).
- [133] A Kallenbach, M Bernert, R Dux, et al. “Analytical calculations for impurity seeded partially detached divertor conditions”. In: *Plasma Physics and Controlled Fusion* 58.4 (2016), p. 045013. DOI: [10.1088/0741-3335/58/4/045013](https://doi.org/10.1088/0741-3335/58/4/045013) (cit. on p. 80).
- [134] J Stober and the ASDEX Upgrade Team. “Improvement of ion-temperature-profile determination from charge exchange measurements by inclusion of total-neutral-flux data”. In: *Plasma Physics and Controlled Fusion* 39.7 (1997), pp. 1145–1152. DOI: [10.1088/0741-3335/39/7/008](https://doi.org/10.1088/0741-3335/39/7/008). URL: <https://doi.org/10.1088/0741-3335/39/7/008> (cit. on p. 82).

- [135] M. Willensdorfer, E. Fable, E. Wolfrum, et al. “Particle transport analysis of the density build-up after the L–H transition in ASDEX Upgrade”. In: *Nuclear Fusion* 53.9 (2013), p. 093020. DOI: [10.1088/0029-5515/53/9/093020](https://doi.org/10.1088/0029-5515/53/9/093020). URL: <https://doi.org/10.1088/0029-5515/53/9/093020> (cit. on p. 82).
- [136] M. Kotschenreuther, X. Liu, D.R. Hatch, et al. “Gyrokinetic analysis and simulation of pedestals to identify the culprits for energy losses using ‘fingerprints’”. In: *Nuclear Fusion* 59.9 (2019), p. 096001 (cit. on p. 85).
- [137] D.R. Hatch, M. Kotschenreuther, S. Mahajan, et al. “Pedestal transport”. In: *10th Plasma Kinetics Working Meeting*. 2017. URL: http://www-thphys.physics.ox.ac.uk/research/plasma/wpi/workshop2017_pdfs/hatch.pdf (cit. on p. 85).
- [138] F. Porcelli, D. Boucher, and M.N. Rosenbluth. “Model for the sawtooth period and amplitude”. In: *Plasma Phys. Control. Fusion* 38 (12 1996). DOI: [10.1088/0741-3335/38/12/010](https://doi.org/10.1088/0741-3335/38/12/010) (cit. on p. 86).
- [139] T. Luda, C. Angioni, M.G. Dunne, et al. “Integrated modeling of ASDEX Upgrade plasmas combining core, pedestal and scrape-off layer physics”. In: *Nuclear Fusion* 60.3 (2020), p. 036023. DOI: [10.1088/1741-4326/ab6c77](https://doi.org/10.1088/1741-4326/ab6c77). URL: <https://doi.org/10.1088/1741-4326/ab6c77> (cit. on pp. 88, 96).
- [140] I. Erofeev, E. Fable, C. Angioni, et al. “Theory-based modeling of LOC–SOC transitions in ASDEX Upgrade”. In: *Nucl. Fusion* 57.12 (2017), p. 126067. DOI: [10.1088/1741-4326/aa8e32](https://doi.org/10.1088/1741-4326/aa8e32). URL: <https://doi.org/10.1088/1741-4326/aa8e32> (cit. on p. 88).
- [141] F. Sommer, J. Stober, C. Angioni, et al. “Transport properties of H-mode plasmas with dominant electron heating in comparison to dominant ion heating at ASDEX Upgrade”. In: *Nuclear Fusion* 55.3 (2015), p. 033006. DOI: [10.1088/0029-5515/55/3/033006](https://doi.org/10.1088/0029-5515/55/3/033006) (cit. on pp. 88, 97).
- [142] C. Konz, W. Zwingmann, F. Osmanlic, et al. “First physics applications of the Integrated Tokamak Modelling (ITM-TF) tools to the MHD stability analysis of experimental data and ITER scenarios”. In: *EPS* (2011), O2 (cit. on p. 91).
- [143] R. Neu, R. Dux, A. Geier, et al. “New results from the tungsten programme at ASDEX Upgrade”. In: *Journal of Nuclear Materials* 313-316 (2003). Plasma-Surface Interactions in Controlled Fusion Devices 15, pp. 116–126. ISSN: 0022-3115. DOI: [https://doi.org/10.1016/S0022-3115\(02\)01386-7](https://doi.org/10.1016/S0022-3115(02)01386-7). URL: <http://www.sciencedirect.com/science/article/pii/S0022311502013867> (cit. on p. 97).
- [144] F. Ryter, J. Stober, A. Stähler, et al. “Confinement and transport studies of conventional scenarios in ASDEX Upgrade”. In: *Nuclear Fusion* 41.5 (2001), pp. 537–550. DOI: [10.1088/0029-5515/41/5/307](https://doi.org/10.1088/0029-5515/41/5/307). URL: <https://doi.org/10.1088/0029-5515/41/5/307> (cit. on p. 103).

- [145] H. Urano, J. Hobirk, C.F. Maggi, et al. “Characterization of electron density based on operational parameters in JET H-mode plasmas with C and ILW”. In: *Proc. 43rd EPS Conference on Plasma Physics*. 2016 (cit. on p. 110).
- [146] C.F. Maggi, S. Saarelma, F.J. Casson, et al. “Pedestal confinement and stability in JET-ILW ELMy H-modes”. In: *Nuclear Fusion* 55.11 (2015), p. 113031. DOI: [10.1088/0029-5515/55/11/113031](https://doi.org/10.1088/0029-5515/55/11/113031). URL: <https://doi.org/10.1088/0029-5515/55/11/113031> (cit. on p. 110).
- [147] G Saibene, R Sartori, A Loarte, et al. “Improved performance of ELMy H-modes at high density by plasma shaping in JET”. In: *Plasma Physics and Controlled Fusion* 44.9 (2002), pp. 1769–1799. DOI: [10.1088/0741-3335/44/9/301](https://doi.org/10.1088/0741-3335/44/9/301). URL: <https://doi.org/10.1088/0741-3335/44/9/301> (cit. on p. 118).
- [148] M G Dunne, L Frassinetti, M N A Beurskens, et al. “Global performance enhancements via pedestal optimisation on ASDEX Upgrade”. In: *Plasma Physics and Controlled Fusion* 59.2 (2016), p. 025010. DOI: [10.1088/1361-6587/59/2/025010](https://doi.org/10.1088/1361-6587/59/2/025010). URL: <https://doi.org/10.1088/1361-6587/59/2/025010> (cit. on p. 118).
- [149] A Merle, O Sauter, and S Yu Medvedev. “Pedestal properties of H-modes with negative triangularity using the EPED-CH model”. In: *Plasma Physics and Controlled Fusion* 59.10 (2017), p. 104001. DOI: [10.1088/1361-6587/aa7ac0](https://doi.org/10.1088/1361-6587/aa7ac0). URL: <https://doi.org/10.1088/1361-6587/aa7ac0> (cit. on p. 118).
- [150] J. Citrin, F. Jenko, P. Mantica, et al. “Nonlinear Stabilization of Tokamak Microturbulence by Fast Ions”. In: *Phys. Rev. Lett.* 111 (15 2013), p. 155001. DOI: [10.1103/PhysRevLett.111.155001](https://link.aps.org/doi/10.1103/PhysRevLett.111.155001). URL: <https://link.aps.org/doi/10.1103/PhysRevLett.111.155001> (cit. on p. 120).
- [151] A. Jansen van Vuuren, B. Geiger, A. S. Jacobsen, et al. “An edge fast-ion D-alpha system installed at ASDEX Upgrade”. In: *Review of Scientific Instruments* 90.10 (2019), p. 103501. DOI: [10.1063/1.5121588](https://doi.org/10.1063/1.5121588) (cit. on pp. 122, 123).
- [152] F. Romanelli. “Ion-temperature-gradient-driven modes and anomalous ion transport in tokamaks”. In: *Phys. Fluids B* 1 (1989), p. 1018 (cit. on p. 122).
- [153] S. C. Guo and F. Romanelli. “The linear threshold of the ion-temperature-gradient-driven mode”. In: *Physics of Fluids B: Plasma Physics* 5.2 (1993), pp. 520–533. DOI: [10.1063/1.860537](https://doi.org/10.1063/1.860537) (cit. on p. 122).
- [154] J Weiland, E Asp, X Garbet, et al. “Effects of temperature ratio on JET transport in hot ion and hot electron regimes”. In: *Plasma Physics and Controlled Fusion* 47.3 (2005), pp. 441–449. DOI: [10.1088/0741-3335/47/3/003](https://doi.org/10.1088/0741-3335/47/3/003). URL: <https://doi.org/10.1088/0741-3335/47/3/003> (cit. on p. 122).

Bibliography

- [155] F. Rytter, C. Angioni, M. Dunne, et al. “Heat transport driven by the ion temperature gradient and electron temperature gradient instabilities in ASDEX Upgrade H-modes”. In: *Nuclear Fusion* 59.9 (2019), p. 096052. DOI: [10.1088/1741-4326/ab3061](https://doi.org/10.1088/1741-4326/ab3061). URL: <https://doi.org/10.1088/1741-4326/ab3061> (cit. on p. 122).
- [156] B. LaBombard, Massachusetts Institute of Technology. Plasma Science, and Fusion Center. *KN1D: A 1-D space, 2-D velocity, kinetic transport algorithm for atomic and molecular hydrogen in an ionizing plasma*. Plasma Science and Fusion Center, Massachusetts Institute of Technology, 2001 (cit. on p. 123).
- [157] G. Verdoolaege, C. Angioni S.M. Kaye, and O.J.W.F. Kardaun. “The updated ITPA global H-mode confinement database: description and analysis”. In: *to be submitted to Nuclear Fusion* (2020) (cit. on p. 123).
- [158] F. Rytter, C. Angioni, G. Tardini, et al. “The upgraded ASDEX Upgrade contribution to the ITPA confinement database: description and analysis”. In: *to be submitted to Nuclear Fusion* (2020) (cit. on p. 124).
- [159] J Citrin, J Garcia, T Görler, et al. “Electromagnetic stabilization of tokamak microturbulence in a high-beta regime”. In: *Plasma Physics and Controlled Fusion* 57.1 (2014), p. 014032. DOI: [10.1088/0741-3335/57/1/014032](https://doi.org/10.1088/0741-3335/57/1/014032). URL: <https://doi.org/10.1088/0741-3335/57/1/014032> (cit. on p. 133).
- [160] G. G. Whelan, M. J. Pueschel, and P. W. Terry. “Nonlinear Electromagnetic Stabilization of Plasma Microturbulence”. In: *Phys. Rev. Lett.* 120 (17 2018), p. 175002. DOI: [10.1103/PhysRevLett.120.175002](https://link.aps.org/doi/10.1103/PhysRevLett.120.175002). URL: <https://link.aps.org/doi/10.1103/PhysRevLett.120.175002> (cit. on p. 133).
- [161] F. Jenko, W. Dorland, M. Kotschenreuther, et al. “Electron temperature gradient driven turbulence”. In: *Phys. Plasmas* 7 (2000), p. 1904 (cit. on p. 133).
- [162] T. Görler, X. Lapillonne, S. Brunner, et al. “The global version of the gyrokinetic turbulence code GENE”. In: *J. Comput. Phys.* 230 (2011), p. 7053 (cit. on p. 133).
- [163] T Lunt. In: *planned to be published in Nuclear Fusion* (2021) (cit. on p. 135).
- [164] E. Fable, C. Angioni, M. Siccino, et al. “Plasma physics for fusion reactor system codes: Framework and model code”. In: *Fusion Engineering and Design* 130 (2018), pp. 131–136. ISSN: 0920-3796. DOI: <https://doi.org/10.1016/j.fusengdes.2018.03.061>. URL: <http://www.sciencedirect.com/science/article/pii/S0920379618302801> (cit. on p. 146).